Investigations of the reactivity of energised species and the development of a new radical source for surface science

A thesis submitted for the degree of
Doctor of Philosophy

by

Felicity Edith Gossan

Supervisor: Professor S. D. Price
Department of Chemistry
University College London
2019

Declaration

I confirm that the work presented in this thesis is my own. Where information has been derived from other sources, I confirm that this has been indicated in the thesis.

Felicity Gossan

Acknowledgements

I would like to thank the following people for their contributions and support over the past four years:

- Professor Steve Price for his guidance and interminable patience;
- Past and present members of the Price group, particularly Dr Helen Kimber, Dr James Fletcher, and Helena Pradip for their camaraderie in (and occasionally out of) the lab;
- Dr Mike Parkes and journal club for advice and science chats;
- The Settlers of UCL Chemistry, for providing a needed, happy distraction;
- Friends and family who have provided endless support over my studies, particularly during an extraordinarily tumultuous final year – Kealan, Nick, Hannah, Jim, Helen, Nicole, Dom, Judith and Jake;
- The NHS.

Abstract

‘Energised species’ is a broad term that encompasses a number of different chemical entities. Three specific types of energised species are investigated in this thesis: anions, dications and radicals. These three chemical groups are relevant in a variety of media, ranging from the planetary ionospheres to industrial plasmas. The study of dications, anions and radicals is therefore crucial to further our understanding of the physical and chemical processes occurring in these environments.

This thesis divides into two distinct thematic branches. The first branch describes the development of a pure source of free radicals for radical-surface chemistry. A novel piece of equipment, RISA, has been built at UCL that can produce a pure beam of radicals. The pure radical source is coupled to an ultra-high vacuum surface science chamber, which enables the study of radical-surface chemistry. These studies will be used to further our understanding of the interstellar medium and in key industrial processes. The building, optimisation and commissioning of this apparatus is described in this thesis, alongside some proof-of-principle results. The generation of an O radical beam is described in detail. The commissioning of each component of the apparatus is also described. A key step in producing a radical beam with the RISA apparatus is the production and manipulation of an anion beam. The generation of O^- and SF_5^- beams are described.

The second thematic branch of this thesis reports the interactions between doubly-charged positive ions and neutral gases. Dications are thought to be important reactive species in ionospheres and interstellar environments, and understanding their reactions is key to furthering our understanding of such media. The investigations of the bimolecular reactivity of Ar^{2+} and SO^{2+} with a variety of neutrals are described. A mass spectrometer equipped with a position-sensitive coincidence ion detector has been used to explore the dynamics of these reactions. Reaction energetics and scattering diagrams have been extracted from this data, which has allowed the determination of some interesting, and unusual reaction mechanisms.

Impact Statement

The contents of this thesis both further our understanding of the gas-phase chemical dynamics of small molecules, and gas-phase radical-surface interactions.

Table of Contents

Frequently used acronyms

AES	Auger electron spectroscopy
COM	Centre-of-mass
DET	Double electron transfer
EI	Electron ionisation
IE	Ionisation energy
KER	Kinetic energy release
LAB	Laboratory
MCP	Microchannel plate
MS	Mass spectrometer
PEC	Potential energy curve
PES	Potential energy surface
PSCO-MS	Position-sensitive coincidence mass spectrometer
PSD	Position-sensitive detector
RAIRS	Reflection absorption infrared spectroscopy
RISA	Radical beam surface science apparatus
SEA	Single electron attachment
SET	Single electron transfer
TOF	Time-of-flight
TPD	Temperature programmed desorption
UHV	Ultra-high vacuum
UHVC	Ultra-high vacuum chamber
XPS	X-ray photoelectron spectroscopy

List of Figures

List of Tables

1 Introduction

"Investigations of the reactivity of energised species" is a broad topic. As such, this thesis divides into two distinct branches under this title. The first branch describes the development of a pure source of free radicals for radical-surface chemistry. Throughout the commissioning and construction of this equipment we studied the reactivity of anions and radicals - energised species - to optimise and improve the apparatus. In chapter 6 of this thesis the design, optimisation and commissioning of this new piece of apparatus is described in detail, and proof-of-principle experiments are presented. The second branch of this thesis reports the interactions between doubly-charged positive ions and neutral gases. In chapters 4 and 5, interesting reactivity is revealed between Ar^{2+} and SO^{2+}, and a variety of neutrals. Energised gaseous species are ubiquitous. Indeed, anions, radicals and dications are thought to contribute to the chemistry of a variety of energised media, such as ionospheres and the interstellar medium (ISM). The topics presented in this thesis explore the interactions of energised species, thus furthering our understanding of various environments.

This chapter is broadly split into two sections. The first section introduces radical-surface chemistry, and highlights the scientific motivation behind the work presented in chapter 6. The second half provides scientific context for the dication studies presented in chapters 4 and 5.

1.1 Radical- surface chemistry

1.1.1 Overview

A free radical is an atom, molecule or ion with one or more unpaired electrons – a feature that provides an inherent instability that leads to a reactive and transient nature. The aim of this research is to develop a piece of apparatus to study the interaction of gas phase radicals with solid surfaces. Our understanding of these reactions has been limited by the absence of a clean source of free radicals for such surface studies. Indeed, in many of the recent experiments in this field, the surfaces studied have been bombarded with a mixture of the radical of interest, radical precursors and other species generated in an 'impure' radical source. This mixture of

products masks any radical-surface interactions when probed experimentally, a problem that has led to a paucity of data in this field. Chapter 6 of this thesis present the design, development and some initial results from an apparatus that was built at UCL, which generates a 'pure' beam of free radicals for radical-surface chemistry.

1.1.2 Gas-phase techniques

Information gained from the experimental studies of radicals is vital to our understanding of a range of energized media as varied as planetary atmospheres, industrial plasmas and the interstellar medium (ISM).[1-7] To model such environments, experimental information about the generation and reactions of these energetic species is required. For example, in the large dust clouds in the ISM, the space between the stars, the interaction of ionizing radiation or energized electrons with neutral molecules can lead to the production of radicals and a vast range of other products.[7-9] It follows that to accurately model such a dust cloud, we need data pertaining to the formation efficiency and subsequent reactions of any radicals formed. Indeed, laboratory studies are vital to our understanding of the role of radicals in the reactive processes that may lead to the molecules observed in these clouds by astronomers. In highly energized media, such as plasmas, the interaction of energetic electrons with neutral molecules leads to the production of radicals amongst a range of other products.[10] Again, as when modelling the dust clouds of the ISM, to accurately model plasmas a detailed understanding of both how the radicals are formed and how they go on to react is required. Thus, laboratory studies of radicals are essential to our understanding of these media.

In the gas phase, there are several well-established techniques that are used to study radical chemistry. Many rely upon a DC discharge to generate the radicals of interest.[11] A radical source of this kind consists of two electrodes at opposite ends of a cell that is filled with a chosen precursor gas. An electric potential is applied to the electrodes, creating an electric field across the cell. When this voltage exceeds a certain value, termed the striking voltage, the gas in the cell ionizes creating a plasma. When the plasma is 'struck', any cations within the cell are accelerated towards the

cathode, and any electrons are accelerated towards the anode. As these species are rapidly accelerated to opposite ends of the cell, they may collide with other neutral precursor gas species, ionizing them. Indeed, DC discharges create a mixture of atoms, ions and radicals. For example, OH radicals have been generated following the dissociation of H_2O in a DC discharge, amongst atomic hydrogen, oxygen and un-dissociated water molecules.[12] Glow discharges produce radicals and present similar problems: the production of a beam that consists of the radical of interest in a bath of impurities.[13]

Laser photolysis can be used to generate free radicals. When a molecule absorbs a resonant photon, an electronic transition occurs. If the excited electronic state is anti-bonding with respect to a certain co-ordinate, then dissociation will follow. Depending upon the system, this process can lead to the formation of a radical. Of course, as with any molecular dissociation, the radical of interest will be formed alongside some impurity species as shown in equation 1.1.

$$HNO_3 + h\upsilon \rightarrow HO + NO_2 \qquad 1.1$$

In this example, OH radicals are formed amongst NO_2 impurities. As the dissociation efficiency is unlikely to be 100%, the radicals will also be formed amongst a high concentration of HNO_3 molecules.[14]

Many gas-phase radical experiments rely upon spectroscopic techniques to selectively probe for radicals of interest.[15] For example, laser induced fluorescence (LIF) is often employed when studying the kinetics of radicals involved in atmospheric processes.[16-18] This probing technique requires a tunable laser and a detector that can monitor fluorescence. The power of this technique lies in the species-specific absorption, and subsequent fluorescence, of photons. A typical LIF experiment involves the irradiation of a gaseous sample with photons of a specific, chosen wavelength. Any species with an electronic transition that is resonant with the laser will absorb radiation, and will fluoresce shortly afterwards. The fluorescence photons will hit the detector and the number of counts recorded

will be proportional to the concentration of the emitting species. In this way, even trace quantities of radicals can be selectively probed following gas-phase experiments. For example, LIF has been employed previously to detect and examine the temporal behavior of CF_2 and CF radicals in a CF_4 plasma etching reactor.[19]

The radical sources described in this section highlight the need for a 'pure' source of free radicals for radical-surface chemistry. That is, a source that produces a beam that consists overwhelmingly of one species: the radical of interest. All methods of production described produce the radicals in a bath of impurities. For gas phase experiments, spectroscopic methods can be used to probe selectively for the radical of interest. However, if any of these sources were used for radical-surface experiments surface-impurity interactions would dominate any surface spectra recorded. Indeed, the radicals would be a trace species in the beams produced and so the target surfaces used would become saturated with impurities preventing any detectable radical-surface interaction. It is worth noting that some radicals are stable and do not require a pure source to generate them, such as NO and O_2.[57] Radical-surface experiments involving such species interacting with metal surfaces have provided relevant data for the models detailed later in this chapter, however they do not provide a general method to study radical-surface chemistry.[58, 59] Thus, a 'pure' beam of free radicals is required to study radical-surface chemistry.

1.1.3 Radical-surface chemistry and industrial processes

A detailed grasp of the reactions between plasmas and surfaces is key to optimize many industrial processes. As many plasmas contain radicals, understanding radical-surface chemistry is crucial to further our understanding of plasma-surface interaction. For example, plasma-etching is a process that is used to produce various electronic components, such as integrated circuits. This process relies upon the selective deposition of radicals onto surfaces to control etching anisotropy and selectivity.[2, 3] The radicals in the plasma are thought to form 'blocking layers' that prevent etching in certain regions of the target surface, however the precise pathway by which the radicals and surface interact is unknown. This example is one

of many industrial processes in which surfaces are processed by plasmas where radicals are thought to play a key role.[4, 5, 20, 21] Clearly, it would be extremely beneficial to improve our understanding of radical-surface chemistry, with a view to optimize such processes.

Plasma-enhanced chemical vapour deposition (PECVD) is another example of an industrial process that relies upon radical-surface chemistry. CVD allows the coating of surfaces with thin films, and has been successfully applied to manufacture coatings as exotic as self-cleaning glass.[20] Indeed, CVD is a ubiquitous process in industrial materials chemistry that has led to the production of many commercially important thin films. In traditional CVD, the material to be coated is placed into an ultra-high vacuum chamber, the size of which typically dictates the maximum size of the substrate to be used. In the chamber, or in a separate adjacent chamber, the coating material is heated, or the pressure around it is lowered, until the film material vaporizes. The coating vapor then settles on the target material, forming a uniform thin film. The temperature and pressure can be adjusted to control film thickness. Typically, reaction rates can be very slow and the temperatures required are very high. PECVD increases the rate of reaction and lowers the required temperatures for CVD, two improvements that have been widely attributed to the presence of radicals in the plasma beam.[22] However, the exact role of radicals in the process is unknown and could be elucidated through radical-surface studies. Again, a ‘pure’ radical source would enable the study of radical-surface interactions to elucidate the mechanism behind an industrially important process.

1.1.4 Radical-surface chemistry and the ISM

The study of radical-surface reactions will not only increase our understanding of commercially relevant industrial processes, but would provide further insight into the chemistry of radicals in the ISM. The ISM is often imagined as the vast empty space between stars. In fact, it houses clouds that are composed of 99% gaseous and 1% solid matter, and are thought to have a rich chemistry.[23, 24] Indeed, many molecules have been detected in these clouds and astronomers strive to model the chemistry occurring within them to account for the relevant column densities of each

species observed.[25] Several radicals have been observed, or predicted to exist, in the ISM ranging from CN, OH, and HCO to more exotic, large radicals such as C_8H.[25, 26]

The solid matter within the clouds is comprised of dust grains, the presence of which were first inferred from the 'extinction' of starlight - the obscuration of the light transmitted from stars behind the dust clouds.[27] There are two main types of dust, ascribed based on their composition: silicate or carbonaceous grains. The dust grains scatter much of the external radiation present in the ISM, allowing the centre of the clouds to reach temperatures as low as 10 K.[25, 28] These conditions cause gaseous species to accrete onto the grains, forming icy molecular mantles on the surface of the dust. Indeed, the grains are thought to be coated in ices that are composed mainly of water, but also contain other small molecules such as NH_3, CO, CO_2, CH_3OH and radicals.[7, 29-31] For ice mantles that are several layers of molecules thick, it is thought that the molecular ices can evolve in complexity through radical-surface chemistry, *via* interactions with both radicals generated in the ices and from the gas-phase.[32] Thus, radical-surface chemistry plays a vital role in the evolution and reactions of the gas phase molecules observed in the clouds. Clearly, deepening our understanding of radical-surface interactions will extend our knowledge of the ISM and the potentially origin-of-life, star forming chemistry that occurs there.

Our motivation for building a 'pure' radical source is rooted in the need to improve our understanding of radical-surface interactions to successfully model highly energized media and the chemistry of the ISM. A brief overview of the different types of models that are used is provided below.

1.1.5 Plasma modelling

Plasma physics involves the numerical modelling of the contents of a plasma. Due to the inherent complexity of plasmas, both experimental and numerical modelling are necessary to characterize plasma systems. There are three main types of numerical model: kinetic, fluid and hybrid. A kinetic numerical model uses Monte-Carlo (MC) methods to model non-equilibrium

systems. A fluid model is faster to compute than a kinetic model, however has a lower accuracy by comparison. Hybrid models aim to find a balance between the precision of a kinetic model and the computational speed of a fluid one.[33-36]

There are several commercial codes, which are generally used to model plasmas for technological applications. COMSOL Multiphysics and ANSYS Fluent are two commonly used examples.[37, 38] In a non-equilibrium system, there is a non-Maxwell free-electron distribution and these commercial models aim to solve the Boltzmann equation for systems to determine the actual distribution of electrons in the plasma. There are also several non-commercial codes that have been developed in universities, such as the non-PDPSIM hybrid code developed by the Kushner group.[39] This code aims to model PECVD by solving transport equations for the charged and neutral species within the plasma, calculates the electric potential and uses MC methods to determine electron energy.[39] Indeed, many groups have used such codes to model the interaction of plasmas with objects and surfaces.[36, 40-45] It is clear that improving our experimental understanding of how radicals and surfaces interact will aid such models in the future.

1.1.6 Modelling in the ISM

The main aim for most numerical astrochemical models of the clouds in the ISM is to account for the various molecular abundances observed within them by astronomers.[46, 47] Early models solved steady-state, time-independent, rate equations that were primarily focused on ion-molecule reactions.[48-50] Indeed, these early models only considered the reactions of H_2 adsorbed on the dust grains within the clouds, assuming most reactivity occurred in the gas phase. Nonetheless, these early codes provided quantitative data that tallied with the molecular abundances that had been observed to date at that time. However, as astronomy became more advanced and the list of observed molecules grew, these early models proved insufficient. A model that accounted for radicals and other species reacting on the surfaces of the dust grains built on these early models,

however a great advance came with the dawn of pseudo-time dependent models.[51]

Pseudo-time independent models, so-called as they account for the evolution of molecules within the clouds over time but neglect any variation of the physical conditions, solve time-dependent rate equations to account for the observed molecular abundances.[52, 53] Models of this type have successfully accounted for many of the gas-phase abundances observed, however there are still vast gaps in our understanding of the chemistry of these clouds.[54, 55] Many of these gaps arise due to a paucity of data surrounding experimental rate constants for radicals interacting with surface species.

1.1.7 Current heterogeneous radical-surface experiments

Despite the limitations of the 'impure' radical sources introduced above, there are several techniques that are currently applied to study radical-surface chemistry, which are detailed below. In this section, the need for a 'pure' source of radicals to have a general method to investigate radical-surface interactions is highlighted.

As mentioned previously, LIF spectroscopy can be used to detect even trace amounts of radicals in the gas phase. This technique has also been applied to investigate radical-surface chemistry and has provided a basic insight into such interactions.[56] Indeed, such experiments have been used to produce data to model the scattering coefficients of incident radicals from surfaces.[57] The basis of these experiments relies upon the collection of two LIF spectra: one of an impure radical beam and one with a target substrate in the radical beam.[11] Information can be gleamed about any radical-surface interactions by comparing the two spectra. This method provides some insight into radical-surface chemistry, however does not provide the mechanistic detail that is much needed in this field.

If a surface and radicals possess complementary functional groups, the radicals can coat the surface through covalent or non-covalent interactions, forming self-assembled monolayers of adsorbates.[61] Of course, this method is limited to just a few specific systems and again does not

provide a general method by which radical-surface chemistry can be investigated. Clearly, experiments cannot be limited to such radicals and the field would be greatly advanced by the production of a ‘pure’ source.

Spin-sensitive scanning tunneling microscopy (SS-STM) has been used to investigate organic radicals deposited on highly oriented pyrolytic graphite surfaces (HOPG).[62] For example, 1,1-diphenyl-2-picrylhydrazyl adsorbed on Au |111 | has been studied using this technique.[62] Although the species investigated using this technique have been limited to stable radicals, SS-STM is a way to monitor most types of radicals interacting with conducting surfaces. An atomically sharp tip is brought within a few nm of a conducting surface and a small voltage is applied between the tip and the sample. If the voltage applied to the tip is positive with respect to the sample a charge gradient is established, causing electrons to tunnel from the surface to the tip. SS-STM differs from ‘normal’ STM in that it is sensitive to the magnetic local density of states of the sample surface, and the spin orientation of tunneling electrons. The tip of an SS-STM microscope must be magnetic, to provide a source or sink of spin-polarized electrons for tunneling. This method also relies upon the surface substrate being electrically conducting, limiting the variety of surfaces that can be studied. Thus, SS-STM does not provide the much-needed generic method to investigate radical-surface chemistry.

Recently, radicals that have a high affinity for forming hydrogen bonds have been deposited onto oxide coated inorganic films by a ‘dip and wash’ technique.[64] For example, a gold surface was readily coated with N-tertbutyl-N-aminoacyl radicals following dipping in a solution containing the radical and a non-polar solvent.[64, 65] This method is hinged upon hydrogen bonds forming between the radical and an OH group on the oxide coated film. Such a pre-requisite means that this approach fails to provide a general way to investigate radical-surface chemistry. Furthermore, the ‘dip and wash’ technique is carried out on the lab bench, as opposed to in the ultrahigh vacuum (UHV) conditions required to investigate the plasma and interstellar chemistry of interest.

One example of a successful UHV radical-surface experiment is the dosing of triparacarboxylic polychlorotriphenylmethyl (PTMTC) radicals onto a gold surface doped with copper.[66] This experiment involves the sublimation of PTMTC onto the surface within the vacuum by heating a quartz crucible to 453 K. Although this radical source does not require a precursor, eliminating the previously discussed masking problems, it must be heated to a very high temperature. This constraint renders this method inappropriate for the investigation of radical-surface interstellar chemistry, due to the low temperatures within the dense molecular clouds (10 K). Also, this technique requires the radical to be readily available by sublimation, limiting its suitability to study just a few specific systems.

The varied approaches summarized above have each provided insight into the chemistry that occurs when specific radicals interact with surfaces. However, it is clear that a pure beam of free radicals is needed to provide a general method to study such interactions. The work presented in chapters 4 and 5 of this thesis describes a new apparatus that has been built at UCL, which aims to elucidate the chemistry that occurs at the radical-surface interface. As discussed, detailed information about such interactions would be beneficial to the fields of plasma and ISM chemistry.

1.2 Dication-molecule reactivity

1.2.1 Overview

Dications, the dipositive ions of atomic and molecular species, have been of great experimental interest since their discovery in the 1930s.[67] A number of experiments have aimed to investigate their properties, and it was found that they behave very differently to monocations.[68] Indeed, a dipositive ion generally has a markedly different chemistry to its monocation counterpart. Over the last 20 years, experiments investigating the reactivity of dications have gained impetus and their properties are now reasonably well understood.[69-74] Chapter 4 and 5 of this thesis present studies of the low energy reactions of dications with neutral molecules. Experimental details are given in chapter 2. The remainder of this chapter introduces the relevant

background information that is crucial to the study of atomic and molecular dications.

1.2.2 Dications in ionospheres

Dications are ubiquitous in energized media as varied as planetary ionospheres, industrial plasmas and are even thought to be present in interstellar dust clouds. In fact, the density of dications in some ionospheres is thought to be comparable to chemically significant monocations.[75, 76] As such, the study of the formation and reactions of dications is key to our understanding of the chemistry of these environments.

Saturn's moon Titan has a characteristic 'haze' around it's atmosphere, which has been imaged by Voyager 1 and the Casini-Huygens probe.[77, 78] Up to 50 ions were detected in the atmosphere and a rich organic chemistry, like that of prebiotic Earth, has been suggested.[79] The presence of N_2^{2+} has been predicted in the upper atmosphere of Titan.[78] Perhaps interestingly, Titan has been found to have a much more complex chemistry than Saturn itself, and the study of low energy dication-neutral interactions will further our understanding of this chemically rich environment.

Dications are not only predicted to be present in the ionosphere of Titan, but have been detected and/or inferred in the atmospheres of three of the inner planets: Venus, Earth and Mars.[76, 81-85] Indeed, CO_2^{2+}, has been predicted to be present in the ionospheres of Mars and Venus, and O^{2+} and N^{2+} have been detected in the ionosphere of Venus and the terrestrial magnetosphere of Earth.

Recent studies have suggested that the dissociation of dications contributes to the atmospheric erosion of planets and other bodies, such as Titan.[86-89] These studies suggest that the kinetic energy associated with the separation of two monocations formed following dication dissociation may cause the fragments to escape into space, therefore depleting the atmosphere from which they came. This process is thought to be particularly significant in the atmospheres of Mars and Titan.[86-89] Thus, to understand the chemistry of dications is crucial to further our understanding of the atmospheres of the inner planets, including our own.

1.2.3 Dications and the interstellar medium

As mentioned previously, the clouds in the ISM have a rich, complex chemistry. In fact, most of the 200+ molecules present in the ISM are contained in these vast, dusty clouds.[25, 90] There are two types of clouds: diffuse and dense. Diffuse clouds have typical densities of 10^7 - 10^9 m^{-3}, and have temperatures of ~ 100 K.[23] Dense clouds have densities of 10^9 – 10^{10} m^{-3} and are colder compared to diffuse clouds, with average temperatures of ~10 K.[90] Ionizing radiation can penetrate the edges of these dense clouds and to the centre of diffuse clouds. As such, both types of cloud are thought to contain dicationic species.[91]

Neutral-neutral reactions often have activation barriers, and occur very slowly at the low temperatures within the clouds.[92] In contrast, ion-neutral reaction rates tend to increase with decreasing temperature, as they are not inhibited by such barriers.[70] Furthermore, the polarization attraction between the reactants pulls the two species together, increasing reaction rates. As such, much interstellar gas-phase chemistry is attributed to ion-neutral reactions.

Dications are thought to have similar, or faster, reaction rates with neutrals compared to monocations, owing to the greater polarization attraction between the reactant species. In fact, it is thought that many dication-neutral reaction rates are close to the collision frequency.[70] The products of dication-neutral reactions often include pairs of product monocations, with significant rovibrational and translational energy. These secondary monocations can go on to react with other species within the clouds, at an elevated collision energy compared to thermal monocations, which may result in different chemistry. Thus, dication-neutral collisions in interstellar clouds can have direct and indirect consequences to the chemical make-up of the ISM. Studying such reactions is of great importance to improve our understanding of this environment.

1.2.4 Forming dications

A positive ion forms when a neutral species loses an electron. This process, termed ionization, occurs when the precursor is supplied with

sufficient energy to eject an electron. If the species is supplied with enough energy to excite two electrons to the continuum, a dipositive species can form – a dication. For this process to occur, the energy supplied must surpass the double ionization energy of the precursor species. There are multiple energy sources that can form dications; the two primary techniques employed experimentally are described below.

1.2.5 Electron Ionization (EI)

Electron ionization (EI) is a process that forms cations through inelastic collisions between free electrons and neutral species. Experimentally, electrons are facile to produce at a chosen energy through thermionic emission from a filament; EI is commonly used in gas-phase ionization studies. In the dication experiments presented in chapters 4 and 5, electrons are produced at 150 eV through thermionic emission from an yttriated tungsten filament. The incident electrons are collimated into a beam, which is aimed across an effusive jet of neutral target species. Ions are generated through inelastic collisions between the electrons and neutrals. Ionization will occur if enough energy is transferred to the neutral to eject an electron.

$$AB + e^- \rightarrow AB^+ + 2e^- \qquad 1.2$$

Generally, single ionization is the dominant process (1.2), although double ionization makes a small contribution to the overall ion yield.[93, 94]

Double electron ionization can occur *via* either a direct or sequential mechanism. The former process is less common as electron correlation, which is required to eject two electrons simultaneously, is generally small for both atoms and molecules. Furthermore, for molecular species, a direct mechanism is less likely to lead to the production of a dication as the Franck-Condon overlap between the neutral and dicationic states is often poor. Indeed, the change in geometry between the neutral and dicationic species can be so great that the double ionization potential is harder to access, and is therefore the process is less likely. Therefore, an indirect, sequential mechanism that involves the formation of a monocation, followed by the ionization of the nascent monocation is thought to be the most likely dication formation process in molecules and atoms.

A drawback in using EI to produce ions for experimental studies is that upon ionization, not all the energy from the colliding electron will be transferred to the neutral species. Indeed, the colliding and ejected electrons will possess some amount of kinetic energy after colliding with the target neutral molecule. Therefore, the exact energetics and the states of the nascent product ions will not be known.

1.2.6 Photoionization

When an energetic photon is absorbed by a neutral species ionization can occur.

$$AB + h\nu \rightarrow AB^{+} + e^{-} \qquad 1.3$$

Initial photon sources used for gas phase studies were discharge lamps, which are a relatively crude photon source that cannot provide control over photon energy.[95] Although discharge lamps are still widely used, more recently, tunable UV/VUV photon sources and synchrotron radiation have been used to produce ions for gas phase studies.[96]

Below the ionization threshold, incident photons must be resonant to be absorbed. That is, they must possess an energy that matches a state to state transition in the target molecule. Furthermore, certain selection rules must be obeyed for a successful transition, which concern the conservation of angular momentum, spin and parity. To excite an electron above the ionization threshold is a non-resonant process. Any excess energy from the absorption of an energetic photon can be dissipated through the ejection of a photoelectron. The photoelectron can possess any value of *l*, the angular momentum quantum number, and therefore the conservation law is obeyed.[97-99]

Like EI, double photoionization can occur in either a direct or step-wise manner. Direct double photoionization can be modelled by considering the interaction of the two outgoing electrons. If the two electrons are produced in a direct photoionization event, the energy dependence of the dication yield can be predicted by Wannier theory, shown in equation 1.4.[100, 101]

$$\sigma \propto E^{1.056} \quad 1.4$$

Equation 1.4 can be used to accurately model the energy dependence of double ionization over a small range of energies close to threshold, where *E* is excess energy and σ is dication yield. [102, 103]During indirect double photoionization, the electrons are ejected sequentially, and so their long-range interaction becomes less important and the model breaks down.[104] Generally, the indirect mechanism involves the formation of a highly excited monocation following the absorption of a photon. The second step involves the ejection of a second electron and the formation of a dication.[105]

1.2.7 The properties of dications

Small, multiply charged ions are often unstable to dissociation due to the Coulombic repulsion between the local like-charges. When considering breaking a bond in a molecular dication, we move towards a dissociation asymptote that involves two monocations. The repulsion between the two like-charges means that the dicationic state generally lies higher in energy than that of the pair of monocations. As such, many dications are thermodynamically unstable to dissociation. Indeed, many electronic states of molecular dications are purely repulsive and rapidly lead to the formation of two monocations. However, for some dication electronic states bonding forces can be strong enough to overcome these repulsive forces and create an energetic barrier to dissociation.[67, 106] Such a barrier creates a potential well in the dications PES, providing kinetic stability to dications in those states. That is, kinetic stability is caused by the creation of a barrier due to the avoided crossing of the diabatic potential energy curves of A^{2+} + B and A^{+}+ B^{+}. These minima usually lie higher in energy compared to charge separation and are therefore termed ‘metastable’.[73]

A metastable dication has a characteristic barrier to dissociation, the height and width of which varies greatly with different species. The height of this barrier can be estimated using the energy difference between Y^{2+} and Z^{+} + Y^{+} asymptotes shown on Figure 1.1, by finding the difference in ionization energies between Y^{+} and Z. Clearly, this value will differ depending upon the

species involved. If this value is close to zero, a dication can even be stable to dissociation.

Vibrational excitation is another factor that can affect dication stability. The vibrational levels within the metastable well can tunnel through the barrier to dissociation with varying levels of efficiency. Vibrational levels at the top of the well tunnel efficiently, and therefore, upon formation, dissociate rapidly to form two monocations. For low-lying vibrational states in the well, the barrier to dissociation is much wider. Therefore, these states do not tunnel as efficiently, and the lifetime to dissociation for a dication formed in one of these states is much longer. At certain pressures, these dications will undergo several collisions prior to charge separation. That is, under certain conditions, these states can be effectively treated as ‘stable’ to dissociation. The example discussed in this section is an atomic dication. However, the presence of potential barriers on the surface due to avoided crossings has also been demonstrated in diatomic and polyatomic dications, and multiply charged molecules.[107-109]

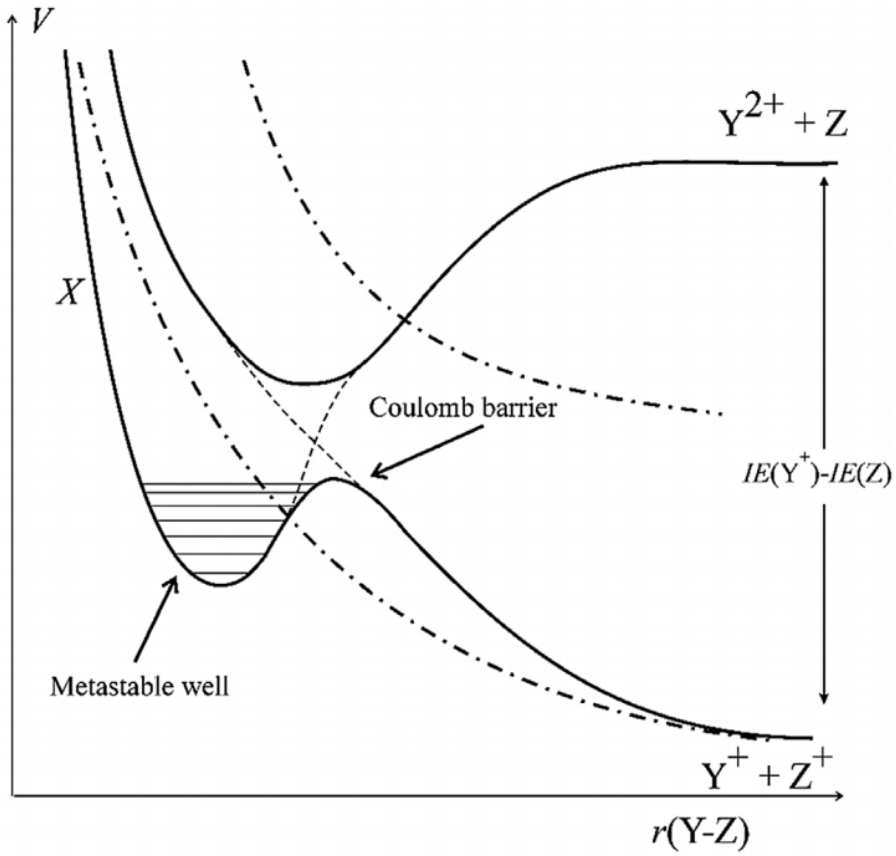

Figure 1.1 Schematic potential energy curves for an atomic dication Y^{2+}. An avoided crossing (dashed lines) between the diabatic curves leads to the formation of a metastable state, stabilised by a coulombic barrier. See text for details. Figure taken from reference 69.

1.2.8 The bimolecular reactions of atomic and diatomic dications

The results presented in chapters 4 and 5 of this thesis describe the reactivity of Ar^{2+} and SO^{2+} following collisions with a variety of neutrals at low collision energies (< 10 eV in the LAB frame). Generally, there are three main reaction types that occur following such collisions: electron transfer (ET), collision induced dissociation (CID) and bond-formation. This section describes the three types of reactivity, and an electrostatic model used to rationalize these reactions is described.

Many studies of dication-neutral collisions have found that single electron transfer (SET) from the neutral species to the dication is the

dominant reaction pathway. That is, most reactivity following such collisions involves the transfer of a single electron forming a pair of monocations

$$AB^{2+} + C \rightarrow AB^{+} + C^{+} \qquad 1.5$$

Any nascent product monocations that are formed in a dissociative state will rapidly fragment to form another monocation and neutral fragments in a process that is termed dissociative SET.

Electron transfer reactivity following dication-neutral low energy collisions can be rationalized by a simple electrostatic model that is based on Landau-Zener theory.[72, 110-114] Figure 1.2 shows schematic PECs for a dication-neutral collision between the symbolic species D^{2+} and N, where D and N represent an arbitrary dication and neutral respectively. At large interspecies separations, the dication potential is dominated by the polarization attraction between the D^{2+} and the N (1, Figure 1.2). At small interspecies separations, this potential becomes dominated by the repulsion between the two species, (2, Figure 1.2). Following electron transfer from the neutral to the dication, two monocations form and the charge-separating asymptote is purely repulsive (3, Figure 1.2). Landau-Zener theory states that SET occurs at the intersection of the reactant and product potentials: the curve crossing.[72, 111, 114] The exothermicity of the SET reaction is given by ΔE (Figure 1.2) and can be found as the difference between the first ionization energy of the neutral and the second ionization energy of the dication.

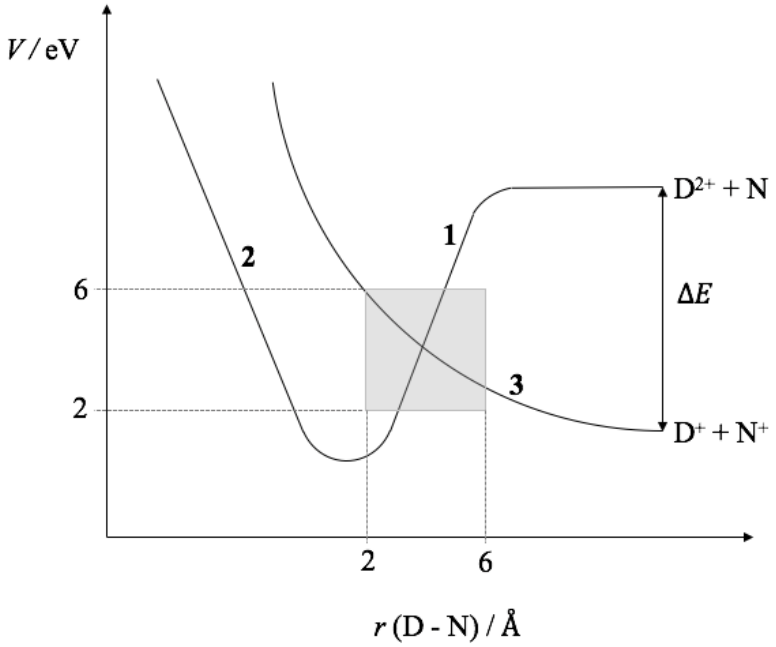

Figure 1.2 Schematic potential energy curves to show the Landau-Zener model for SET following dication-neutral interaction. ET occurs at the intersection between the reactant and product potentials. The grey box indicates the reaction window, the range of interspecies separations over which ET can occur efficiently. The exothermicity of the reaction is shown by ΔE. See text for further details.

The Landau-Zener model for SET between a dication and a neutral state that ET occurs at the intersection of the reactant and product potentials. In Figure 1.2, for SET to occur between the dication (D^{2+}) and the neutral (N), the system must pass from point 1 to point 2 on the 'D^{2+} + N' PEC, prior to crossing to point 3 on the 'D^{+} + N^{+}' curve. That is, for successful SET the system must pass through the curve crossing twice, whilst switching potentials only once.

If the curve crossing occurs at large interspecies separations, the reactant and product potentials are not coupled strongly and an electron would not be able to tunnel from one potential to the other. Whereas, if the curve crossing occurs at small interspecies separations, the potentials are

coupled strongly, and it is facile for the electron to switch potentials. However, if the coupling is too strong, the electron may exchange potentials on both passes through the curve crossing, resulting in no net ET. Therefore, for efficient SET, the crossing radius of the system must coincide with interspecies separations where the coupling between the reactant and product potentials is neither too strong nor too weak. The range of interspecies separations over which efficient SET is predicted is termed the reaction window (RW).[113]

Landau-Zener theory is a semi-classical description of the probability, δ, of remaining on a PEC as a system passes through an intersection with another PEC. RW theory states that the probability, *P*, of SET following a dication-neutral collision can be given by 1.6

$$P = 2\delta(1-\delta) \qquad 1.6$$

As discussed above, for efficient SET the crossing radius must lie at interspecies separations where the coupling between the reactant and product potentials is intermediate, where $\delta \approx 0.5$. To explore this theory, we will now consider the different curve-crossings for different values of δ. In a system where the coupling between the two potentials is very strong, where $\delta \ll 0.5$, the likelihood of two curve-crossings occurring is great and *P* approaches zero. In a system where the crossing radius lies at large interspecies separations, where $\delta \gg 0.5$, the PECs are not strongly coupled and *P* approaches zero. Thus, the RW indicates the range of dication-neutral separations where $\delta \approx 0.5$. For typical dication-neutral collisions the RW lies at 2-6 Å, which corresponds to a reaction exothermicity of 2-6 eV. RW theory has been used to rationalize ET reactivity for several dication-neutral systems.[71]

In chapters 4 and 5 of this thesis, Landau-Zener theory is used to determine the cross-sections to SET for a variety of neutral-dication systems. The probability of a system staying on a PEC is given below.

$$\delta = \exp\left(\frac{-\pi|H_{12}|^2}{2\hbar|V_1' - V_2'|v_r}\right) \qquad 1.7$$

It is a function of the radical velocity v_r, the gradients at the cross points of the two PECs, V_1' and V_2', and the electronic coupling matrix element H_{12}.[113] The cross-section to SET can then be determined as a function of impact parameter, as shown below.

$$\sigma = \int_0^{bmax} P 2\pi b \ \mathrm{d}b \qquad 1.8$$

In chapters 4 and 5, we employ the equation above to quantify the likelihood of SET occurring between a given neutral and dication.

1.2.9 Double electron transfer

Double electron transfer (DET) can occur following dication-neutral collisions. DET is a process where two electrons are transferred from the neutral species to the dication, yielding a new dication and a neutral. The 'new' product dication can then go on to dissociate, forming two product monocations.[71, 115-118]

Many experiments used to study ET processes between dications and neutral rely upon mass spectrometry to detect any products of reaction. As such, only ions can be detected and any neutral bodies are lost. Therefore, excluding coincidence techniques (described below), to detect the products of DET a dication must be formed that has a lifetime to dissociation that exceeds the time taken to reach the detector. This experimental limitation has led to the poor characterization and under-estimation of the contribution of DET reactivity to the overall product ion yield following dication-neutral collisions.[118]

Using a simple electrostatic model to rationalize DET reactivity implies two possible reaction mechanisms: sequential or concerted electron transfer. The sequential transfer of two electrons from the neutral species to the dication would involve the system moving from the D^{2+} + N PEC to the D + N^{2+} asymptote *via* a D^+ + N^+ intermediate. Indeed, sequential DET is in direct competition with SET. The concerted mechanism depicts a system where two electrons are transferred from the neutral to the dication at a single intersection of the PECs. As shown in Figure 1.3, in the concerted DET

model the two PECs are of the dication-neutral form and are inherently very similar. In fact, the only difference between the curves would be due to the polarizability of the neutral reactant and neutral product. Therefore, under this model the exothermicity of the reaction would be small. Conversely, Figure 1.3 shows that the sequential transfer of electrons would allow for a much wider range of reaction exothermicities. Initial investigations of dication-neutral collisions have indicated that the concerted model is the most likely mechanism by which DET occurs, however further investigations are required.[69, 71]

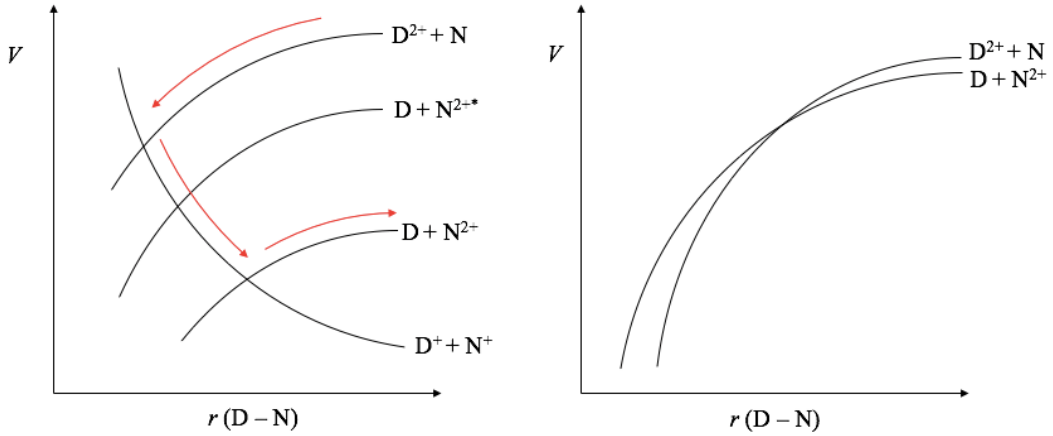

Figure 1.3 Schematic potential energy curves to show the electrostatic models for DET occurring in a sequential (left hand side) and concerted (right hand side) manner. See text for details.

1.2.10 Collision induced dissociation

Following a dication-neutral collision, fragmentation of the dication can occur whilst leaving the neutral intact. This process is termed collision induced dissociation (CID) and involves some of the collision energy exciting the dication to a dissociative or pre-dissociative state. The excited dication can either form a pair of monocations or retain its dipositive charge and lose a neutral body. Similarly, the neutral collision partner could fragment forming several neutral bodies. As mentioned above, usual experimental techniques used to study dication-neutral collisions involve mass spectrometry. As such, the detection of neutral fragments is not possible however, their existence

can be inferred if certain product ions are detected in coincidence following a single ionization event. There are several examples available in the literature that demonstrate this behavior, such as the reaction shown in equation 1.9.[119]

$$CF_3^{2+} + Xe \rightarrow CF_2^{2+} + F + Xe \qquad 1.9$$

1.2.11 Bond-forming reactivity

As described in detail above, when a dication and neutral approach several PEC crossings are likely to be available that lead to ET from the neutral to the dication. At small interspecies separations, the dication and neutral can associate to form a transitory, dipositively charged complex. For this to occur, the system must avoid crossing onto the potentials that would lead to ET. Indeed, the formation of a collision complex is in direct competition with SET.[70] Most bond-forming reactions occur *via* the formation of such a collision complex. That is, the complexation of reactants needs to occur to enable the close-range interactions associated with the rearrangement of chemical bonds. As such, the reactions of dications that involve the formation of new chemical bonds tend to have much smaller reactive cross-sections compared to those for ET reactions.[120, 121] That said, a rich bond-forming chemistry has been observed following dication-neutral collisions, examples of which are shown below.[71, 122]

$$O_2^{2+} + CH_4 \rightarrow HCO^+ + H_3^+ + O \qquad 1.10$$

$$I^{2+} + CS_2 \rightarrow IC^+ + S^+ + S \qquad 1.11$$

The bond-forming reactivity described above can be rationalized by a simple electrostatic model that was first proposed by Herman, as shown in Figure 1.4.[72] A brief description of this model, based on the reaction between the model D^{2+} and AB species, is provided below and more detail can be found in chapters 4 and 5. As the two species approach they traverse the entrance channel (1, Figure 1.4), which is dominated by the polarization attraction between the dication and the neutral. This entrance channel is crossed with several repulsive, charge separating curves that would lead to

SET. Crossing onto these states is generally very likely as some combination of states that lead to SET are likely to be in the RW, as described above. However, if the system avoids crossing onto these curves the reactants may associate to form a collision complex, $[DAB]^{2+}$. Following association, the complex may back dissociate into reactants or the complex may separate along a different reaction coordinate, with new connectivity (2, Figure 1.4). Many repulsive states cross this 'exit' channel that would lead to the production of a pair of monocations, which are typically significantly exothermic compared to the complex (3, Figure 1.4). As such, the products of the dissociation of a complex often involve the production of a pair of monocations that display some new chemical connectivity. The PEC asymptote that corresponds to the formation of DA^{2+} is often energetically inaccessible, and the likelihood of forming a dication with new connectivity is small. Nonetheless, a few groups have previously detected dications that exhibit new bonds following dication-neutral collisions.[123-125]

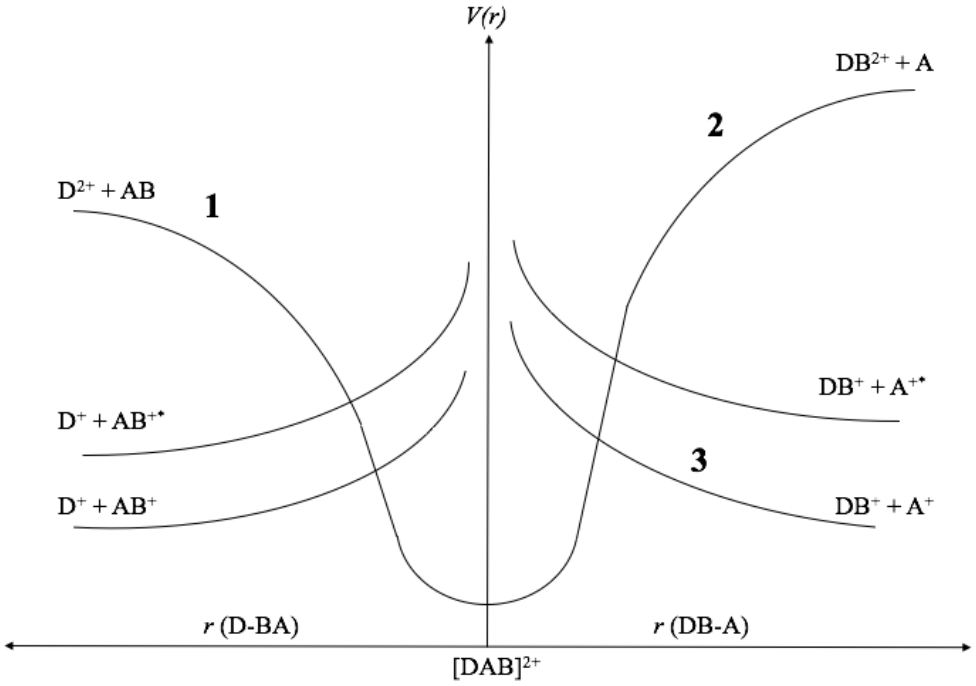

Figure 1.4 Schematic PECs for the formation of a collision complex following the collision between D^{2+} and AB. See text for details.

Computational techniques can be employed to explore the likely structure of the collision complexes that may form following dication-neutral collisions. In previous work, Møller-Plesset theory (MP2) and density functional theory (DFT) have been employed to characterize the potential energy surfaces (PESs) of proposed dication-neutral collision complexes. Such computational investigations have previously revealed potential energy minima in the PESs, in the general form of the schematic model above, and therefore predicted likely skeletal rearrangements and structures of collision complexes.[122, 126]

1.2.12 Experimental techniques to investigate dications

To successfully study the reactivity of dications the properties of the multiply charged species must be known; there are several experimental techniques that are used to characterize dications. Properties such as ionization energies and the spacing of electronic states are powerful tools in rationalizing observed dication-neutral reactivity. For example, following a dication-neutral collision at a known energy, the products one might expect to form with a chosen collision partner can be predicted. Some of the experimental techniques used to determine such properties are discussed below, with a particular focus on coincidence studies. Later in this section, some of the experiments that are used to study the reactivity of dications are described.

1.2.13 Coincidence studies

The term ‘coincidence studies’ encompasses a range of experimental techniques that can detect multiple charged species formed following a single reactive event, be that a collision, ionization, or excitation. The power of such a tool is that the charged products of single reactions can be fully characterized, and the nature and energetics of any neutrals formed can be inferred. Single reaction conditions are crucial for these techniques to work.

To demonstrate the power of coincidence techniques, consider the single electron transfer reaction between a dication (XY^{2+}) and a neutral (N_2) shown below.

$$XY^{2+} + N_2 \rightarrow X^+ + N^+ + Y + N \qquad 1.12$$

A simple mass spectrum of the products of reaction 1.12 would show peaks for X^+ and N^+. However, the X^+ fragment ion could be formed through the SET reaction shown above, or alternatively *via* the unimolecular dissociation of the XY^{2+} dication. To successfully investigate such a reaction, a coincidence technique should be used that focusses on the detection of pairs of product ions; the detection of X^+ and N^+ as an ion pair would be indicative of a SET reaction.

Early coincidence experiments involved the detection of multiple charged ions in coincidence with the electrons ejected upon ionization, enabling the ionic charge of the detected species to be determined.[68, 127] Later, coincidence techniques were used for photoion-photoion coincidence spectroscopy (PIPICO). This technique involves the formation of a dication by photo-absorption, followed by the dications unimolecular dissociation *via* a charge-separating pathway. This process leads to the production of two monocations that are detected in coincidence. The time delay between the detection of each monocation allows the determination of the kinetic energy release (KER) associated with the dication dissociation. Using this KER, the energetics of the dication electronic states involved in the reaction can be investigated.[128, 129] For example, Dujardin *et al* produced NH_3^{2+} dications through the double photoionization of neutral ammonia molecules using synchrotron radiation. The PIPICO method was used to detect the products of dication fragmentation at different ionizing photon energies. For a fragment ion pair, the difference between the ion flight times, Δt, was measured at a number of different ionizing photon energies. PIPICO spectra were produced detailing the number of ion pairs detected in coincidence at each Δt, for each photon energy. The KER associated with the separating product monocations was determined through the comparison of these experimental PIPICO spectra with simulated PIPICO curves, calculated using ion ion-trajectory calculations. This PIPICO study provided information about the dissociative nature of the electronic states of the NH_3^{2+} dication. [134]

Since the pioneering experiments described above, several different forms of spectroscopy that couple coincidence techniques with other experimental procedures have been developed that can fully characterize the properties of dications.[130] Some examples include photoelectron-photoelectron coincidence spectroscopy (PEPECO), photoelectron-photoion-photoion coincidence spectroscopy (PEPIPICO), threshold photoelectrons coincidence spectroscopy (TPEsCO) and photoion fluorescence coincidence spectroscopy (PIFCO).[104, 131-133] This is a non-exhaustive list and there are many available experiments that are used to characterize dications and multiply charged species that rely upon coincidence techniques.

1.2.14 Experiments to investigate dication reactivity

Crossed beam experiments have been employed to study dication-neutral reactions. Early experiments of this kind involved the study of high energy (> 1 keV) collisions using modified mass spectrometers.[135-137] At low collision energies (< 10 eV), these experiments have identified products of such collisions with new bonds, and have elucidated the dication electronic states taking part in some SET reactions with neutrals.[138, 139] Generally, these experiments involve the production of an ion beam *via* EI, mass selection, deceleration to a chosen collision energy and interaction of the beam with a jet of neutral molecules perpendicular to the beam. For example, Maier *et al* studied ET reactions between rare gas dications and rare gas atoms using such a crossed beam technique. The experiment followed the general description provided above, and the ions were detected using a quadrupole mass filter and a particle multiplier. Cross-sections were determined for the dication-neutral reactions, and were linked to the PECs of the reactants and products, which provided a qualitative explanation of the observations.[135]

Building on these early experiments, Price *et al* coupled such a set-up with a time-of-flight mass spectrometer to determine the products of collision and relevant reaction dynamics.[138] For example, this apparatus was used to study the bond-forming reactivity following molecular dication-neutral collisions between 30-50 eV, for a number of systems.[138] The TOF-MS enabled the identification of product ions that displayed new chemical

connectivity, such as the formation of DCF_2^+ following collisions between CF_3^{2+} and D_2.

Herman *et al* used rotated beams and a detector about the central axis of ion travel to produce angularly resolved scattering diagrams following dication-neutral collisions.[140,141] This set up was used to produce Ar^+ product ion scattering diagrams following charge transfer between Ar^{2+} (^3P/ ^1D) and He. These scattering diagrams highlighted different dynamics for the two states of Ar^{2+}.[140] Such experiments have provided great insight into dication-neutral collisions and have greatly advanced our understanding of the reactivity of dications.

Guided ion beam (GIB) experiments have also been used to study dication-neutral reactions. This type of experiment usually involves the use of tandem mass spectrometers to accurately measure the cross-sections and branching ratios of certain reaction channels following dication-neutral interactions.[124] Generally, a GIB experiment involves the formation of ions *via* EI, beam mass selection and collision with a neutral target gas. The main difference between GIB and crossed beam experiments is that the former employs RF fields to collimate the reactant and product ion beams.[142, 143] As such, all charged products formed following dication-neutral interactions are detected. This high detection efficiency enables the accurate determination of reaction cross-sections, however information pertaining to the reaction dynamics is harder to acquire, and is often lost. For example, Herman *et al* used such a GIB experiment to investigate the collision energy dependence of the reaction cross-sections of charge-transfer reactions following collisions between $CHCl^{2+}$ and Ar.[144]

Both types of experiment discussed in this section have been successfully used to garner information pertaining to certain aspects of dication-molecule reactions. However, neither can detect products in coincidence, and therefore are unable to completely characterize a dication reaction. Coincidence techniques, as described previously, enable the detection of charged products following a single reactive event. Chapters 4 and 5 present work carried out on a position sensitive coincidence mass

spectrometer (PSCO-MS) investigate low energy (< 10 eV) dication-neutral collisions. This experiment, described in detail in chapter 2, couples a crossed beam methodology with coincidence detection to provide full insight into dication-neutral collisions.

1.3 Summary

This chapter has described radical-surface chemistry and has highlighted the need for the proposed ‘pure’ source of free radicals. Current radical sources and radical-surface methodologies have been outlined, and the scientific relevance of such work has been discussed. In the second part of this introduction, the different properties and techniques for forming and studying the reactions of dications have been outlined. The following chapters provide experimental details for both the apparatus that has been developed to study radical-surface chemistry and the PSCO-MS that has been used to study the reaction of dications with neutrals.

1.4 Bibliography

1. M. Hori and T. Goto, *Applied Surface Science*, 2007, **253**, 6657-6671.
2. G. Cunge, P. Chabert and J. P. Booth, *Journal of Applied Physics*, 2001, **89**, 7750-7755.
3. G. Cunge, P. Bodart, M. Brihoum, F. Boulard, T. Chevolleau and N. Sadeghi, *Plasma Sources Science & Technology*, 2012, **21**.
4. T. Terasawa and K. Saiki, *Carbon*, 2012, **50**, 869-874.
5. I. Jeon, H. Yang, S. H. Lee, J. Heo, D. H. Seo, J. Shin, U. I. Chung, Z. G. Kim, H. J. Chung and S. Seo, *Acs Nano*, 2011, **5**, 1915-1920.
6. A. Sternberg, A. Dalgarno and S. Lepp, *Astrophysical Journal*, 1987, **320**, 676-682.
7. P. Theule, F. Duvernay, G. Danger, F. Borget, J. B. Bossa, V. Vinogradoff, F. Mispelaer and T. Chiavassa, *Advances in Space Research*, 2013, **52**, 1567-1579.
8. J. M. C. Rawlings, D. A. Williams, S. Viti, C. Cecchi-Pestellini and W. W. Duley, *Monthly Notices of the Royal Astronomical Society*, 2013, **430**, 264-273.
9. R. T. Garrod, V. Wakelam and E. Herbst, *Astronomy & Astrophysics*, 2007, **467**, 1103-1115.
10. P. Tosi, D. Ascenzi, P. Franceschi and G. Guella, *Plasma Sources Science & Technology*, 2009, **18**.
11. J. A. Stillahn, K. J. Trevino and E. R. Fisher, in *Annual Review of Analytical Chemistry*, Annual Reviews, Palo Alto, 2008, vol. 1, pp. 261-291.
12. J. J. T. Meulen, W. L. Meerts, G. W. M. Vanmierlo and A. Dymanus, *Physical Review Letters*, 1976, **36**, 1031-1034.
13. D. M. Sonnenfroh, R. G. Macdonald and K. Liu, *Journal of Chemical Physics*, 1991, **94**, 6508-6518.
14. M. Alagia, N. Balucani, P. Casavecchia, D. Stranges and G. G. Volpi, *Journal of Chemical Physics*, 1993, **98**, 8341-8344.
15. J. M. Stillahn and E. R. Fisher, *Journal of Physical Chemistry A*, 2010, **114**, 5287-5294.
16. C. Bourbon, M. Brioukov, B. Hanoune, J. P. Sawerysyn and P. Devolder, *Chemical Physics Letters*, 1996, **254**, 203-212.
17. E. Assaf, B. Song, A. Tomas, C. Schoemaecker and C. Fittschen, *Journal of Physical Chemistry A*, 2016, **120**, 8923-8932.

18. A. G. Zogka, A. Mellouki, M. N. Romanias, Y. Bedjanian, M. Idir, B. Grosselin and V. Daele, *Journal of Physical Chemistry A*, 2016, **120**, 9049-9062.

19. J. P. Booth, G. Hancock, N. D. Perry and M. J. Toogood, *Journal of Applied Physics*, 1989, **66**, 5251-5257.

20. A. Mills, A. Lepre, N. Elliott, S. Bhopal, I. P. Parkin and S. A. O'Neill, *Journal of Photochemistry and Photobiology a-Chemistry*, 2003, **160**, 213-224.

21. C. H. Liu, T. K. Lin and S. J. Chang, *Solid-State Electronics*, 2005, **49**, 1077-1080.

22. M. Meyyappan, L. Delzeit, A. Cassell and D. Hash, *Plasma Sources Science & Technology*, 2003, **12**, 205-216.

23. D. Smith and P. Spanel, *Mass Spectrometry Reviews*, 1995, **14**, 255-278.

24. N. Sakai, T. Sakai, Y. Osamura and S. Yamamoto, *Astrophysical Journal*, 2007, **667**, L65-L68.

25. E. Herbst, *Chemical Society Reviews*, 2001, **30**, 168-176.

26. J. Cernicharo and M. Guelin, *Astronomy & Astrophysics*, 1996, **309**, L27-L30.

27. J. L. Neill, A. L. Steber, M. T. Muckle, D. P. Zaleski, V. Lattanzi, S. Spezzano, M. C. McCarthy, A. J. Remijan, D. N. Friedel, S. L. W. Weaver and B. H. Pate, *Journal of Physical Chemistry A*, 2011, **115**, 6472-6480.

28. E. A. Bergin and M. Tafalla, in *Annual Review of Astronomy and Astrophysics*, Annual Reviews, Palo Alto, 2007, vol. 45, pp. 339-396.

29. K. Acharyya, G. E. Hassel and E. Herbst, *Astrophysical Journal*, 2011, **732**, 15.

30. J. C. Weingartner and B. T. Draine, *Astrophysical Journal*, 2001, **553**, 581-594.

31. V. Wakelam, I. W. M. Smith, E. Herbst, J. Troe, W. Geppert, H. Linnartz, K. Oberg, E. Roueff, M. Agundez, P. Pernot, H. M. Cuppen, J. C. Loison and D. Talbi, *Space Science Reviews*, 2010, **156**, 13-72.

32. S. E. Bisschop, G. W. Fuchs, E. F. van Dishoeck and H. Linnartz, *Astronomy & Astrophysics*, 2007, **474**, 1061-1071.

33. E. Esarey, C. B. Schroeder and W. P. Leemans, *Reviews of Modern Physics*, 2009, **81**, 1229-1285.

34. F. C. Jones and D. C. Ellison, *Space Science Reviews*, 1991, **58**, 259-346.

35. S. Ichimaru, H. Iyetomi and S. Tanaka, *Physics Reports-Review Section of Physics Letters*, 1987, **149**, 91-205.

36. P. K. Shukla, *Physics of Plasmas*, 2001, **8**, 1791-1803.

37. M. Tang, P. Albertus and J. Newman, *Journal of the Electrochemical Society*, 2009, **156**, A390-A399.

38. Y. Z. Zheng, Q. Li, Z. H. Zheng, J. F. Zhu and P. L. Cao, *Applied Surface Science*, 2014, **317**, 526-533.

39. M. J. Kushner, *Journal of Applied Physics*, 1988, **63**, 2532-2551.

40. G. S. Selwyn, K. L. Haller and E. F. Patterson, *Journal of Vacuum Science & Technology a-Vacuum Surfaces and Films*, 1993, **11**, 1132-1135.

41. J. H. Chu and L. I, *Physical Review Letters*, 1994, **72**, 4009-4012.

42. C. M. Ticos, Z. H. Wang, G. L. Delzanno and G. Lapenta, *Physics of Plasmas*, 2006, **13**.

43. R. D. Smirnov, A. Y. Pigarov, M. Rosenberg, S. I. Krasheninnikov and D. A. Mendis, *Plasma Physics and Controlled Fusion*, 2007, **49**, 347-371.

44. L. Vignitchouk, P. Tolias and S. Ratynskaia, *Plasma Physics and Controlled Fusion*, 2014, **56**.

45. 1-2, 2012.

46. A. I. Vasyunin and E. Herbst, *Astrophysical Journal*, 2013, **769**.

47. A. I. Vasyunin and E. Herbst, *Astrophysical Journal*, 2013, **762**.

48. W. D. Watson, *Astrophysical Journal*, 1974, **188**, 35-42.

49. W. D. Watson, *Astrophysical Journal*, 1973, **183**, L17-L20.

50. E. Herbst and W. Klemperer, *Astrophysical Journal*, 1973, **185**, 505-533.

51. M. Allen and G. W. Robinson, *Astrophysical Journal*, 1977, **212**, 396-415.

52. C. M. Leung, E. V. Obrien and R. Dubisch, *Astrophysical Journal*, 1989, **337**, 293-305.

53. M. Agundez and V. Wakelam, *Chemical Reviews*, 2013, **113**, 8710-8737.

54. S. Viti and D. A. Williams, *Monthly Notices of the Royal Astronomical Society*, 1999, **305**, 755-762.

55. M. P. Collings, M. A. Anderson, R. Chen, J. W. Dever, S. Viti, D. A. Williams and M. R. S. McCoustra, *Monthly Notices of the Royal Astronomical Society*, 2004, **354**, 1133-1140.

56. P. R. McCurdy, V. A. Venturo and E. R. Fisher, *Chemical Physics Letters*, 1997, **274**, 120-126.

57. T. J. Millar and D. A. Williams, *Monthly Notices of the Royal Astronomical Society*, 1975, **173**, 527-535.

58. W. A. Brown and D. A. King, *Journal of Physical Chemistry B*, 2000, **104**, 2578-2595.

59. T. Katayama, D. Sekiba, K. Mukai, Y. Yamashita, F. Komori and J. Yoshinobu, *Journal of Physical Chemistry C*, 2007, **111**, 15059-15063.

60. P. Krukowski, Z. Klusek, W. Olejniczak, R. Klepaczko, M. Puchalski, P. Dabrowski, P. J. Kowalczyk and K. Gwozdzinski, *Applied Surface Science*, 2009, **255**, 8769-8773.

61. N. Crivillers, M. Mas-Torrent, S. Perruchas, N. Roques, J. Vidal-Gancedo, J. Veciana, C. Rovira, L. Basabe-Desmonts, B. J. Ravoo, M. Crego-Calama and D. N. Reinhoudt, *Angewandte Chemie-International Edition*, 2007, **46**, 2215-2219.

62. P. Messina, M. Mannini, A. Caneschi, D. Gatteschi, L. Sorace, P. Sigalotti, C. Sandrin, S. Prato, P. Pittana and Y. Manassen, *Journal of Applied Physics*, 2007, **101**, 14.

63. W. Wulfhekel and J. Kirschner, *Applied Physics Letters*, 1999, **75**, 1944-1946.

64. H. Murata, M. Baskett, H. Nishide and P. M. Lahti, *Langmuir*, 2014, **30**, 4026-4032.

65. M. Baskett and P. M. Lahti, *Polyhedron*, 2005, **24**, 2645-2652.

66. F. Grillo, H. Fruchtl, S. M. Francis, V. Mugnaini, M. Oliveros, J. Veciana and N. V. Richardson, *Nanoscale*, 2012, **4**, 6718-6721.

67. A. L. Vaughan, *Physical Review*, 1931, **38**, 1687-1695.

68. K. E. McCulloh, T. E. Sharp and H. M. Rosenstock, *Journal of Chemical Physics*, 1965, **42**, 3501-+.

69. S. D. Price, *International Journal of Mass Spectrometry*, 2007, **260**, 1-19.

70. S. D. Price, *Physical Chemistry Chemical Physics*, 2003, **5**, 1717-1729.

71. S. D. Price, J. D. Fletcher, F. E. Gossan and M. A. Parkes, *International Reviews in Physical Chemistry*, 2017, **36**, 145-183.

72. Z. Herman, *International Reviews in Physical Chemistry*, 1996, **15**, 299-324.

73. D. Schroder and H. Schwarz, *Journal of Physical Chemistry A*, 1999, **103**, 7385-7394.

74. Z. Herman, *International Journal of Mass Spectrometry*, 2015, **378**, 113-126.

75. R. Thissen, O. Witasse, O. Dutuit, C. S. Wedlund, G. Gronoff and J. Lilensten, *Physical Chemistry Chemical Physics*, 2011, **13**, 18264-18287.

76. G. Gronoff, J. Lilensten, C. Simon, O. Witasse, R. Thissen, O. Dutuit and C. Alcaraz, *Astronomy & Astrophysics*, 2007, **465**, 641-645.

77. T. E. Cravens, I. P. Robertson, J. Clark, J. E. Wahlund, J. H. Waite, S. A. Ledvina, H. B. Niemann, R. V. Yelle, W. T. Kasprzak, J. G. Luhmann, R. L. McNutt, W. H. Ip, V. De La Haye, I. Muller-Wodarg, D. T. Young and A. J. Coates, *Geophysical Research Letters*, 2005, **32**.

78. I. P. Robertson, T. E. Cravens, J. H. Waite, R. V. Yelle, V. Vuitton, A. J. Coates, J. E. Wahlund, K. Agren, K. Mandt, B. Magee, M. S. Richard and E. Fattig, *Planetary and Space Science*, 2009, **57**, 1834-1846.

79. M. J. McEwan and V. G. Anicich, *Mass Spectrometry Reviews*, 2007, **26**, 281-319.

80. V. Vuitton, P. Lavvas, R. V. Yelle, M. Galand, A. Wellbrock, G. R. Lewis, A. J. Coates and J. E. Wahlund, *Planetary and Space Science*, 2009, **57**, 1558-1572.

81. O. Witasse, O. Dutuit, J. Lilensten, R. Thissen, J. Zabka, C. Alcaraz, P. L. Blelly, S. W. Bougher, S. Engel, L. H. Andersen and K. Seiersen, *Geophysical Research Letters*, 2002, **29**, 4.

82. A. F. Nagy, T. E. Cravens, S. G. Smith, H. A. Taylor and H. C. Brinton, *Journal of Geophysical Research-Space Physics*, 1980, **85**, 7795-7801.

83. J. H. Hoffman, R. R. Hodges, T. M. Donahue and M. B. McElroy, *Journal of Geophysical Research-Space Physics*, 1980, **85**, 7882-7890.

84. E. L. Breig, M. R. Torr, D. G. Torr, W. B. Hanson, J. H. Hoffman, J. C. G. Walker and A. O. Nier, *Journal of Geophysical Research-Space Physics*, 1977, **82**, 1008-1012.

85. C. R. Chappell, R. C. Olsen, J. L. Green, J. F. E. Johnson and J. H. Waite, *Geophysical Research Letters*, 1982, **9**, 937-940.

86. S. Falcinelli, M. Rosi, P. Candori, F. Vecchiocattivi, F. Pirani, N. Balucani, M. Alagia, R. Richter and S. Stranges, *Abstracts of Papers of the American Chemical Society*, 2013, **246**, 1.

87. S. Falcinelli, M. Rosi, P. Candori, F. Vecchiocattivi, J. M. Farrar, F. Pirani, N. Balucani, M. Alagia, R. Richter and S. Stranges, *Planetary and Space Science*, 2014, **99**, 149-157.

88. S. Falcinelli, F. Pirani, M. Alagia, L. Schio, R. Richter, S. Stranges and F. Vecchiocattivi, *Chemical Physics Letters*, 2016, **666**, 1-6.

89. J. Lilensten, C. S. Wedlund, M. Barthelemy, R. Thissen, D. Ehrenreich, G. Gronoff and O. Witasse, *Icarus*, 2013, **222**, 169-187.

90. T. P. Snow and V. M. Bierbaum, *Annual Review of Analytical Chemistry*, 2008, **1**, 229-259.

91. S. Leach, *Journal of Electron Spectroscopy and Related Phenomena*, 1986, **41**, 427-438.

92. I. W. M. Smith, in *Annual Review of Astronomy and Astrophysics, Vol 49*, eds. S. M. Faber and E. VanDishoeck, Annual Reviews, Palo Alto, 2011, vol. 49, pp. 29-66.

93. M. R. Bruce and R. A. Bonham, *International Journal of Mass Spectrometry and Ion Processes*, 1993, **123**.

94. M. R. Bruce and R. A. Bonham, *Zeitschrift Fur Physik D-Atoms Molecules and Clusters*, 1992, **24**, 149-154.

95. C. S. Leasure, M. E. Fleischer, G. K. Anderson and G. A. Eiceman, *Analytical Chemistry*, 1986, **58**, 2142-2147.

96. J. H. D. Eland, *Journal of Physics E-Scientific Instruments*, 1978, **11**, 969-977.

97. N. Chandra, *Journal of Physical Chemistry*, 1992, **96**, 7207-7218.

98. A. Eppink and D. H. Parker, *Review of Scientific Instruments*, 1997, **68**, 3477-3484.

99. C. Bordas, F. Paulig, H. Helm and D. L. Huestis, *Review of Scientific Instruments*, 1996, **67**, 2257-2268.

100. G. H. Wannier, *Physical Review*, 1955, **100**, 1180-1180.

101. G. H. Wannier, *Physical Review*, 1953, **90**, 817-825.

102. S. Hsieh and J. H. D. Eland, *Journal of Physics B-Atomic Molecular and Optical Physics*, 1996, **29**, 5795-5809.

103. U. Becker, O. Hemmers, B. Langer, A. Menzel, R. Wehlitz and W. B. Peatman, *Physical Review A*, 1992, **45**, R1295-R1298.

104. G. Dawber, A. G. McConkey, L. Avaldi, M. A. Macdonald, G. C. King and R. I. Hall, *Journal of Physics B-Atomic Molecular and Optical Physics*, 1994, **27**, 2191-2209.

105. R. Feifel, J. H. D. Eland and D. Edvardsson, *Journal of Chemical Physics*, 2005, **122**.

106. M. Larsson, P. Baltzer, S. Svensson, B. Wannberg, N. Martensson, A. N. Debrito, N. Correia, M. P. Keane, M. Carlssongothe and L. Karlsson, *Journal of Physics B-Atomic Molecular and Optical Physics*, 1990, **23**, 1175-1195.

107. D. Mathur, *Physics Reports-Review Section of Physics Letters*, 1993, **225**.

108. D. Mathur, *Physics Reports-Review Section of Physics Letters*, 2004, **391**, 1-118.

109. D. Mathur and F. M. Harris, *Mass Spectrometry Reviews*, 1989, **8**, 269-291.

110. S. D. Price, *Journal of the Chemical Society-Faraday Transactions*, 1997, **93**, 2451-2460.

111. S. A. Rogers, S. D. Price and S. R. Leone, *Journal of Chemical Physics*, 1993, **98**, 280-289.

112. C. Wittig, *Journal of Physical Chemistry B*, 2005, **109**, 8428-8430.

113. C. Zener, *Proceedings of the Royal Society of London Series a-Containing Papers of a Mathematical and Physical Character*, 1932, **137**, 696-702.

114. S. D. Price, S. A. Rogers and S. R. Leone, *Journal of Chemical Physics*, 1993, **98**, 9455-9465.

115. R. K. Janev and H. Winter, *Physics Reports-Review Section of Physics Letters*, 1985, **117**, 265-387.

116. M. A. Parkes, J. F. Lockyear and S. D. Price, *International Journal of Mass Spectrometry*, 2009, **280**, 85-92.

117. R. Hodyss, J. D. Goguen, P. V. Johnson, C. Campbell and I. Kanik, *Icarus*, 2008, **197**, 152-156.

118. J. D. Fletcher, M. A. Parkes and S. D. Price, *Chemistry-a European Journal*, 2013, **19**, 10965-10970.

119. S. D. Price, M. Manning and S. R. Leone, *Chemical Physics Letters*, 1993, **214**, 553-558.

120. P. W. Burnside and S. D. Price, *International Journal of Mass Spectrometry*, 2006, **249**, 279-288.

121. P. W. Burnside and S. D. Price, *Physical Chemistry Chemical Physics*, 2007, **9**, 3902-3913.

122. J. D. Fletcher, M. A. Parkes and S. D. Price, *Molecular Physics*, 2015, **113**, 2125-2137.

123. W. Y. Lu, P. Tosi and D. Bassi, *Journal of Chemical Physics*, 2000, **112**, 4648-4651.

124. D. Ascenzi, P. Tosi, J. Roithova, C. L. Ricketts, D. Schroder, J. F. Lockyear, M. A. Parkes and S. D. Price, *Physical Chemistry Chemical Physics*, 2008, **10**, 7121-7128.

125. J. Roithova, C. L. Ricketts, D. Schroder and S. D. Price, *Angewandte Chemie-International Edition*, 2007, **46**, 9316-9319.

126. M. A. Parkes, J. F. Lockyear and S. D. Price, *International Journal of Mass Spectrometry*, 2014, **365**, 68-74.

127. G. Dujardin, S. Leach, O. Dutuit, P. M. Guyon and M. Richardviard, *Chemical Physics*, 1984, **88**, 339-353.

128. H. M. Rosenstock, K. E. McCulloh and F. P. Lossing, *International Journal of Mass Spectrometry and Ion Processes*, 1977, **25**, 327-341.

129. D. M. Curtis and J. H. D. Eland, *International Journal of Mass Spectrometry and Ion Processes*, 1985, **63**, 241-264.

130. J. H. D. Eland, *Chemical Physics*, 2003, **294**, 171-186.

131. G. Dujardin and S. Leach, *Journal of Chemical Physics*, 1981, **75**, 2521-2531.

132. S. D. Price and J. H. D. Eland, *Measurement Science and Technology*, 1992, **3**, 306-315.

133. R. I. Hall, L. Avaldi, G. Dawber, A. G. McConkey, M. A. Macdonald and G. C. King, *Chemical Physics*, 1994, **187**, 125-135.

134. D. Winkoun and G. Dujardin, *Zeitschrift Fur Physik D-Atoms Molecules and Clusters*, 1986, **4**, 57-64.

135. W. B. Maier and B. Stewart, *Journal of Chemical Physics*, 1978, **68**, 4228-4232.

136. J. H. Agee, J. B. Wilcox, L. E. Abbey and T. F. Moran, *Chemical Physics*, 1981, **61**, 171-179.

137. G. H. Bearman, F. Ranjbar, H. H. Harris and J. J. Leventhal, *Chemical Physics Letters*, 1976, **42**, 335-338.

138. S. D. Price, M. Manning and S. R. Leone, *Journal of the American Chemical Society*, 1994, **116**, 8673-8680.

139. Z. Herman, J. Zabka, Z. Dolejsek and M. Farnik, *International Journal of Mass Spectrometry*, 1999, **192**, 191-203.

140. B. Friedrich and Z. Herman, *Chemical Physics Letters*, 1984, **107**, 375-380.

141. B. Friedrich, J. Vancura, M. Sadilek and Z. Herman, *Chemical Physics Letters*, 1985, **120**, 243-246.

142. J. Glosik, A. Luca, S. Mark and D. Gerlich, *Journal of Chemical Physics*, 2000, **112**, 7011-7021.

143. S. Mark, C. Schellhammer, G. Niednerschatteburg and D. Gerlich, *Journal of Physical Chemistry*, 1995, **99**, 15587-15594.

144. J. Roithova, R. Thissen, J. Zabka, P. Franceschi, O. Dutuit and Z. Herman, *International Journal of Mass Spectrometry*, 2003, **228**, 487-495.

2 The position-sensitive coincidence mass spectrometer

2.1 Introduction

This chapter will describe the position-sensitive coincidence time-of-flight mass spectrometer (PSCO-MS) that was used to perform the experimental work presented in chapters 4 and 5. Additionally, the relevant data processing and analysis techniques used to interpret the rich coincidence spectra that this apparatus provides are detailed below. A brief overview of the PSCO-MS is presented, followed by a more in-depth description of each component part of the apparatus.

2.2 Overview

The PSCO apparatus was designed to study the gas-phase reactions of dications and neutral molecules. The common outcome of such a reaction is the generation of a pair of monocations. This apparatus pairs a TOF-MS with a position-sensitive detector (PSD) to collect such a pair of monocations, generated from a single dication-neutral collision, in coincidence. Combining these two techniques enables the determination of the identity and velocity vectors of the product ions formed following the collision. Figure 2.1 shows a schematic of the PSCO-MS at UCL.

In this experiment ions are formed by the electron ionisation (EI) of a neutral gas. Any ions formed are extracted from the source and enter a hemispherical energy analyser, where ions of a chosen kinetic energy range are selected. Upon exiting the hemisphere, the monoenergetic ion beam is pulsed into discrete ion packets, which are subsequently focussed by a series of electrostatic lenses. The ion packets then enter a velocity filter that selects dications of a chosen mass-to-charge ratio (*m/z*). The mass-selected dication beam is then decelerated to a known collision energy and enters an interaction region. It is here where the dication-neutral collisions occur. This region is also the source region for the TOF-MS. Ions that exit the TOF-MS source region are accelerated into a field-free drift tube, at the end of which they impinge upon the PSD. The time-of-flight and impact position of each

ion are recorded on an event-by-event basis, thus enabling the extraction of the nascent velocities of the products.

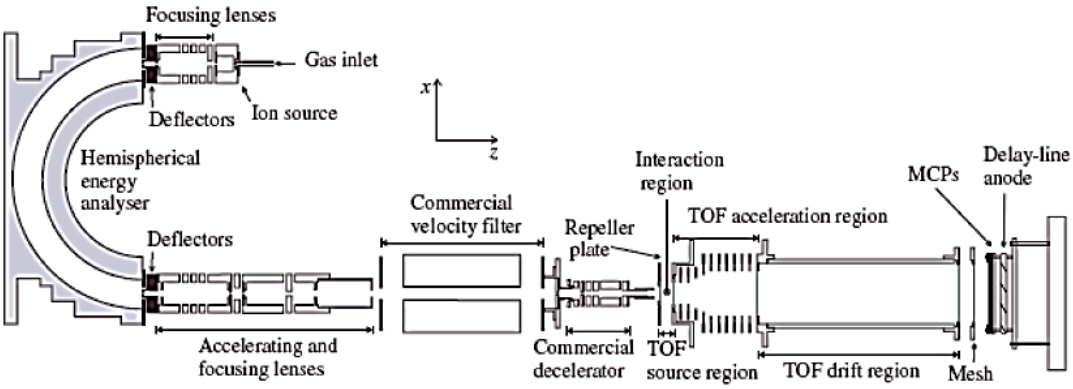

Figure 2.1 A schematic of the PSCO TOF-MS.[1] Dications are formed *via* electron ionisation. The hemispherical analyser is used to energy select the ion beam, and the velocity filter is used to mass select the ion beam. The beam interacts with a neutral gas and a TOF-MS is used to detect any product ions that may form in coincidence.

2.3 Experimental Details

2.3.1 Ion formation

Ions are formed in the source region by the electron ionisation (EI) of a neutral gas. An electron beam is formed by passing a high current (~ 4 A) through a tungsten filament, which causes electrons to be ejected *via* thermionic emission. The electrons are extracted and guided into a cavity in the source block by electrostatic lenses. The source block is filled with a chosen neutral precursor gas. The neutral gas is admitted to this chamber as an effusive jet by a precision needle valve, which provides control over the pressure in the ion source region. This pressure is kept to ~ 4×10^{-6} Torr. A positive voltage is applied to the source block to define the 'rest potential' of any ions formed. This voltage is usually set between 2 and 10 V and determines the velocity of the ions as they enter the interaction region. As a result of this configuration, varying this potential changes the collision energy between dication and neutral.

2.3.2 Ion extraction and hemispherical analyser

Any monocations or dications formed in the ion source are extracted by the application of a negative potential (-250 V) to an extraction lens, which is positioned just beyond the exit of the ion source. A further three lenses are housed immediately behind the extraction lens are used to shape and guide the ion beam out of the source. An additional lens then accelerates the beam into the hemispherical analyser. A pair of deflectors are used to finely tune the alignment of the beam to maximise transmission into the analyser. Figure 2.2 shows a schematic of the lenses and deflectors described above.

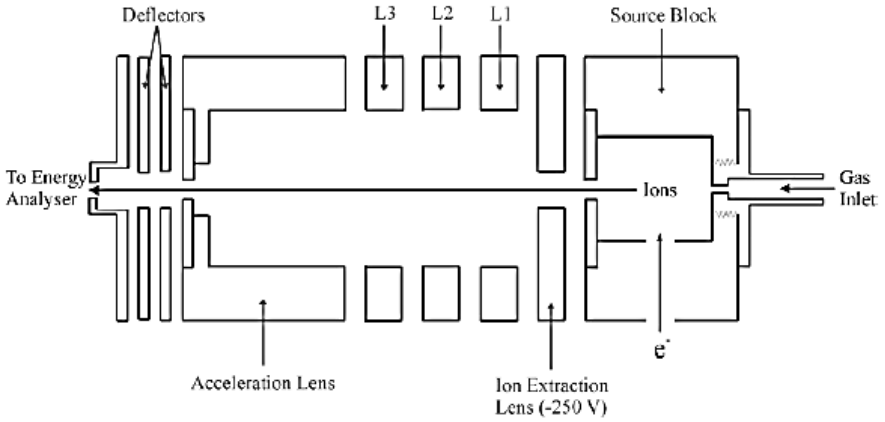

Figure 2.2 A schematic of the ion source, extraction lenses and deflectors that are housed at the entrance to the hemispherical analyser.

The ion source geometry and fields are designed to minimise the energy spread of any cations formed. Despite this, stray fields and charging of elements within the source region can lead to the ions possessing a range of translational energies centred around the ‘rest potential’. Consequently, the ions must be further energy-selected to maximise the energy resolution of the PSCO apparatus.

A hemispherical analyser is used to select ions of a specific kinetic energy range. The analyser consists of two concentric hemispheres of radii R_1 and R_2, as shown in Figure 2.3. There are slits located at both the entrance and exit to the analyser. For an ion to successfully traverse the hemisphere it must have the correct trajectory to pass through both of these

slits. This trajectory is a semi-circular path with a radius equal to the mean radius of the inner and outer hemispheres, H_1 and H_2 (equation 2.1).

$$R_0 = \frac{(R_1 + R_2)}{2} \qquad 2.1$$

The trajectories of the ions in the analyser are governed by the field generated by the potentials applied to the inner and outer hemispheres, V_{inner} and V_{outer} respectively. These potentials are chosen to allow only ions of a specific energy, termed the pass energy (V_0), to travel along R_0.

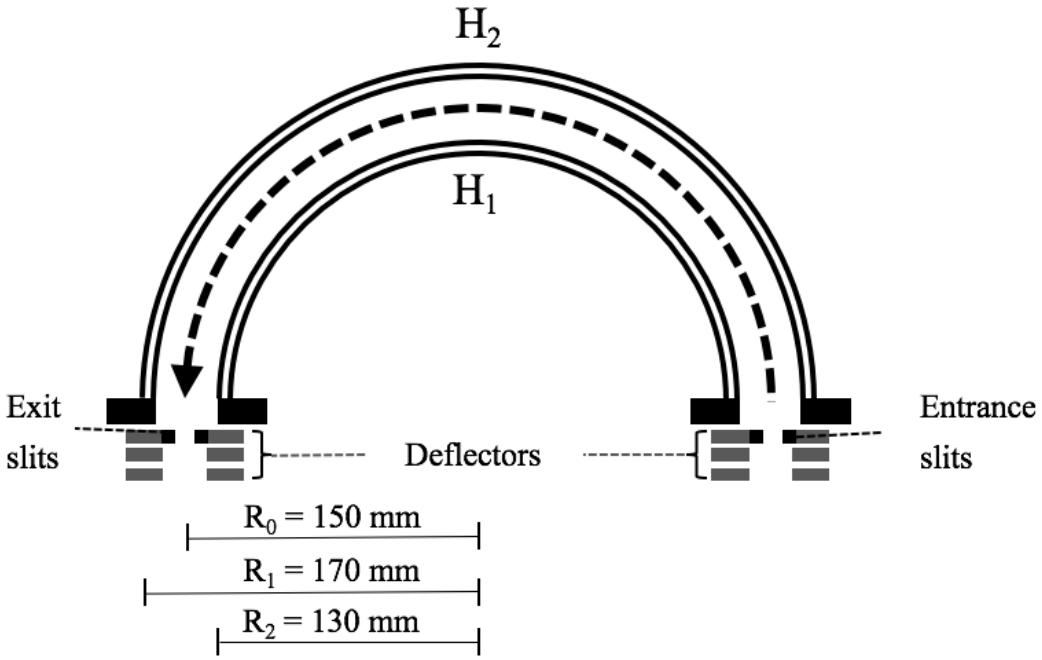

Figure 2.3 A schematic of the hemispherical energy analyser that consists of two hemispheres, H_1 and H_2, with radii R_1 = 130 mm and R_2 = 170 mm respectively. The mean radius is R_0 = 150 mm.

Ions are brought up to V_0 by application of an acceleration voltage, V_r (equation 2.2).

$$V_0 = T - V_r \qquad 2.2$$

The potentials that must be applied to the inner and outer hemispheres to allow ions with rest potential *T* to successfully traverse the hemisphere can be calculated using equations 2.3 and 2.4.[2]

$$V_{outer} = -V_0\left(\frac{2R_0}{R_2} - 1\right) + T \qquad 2.3$$

$$V_{inner} = -V_0\left(\frac{2R_0}{R_1} - 1\right) + T \qquad 2.4$$

It follows that the potential difference across the two hemispheres that will allow the passage of ions formed at *T* to travel along R_0 can be calculated using equation 2.5.

$$\Delta V = V_{outer} - V_{inner} = V_0\left(\frac{R_2}{R_1} - \frac{R_1}{R_2}\right) \qquad 2.5$$

Of course, there will always be a small spread of energies within the ion beam as there is a play-off between ion transmission and energy resolution. Indeed, the higher the energy resolution, the lower the flux of the transmitted ion beam.

2.3.3 Pulsed beam

Beyond the exit slit of the hemispherical analyser are another set of vertical and horizontal deflectors. The vertical deflectors are used to adjust the trajectory of the ion beam if necessary. The primary function of the horizontal deflectors is to pulse the ion beam into discrete ion packets. This pulsing is achieved by the application of a triangular oscillating waveform to each deflector.[1] The waveforms are out of phase, and so apply alternating voltages to the deflectors. Such conditions cause the ion beam to oscillate across a central aperture, thus creating temporally and spatially distinct ion packets. The duration and separation of each pulse is determined by the amplitude and frequency of the waveforms respectively; factors over which we have precise control over.

A pulsed dication beam offers several advantages over a continuous beam. When operating with a continuous ion beam, ions are present in the source, acceleration and drift regions of the mass spectrometer prior to the application of a positive voltage to the repeller plate. This step initiates the

collection of the TOF mass spectrum. When the repeller plate is energised any ions are accelerated towards the detector. Ions source region are in the correct focussing conditions to produce a defined peak at a TOF that corresponds to their *m/z* and that is independent of their starting position in the source region. However, ions that are elsewhere in the spectrometer when the repeller plate is pulsed will be non-focussed and will arrive at a range of flight-times that are unrelated to their *m/z*. The early arrival of such ions gives rise to a non-zero background level at flight times earlier than the unreacted reactant ion. These early ions also cause an increase in false coincidences recorded at short flight times in the coincidence mass spectrum, as there is a high probability that two such ions would arrive at the detector during the same timing cycle despite not being formed after the same reactive event.

A pulsed ion beam consists of ions packets of a defined, finite temporal and spatial duration. We can tune the oscillating waveform and set the timings of the apparatus such that the repeller plate is only pulsed when an ion packet is in the centre of the source region of the spectrometer. Thus, all reactant ions will be focussed to form a sharp peak in the mass spectrum. Typical pulse separations are 30-80 μs.

A pulsed beam can increase mass resolution by reducing the ion-neutral interaction volume compared to a continuous beam. The spatial width of the ion packets formed by pulsing the beam can be reduced to significantly less than the width of the ion source region, whereas a continuous beam of dications can interact with neutrals across the full volume of the source region. It follows that ions formed following pulsed dication-neutral collisions will have a smaller distribution of possible starting positions compared to interactions involving a continuous beam of dications. Therefore, mass resolution for a pulsed ion beam is relatively improved. Furthermore, the location of the dication-neutral collision centre is defined with greater precision for a pulsed dication beam compared to a continuous beam, as the interaction volume is reduced, thus the uncertainty in the kinematic data is reduced.

Although the advantages of using a pulsed beam over a continuous beam are stark, it should be noted that incorrect pulsing settings can perturb the energy of the beam. For example, if the deflector plates are pulsed too quickly, the beam may not have time to adjust to the changing voltages and experience a shift in potential, thus leading to a shift in TOF. Such perturbations can be minimised by operating at pulse frequencies < 50 kHz. As TOF is a sensitive probe of beam energy, the continuous beam and pulsed ion flight times are compared before each experiment to ensure that the pulsing conditions do not affect the energy of the ion beam.

2.3.4 Acceleration, focussing and mass selection

After pulsing, the ion beam is focussed by a series of electrostatic lenses. Each lens is tuned to accelerate and optimise the shape of the ion beam. After passing through these lenses, the beam enters a velocity filter.

$$qV = E_k = \frac{1}{2}\frac{m}{z}v^2 \qquad 2.6$$

The ion beam is close to mono-energetic upon entry into the velocity filter. The ion pulses consist of ions of charge *q* that have experienced an acceleration voltage *V*. Upon acceleration, the ions possess equal kinetic energy, E_k. It follows that ion velocity, *v*, is inversely proportional to the square root of its mass-to-charge ratio (equation 2.6). Thus, one can form a beam that consists overwhelmingly of ions with a particular *m/z* by selecting based on ion velocity, whilst ions possessing other *m/z* are filtered out. To this end, a commercially bought Colutron Velocity Filter is employed.[3, 4]

The filter consists of an electromagnet and a pair of electrostatic deflection plates that generate a pair of perpendicular magnetic and electrostatic fields. The field conditions, which we control, are such that an ion of a chosen *m/z* can traverse the filter following a linear path whereas all other ions are deflected out of the ion beam.

$$F_B = Bqv \qquad 2.7$$

$$F_E = Eq \qquad 2.8$$

For an ion of charge *q* and velocity *v* to maintain a linear path through the filter, the magnetic and electrostatic forces acting on it must balance, which are given by F_B and F_E respectively. The resulting relationship is given in equation 2.9.

$$F_E = F_B \Rightarrow v = \frac{E}{B} \qquad 2.9$$

If the forces are mismatched, the ion will be deflected out of the beam following a curved trajectory and fail to leave the filter *via* its exit aperture. Thus, for set values of *E* and *B*, only one velocity of ion will pass through the filter following a linear path. Therefore, we can achieve a beam that consists overwhelmingly of ions that possess a specific *m/z*. As the kinetic energy of the ions is determined by the voltage to which they are accelerated before entry to the filter *V*, the relationship between field strength and *m/z* is shown in equation 2.10.

$$E = B\left(\frac{2E_k}{m}\right)^{\frac{1}{2}} \qquad 2.10$$

In this apparatus, we keep the magnetic field constant and vary the electric field to tune for ions of different *m/z*. This minimises hysteresis losses that may occur due to cycles of heating and cooling of the electromagnet as the current is varied.

A disadvantage of this method of mass selection is that we cannot distinguish between singly charged atomic ions and doubly charged molecular ions of the same *m/z*, for example O_2^{2+} (*m/z*=16) and O^+ (*m/z*=16).

2.3.5 Deceleration of the beam

Following the velocity filter, the ion beam is decelerated to a desired lab collision energy to the order of a few eV. Such low collision energies increase the likelihood of bond-forming reactions occurring by increasing the dication-neutral interaction time.[5] These low collision energies are achieved by the use of a decelerator of commercial design. The decelerator consists of eight optical lenses in series, as shown in Figure 2.4. The potential applied to each lens is tuned to achieve an ion beam of optimum shape and intensity.

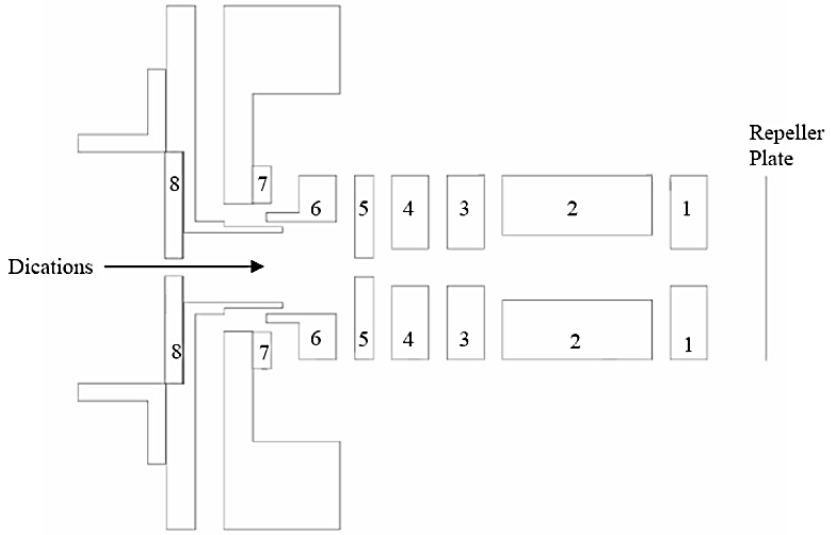

Figure 2.4 A schematic of the decelerating lenses that are situated after the velocity filter and before the repeller plate. The decelerator slows the beam to the desired collision energy (typically < 10 eV) prior to entering the interaction region.

Lens 8 is the first lens in the decelerator, located immediately after the velocity filter. The potential applied to this lens tends to be matched to the velocity of the beam to maximise the transmission of ions through the exit aperture of the filter. Lens 7 is more positive than lens 8. Lenses 4-6 decelerate the beam with lens 4 typically held at -200 V, and lenses 5,6 being held close to -40 V. As the beam is decelerated on-axis, the ions' off-axis velocity vectors become more significant. Lenses 1-3 form an Einzel lens that focusses the ion beam prior to it reaching the reaction region to prevent loss of transmission due to transverse velocities. Lenses 1,3 are grounded in the chamber and lens 2 is varied between 0-10 V to maximise beam shape. Initially, the beam shape and ion current are optimised under continuous beam conditions. Further tuning can occur after pulsing the beam if needs be.

2.3.6 Reaction region

Following deceleration, the reactant ion beam passes into the interaction region *via* a small aperture in the repeller plate that is covered by

an electrode mesh. Perpendicular to the ion beam an effusive jet of neutral collision gas is introduced into the chamber *via* a hypodermic needle. The interaction region also acts as the source region of the TOF-MS, and is kept field-free whilst the ion pulse interacts with the collision gas. Shortly after this interaction, a positive potential is applied to the repeller plate. The voltage is turned off before the next ion pulse enters the interaction region. We can vary the voltage applied to the plate. At low repeller plate voltages (< 150 V) ions with significant velocity perpendicular to the beam can be lost and will not be included in the angular scattering data that we collect. However, these low repeller plate voltages achieve a higher ion energy resolution compared with high voltages. If a higher repeller plate voltage is used (300 V), complete angular scattering data can be collected at the expense of energy resolution.

The timing chain associated with this experiment starts with the waveform generator that controls the deflector pulses described in section Once an ion pulse is formed, the generator triggers a delay generator that controls the application of the voltage pulse to the repeller plate and also starts a time to digital converter (TDC). The time between the triggering of the delay generator and the repeller plate is adjusted so that the reactant dication pulse is in the centre of the reaction region when the voltage is applied to the repeller plate. The signal to start the TDC is also delayed so that no RF noise associated with the pulsing of the repeller plate reaches the TDC when it is activated.

The conditions in the interaction region are kept such that false coincidences are kept to a minimum. Single collision conditions are maintained by ensuring that the neutral gas pressure is kept low ($< 4 \times 10^{-6}$ Torr) and that a low flux of dications is used.[6] These precautions ensure that, on average, many times less than one ion is detected per pulse of the repeller plate, which minimises false coincidences and increases the signal to noise ratio. The run time of each experiment is chosen appropriately for these conditions in order to collect statistically meaningful data. For the experiments detailed in chapters 6-7 typical acquisition times were several days.

2.3.7 Time of flight mass spectrometer

The TOF-MS is composed of three sections: a source region, acceleration region and field-free drift tube. The interaction region, described in section 2.3.6, is also the source region of our TOF-MS. After an ion pulse has interacted with the neutral gas, the repeller plate is pulsed to a positive voltage, which creates a potential gradient that accelerates the ions towards the detector. The ions then enter the acceleration region where another series of electrostatic lenses produce a linear potential gradient that further accelerates the ions towards the detector. Immediately following the acceleration region is the drift tube that is field-free. At the end of the drift region, the ions are rapidly accelerated to impinge upon the position-sensitive detector (PSD), which results in their detection. A schematic of the TOF-MS is shown in Figure 2.5.

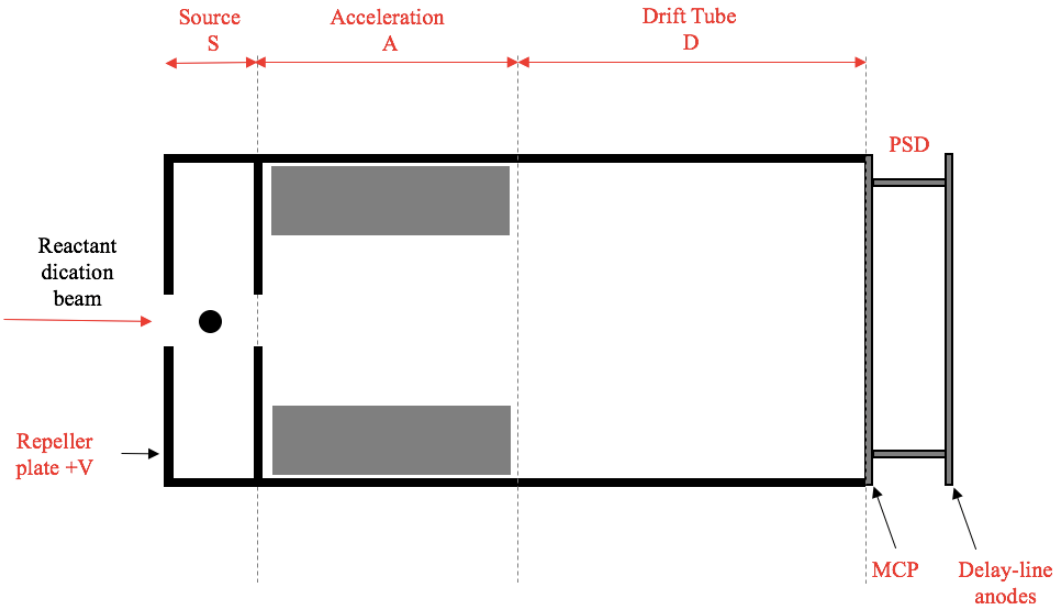

Figure 2.5 Schematic (not to scale) of the two-field PSCO-MS, showing the source, acceleration and drift regions. The acceleration region houses electrostatic lenses (grey boxes) that provide a potential gradient to accelerate the ions towards the PSD. The PSD consists of multi-channel plates and delay lines.

The basic principle of time-of-flight mass spectrometry is that we can distinguish between ions of different *m/z*, which have been accelerated to the

same kinetic energy, based on the time it takes each ion to traverse a field-free drift tube of a fixed distance. Hence, recording the flight times of each ion leads to the determination of their *m/z*. Newtonian mechanics can be used to show that the time-of-flight, t_{TOF}, of an ion is proportional to the square root of its *m/z*. Equation 2.11 details this relationship, where *k* is a constant that relates to the magnitudes of the source and acceleration fields and the dimensions of the spectrometer. The values of *k* and *c* can be determined by calibrating the flight times of two known ionic fragments.

$$t_{TOF} = k\sqrt{\frac{m}{z}} + c \qquad 2.11$$

Early TOF-MSs excluded the acceleration region, instead relying upon the field in the source region alone to accelerate the ions formed to high velocities. This type of spectrometer is termed a 'single field' TOF-MS. In such a spectrometer, ions formed in different positions in the source region experience different accelerating fields, and therefore reach different maximum velocities before entering the field-free drift tube. This range of ion starting positions in the source causes ions formed at further points from the detector to acquire a greater initial potential energy, and therefore reach a greater kinetic energy upon entering the drift tube. Such ions would have a greater velocity when traversing the field free region, and would have a shorter TOF compared to ions formed closer to the detector. Specific conditions are required to overcome this effect, which are described below.

The dimensions of both the source region and drift tube must be precisely engineered to exact dimensions to avoid ions of the same *m/z* arriving at a wide range of TOFs. The reliance on such precision engineering is a major disadvantage to single-field TOF-MS.[7] In 1954, Wiley and McLaren discovered that space-focussing could be achieved with two separate fields of magnitudes in a specific ratio, termed two-field TOF mass spectrometry.[8] Space-focussing allows the spread of starting positions in the *z* direction to be neglected, whilst the *x* and *y* directions remain significant. Figure 2.5 shows a schematic of the two-field TOF-MS used in the PSCO apparatus.

This TOF-MS is designed to achieve second-order space-focussing conditions, first formulated by Eland, which ensure that the time-of-flight for ions with the same *m/z* is largely independent of the starting position within the source.[9] In this case, the geometry of the spectrometer and magnitude of the acceleration fields result in both the first and second-order derivatives of t_{TOF} being equal to zero with respect to source position (equation 2.12).

$$\left(\frac{\partial^2 t_{TOF}}{\partial s^2}\right)_{\substack{U=0 \\ S_0}} = 0 \qquad 2.12$$

Second-order focussing means that the spread of flight times for ions formed at different positions around the centre of the source is even smaller compared to first-order conditions.[10] Second-order designs generally require longer acceleration regions compared to Wiley-McLaren spectrometers, meaning many of the early mass spectrometers had the wrong dimensions for second-order focussing.[8] The PSCO TOF-MS has source, acceleration and drift-tube lengths of 1.63 cm, 11 cm and 27.5 cm respectively. Typical parent ion peaks in a mass spectrum have a FWHM of approximately 3 ns.

2.3.8 Position Sensitive Detector

The position-sensitive detector (PSD) used in this apparatus is of commercial design consisting of two microchannel plates (MCPs) and a wire wound delay-line anode.[11, 12] The MCP is used to record ion arrival times and the delay-line anode is used to record the positional data associated with each ion that impinges on the face of the detector. The PSD is mounted at the end of the drift tube of the TOF-MS.

The MCPs are specialist glass plates, which incorporate channels that are 10 microns wide. When an ion impinges upon the front of the detector, an electron cascade is produced in one of the channels and accelerated down the channel towards the output end. The ions must be accelerated to around 2 kV prior to impingement with the detector face to ensure that the ion impact is energetic enough to cause such an electron cascade.

From the output of an MCP channel, the electron cascade hits the delay lines, of which there are two, that are wound around an insulating

former in both the *x* and *y* directions. These delay lines are positioned perpendicular to the axis of the spectrometer. The charge pulse propagates in both directions along both the *x* and *y* delay lines. Once the charge pulse reaches the end of a wire, a 'stop' signal is sent to the timing circuitry. The position of the detected ion fragment is encoded by the signal arrival time difference at both ends for each pair of delay-lines.

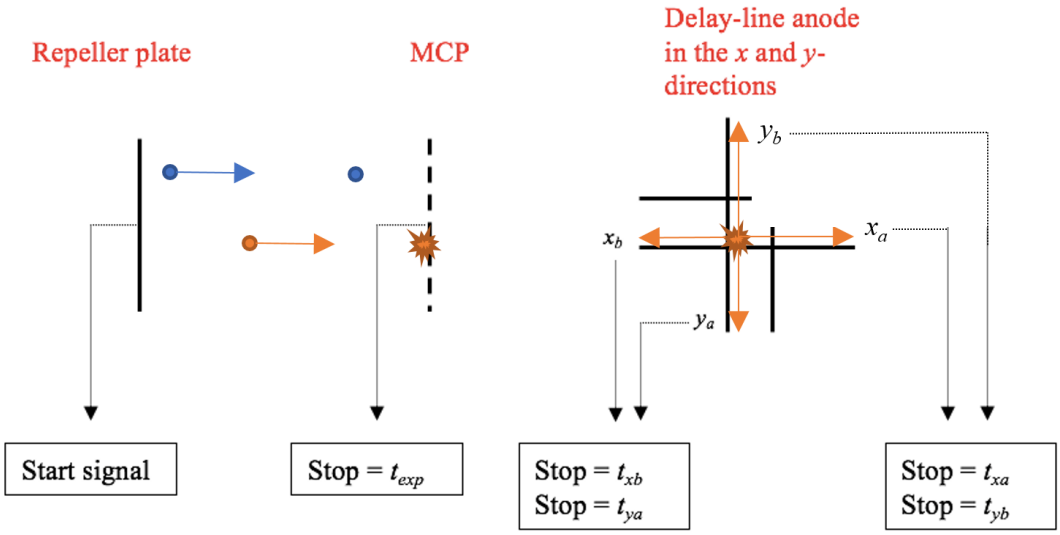

Figure 2.6 Schematic to indicate the timing signals that are sent to the PC per ion that arrives at the detector. Each ion has five times associated with it. T_{exp} is the ions experimental time of flight.

Figure 2.6 shows the five signals that are sent to the TDC per single ion that is detected. When the repeller plate is pulsed, a 'start' signal is sent to the TDC. When an ion hits the face of the MCP, a 'stop' signal is sent to the TDC. The difference between the start signal and this stop signal is the experimental time-of-flight for the ion, $t_{exp}(i)$, where i is equal to the number of ions detected in coincidence. The four stop signals pertaining to the delay-line anodes described above are also recorded relative to the start signal, giving $t_{xa}(i)$, $t_{xb}(i)$, $t_{ya}(i)$ and $t_{yb}(i)$. Thus, for every ion detected by the PSD, a total of five times are recorded. It follows that when a pair of ions are detected in coincidence, ten times would be recorded. These signals are

amplified by the electronics, and then the TDC send the digitised data to a data collection programme on a PC. Events that involve the detection of a single ion following the pulse of the repeller plate, where i = 1, are termed ‘singles’. The TOFs, $t_{exp,}$ recorded for such events are added to a one-dimensional mass-spectrum. Events where two ions are recorded in coincidence following a single pulse of the repeller plate, where i = 2, are termed ‘pairs’ and the ten times associated with their detection are stored in a list and are analysed off-line as described below.

2.4 Data processing

All the raw data collected, in the form of ‘stop’ signal times, is stored on a PC to be later processed off-line. A detailed analysis of the data leads to information pertaining to the chemical identity, the energetics and dynamics of any reactions that may have occurred following the interaction of a dication beam with a neutral gas. The processes by which the data are analysed are described below.

2.4.1 Coincidence spectra

When two ions are detected in coincidence ten sets of times are recorded, as described in section 2.3.8. This information is first used to form a ‘pairs’ coincidence spectrum: a 2D histogram of the flight times of ions detected in pairs. For example, if ions A and B were detected in coincidence, the pairs spectrum would consist of a histogram of the time-of-flight of ion A plotted against the flight time of ion B. Each reaction channel results in one lozenge shaped peak.

Many unreacted dications traverse the mass spectrometer and impinge upon the face of the detector. In fact, many more reactant dications are detected compared to ions that are the product of a reaction because the number density of unreacted reactant ions in the interaction region vastly exceeds that of product ions. It follows that unreacted dications will feature in coincidence spectra as false coincidence peaks. These false coincidence peaks occur at a wide range of flight times, and lead to a band of noise across the coincidence spectra at a mass that corresponds to the TOF of the

unreacted dication. To avoid these false coincidences slowing down the data recording process and producing convoluted spectra, we set an ‘exclusion zone’. As the name suggests, all pairs recorded within the exclusion zone are not counted, and are omitted from the pairs spectrum. This process reduces the size of the data-sets, however, by excluding ions with the same mass as those originating from the ion beam, singly charged ions with the same *m/z* formed in ion-molecule reactions are also potentially excluded. Figure 2.7 shows an example of a coincidence spectrum with the exclusion zone clearly marked.

2.4.2 Peaks and tails

Every ‘real’ peak in a coincidence spectrum corresponds to a pair of monocations detected in coincidence, which are the products of a dication-neutral collision in the source region of the TOF-MS. As described above, the second-order space focussing conditions of the mass spectrometer are calibrated so that any ions with the same *m/z* formed in the source region are focussed to arrive at the detector with an identical TOF. As shown in Figure 2.7 many coincidence peaks exhibit long, curved tails. The tails are caused by the reaction products generated by the same process as those in the main peak that they are attached to, but the products originate from reactions that occur in the acceleration region of the mass spectrometer.

Neutral collision gas enters the acceleration region from the source region *via* an effusive beam. Unreacted dications are accelerated out of the source region when the repeller plate is pulsed and can collide with any stray neutral molecules in the acceleration region. Such reactions occur at higher collision energies compared to those that occur in the source region. Any product ions that may form in the acceleration region do not experience the correct focussing conditions to arrive at the detector with a TOF that corresponds to their *m/z*. Therefore, these product ions lead to counts in the coincidence spectrum at different TOFs than those of the same reaction occurring in the source region. That is, the tails correspond to the different product ion flight times related to the distance travelled into the acceleration region by the reactant ion prior to collision. Dication derived product ions that originate in the acceleration region will be recorded at shorter flight times

compared to reactions that originated in the source region. Whereas, product ions derived from the neutral that occur in the acceleration region will be recorded at longer flight times compared to reactions that originated in the source region. This behaviour results in the reaction peaks having tails, as shown below.

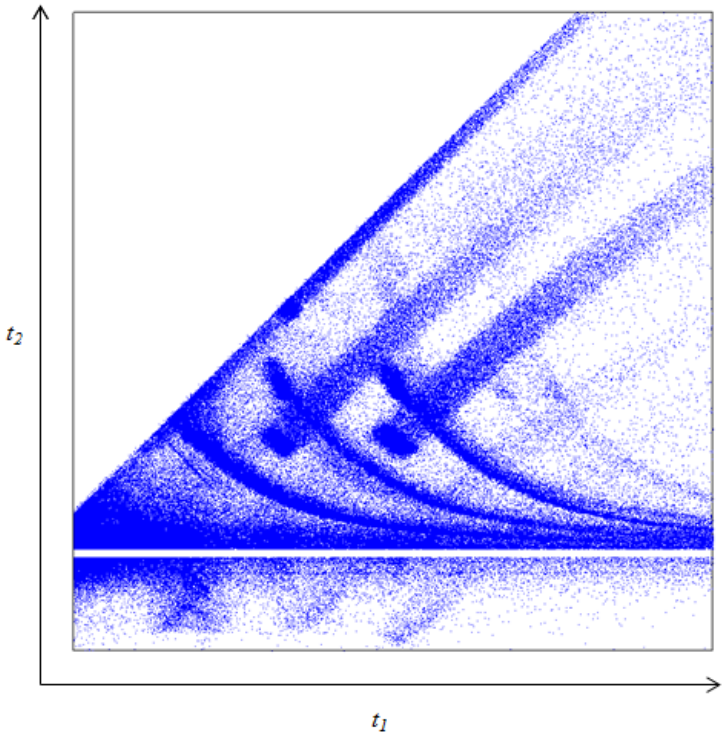

Figure 2.7 A coincidence spectrum recorded following Ar^{2+}/C_2F_6 collisions. The flight time of the first ion to arrive at the detector, t_1, is plotted along the *x* axis. The TOF of the second ion to arrive, t_2, is plotted on the *y* axis. Tails and background counts are also recorded. The 'exclusion zone', discussed in the text, is clearly seen. The data are presented as single spots, irrespective of the number of counts at each coordinate, to highlight bond-forming reactions which have lower cross sections compared to simple electron transfer reactions. Reaction tails are also highlighted owing to this method of presentation.

Some reaction channels do not have tails connected to their coincidence peaks. Such peaks can be explained by considering reactions where the reaction cross-section decreases rapidly with increasing collision energy. For reactions where this is the case there will be no reactivity in the acceleration region, where the collision energy is far greater than in the source. Thus, coincidence peaks that correspond to such reactions will not exhibit a tail. Such coincidence peaks usually correspond to bond-forming reactions, which do not often occur at high collision energies.

2.4.3 Product velocities in the COM and LAB frames

Following the interaction of a dication with a neutral, a detailed understanding of the product ion velocities must be known in order to predict product ion trajectories. Perhaps the most intuitive analysis is to consider these velocities relative to the PSCO apparatus, which is termed the LAB frame. Prior to collision in the LAB frame, the dication has a significant velocity and the neutral is effectively stationary. Upon collision, not all the lab collision energy is available for reactive processes, as the linear momentum of the system must be conserved. It follows that a complex analysis, in which linear momentum is considered, is required to extract information about the dynamics of a system using the LAB frame velocities alone.

Product ion velocities in the LAB frame are determined by the interpretation of the 'stop' signal times recorded by the TDC. The first step in this determination is to ascertain the position the ion hit relative to the centre of the detector in the *x* and *y* directions. For ion *i,* the position in the *x* direction can be determined by evaluating equation 2.12, where t_{xa} and t_{xb} are the two stop signal recorded by the TDC when the charge propagation pulse reaches each end of the delay line, and s_x is the charge propagation speed. The position in the *y* direction can be determined in the same way, by substituting t_{xa} and t_{xb} for the stop signals reaching the end of the delay line in the *y*-direction, and s_x for s_y.

$$x(i) = \frac{t_{xa}(i) - t_{xb}(i)}{s_x} \qquad 2.13$$

The velocity vector in the *z* direction, in line with the beam, is determined using the Wiley-McLaren 'braking time' relationship and is shown in equation 2.12, where *e* is the charge of an electron, *Z* is the charge number of the ion, *F* is the electric field strength, which is determined in a calibration experiment, and m(*i*) is the mass of ion *i*.[8, 15, 16] This velocity is determined using the ionic TOF of an ion formed with no initial kinetic energy t_0(i).

$$v_z = -\frac{\left(t_{exp}(i) - t_0\right)eZF}{m(i)} \qquad 2.14$$

To determine the LAB frame velocity from the coincidence data, the position of the unreacted dication beam on the detector must also be known, x_0 and y_0, which can be established by recording a spectrum of the unreacted dication beam on the detector. The position of the beam can be shaped and optimised using the electrostatic lenses described in section 2.3.5. This positional information provides an estimate of the position of any dication-neutral reactions and, coupled with the recorded TOF of the product ion (t_{exp}), the velocity vectors in the *x* and *y* directions can be determined. Equation 2.12 shows how the velocity in the *x* direction is determined for ion *i*, where *c* is a constant to account for the electronic delay between the pulse of the repeller plate and the 'start' signal arriving at the TDC.

$$v_x = \frac{x(i) - x_0}{t_{exp} + c} \qquad 2.15$$

Using equations 2.13-2.15, the velocity in the LAB frame of a product ion can be determined, $v(i) = (v_x, v_y, v_z)$.

To simplify the analysis of the reaction dynamics that occur following dication-neutral collision, the reactant and product ion velocities are considered relative to the movement of the centre of mass (COM) of the collision system - the COM frame. In the COM frame, the sum of the reactant and product ions momenta is equal to zero. As such, the reactant ions are thought to be travelling towards the COM of the collision. Upon collision, the product velocities are thought to be travelling away from the collision centre.

As the total linear momentum is zero in the COM frame, all collision energy can be used for reactive processes.[17, 18]

The LAB ion velocities can be converted into the COM frame. First, we determine the velocity of the centre-of-mass of the system itself v_{CM}, where m and v are, respectively, the mass and LAB frame velocity of the reactants.

$$v_{cm} = \frac{m_{ion}v_{ion} + m_{neutral}v_{neutral}}{m_{ion} + m_{neutral}} \qquad 2.16$$

Equation 2.16 describes how to calculate the velocity (v_{COM}) of the COM, where m_{ion} and v_{ion} are the mass and velocity of the reactant dication and m_{neu} and v_{neu} are the mass and velocity of the neutral reactant respectively.[19, 20] The kinetic energy of the COM can also be determined, as shown below.

$$T_{COM} = \frac{1}{2}(m_{ion} + m_{neu}){v_{COM}}^2 \qquad 2.17$$

The velocity of a particle in the lab frame is the sum of the velocity of the particle in the COM frame and the velocity of the COM. Therefore, the COM velocity of a particle is the difference between the LAB frame velocity and the velocity of the COM, as shown in equation 2.18.

$$w_a = v_a - v_{cm} \qquad 2.18$$

In the LAB frame, not all of the total kinetic energy (T_{lab}) of the system is available for reactive processes, as some is required to move the COM. The total kinetic energy in the lab frame is given by the sum of the kinetic energies of the reactants in the collision system – the neutral and the dication.

$$T_{lab} = \frac{1}{2}m_{ion}v_{ion}^2 + \frac{1}{2}m_{neu}v_{neu}^2 \qquad 2.19$$

It follows that the total available COM collision energy (E_{cm}) is the difference between the total kinetic energy available in the COM frame, and the total kinetic energy available in the LAB frame.

$$E_{cm} = T_{LAB} - T_{COM} = \frac{1}{2}\mu {v_{rel}}^2 \qquad 2.20$$

$$= \tfrac{1}{2}m_{ion}v_{ion}^2 + \tfrac{1}{2}m_{neu}v_{neu}^2 - \tfrac{1}{2}(m_{ion} + m_{neu})v_{cm}^2$$

Where

$$\mu = \frac{m_{ion}m_{neutral}}{m_{ion} + m_{neutral}}$$

$$v_{rel} = v_{ion} - v_{neutral}$$

In this experiment, the neutral gas is admitted to the chamber *via* an effusive jet. As such, the neutral gas is approximated to be aligned with the direction of the ion beam. That is, the velocity of the neutral is approximated to be zero, $v_{rel} = v_{ion}$, and $T_{lab} = \tfrac{1}{2}m_{ion}v_{ion}^2$. This approximation enables us to simplify equation 2.19 to equation

$$E_{cm} = \frac{\mu T_{lab}}{m_{ion}} \qquad 2.21$$

Unlike the LAB frame kinetic energy, the COM collision energy is wholly available for reactive processes. The COM kinetic energy release is therefore the sum of the COM collision energy and any energy released following a reaction.

In the COM frame, the energy after the collision between the dication and the neutral is shared so that the momenta is conserved and equal to zero. The product velocities of ions formed following a simple, two body reaction are linked through equation 2.22

$$m_1 w_1 = m_2 w_2 \quad \Rightarrow \quad w_2 = -w_1 \frac{m_1}{m_2} \qquad 2.22$$

It is clear that the product ions formed in a two-body reaction will be scattered in opposite directions, in order to conserve momenta.

The picture described above becomes more convoluted when a third body is considered, as depicted in equation 2.23.

$$\mathrm{A^{2+} + BC \rightarrow A^{+} + B^{+} + C} \qquad 2.23$$

As the neutral body (C) is not detected directly, the identity of such a fragment is often inferred from the identity of the ions detected in coincidence. In the PSCO experiment, the velocity of a neutral body cannot be determined directly in the COM frame but can be calculated on an event-by-event basis using equation 2.24, which is based on the conservation of momentum. *w*(*i*) is the velocity of the ion (*i* = 1, 2 or 3) and *m*(*i*) is its mass.[25]

$$\omega_3 = \frac{-m_1\omega_1 + m_2\omega_2}{m_3} \qquad 2.24$$

Thus, full energetics and dynamics can be extracted from the data sets collected following two or three body reactions that occur after a dication-neutral collision.

2.4.4 Scattering diagrams

In order to study the COM product velocities, they are presented as scattering diagrams. A scattering diagram is a polar histogram (*r*, θ). When two ions are detected in coincidence, the radial coordinate *r* is determined by the magnitude of the velocity vectors of the product ions, and the angular coordinate θ is given by the angle between the two product ion velocities. This angle can be determined by the dot product of the velocities, as shown in equation 2.25.

$$\cos\theta = \frac{\omega_1 \cdot \omega_2}{|\omega_1||\omega_2|} \qquad 2.25$$

In chapters 4 and 5, the scattering diagrams are constructed in two different frames of reference: COM and internal scattering.

2.4.5 COM scattering diagrams

A COM scattering diagram is plotted relative to the direction of the LAB frame velocity of the COM of the system, v_{COM}. The angular coordinate of a COM scattering data point corresponds to the angle between the velocity of the product *w*(*i*) relative to v_{COM} and the radial coordinate is the magnitude of *w*(*i*). In the LAB frame, v_{COM} is more or less the same as the reactant dication beam, as the velocity of the neutral is negligible compared to that of the dication. Therefore, the product velocities in a COM scattering

diagram are often expressed relative to the reactant dication velocity. The histograms are cylindrically symmetrical around v_{COM}. To enable the depiction of both product ion scattering patterns, the diagrams are split into two halves. For example, in a dication-neutral reaction where the product monocations *x* and *y* form, the top half of the scattering diagram would depict the scattering of ion *x*, and the bottom half ion *y*. Generally, the ion with the greatest mass is depicted by black points, and the scattering of the lighter ion is shown in red.

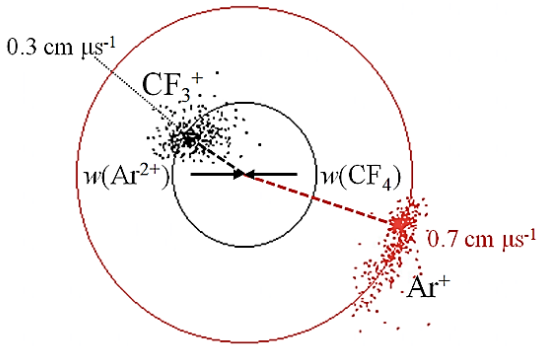

Figure 2.8 COM frame scattering diagram of the Ar^+ and CF_3^+ product ions formed following the non-dissociative SET between Ar^{2+} and CF_4. The directions of the reactants are shown by the full headed arrows: prior to the collision the dication was travelling right and the neutral was travelling left. The dashed open headed arrows represent the product ion velocities. The scattering pattern is clearly anisotropic; the product ions continue to travel in the direction of their associated precursor species. This reaction exhibits strong forward scattering.

Figure 2.8 shows a typical COM scattering diagram. The full headed arrows indicate the initial directions of travel for both the dication and the neutral.. For each ion pair that is detected, the calculated COM frame velocities are plotted as a pair of points on a scattering diagram such as the one shown in Figure 2.8. The colour coded circles on the diagram show the

average velocity of the relevant product ions. The open headed arrows, which are also colour coded, show the radii of these circles. Studying the scattering patterns displayed in these diagrams can provide information about the dynamics of the reaction.

There are two COM scattering pattern motifs that are commonly observed: those that exhibit forward scattering and those that exhibit isotropic scattering with respect to the COM. Figure 2.9 is a COM scattering pattern that displays strong forward scattering. Specifically, in the figure, we can clearly see that the Ar^+ product ion is scattered strongly in the direction of travel of the incoming Ar^{2+} reactant. This strong forward scattering arises because the electron transfer is occurring at large interspecies separations between the dication and the neutral. As predicted by Landau-Zener reaction window theory, outlined in section 1, efficient electron transfer occurs when the reactant and product potential energy surface crossing occurs between 3 – 6 Å. Such a large interspecies separation at the point of electron transfer means that the two reactants do not interact slowly with one another, rather, they simply rapidly pass one another and an electron hops from the neutral to the dication. Thus, the product ions are scattered broadly in the same direction as their reactant precursors. Though few, some products are scattered near 180^0 to their reactants. These are attributed to head on collisions of the two reactants. Most scattering diagrams that exhibit forward scattering are attributed to SET reactions.

Figure 2.9 displays the second common COM scattering motif: isotropic scattering. This pattern is displayed when the two reactant bodies form a long lived complex before dissociating into product ions. Indeed, the complexes formed have long enough life times to rotate at least once. As such, any directional information about the reactants is lost and the product ions are ejected isotropically.

Both scattering motifs described above share a common property: they both display zero scattering of a product ion at 0º or 180º to its relevant reactant trajectory. This trait can be explained by considering the dynamics of a reaction that would lead to such scattering. If a product ion scattered

with 0º change from its reactant trajectory, it would imply that the species had zero deflection upon reaction. Similarly, in a reaction where a product ion would scatter at 180º to its reactant trajectory implies a mechanism where the product is perfectly back scattered upon reaction. The cross-sections for both mechanisms are small, hence most scattering diagrams share this common property.

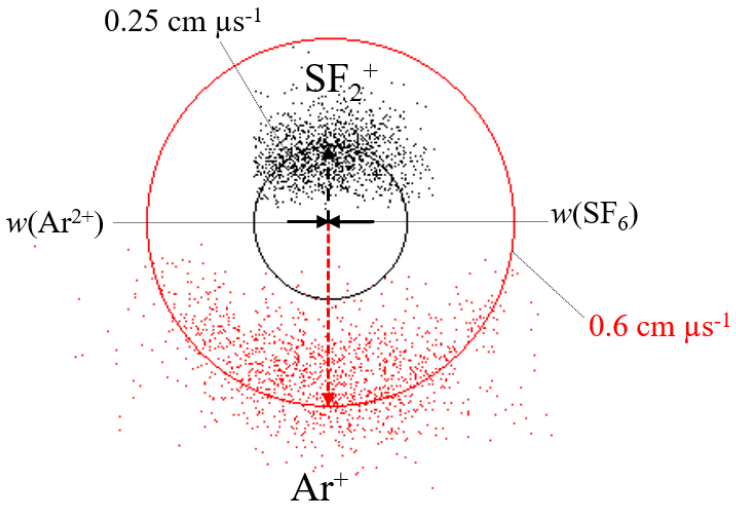

Figure 2.9 COM scattering diagram of the SF_2^+ and Ar^+ product ions formed following SET between Ar^{2+} and SF_6. The scattering is clearly isotropic; the product ion trajectories show no correlation to the direction of travel of their respective reactant species.

2.4.6 Internal frame scattering diagrams

When the COM velocities can be determined for all the products formed in a three-body reaction, an internal frame scattering diagram can be constructed. This type of polar histogram displays two of the product ion velocity vectors relative to the direction of the third body. That is, an internal frame scattering diagram enables the study of the correlation between the COM velocity vectors in three body reactions. For example, if w_1 were

chosen as the velocity vector of reference, $w(i)$ (i = 2, 3) would be plotted relative to it. The angular coordinate would be given by equation 2.25 and the radial coordinate would be the magnitude of $w(i)$. An example of an internal frame scattering diagram is given in Figure 2.10.

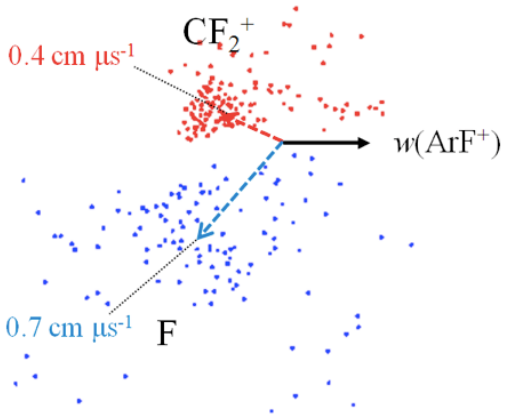

Figure 2.10 Internal frame scattering diagram constructed showing the product species trajectories relative to a third ArF^+ ion, following Ar^{2+} and CF_4 collisions.

2.4.7 Translational energy release

The kinetic energy of a dication-neutral system, i, in the LAB frame is equal to the sum of the individual kinetic energies of each, as shown below.

$$T_{LAB} = \frac{1}{2} m_{ion} {v_{ion}}^2 + \frac{1}{2} m_{neu} {v_{neu}}^2 \qquad 2.26$$

When considering the energetics of a reaction in the LAB frame, not all the collision energy is available for reactive processes, as some is required to move the COM itself. The total available collision energy, E_{COM}, is therefore the difference between T_{LAB} and T_{COM}, where μ is the reduced mass of the system.

$$E_{COM} = T_{LAB} - T_{COM} = \frac{1}{2} \mu (v_{ion} - v_{neu})^2 \qquad 2.27$$

$$\mu = \frac{m_{ion} m_{neutral}}{m_{ion} + m_{neutral}} \qquad 2.28$$

The translational energy release for a 2-body reaction in the COM frame, T_{Prod}, can be calculated using the ionic velocity vectors in the LAB frame as shown in equation 2.26, where μ_{prod} is the reduced mass of the product ion pair and $v_{x,y,z}$ is the ionic velocity vector.

$$T_{Prod} = \frac{1}{2}\mu_p \left[(v_{x1} - v_{x2})^2 + \left(v_{y1} - v_{y2}\right)^2 + (v_{z1} - v_{z2})^2\right] \quad 2.29$$

The first law of thermodynamics is given below, where U is the internal energy of the system, H is the enthalpy, p is pressure and V is volume.

$$\Delta U = \Delta H - \Delta(pV) \quad 2.30$$

In the COM frame the collision energy is totally available for reactive processes. Therefore, the kinetic energy of the product ions, T_{prod}, will be the sum of the available collision energy, E_{COM}, and the exoergicity of the reaction between the dication and neutral, ΔE (equation 2.31). Throughout chapters 4 and 5, this exoergicity is referred to as exothermicity based upon the assumption that the pressure in the PSCO chamber is very small compared to the other variables. Therefore, it can be approximated to zero. The volume of the chamber is constant, therefore the internal energy of the system becomes equal to the enthalpy. Based on this assumption, the exoergicity of a dication-neutral system is equal to its exothermicity. Thus, the exothermicity of the reaction can be determined by assessing the difference between the translation energy release and the collision energy.

$$T_{Prod} = E_{COM} + \Delta E \quad 2.31$$

$$\Delta E = E_{products} - E_{reactants} = T_{Prod} - E_{COM} \quad 2.32$$

$$E_{COM} = \frac{1}{2}\mu_R v_{ion}^2 \quad 2.33$$

In the reactions presented in chapters 4 and 5, the exothermicity is the energy difference between reactant and product states. The ability to probe the exothermicity of a given reaction is a powerful tool that provides insight into the reactant and product electronic states involved in an ion-neutral

reaction. As shown in Figure 2.11, the exothermicity of a given reaction is independent of collision energy, E_{COM}. Indeed, varying the collision energy of a reaction does not change the exothermicity. Thus, a histogram of different ΔE calculated for the same reaction channel can be compared to literature exothermicities, which enables us to identify the electronic states, and sometimes even vibrational states, involved in the ion-molecule reaction.

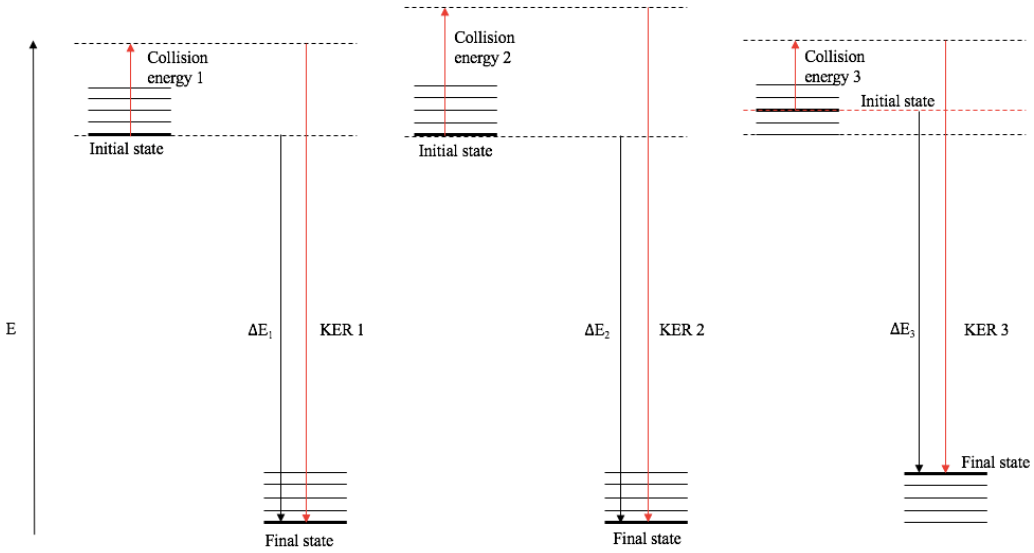

Figure 2.11 A schematic diagram showing the how ΔE, T_{prod} and E_{COM} are related to the initial states of the reactants and final states of the products following a dication-molecule reaction. The exothermicity of the reaction does not vary with collision energy. The only variation in exothermicity arises with different combinations of initial and final states.

2.4.8 Summary

This chapter has described the PSCO-MS apparatus that was used to perform the experiments outlined in chapters 4 and 5 of this thesis. A detailed description of the data analysis has also been given. This apparatus has been used to perform detailed studies of the dynamics and energetics of reactions that occur following the interaction of a dication with a neutral species.

2.5 Bibliography

1. W. P. Hu, S. M. Harper and S. D. Price, *Measurement Science & Technology*, 2002, **13**, 1512-1522.
2. G. K. Ovrebo and J. L. Erskine, *Journal of Electron Spectroscopy and Related Phenomena*, 1981, **24**, 189-204.
3. S. M. Harper, S. W. P. Hu and S. D. Price, *Journal of Chemical Physics*, 2004, **120**, 7245-7248.
4. W. Aberth and H. Wollnik, *Mass Spectrometry Reviews*, 1990, **9**, 383-404.
5. S. D. Price, *Physical Chemistry Chemical Physics*, 2003, **5**, 1717-1729.
6. K. Yamasaki and S. R. Leone, *Journal of Chemical Physics*, 1989, **90**, 964-976.
7. V. H. Dibeler, *Analytical Chemistry*, 1954, **26**, 58-65.
8. W. C. Wiley and I. H. McLaren, *Review of Scientific Instruments*, 1955, **26**, 1150-1157.
9. J. H. D. Eland, *Measurement Science and Technology*, 1993, **4**, 1522-1524.
10. J. H. D. Eland, *Molecular Physics*, 1987, **61**, 725-745.
11. A. Oelsner, O. Schmidt, M. Schicketanz, M. Klais, G. Schonhense, V. Mergel, O. Jagutzki and H. Schmidt-Bocking, *Review of Scientific Instruments*, 2001, **72**, 3968-3974.
12. I. Ali, R. Dorner, O. Jagutzki, S. Nuttgens, V. Mergel, L. Spielberger, K. Khayyat, T. Vogt, H. Brauning, K. Ullmann, R. Moshammer, J. Ullrich, S. Hagmann, K. O. Groeneveld, C. L. Cocke and H. Schmidt-Bocking, *Nuclear Instruments & Methods in Physics Research Section B-Beam Interactions with Materials and Atoms*, 1999, **149**, 490-500.
13. S. J. King and S. D. Price, *Journal of Chemical Physics*, 2007, **127**, 16.
14. N. A. Love and S. D. Price, *Physical Chemistry Chemical Physics*, 2004, **6**, 4558-4565.
15. S. Hsieh and J. H. D. Eland, *Journal of Physics B-Atomic Molecular and Optical Physics*, 1997, **30**, 4515-4534.
16. S. Hsieh and J. H. D. Eland, *Journal of Physics B-Atomic Molecular and Optical Physics*, 1996, **29**, 5795-5809.
17. J. F. Lockyear, M. A. Parkes and S. D. Price, *Journal of Physics B-Atomic Molecular and Optical Physics*, 2009, **42**, 9.
18. C. L. Ricketts, D. Schroder, J. Roithova, H. Schwarz, R. Thissen, O. Dutuit, J. Zabka, Z. Herman and S. D. Price, *Physical Chemistry Chemical Physics*, 2008, **10**, 5135-5143.

19. J. F. Lockyear, C. L. Ricketts, M. A. Parkes and S. D. Price, *Chemical Science*, 2011, **2**, 150-156.

20. M. A. Parkes, J. F. Lockyear, D. Schroder, J. Roithova and S. D. Price, *Physical Chemistry Chemical Physics*, 2011, **13**, 18386-18392.

21. M. A. Parkes, J. F. Lockyear, S. D. Price, D. Schroder, J. Roithova and Z. Herman, *Physical Chemistry Chemical Physics*, 2010, **12**, 6233-6243.

22. M. A. Parkes, J. F. Lockyear and S. D. Price, *International Journal of Mass Spectrometry*, 2009, **280**, 85-92.

23. J. D. Fletcher, M. A. Parkes and S. D. Price, *International Journal of Mass Spectrometry*, 2015, **377**, 101-108.

24. J. D. Fletcher, M. A. Parkes and S. D. Price, *Molecular Physics*, 2015, **113**, 2125-2137.

25. S. Hsieh and J. H. D. Eland, *Rapid Communications in Mass Spectrometry*, 1995, **9**, 1261-1265.

3 The radical source to investigate surface science apparatus (RISA)

3.1 Introduction

In this chapter, the experimental details of the radical beam surface science apparatus (RISA) are described. The apparatus has been developed to probe the products formed following the interaction of a pure, neutral radical beam with a surface. This chapter is divided into three sections. The first section will briefly describe the vacuum systems in place that pump the apparatus to various pressures across the two component chambers. The second section will describe how the incident pure radical beam is formed. The final section will outline the surface science ultra-high vacuum chamber (UHVC). The UHVC houses the target substrate and supports several analytical tools that are used to probe any surface chemistry that may occur following radical-surface interactions. Details of the building and development of the RISA apparatus, and some proof-of-principle results, are provided in chapter 6.

3.2 Overview

The RISA apparatus produces a collimated, pure beam of free radicals *via* the photo-detachment of electrons from an anion beam. A ‘pure’ beam refers to one that consists overwhelmingly of one species. Over the course of the development of the RISA apparatus, several ion sources have been designed, built and optimised to produce beams of anions. The varying successes of each ion source are detailed in chapter 6, however, the experimental details for each are provided later in this chapter. Following ionisation, the beam is extracted from the source region by a potential gradient that is established by a set of electrostatic lenses. The beam is then shaped by a further set of optics. The focussed beam enters a velocity filter, where it is mass selected. A vertical deflector assembly is used to ensure the beam is aligned with the entrance to the filter. Only ions of a chosen mass-to-charge ratio (*m/z*) will follow a linear path through the filter to the exit aperture. The beam is then accelerated and shaped by a further set of electrostatic lenses before entering a quadrupole assembly, which is used to

turn the beam through 90°. The beam is then decelerated before entering a field-free drift region. This drift-region is an interaction chamber where a visible light laser (532 nm) is admitted along the same axis as the ion beam. If a photon with sufficient energy interacts with an anion, an electron will be photo-detached. That is, if the photon energy exceeds the electron affinity of the anion a neutral radical will be produced. Any electrons and un-detached anions are removed from the beam by a set of electrostatic deflectors, leaving the neutral radicals unperturbed from their nascent trajectory. Thus, this interaction produces a radical beam that consists overwhelmingly of one species: neutral radicals of the same mass of the initial anion.

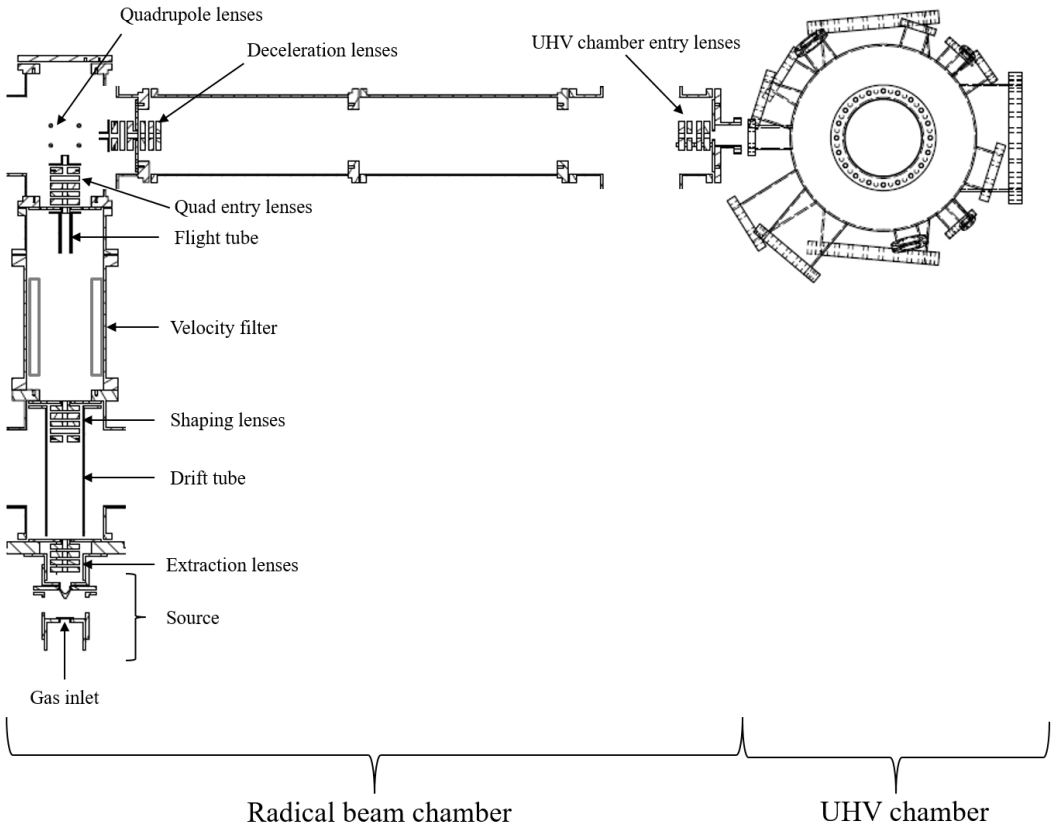

Figure 3.1 A scale diagram of the RISA apparatus. Anions are formed *via* secondary electron attachment. The velocity filter is used to mass select the anion beam. The beam is turned through 90° by the quadrupole lenses. A 532 nm laser is used to photo-detach electrons from the anions.

Following generation, the radical beam passes into a UHVC, where it irradiates a chosen surface. Any chemistry that may occur following such an interaction is probed by a variety of analysis techniques, namely temperature programmed desorption (TPD), X-ray photoelectron spectroscopy (XPS), reflection adsorption infrared spectroscopy (RAIRS) and Auger electron spectroscopy (AES). In combination, these powerful surface science techniques are used to interrogate any species that may form following radical-surface interactions. shows a diagram of the RISA apparatus that was developed and built over the course of this work. The details of the experiment are provided below.

3.3 Vacuum systems

Different regions of the RISA apparatus are evacuated to various pressures. To minimise collisions between the radical beam and background gases, the radical beam chamber (RBC) is held under high vacuum (10^{-3} – 10^{-8} Torr). This chamber is pumped by four turbomolecular pumps, which are backed by rotary pumps. The pressure is monitored through a wide-range gauge and three ion gauges, which are positioned along the length of the chamber.

Perhaps unsurprisingly, ultra-high vacuum conditions are maintained in the UHVC (10^{-9} – 10^{-10} Torr). The reasons to maintain such a low pressure within the surface chamber are manifold. Firstly, UHV conditions are required to prevent the surface quickly becoming saturated with background gases, which would potentially mask any radical-surface chemistry occurring when probed spectroscopically. Secondly, this pressure range is maintained to keep collisions of desorbing species with residual gases to a minimum. Furthermore, the UHVC is equipped with XPS, and such low pressures are required to prevent photoelectrons being deflected by residual gases. This chamber is pumped by both a turbomolecular pump that is backed by a rotary pump, and also a combined ion and titanium sublimation pump (TSP). The latter is a sequestering pump that, as an ion pump, ionises background gas within the UHVC and employs a strong electrical potential (4-7 kV) to accelerate the ions into solid electrodes. As a TSP, this pump lowers the

chamber by coating the pump walls with a reactive coating of titanium through the heating of a titanium filament. Residual gases react with this coating to form a solid, stable product. We can achieve UHV conditions by employing this type of pump, combined with 'baking' the chamber to a high temperature (~ 450 K), which desorbs any contaminant adsorbants off the surface and chamber walls into the gas-phase to be pumped away.

The RBC and the UHVC are separated by a gate valve, which must be open to irradiate the surface with the radical beam. Owing to the pressure gradient across the two chambers, a liquid nitrogen chevron trap is employed to prevent residual gases from the HV side diffusing into the UHVC. The trap is filled with 5 L of liquid nitrogen and acts as a cold finger, freezing out background molecules to prevent them entering the UHVC. The UHVC has been found to maintain UHV conditions after the opening of the gate valve whilst using the trap.

3.4 Experimental details: radical beam chamber

3.4.1 Anion beam generation

Several different anion sources have been designed and optimized during the development of the RISA apparatus, each of which is described in detail below. Several of the ion sources discussed rely upon the electron ionization of a target gas to produce negative ions *via* secondary electron attachment (SEA). To generate negative ions *via* this method, a free jet of neutral molecules is admitted into the chamber. These neutrals cool rapidly by expansion into the vacuum, which gives rise to target species with low internal energies. An electron beam is aimed across the jet of neutrals. If an electron of sufficient energy successfully collides with a neutral ionisation will occur, generating a cation and an electron. This secondary electron may then go on to ionise another neutral molecule, generating a further cation and electron pair. This process continues until low energy (< 10 eV) secondary electrons are produced, which efficiently form negative ions by dissociative attachment, as shown below.

$$AB + e^- \rightarrow [AB]^- \qquad 3.1$$

Then $[AB]^- \rightarrow A + B^-$

Figure 3.2 is a schematic of the RBC ion source region. A pulsed valve was included in the design to allow us to pulse the beam should we wish to in the future. However, to date it has only been used unpulsed, and appropriately biased to act as a repeller plate to push negatively charged species through the skimmer; the beams generated have been continuous waves.

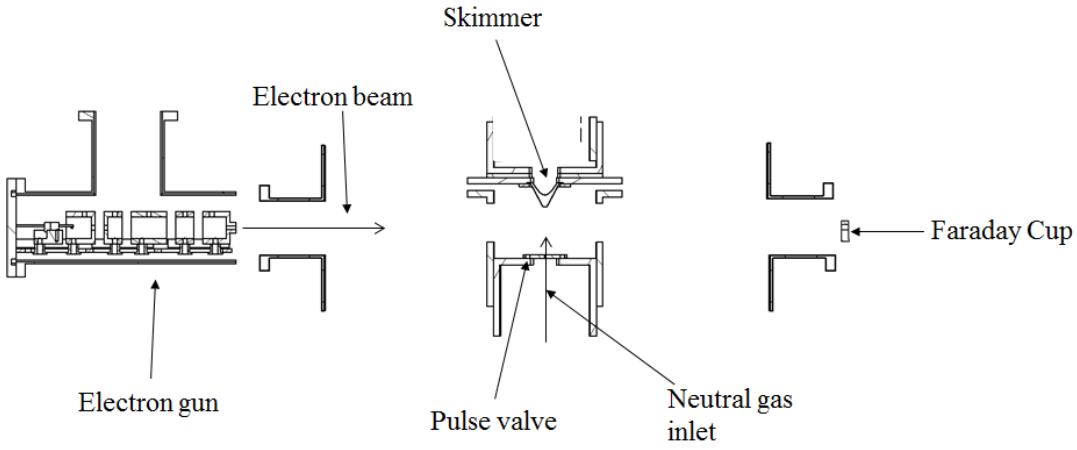

Figure 3.2 A schematic diagram of the experimental arrangement of the ion source region in the RBC. The Faraday cup is a copper plate connect to an electrical output, where the current generated by impinging electrons or ions can be measured using a picoammeter.

During the development of this apparatus, the effect of changing the electron source on anion flux was explored. Each electron gun used was optimised to produce a focused beam of electrons across the source region. The flux of electrons was measured on a Faraday cup. The Faraday cup consists of a copper plate connected to an electrical output, where the current generated by electrons colliding with the plate can be measured using a picoammeter.

Once the electron gun settings were optimised to maximise this measured current, an effusive jet of target gas was admitted to the chamber, and the fields within the source region were adjusted to efficiently produce negative ions. The anion flux was measured on another Faraday plate positioned orthogonally to the flow of electrons behind the skimmer.The results of the electron gun optimisation work are presented below, whereas the anion results can be found in chapter 6.

Table 3.1 The different anion sources and the electron and anion fluxes generated by each.

Anion source name	Source type	Electron flux generated in source region	Anion flux generated
Yttria-coated iridium cathode (YCIC) electron gun	Cathode electron gun	-85 μA	-10 nA
Yttriated tungsten filament electron gun	Filament electron gun	-5 μA	~0 nA
Mounted filament	Filament electron gun	-200 μA	-100 nA
Adapted YCIC	Cathode electron gun	-120 μA	-10 nA
DC discharge	Discharge	N/A	N/A

Each anion source is described in detail below.

3.4.2 Yttria-coated iridium cathode electron gun (YCIC)

The first electron gun to be optimised within the RBC was an yttria coated iridium cathode electron gun (YCIC), of commercial design (Kimball Physics). The gun consists of a cathode, a ‘grid’ and a grounded anode. Electrons were produced *via* thermionic emission from an yttria-coated

iridium cathode. The electrons are then accelerated to a chosen kinetic energy by fields established within the gun. A set of deflector lenses within the gun position the beam through an exit slit. Figure 3.3 shows a schematic of this electron gun, taken from the Kimball Physics manual.

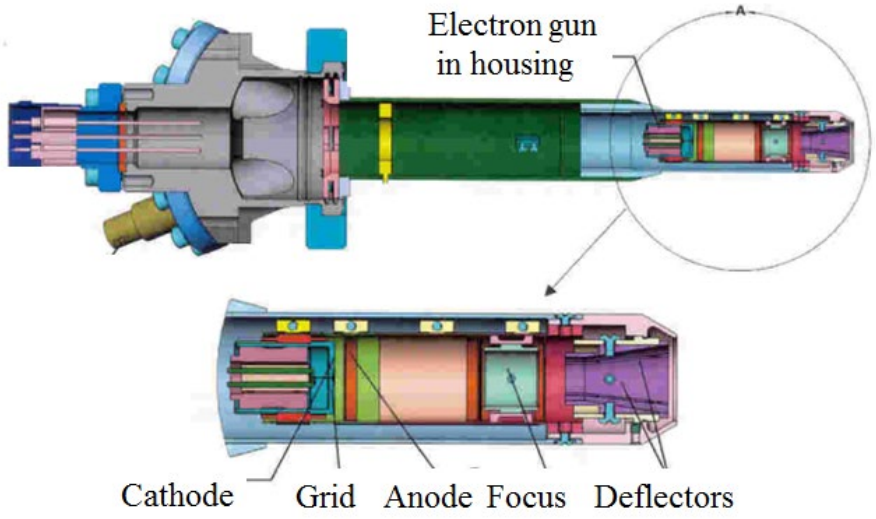

Figure 3.3 A diagram of the Kimball Physics electron gun. Electrons are produced by a yttria-coated iridium cathode via thermionic emission. The anode is grounded. Diagram taken from the Kimball Physics manual.

The ‘grid’ is a tubular structure that houses the cathode and has an aperture on one end. The grid potential is controlled by a voltage source referenced to a negative energy supply. Increasing this voltage makes the grid aperture more negative with respect to the cathode. Thus, as the grid bias increases the electric field between the grid and the cathode suppresses electron emission from around the cathode edges, leaving only the centre of the cathode to emit.

The anode is a plate with a central aperture, which is at ground potential. The magnitude of the electric field created by the potential difference between the cathode and the anode is modified by the grid potential and determines the energy and trajectory of the emitted electrons.

The focus lens consists of three elements that behave as an Einzel lens. The first and the third elements are grounded, whilst the central element is at focusing potential. The spot size of the beam depends upon this focusing voltage and the beam energy. The deflection component of the gun consists of two pairs of deflection plates (*x* and *y*) before the exit of the gun. These plates produce a deflecting force perpendicular to the direction of electron travel when a voltage is applied to them, allowing the beam trajectory to be aimed and guided to the Faraday plate.

To ensure the electron beam was well aligned to pass through the target gas the electron gun settings were optimized prior to admitting the gas into the source region. The beam energy was set to 1000 eV. The grid voltage was adjusted to produce the optimum ratio of beam current to emission current, which was found to be at around 5 V. The potentials applied to the focus lens and *x, y*-deflectors were adjusted to maximize the negative current measured on the Faraday cup. The focus lens potential was optimized to around 700 V. The *x, y*-deflectors were held at close to 0 V, which indicated that there was good alignment of the electron gun and faraday cup. These settings yielded an electron current of -85 μA on the Faraday cup.

3.4.3 Yttriated tungsten filament electron gun

A gun was produced that provided more control over the fields established within the electron source compared to the commercial gun described above. This homemade gun, shown in Figure 3.4, uses an yttriated tungsten filament to produce electrons *via* thermionic emission. The gun consists of a grid, a set of three electrostatic lenses for shaping and a needle with an aperture of 5 mm. Precise control over the voltages applied to each element ensures that the field within the gun maximises electron emission.

Prior to the admission of the target gas the gun was optimised to produce a flux of electrons that measured – 5 μA on the Faraday plate. A filament current of 1.84 A was used to achieve this electron beam, with an applied bias of 200 V. A voltage of – 235 V was applied to the filament

mounting plate and the grid was held at – 170 V. Shaping lenses 1, 2 and 3 were held at + 25 V, - 168 V and – 90 V respectively and the needle was held at + 36 V. Due to the change in emissivity of the filament with increasing gas pressure, when gas was admitted to the chamber the electron current dropped to – 3 μA at 1 × 10^{-5} Torr.

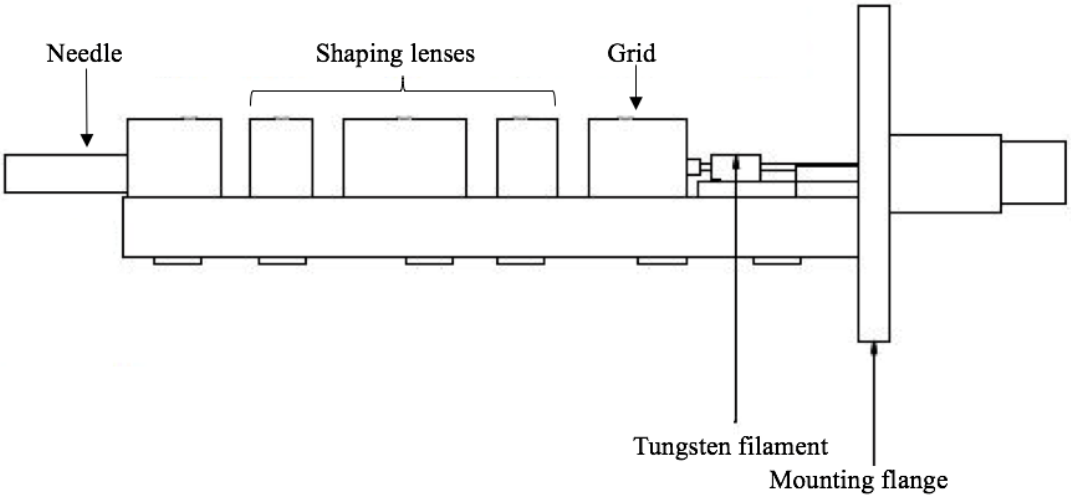

Figure 3.4 A diagram of the yttriated tungsten filament electron gun. This homemade gun has a grid, a set of three shaping lenses and a needle.

3.4.4 Modification to the source region

When optimising the source region settings to produce anions, rather than electrons, the fields within this part of the chamber were adjusted. As such, the fields established to extract the electrons from each electron gun were changed. The optimisation of both set-ups was an iterative process of adjusting the fields within the source region to achieve a trade-off between optimum electron extraction and anion acceleration out of the source region. Comparing the current on the Faraday cup adjacent to the electron source to the current measured on the Faraday cup behind the skimmer gave some indication of electron and anion flux respectively.

Whilst optimising each source region we were aware that the negative current measured behind the skimmer may be due to electrons or anions impinging upon the Faraday cup. To account for this effect, we compared the current measured on the skimmer Faraday cup in the presence and absence of the target gas.

When optimising the YCIC and homemade yttriated filament set-ups to produce anions, it was found that the fields established within the source to extract any negative ions formed were significantly affecting the fields within the electron gun and deflecting the electron beam. To minimise the effect of these stray fields on the electron beam some modifications were made to the source region. A shielding plate was mounted in front of the skimmer and was held at roughly the same voltage as the pulsed valve. From here on in, despite changes to the electron source, this modification was made permanent. The shielding plate is shown in Figure 3.5.

3.4.5 Mounted filament electron gun

The electron guns described above were mounted on an ISO-KF flange on the chamber. The distance between the exit aperture of both guns and the centre of the source region was approximately 150 mm. The centre of the source region is directly in front of the gas inlet, and is therefore where the density of target molecules is highest. To minimise the effect of stray fields on the electron beam prior to interaction with the target gas, we sought to minimise this distance by mounting an electron gun very close to the target gas jet.

The third electron source we designed was mounted onto an electrically insulated hollow shroud, as shown in Figure 3.5. The shroud mounts onto the face of the pulse valve, and is insulated by ceramic spacers and Teflon screws. The shroud is a cylindrical piece, with an inner diameter of 10mm. The cylinder is open at one end, where it attaches to the pulse valve. The opposite end of the cylinder features an interchangeable face plate. We made three face plates, with a central aperture of 1 mm, 2 mm and 4 mm. The 2 mm aperture was used for the experiments described in chapter 6.

The cylinder has a 4 mm aperture in one of its sides, where the electron beam can enter and interact with the target gas.

This electron gun, of homemade design, produces electrons *via* thermionic emission from a tungsten filament. The filament is mounted to the shroud, aligned to its electron beam entry aperture. Either side of the filament we placed metal plates to which we applied appropriate voltages to produce 200 eV electrons that were accelerated into the hollow shroud. Figure 3.5 shows this mounted filament electron gun.

The electron source was optimised prior to the admission of target gas by monitoring the electron beam current generated on the cylindrical structure mounted onto the gas inlet. With the 'repeller plate' held at - 200 V and the 'grid' held at – 175 V, the measured electron beam current was – 200 μA.

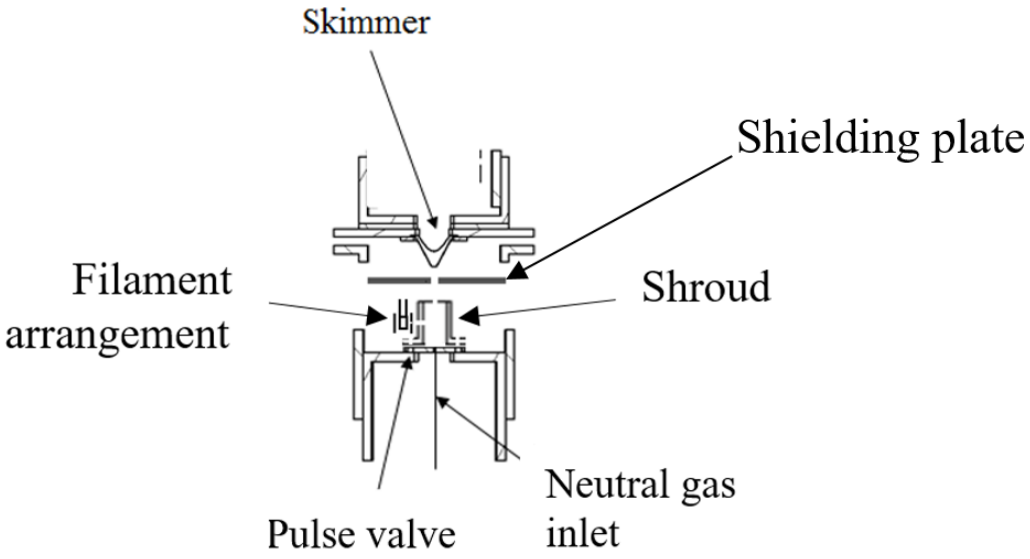

Figure 3.5 A schematic diagram of the mounted filament with shroud source region. Clearly, the distance between the electron source and the interaction region is vastly reduced in this arrangement compared to the source regions described above.

This electron source was successfully used to produce a radical beam – details about these results can be found in chapter 6. Following the production of this radical beam, we sought to increase the flux of radicals. The success of this electron gun was attributed to the decreased distance between the electron source and the gas inlet for two main reasons. Firstly, the vastly reduced the distance between the filament and the centre of the source region meant that the electron beam was less likely to be deflected by stray fields as it has a shorter distance to travel from the gun to the interaction region. Therefore, the probability of a successful electron-target molecule collision is increased. Secondly, the addition of the cylindrical structure to the gas inlet enabled us to increase the target gas pressure in the electron-neutral interaction region whilst maintaining a relatively low pressure (< 10^{-6} Torr) throughout the rest of the source chamber. Broadly speaking, the probability of a successful collision between a secondary electron and a neutral molecule increases with pressure in the 10^{-7}-10^{-5} Torr range, therefore this adaptation increased the likelihood of producing negative ions.

3.4.6 YCIC flange adaptation

During development, the metal filament and electron gun structure described in the previous section were removed from the mounted filament set-up. The YCIC was installed as an electron source. The ISO-KF YCIC mounting flange was replaced by a zero-length flange. This adaptation reduced the distance from the end of the electron gun and the centre of the source region to 100 mm. The electron gun aperture was positioned facing the electron entry aperture in the cylindrical shroud. Following optimising this gun, an electron flux of -0.1 mA was measured on the cylindrical shroud prior to the admission of target gas. Despite an increase in electron flux produced, this adaptation did not affect the flux of anions produced.

3.4.7 DC discharge source

To investigate ways to increase the flux of anions produced by the RISA apparatus, we designed an anion source that could be used at higher pressures compared to the electron guns used. A DC discharge source was

designed, built and installed into the chamber. Ions are generated in a glow-discharge cell that contains a chosen precursor gas. The ion source is of homemade design and consists of a gas inlet and a series of stainless steel plates separated by Macron insulators. To generate a plasma, a high, negative voltage is applied to the anode (-350 V) whilst the cathode is grounded. The dimensions of the cell are such that the pressure between the two plates is high (~ 1 Torr), and a glow discharge can be established.

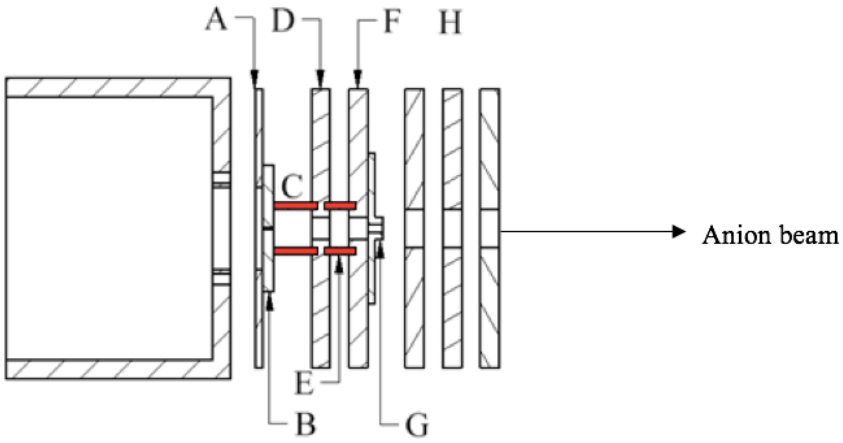

Figure 3.6 Diagram of discharge ion source that produces fluxes of anions where A = plate to mount the pulse valve, B = pulse valve, C = insulator 11 mm long, D = anode, E = insulator 8 mm long, F = cathode, G = face plate with aperture (2 mm), H = set of three lenses to focus the anion beam following the generation of a discharge. The material depicted in red is Macron, an insulating material that can withstand high temperatures (x K), and the lined material is stainless steel

The dominant process of negative ion formation in a plasma is dissociative electron attachment.[1] Within the discharge, electrons ionise the neutral gas to produce cations and electrons. These secondary electrons in turn cause additional ionisation. Eventually, low energy (< 10 eV) secondary

electrons are produced. Such low energy electrons efficiently form anions *via* dissociative attachment.

Figure 3.6 shows a diagram of the discharge source. The glow discharge is generated between plates D and F, across the cavity provided by the Macron insulator. Plate A is held at a high negative voltage (-1.5 kV) to produce a potential gradient that accelerates any anions formed out of the source unit. The anion beam passes through an aperture of 2 mm (G, Figure 3.6), to be shaped by a series of three electrostatic lenses (H, Figure 3.6). Lenses 1 and 3 tend to be held close to ground, with lens 2 being held at + 400 V. This anion source is currently being optimised.

3.4.8 Ion extraction and acceleration

Any anions formed in the source region in use were extracted by a set of electrostatic lenses positioned behind the skimmer. A radical beam was produced following photo-detachment from an anion beam formed in the mounted filament source region. As such, the settings outlined in this section pertain to the optimisation of this anion beam.

Ions are extracted from the source region by fields generated by a series of electrostatic lenses, as shown in Figure 3.7. The copper plate and skimmer feature central apertures that are 5 mm in diameter. For the mounted filament experiments presented in chapter 6, the copper plate is usually held at +350 V and the skimmer is usually held at +400 V. The resultant field extracts the anions from the discharge source. The extraction lens is typically held at a high positive voltage, at around +400 V. Lenses 1-3 are used to shape the beam with lenses 1 and 3 usually set at around +200 V, and lens 2 usually at 0 V. Lenses 1-3 are used to shape the beam with lenses 1 and 3 usually set at around +200 V, and lens 2 usually at 0 V. The anion beam then enters a drift tube, which is held at around +20 V.

The ion flux can be determined by measuring the current generated by negative charge hitting a copper flag or a metal element within the chamber using a picoammeter. Whilst measuring the negative current in the drift region, it was found that a large amount of charge was hitting the drift tube structure, with a small amount of negative charge traversing the chamber

following a linear path. By applying a transverse magnetic field across this region we were able to determine that the negative charge detected on the drift tube was due to electrons, as the current measured there was very unstable with respect to the magnetic field. The trajectory of the relatively heavy anions was assumed to be unperturbed by the magnet.

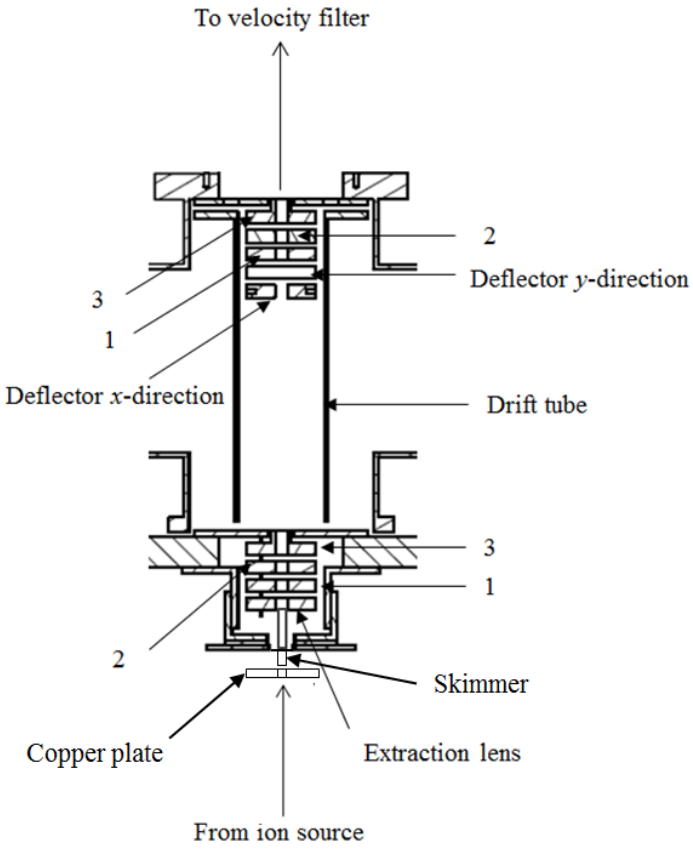

Figure 3.7 A diagram to show the electrostatic lenses that are used to extract, focus and accelerate any negatively charged ions that may be formed in the glow-discharge ion source towards the velocity filter. See text for further details.

The lenses housed within the drift tube are used to accelerate the beam prior to entry into the velocity filter. Lenses 1 and 3 are held at high positive potentials, typically > +250 V and lens 2 is usually held at around +25 V. In order to maximise the transmission of anions into the velocity filter we use a pair of deflectors that can adjust the beam trajectory in the *x* and *y*-directions. These deflectors are usually held at around 0 V, indicating that the the beam, and the lenses within the chamber, are well aligned.

3.4.9 Mass selection of the anion beam

After being focussed in the drift tube, the ion beam enters a velocity filter. This filter, of commercial design, uses a pair of perpendicular electrostatic and magnetic fields to mass select the beam of anions as described in chapter 5.[2] As the anions are close to mono-energetic, selecting ions by velocity effectively selects by *m/z*.

3.4.10 Acceleration, quadrupole manipulation and deceleration

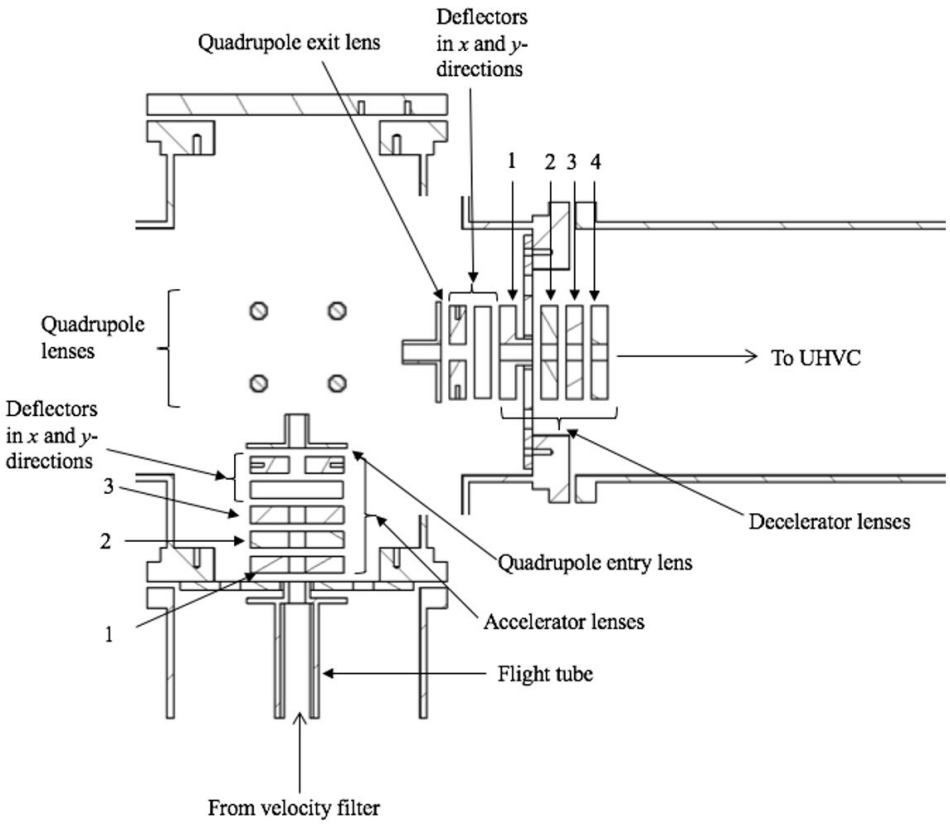

Figure 3.8 A diagram to show the lenses that are used to guide the ion beam out of the velocity filter and accelerate them into the quadrupole lenses. The potentials applied to the quadrupole lenses are such that the ion beam is turned through 90°. The decelerator lenses are used to shape and decelerate the ion beam into the drift region.

After exiting the velocity filter, as shown in Figure 3.8, the anion beam is guided into a flight tube that is held at a high positive voltage (~ +400 V). The beam is then shaped by three optical lenses. The trajectory of the beam can be adjusted by a pair of *x*- and *y*-direction deflectors, which are used to guide the beam into a set of quadrupole rods. The potentials applied to the quadrupole rods are such that the ion beam is turned through 90º. Lenses A and C are typically held at around -250 V and lenses B and D are usually held at close to 0 V. Ion transmission varies greatly with the potential applied to these lenses and the voltages applied to the quadrupole entry and exit lenses. These two plates are held at similar potentials, close to +50 V. The deceleration lenses consist of a pair of x and y-direction deflectors and four focussing lenses. The purpose of this lens stack is to decelerate the beam to increase the probability of a photon-anion collision when the beam is irradiated by a laser. However, during the development of this apparatus the lenses were tuned to maximise ion transmission.

The field established in this region is crucial to the generation of a radical beam, as the anion beam must be shaped and positioned to ensure maximum transmission of ions and high overlap with the laser beam that is used for photo-detachment. Of the ions measured at the entrance to the quadrupole, we have achieved a maximum of 40% transmission of the ion beam to the entrance of the UHVC.

3.4.11 Electron detachment

To produce a beam of free radicals, a green laser is employed to photo-detach electrons from the anion beam. The laser used is a continuous wave 16 W, 532 nm diode laser (Quantum Finesse).

$$\mathrm{AB} + \mathrm{e}^- \rightarrow [\mathrm{AB}]^- \qquad 3.2$$

$$\text{Then } [\mathrm{AB}]^- \rightarrow \mathrm{A} + \mathrm{B}^-$$

As shown the consequence of laser irradiation of a singly charged anion can be the loss of an electron leading to the production of the oxidized form of the anion: a neutral radical. Following the production of the neutral radical,

fragmentation may occur depending upon the energy of the system. To successfully detach an electron from an anion, the excitation energy of the departing electron following laser irradiation must be greater than the electron binding energy of the anion. Typical electron binding energies of many small molecules (< 4 atoms), which are of astrophysical interest, vary in the 0-2 eV range.[3, 4] As such, the laser used in this experiment has sufficient energy to produce a radical beam from many 'small molecule' anion beams.

The excess energy of the system following photo-excitation is distributed between the neutral and the departing electron as kinetic energy, rotation and vibration. As the energy of the laser used in this experiment is 2.33 eV, we can assume that the excess energy that will be partitioned to the neutral following photo-excitation is unlikely to be of the magnitude to cause significant molecular fragmentation. Thus, (ideally) the resultant beam consists of one type of radical, un-detached anions and detached electrons following laser irradiation.

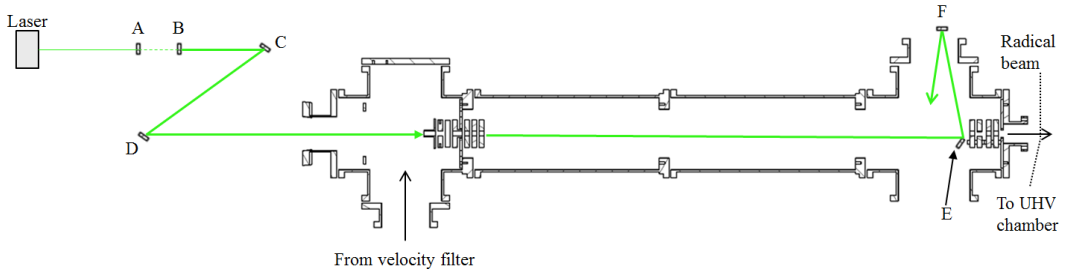

Figure 3.9 A diagram to show the path of the laser beam through the RISA chamber where A = concave lens, B = convex lens and C-F = flat mirrors. A has a -25 mm focal length and B has a +150 mm focal length, providing a 6x magnification. The distance between A and B is 125 mm. An aperture can be used between D and the entrance to the chamber. E is a flat faced mirror on a homebuilt, adjustable mount. F is placed outside the chamber.

The laser beam has a diameter of 2.25 mm. To maximise anion-photon interaction, a beam expander, of homemade design, is used to expand the

laser beam to a diameter of approximately 13 mm. A series of mirrors provide high-precision control over the laser beam position in the *x* and *y*-directions. These mirrors are used to align the beam so it can enter the apparatus through a viewport and pass through the central aperture of the quadrupole exit lenses. The arrangement is depicted in Figure 3.9. A mirror is located within the chamber at the entrance to the UHVC that is used to direct the laser beam out of the apparatus through a second viewport. The laser beam is directed back into the chamber by a mirror located facing the laser-exit port. The beam then reflects off the interior stainless-steel walls of the chamber, crossing the ion beam several times. We have achieved a maximum of 9% anion photo-detachment.

3.4.12 Entering the UHV chamber

The exit chamber lenses are shown below, A set of lenses are employed to remove any electrons and un-detached anions from the beam following laser irradiation. As the radicals are neutral their trajectory remains unaffected by any potential gradients that may be present in this region. Conversely, any negatively charged particles that may be in the beam can be manipulated by an applied field. An *x*-deflector is used for this purpose that consists of two electrically isolated semi-circular lenses. We apply a negative voltage to one of the two plates, thus repelling any negatively charged particles out of the beam, leaving a neutral radical beam that consists overwhelmingly of one type of radical. The radical beam then enters the UHVC, the details of which are described in the next section.

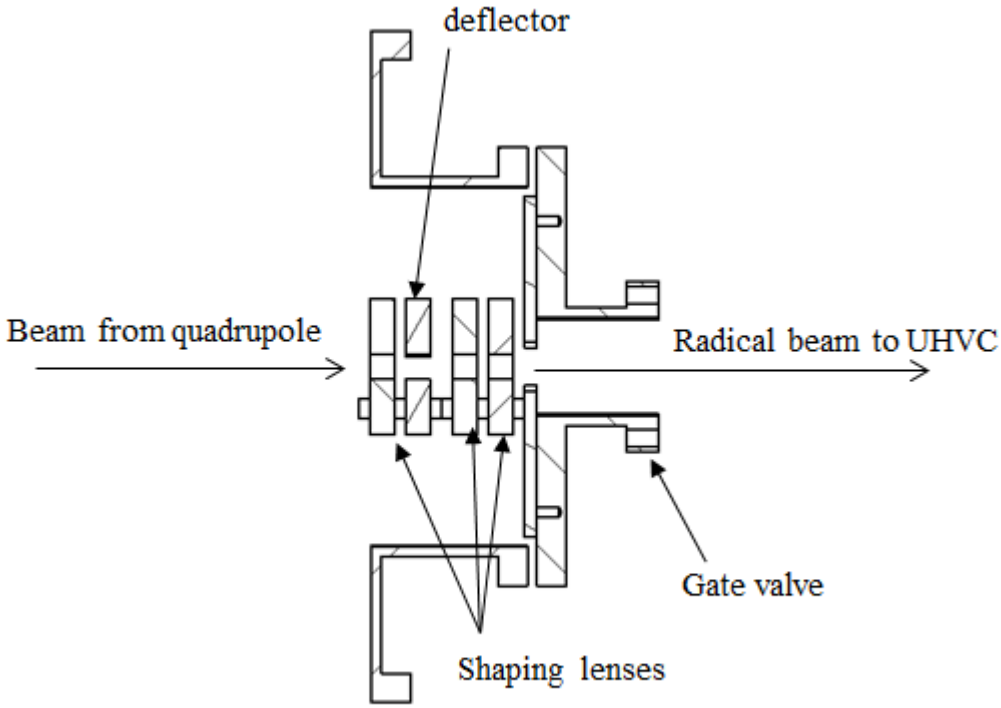

Figure 3.10 The exit chamber lenses located at the entrance to the UHVC. When producing a pure radical beam, the deflector is used to purge the beam of any negatively charged species by creating a potential gradient. The shaping lenses have been installed to provide the option of performing anion-surface chemistry with the RISA apparatus instead of radical-surface chemistry.

3.5 Experimental details: UHV chamber

The UHVC that houses the target surface is of cylindrical design. The chamber is split into two levels that are 180 mm apart, with ports branching off the main chamber. The radical beam chamber is coupled to the UHV chamber through a gate valve that is mounted on a port on the lower level of the chamber (level B, Figure 3.11). It is through this port that the incident radical beam enters the UHVC to irradiate the target surface. The surface is mounted on a helium cryostat cooled cold finger that is positioned to run

down the centre of the cylindrical chamber, along the *z*-axis in Figure 3.11. The cold finger is mounted through a port on the top of the chamber (C, Figure 3.11), and is attached to a manipulator that enables movement of the sample in all directions to millimetre precision. Sample rotation through 360° is provided by a differentially pumped, rotating feedthrough. Thus, the sample position can be manipulated to a high-degree of accuracy under UHV conditions.

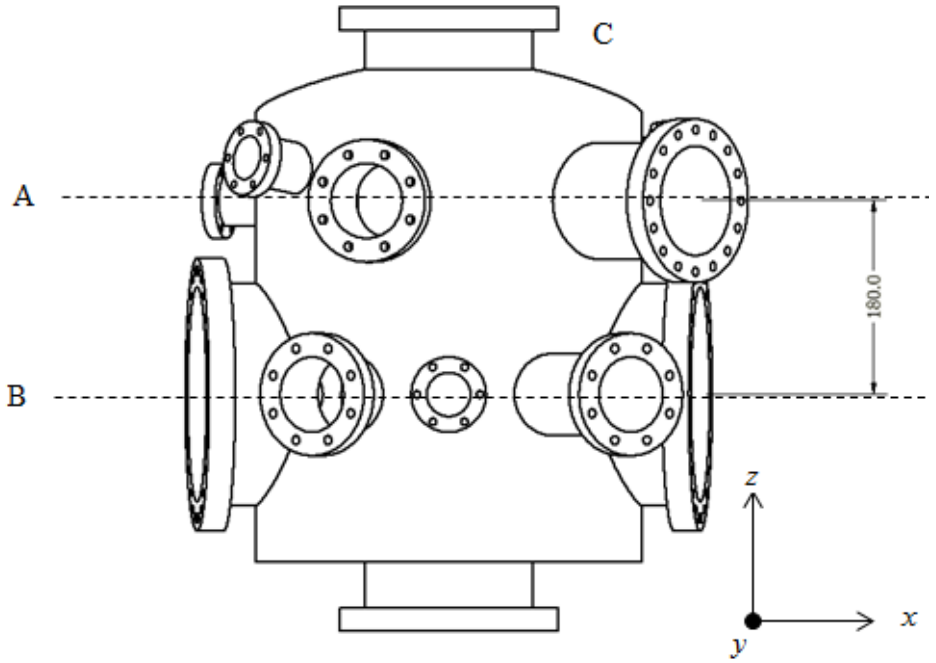

Figure 3.11 A diagram to show the two experimental levels of the UHVC, labelled A and B. Each port houses experimental apparatus that are used to interrogate the surface following radical beam irradiation. C shows the port through which the cold finger is mounted.

Each port around the chamber mounts a piece of equipment. The upper level houses an electron gun, an ion gun, an x-ray gun and a hemispherical energy analyser, which are used for AES, surface sputtering and XPS respectively. The lower level is equipped with an ion gauge, a quadrupole mass spectrometer and two KBr windows through which infrared radiation is passed. Each piece of equipment will be described in detail later in this chapter. Lead covered viewports are positioned around each level.

Figure 3.12 shows the positions of each port around the central cavity for each level.

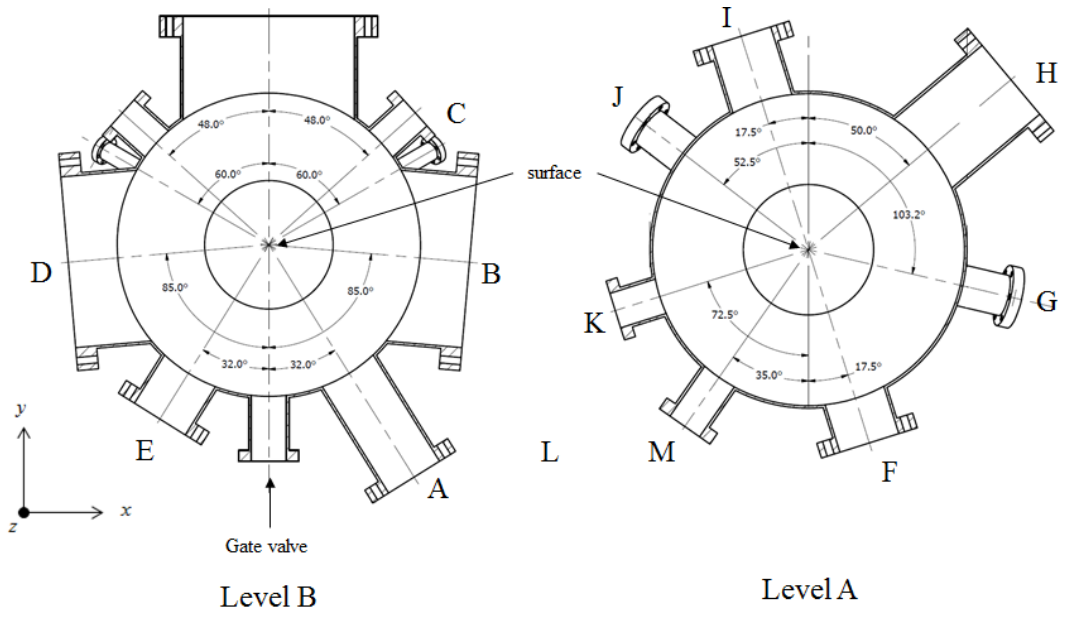

Figure 3.12 A diagram showing the positions of each port around the surface for levels A and B, which are 180 mm apart along the z-axis. The surface is mounted on a cold finger that runs along the central z-axis of the chamber. A description of the apparatus used to manipulate the position of the surface is given in the text. In this diagram A = quadrupole mass spectrometer (QMS), B = KBr window (IR entry), C = ion gauge, D = KBr window (IR exit), E = viewport, F = hemispherical energy analyser, G = X-ray gun, H = viewport, I = ion gun, J = leak valve, K = viewport and M = electron gun. Any unlabelled ports are unused and are sealed with blank stainless-steel flanges.

3.5.1 Heating and cooling the surface

For this apparatus to be equipped to perform experiments that are relevant to such varied fields as plasma-surface science and the interstellar medium (ISM), the ability to both warm and cool the sample in a controlled manner is required. The temperature range that the apparatus must be able

to produce and withstand is 10 K – ~ 700 K. The ability to cool the sample to low temperatures (< 30 K) is especially crucial for astrochemical studies in order to mimic the temperature of dust in the ISM. Prior to such a study, the sample must be annealed to a high enough temperature to ensure surface cleanliness (~ 500 K). Furthermore, the sample must be cooled rapidly from the annealing temperature to the base temperature (~ 12 K) to prevent residual gases in the chamber adsorbing onto the cleaned surface. The materials and equipment used in this apparatus fulfil such requirements and are described below.

3.5.2 Cooling

The target is attached to the end of a closed cycle cold head *via* a sample mount and a cold finger. The cold head relies upon the free expansion of high pressure helium to refrigerate to cryogenic temperatures (< 10 K). The resultant low-pressure helium is compressed and recycled after expansion. The cold head has two ‘heat stations’ that are gradually cooled with each expansion: the first stage and the second stage. When fully cooled, the base temperatures of the first and second stages of the cold head are 30 K and 5 K respectively.

3.5.3 Cold finger

The cold finger is a solid copper rod that is 750 mm length. The rod connects the sample mount to the second stage of the cold head. To ensure good thermal contact, silver foil is sandwiched between the cold finger and the cold head and gold foil is sandwiched between the rod and the sample mount. Two N-type thermocouples, which effectively monitor temperatures in the 3-1500 K range, are mounted at the top and bottom of the cold finger. When fully cooled, the top of the cold finger has a base temperature of 7 K, and the lowest temperature measured at the bottom of the rod is 10 K. To ensure the surface temperature is as low as possible for ISM studies, a cold shield is used to shroud the cold finger with a view to minimise the temperature gradient between along the rod by limiting radiative losses. There is a cut out in the shield that exposes the target surface. The cold shield is 940 mm in length and is mounted on the first stage of the cold head.

An N-type thermocouple is mounted on the shield and, when the system is fully cooled, the measured base temperature is ~ 50 K.

3.5.4 Heating

A cartridge heater of commercial design is employed to heat the surface. The cartridge is a tube-shaped, resistive heating element that can heat the target to temperatures > 1000 K. The heater is connected to the surface through a custom built mount. When high temperature experiments are being performed it is imperative to ensure that heat transfer from the target to the cold head is kept to a minimum. Additionally, as resistive heating is employed the surface must be electrically insulated from the cold finger. These factors were considered when designing the sample mount.

3.5.5 Sample Mount

The target is attached to the cold finger *via* a custom-built sample mount, as shown in Figure 3.13. To ensure good thermal contact, a piece of gold foil is sandwiched between the surface and the mount. There is a copper clamp that sits over the surface to hold it in place, which can be easily removed if we desire to change the surface. The mount is equipped with two thermocouples, an N-type and a K-type, that monitor the surface temperature. A K-type thermocouple effectively monitors temperature in the 273-1373 K range. The heater mount is positioned above the surface and is held in place by two M3 screws.

Three M4 ceramic screws hold the surface mount to the base of the cold finger. To ensure electrical isolation, an insulator is sandwiched between the two. Sapphire was chosen for this purpose as, in addition to providing electrical isolation, it has properties that fulfil the criteria pertaining to thermal conductivity outlined earlier in this section. At very low temperatures (< 80 K) the thermal conductivity of sapphire is high, whereas at elevated temperatures (> 80 K) the thermal conductivity of sapphire is poor.[5] The sapphire is sandwiched between two pieces of gold foil to ensure high thermal conductivity between the cold finger, the sapphire and the mount.

3.5.6 The surface

The commissioning experiments described in this thesis use an amorphous silver surface (Goodfellows Ltd, UK). The sample is 20 mm x 20 mm x 2 mm and is mounted as described above. The surface atoms of an amorphous surface are oriented in a random, unknown configuration.

In crystallography, bulk silver is classed as a face centred cubic (FCC) material.[14] As such, the atomic structure of a unit cell of a silver crystal is known, as shown in Figure 3.14. An ordered surface can be obtained by cutting the bulk material along a particular plane, therefore exposing the underlying atoms. The miller indices, depicted as *hjk*, indicate how the surface plane intersects the 3D structure and are used to describe the orientation of the atoms at the surface.

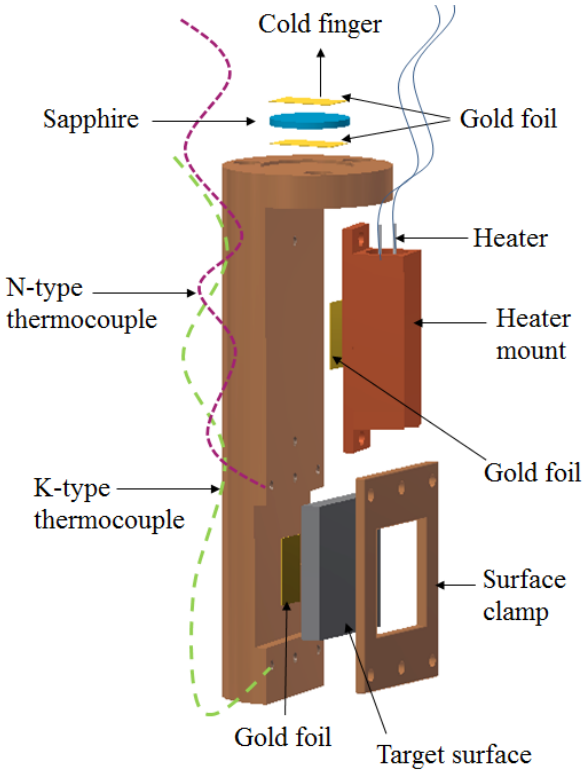

Figure 3.13 A diagram of the sample mount used to attach the target surface to the cold finger. Ceramic insulators and screws have been omitted. The sample mount is electrically insulated from the cold finger, whilst maintaining the best possible thermal contact.

Future experiments will use a single crystal silver 111 surface, of the same dimensions as the amorphous piece (Goodfellows Ltd, UK) described above. As such, this single crystal surface has been installed into the UHVC. The atomic arrangement of this surface is known, therefore different adsorption sites, with different binding energies, can be identified. Indeed, when performing monolayer (one molecule thick layer of adsorbates) desorption experiments one can determine the different binding energies of each site. The different possible adsorption sites on a silver 111 surface are shown in Figure 3.14.

Both surfaces are mirror polished to 1 μm and are excellent substrates for use in RAIRS experiments as they obey the metal surface selection rule, which is described later in this chapter.

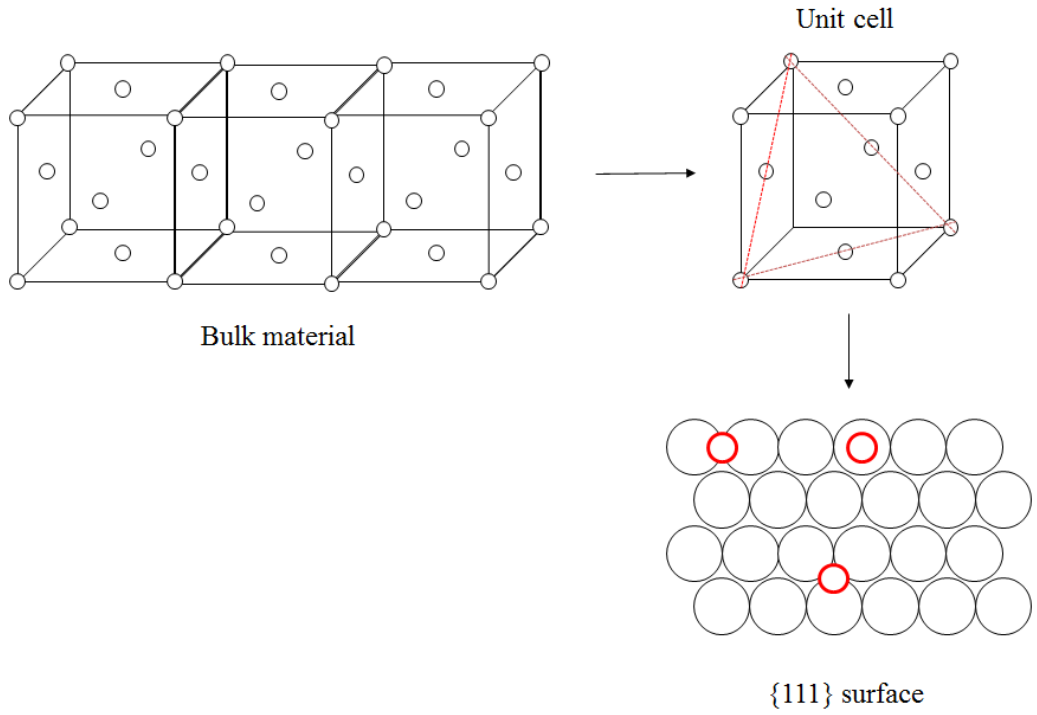

Figure 3.14 A schematic to show the FCC unit cell of bulk silver. The red dashed line indicates the plane along which silver is cut to achieve a 111 oriented surface. The white circles with black outline represent silver atoms and the white circles with a red outline represent adsorbates onto the surface. There are clearly three adsorbate sites on the 111 surface.

3.5.7 Cleaning the target

The sample requires cleaning prior to each experiment to ensure no residual background gases from the chamber have adsorbed onto the surface. To this end, cycles of sputtering and annealing of the surface are employed. This process is described in detail in chapter 6. In brief, a high energy beam of Ar^+ ions are aimed at the target, which 'dislodge' any surface impurities and also silver atoms indiscriminately. The surface is annealed to 700 K, which brings about a reconstruction of a well-ordered surface. However, annealing can also bring impurities to the surface from the bulk. The identity and abundance of surface impurities can be determined by recording an XPS spectrum of the surface. Repeated cycles of sputtering and annealing produce a well ordered, clean surface.

3.6 Experimental techniques

This section will describe in detail the analytical instruments that are used to interrogate the surface following radical irradiation. The experimental techniques and data processing procedures will be outlined for both the proposed radical beam experiment and the desorption experiments described in chapter 6, where details of the commissioning of this apparatus can also be found.

3.6.1 Reflection Absorption Infrared Spectroscopy (RAIRS)

RAIRS is a vibrational spectroscopic technique that is used to study adsorbates on surfaces. The use of RAIRS enables the identification of surface species and provides information pertaining to the chemical environment and geometry of adsorbates.[15] RAIRS is commonly used to study metal-adsorbate systems, but has also been used to study other surfaces, such as highly oriented pyrolitic graphite (HOPG).[6, 7] RAIRS is used in the experiments outlined in chapter 6.

The theory behind RAIRS is rooted in transmission infra-red (IR) spectroscopy, where a spectrum is constructed by comparing the IR radiation transmission before and after passing through a sample. IR photons are absorbed by electrons in the adsorbate layer, if an electronic

transition is possible, or by vibrations of molecules within the sample that exhibit a dipole. These molecules only absorb IR radiation when the frequencies of the light and the oscillation of the dipole are resonant, which are termed the 'normal modes of vibration'. An absorption spectrum shows the different frequencies of light that couple with the excitations in the sample and is usually plotted as either a % transmission (*T*) *vs* frequency or as an absorbance (*A*) *vs* frequency plot. The relationship between absorbance and transmission is given in equation 3.3.

$$A = -\log T \qquad 3.3$$

This technique is used for studies of thin films (< 200 μm thick), liquid and gaseous samples. However, transmission IR is not appropriate for surface studies of solid metal-adsorbate samples, as metals are not IR transparent. Furthermore, the sample would have to be < 200 μm thick for the IR to successfully pass through to the detector. Thus, reflectance spectroscopy is relied upon to study such systems.[15, 16]

In RAIRS, IR radiation is passed, at a grazing angle, through an adsorbate layer on a reflective surface and is reflected to a detector. Like in transmission IR spectroscopy, the reflected light is subject to absorption at any frequencies that are resonant with the vibrational modes of adsorbate molecules. However, in RAIRS radiation intensity can also be lost through any vibrational modes that may form as a result of adsorbate-surface interactions. The absorption spectra in chapter 6 were constructed in the same way as a typical transmission IR spectrum, and are a plot of absorbance *vs* wavenumber.

The extent to which adsorbates absorb IR light can be assessed by considering the electric fields associated with the radiation at the surface. An electric field of light adjacent to a surface can be separated into *s*-polarised (E_s) and *p*-polarised (E_p) light, which are in the plane of incidence and perpendicular to the surface respectively, as shown in Figure 3.15. At all angles of incidence, the s-polarised light will undergo an 180º phase change.

As the surface is highly reflective, upon reflection the *s*-component of light is cancelled out and so there is no electric field available to interact with any adsorbate dipoles that are parallel to the surface. However, p-polarised light undergoes a reflection phase change that depends strongly upon the angle of incidence. At certain grazing angles of incidence, the perpendicular component of the *p*-polarised light can be enhanced. In fact, at certain grazing angles of incidence it is enhanced to almost twice the amplitude of the incident *p*-polarised component. For a vibration to be observable in RAIRS, a component of the oscillating dipole moment of an adsorbate species must be perpendicular to the surface in order to interact with the enhanced component of the *p*-polarised light. This is termed the 'metal surface selection rule'

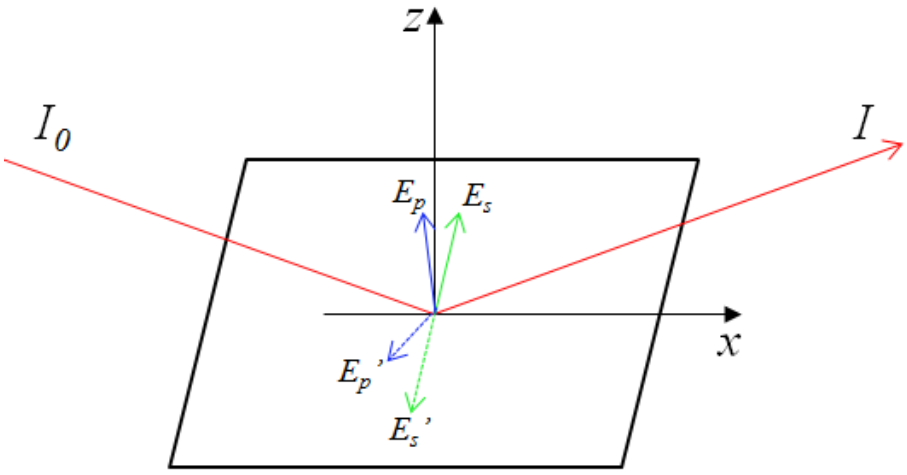

Figure 3.15 A schematic to show the electric fields associated with the reflection of infra-red radiation. The red line indicates the IR beam, where I_0 represents the incident radiation and I represents the reflected radiation. The green and blue lines are the s-polarised and p-polarised components of the beam, and the dashed lines represent the respective reflected components.

3.6.2 RAIRS experimental arrangement

When performing RAIRS, IR radiation from a Fourier transform infra-red (FTIR) spectrometer is focussed onto the surface within the chamber by a

flat mirror coupled with a parabolic mirror. The reflected light that exits the chamber is re-focussed by a further pair of parabolic mirrors that are arranged to focus the IR beam into a mercury cadmium telluride (MCT) detector. The light enters and exits the chamber through a pair of KBr windows, which are transparent to photons from the near UV to longwave IR wavelengths. The IR beam pathway is shown in Figure 3.16. When an absorption spectrum is recorded, the signal is fed from the detector back to the FTIR spectrometer, which in turn sends the spectrum to a PC. A commercial piece of software is used to convert the absorption plot to an absorbance *vs* wavenumber IR spectrum.

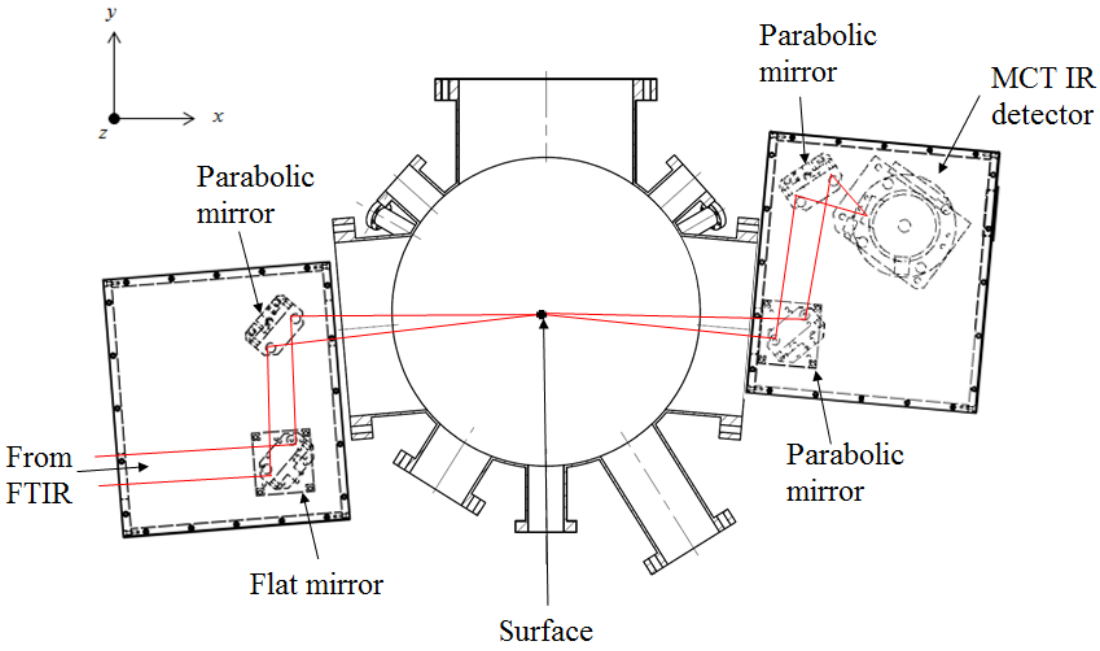

Figure 3.16 A schematic to the pathway of the IR beam through the chamber to the liquid cooled MCT-IR detector. The beam is focussed on the adsorbate layer by a flat mirror paired with a parabolic mirror. The reflected IR beam is then re-focussed into the detector by an additional pair of parabolic mirrors. The arrangement of these mirrors is crucial to get the focussing conditions correct, and to interact with the surface at a grazing angle that amplifies the p-polarised component of the electric field of the IR beam.

3.6.3 RAIRS experimental procedure

The RAIRS spectra reported in chapter 6 were recorded in the following manner. Prior to a RAIRS experiment the MCT detector must be cooled with liquid nitrogen. The detector was cooled at least an hour before any spectra were recorded to ensure that the purge gas flow stabilised following the exposure to the atmosphere associated with filling the detector. The target position was adjusted to maximise the IR signal reaching the detector. Each RAIRS spectra is a result of the addition of 50 scans, which takes 10 minutes. To confirm a stable background, several blank spectra were recorded of the clean surface to monitor the carbon dioxide and water levels present. Once stable, a final background spectrum of the clean surface was recorded. The adsorbate gas was admitted to the chamber through a high precision leak valve for varying amounts of time to achieve different surface coverage schemes. A RAIRS spectrum was recorded of the sample-adsorbate system and absorption plots were then generated by subtracting the final background spectrum from the sample spectrum.

3.6.4 Temperature programmed desorption

Temperature programmed desorption (TPD) is an experimental technique that can be used to obtain thermodynamic information about an adsorption system. TPD has been used by many groups to study the kinetics and surface reactivity of species on interstellar dust grains.[8-13] In the proposed radical beam experiment, we will dose the target with a beam of radicals. Upon heating, the identity of the desorbing species will reveal the reactivity of the radical on the surface. For the desorption experiments described in chapters w, the silver target was dosed with different neutral gaseous adsorbates. Upon performing the TPD the temperatures at which the adsorbate species left the surface gave insight into the energetics and kinetics of the system.[17, 18]

A basic TPD experiment involves the adsorption of species onto a target followed by the controlled, linear in time heating of the sample. The evolution of species into the gas phase, in order of decreasing volatility, is monitored by mass spectrometry. Each adsorbate is bound to the surface

with a specific energy. As the surface is heated the adsorbate species gain enough energy to desorb. Once in the gas-phase, the adsorbates are detected by a mass spectrometer as a function of surface temperature. Figure 3.17 shows a typical TPD spectrum, which was recorded following desorption of CO_2 from an amorphous silver surface at three different exposures.

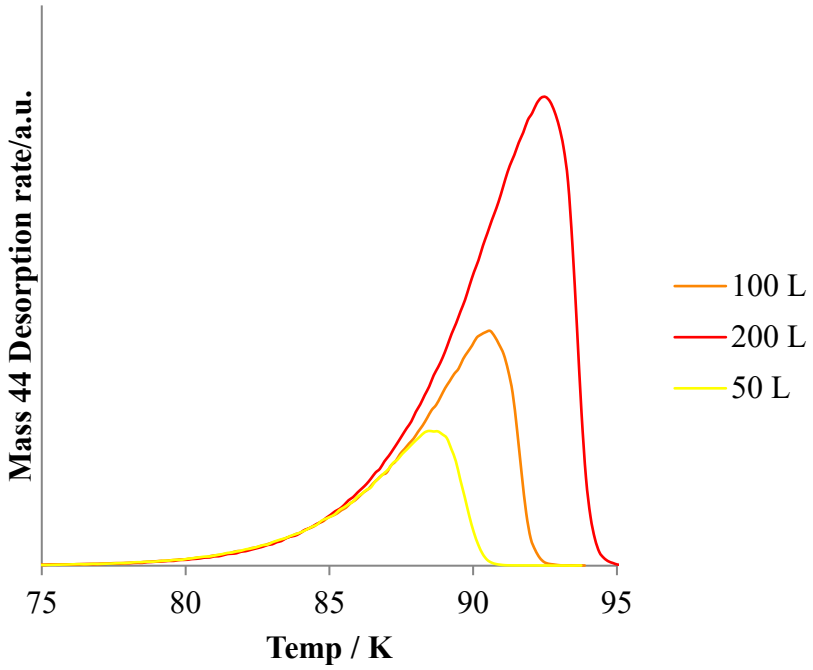

Figure 3.17 TPD spectra recorded following exposures of CO2 adsorbed on amorphous silver at 12 K. The figure shows three spectra recorded following exposures between 50 – 200 L.

3.6.5 TPD experimental procedure

All TPD spectra presented in chapter 6 were performed following the procedure outlined below. A set of TPD data studying a specific adsorbate-substrate system consists of several spectra, each performed with a different initial surface coverage. For the data presented in chapter 6, to enable the comparison of the TPD data all spectra were recorded at the same starting temperature. For the experiments presented in chapter 6, and amorphous silver surface was heated from 20 K to 250 K at a heating rate of 0.5 K s^{-1}.

Prior to each desorption experiment the surface was cleaned, as described previously, and was allowed to cool. When the pressure within the chamber returned to the base pressure recorded before heating, the adsorbate gas was admitted to the chamber via a high-precision leak valve. Chamber pressure is monitored on an ion gauge. To achieve each coverage, the sample was exposed to the desired pressure of target gas for a set amount of time. All exposures reported in this thesis are measured in Langmuir (L), where an exposure of 1 L is equivalent to background filling the chamber to a pressure of 7.5 × 10^{-7} Torr for one second. Once the pressure in the chamber had returned to its usual base pressure, the manipulator was used to turn the surface to face the quadrupole mass spectrometer (QMS). The cartridge heater was then used in combination with a commercially bought temperature controller (Nanodac, Eurotherm) to heat the surface at a linear heating rate. Simultaneous to the start of heating, the QMS was activated to monitor desorbing species at chosen mass to charge ratios *(m/z).* The temperature controller is coupled to the QMS via a 0-10 V output, which enabled the spectrometer to produce spectra of intensity vs temperature for each *m/z* that was monitored. All spectra were constructed by software called 'MASsoft' on a PC coupled to the QMS. Once the experiment was complete, the temperature of the surface was held at 250 K until the chamber pressure stopped falling, which was indicative that desorption from the surface had ceased. By following this procedure, it was ensured that background adsorbates on the surface were kept to a minimum.

3.6.6 Thermodynamic analysis

The rate of desorption of an adsorbate in a TPD experiment is given by the Polanyi-Wigner equation.

$$R_{des} = \frac{-d\theta}{dt} = A\theta^{n}\mathrm{e}^{\frac{-E_{des}}{RT}} \qquad 3.4$$

Equation 3.4 relates the rate of desorption (R_{des}) to the total surface coverage (θ), desorption activation energy (E_{des}), a pre-exponential factor (A), the gas constant *(R)* and the surface temperature (T). Equation 3.4 shows that the rate of desorption is equivalent to the rate of decreasing

surface coverage over time. The Polanyi-Wigner equation can be used to interpret TPD spectra in several ways. The general relationship between TPD peak intensity, surface coverage and the energy of the desorption site is outlined below.

The rate of coverage with respect to time can be linked to the rate of coverage with respect to temperature by considering the heating rate of the surface during the experiment, β. If the surface is heated from an initial temperature, T_0, then:

$$T = T_0 + \beta t \Longrightarrow \beta = \frac{dT}{dt} \qquad 3.5$$

It follows that

$$\frac{d\theta}{dt} = \frac{d\theta}{dT}\frac{dT}{dt} = \frac{d\theta}{dT}\beta \qquad 3.6$$

The heating rate of the surface is constant for the experiments in chapter 6, therefore equation 3.6 becomes

$$\frac{d\theta}{dt} \propto \frac{d\theta}{dT} \qquad 3.7$$

The intensity, $I(T)$, of a TPD signal is proportional to the rate of change of coverage with respect to temperature. The absolute coverage is not measured in the experiments described in this thesis, instead a relative coverage is obtained. Thus, equation 3.4 becomes

$$I(T) \propto -\frac{d\theta}{dT} = A{\theta_{rel}}^{n}\mathrm{e}^{\frac{-E_{des}}{RT}} \qquad 3.8$$

Re-arranging and taking logarithms gives

$$\ln I(T) \propto n\ln[A\theta_{rel}] - \frac{E_{des}}{RT} \qquad 3.9$$

Equation 3.9 is manipulated in three different ways to extract desorption energies from the TPD data presented in chapter 6, where a detailed mathematical derivation for each method is given.[16-18]

3.6.7 X-ray photoelectron spectroscopy

When an atom or molecule forms a chemical bond to a surface during adsorption, an electron transfer occurs that changes the electronic structure of the surface. Such changes can be detected by x-ray photoelectron spectroscopy (XPS). In the proposed radical beam experiment, XPS will be used to identify species present in the adsorbate overlayer following target irradiation with a radical beam. In the experiments described in chapter 6, XPS was used to confirm the surface was clean after the cycles of sputtering and annealing.

3.6.8 Theory of XPS

XPS probes the electronic structure of an adsorbate overlayer by bombarding the surface with high energy X-rays, which are usually generated from an anode that produces either AlKα or MgKα radiation. X-rays of sufficient energy can eject core electrons from a surface species. These ejected electrons are detected by an electrostatic collection lens and the electron kinetic energy is subsequently analysed. When an electron is ejected, the conservation of energy dictates that:

$$E_k = hv - E_b \qquad 3.10$$

where E_k is the kinetic energy of the ejected electron, E_b is the binding energy of the ejected electron and hv is the energy of the photon. Hence, the binding energy of an ejected electron can be determined by measuring the kinetic energy of the electron after the sample has been bombarded by photons of known energy.[19-22]

The binding energies of core electrons are unique to each element, making XPS a powerful, chemically specific tool for elemental analysis. Furthermore, the intensity of a signal in an XPS spectrum is proportional to the number of species on the surface. A third advantage of using XPS is that

the ionisation potential of a core electron, in a given atom, depends upon the chemical environment of the atom. Thus, if a shift in the energy of an ejected electron is observed it is indicative of a change in chemical environment. Chemical shifts can be as large as a few electron volts and can result from a change in nearest neighbour, the oxidation state, the compound or the crystal structure. We can identify the chemical environment of the atom as the chemical shifts are known. Therefore, in the proposed radical beam experiment, by comparing two XPS spectra recorded before and after radical irradiation the identity of any products formed can be identified.[19-22]

3.6.9 XPS experimental arrangement

All XPS spectra reported in this thesis were performed using an X-ray source (PreVac) coupled with a high-resolution electron energy analyser (VG Scienta). The X-ray source consists of an Mg/Al twin anode mounted on a z-axis manipulator, which enables the source to be positioned 14 mm from the sample during operation, whilst being able to retract it for safety when not in use. The Al and Mg anodes produce Kα radiation at 1486.6 eV and 1253.6 eV respectively, which corresponds to an electron transition from the $2p_{\frac{3}{2}}$ state to the 1s state in each material.

Once the high-energy radiation has interrogated the sample, the resultant ejected core electrons enter the energy analyser. The energy analyser consists of an optical lens, a hemispherical energy analyser and a detector assembly with a camera. The optical lens is used to guide the electrons into the energy analyser. The hemispherical analyser determines the energy resolution of the electron spectrometer. By varying the entrance slit size and pass energy, E_p, it is possible to modify the energy resolution and signal intensity. The principles of a hemispherical analyser are described in detail in chapter 2, but, in brief, the pass energy is determined by the electrostatic field between the inner and outer hemispheres. The energy resolution can be approximated to

$$\Delta E \approx \frac{s \times E_p}{2r} \qquad 3.11$$

where s is the slit width and r is the mean analyser radius. As a rule of thumb, high pass energy coupled with a small slit gives the best count rate.

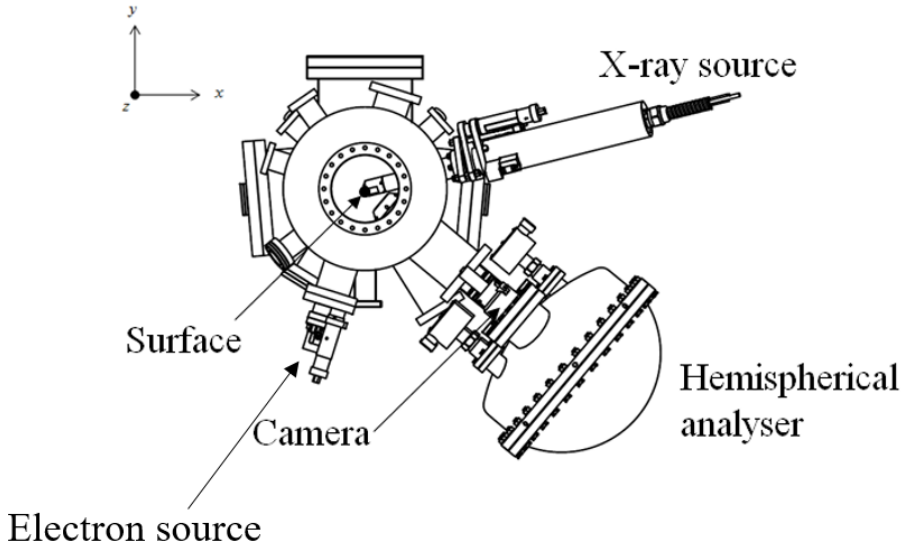

Figure 3.18 A diagram to show the experimental arrangement of the XPS equipment. The entrance to the analyser is positioned 53.2° from the x-ray source around the central *z*-axis of the chamber, ensuring that ejected electrons from the sample enter the hemisphere. The electron source is for Auger Electron spectroscopy, which is described in the next section.

A multichannel plate (MCP) detector is used, which is also described in detail in chapter 1, coupled with a camera to produce a 2D image of the ejected electrons. Within the detector there are two MCP plates that multiply impinging electrons. The resultant electron cascade hits a phosphor screen causing a phosphorescing dot to appear on the screen. The phosphor screen image is recorded by a camera through a viewport, and the image is sent to the instrument computer. A flash from an electron is registered by the camera and the positional information gives the energy and angular origin of the particle. A computer program, of commercial design, then converts the energetic information into a spectrum that consists of peak intensity *vs* kinetic energy. Figure 3.18 shows a bird's eye view of the experimental

arrangement of the x-ray source, energy analyser and camera around the central UHVC.

3.6.10 Experimental procedure

Prior to every desorption experiment reported in this thesis cycles of sputtering and annealing were employed to remove any surface contaminants. After each cycle an XPS spectrum was recorded. Any peaks that did not correspond to the surface material in each spectrum were used as an indication of how clean the surface was. The cycles were stopped once any contaminant peaks were eliminated from the spectrum.

3.6.11 Auger electron spectroscopy

Auger electron spectroscopy (AES) is an analytical technique based on the Auger effect. The Auger effect is an electronic process in which an energetic electrons are emitted from an excited atom following a series of electronic relaxations. Analysing the energy of the 'Auger electron' enables the identification of the atom from which it originated. Furthermore, the intensity of any peaks in an Auger electron spectrum is proportional to the amount of the emitting substance. Indeed, performing AES on a surface enables the identification and determination of the yield of any surface species. In the proposed radical beam experiment, AES will be used to determine the yield and identity of any species formed following the irradiation of the surface with the radical beam.

3.6.12 Theory of AES

When an atom is probed by high energy (> 10 keV) radiation an ionisation process of electron core levels may occur. Indeed, as outlined above, this process forms the basis of XPS. When the core electron is removed, it leaves behind a positively charged hole and the resulting ion is in a highly-excited state. This core hole can be filled by an outer shell electron to lower the energy of the ion. The transition energy of this outer shell electron is equal to the difference in orbital energies of the two states it has moved between. To liberate any excess energy following the transition a second electron may then be ejected; this second electron is termed an

Auger electron. The kinetic energy (E_k) of this electron is probed and is equal to:

$$E_k = E_{core} - E_x - E_{auger} \qquad 3.12$$

where E_{core}, E_x and E_{Auger} are the electron binding energies of the core state, the outer shell and the state from which the Auger electron is emitted respectively. Thus, the kinetic energy of the Auger electron depends only on the energy levels of the atom from which it originates. [23, 24] The different states are shown diagrammatically in Figure 3.19.

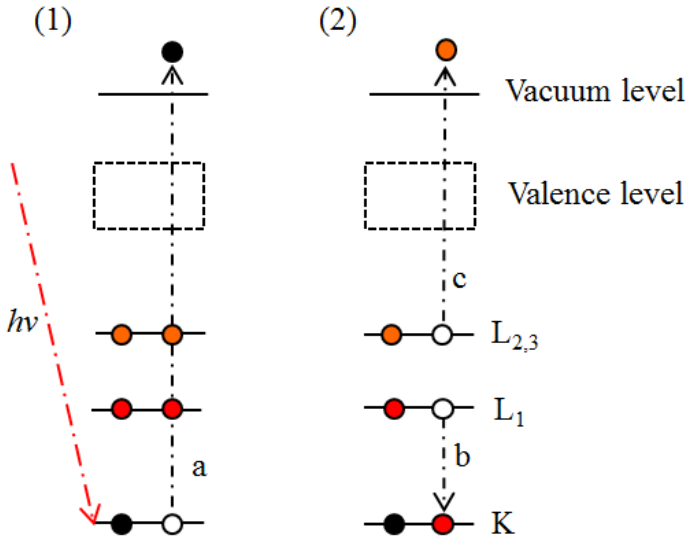

Figure 3.19 A schematic to show the Auger effect. Part (1) shows the irradiation of an atom with a high energy photon causing a core electron to be ejected. Part (2) shows the Auger effect that may happen following the process depicted in part (1). The filled circles represent electrons and the empty circles represent positive holes. (b) depicts an electron from L_1 filling the positive hole in the K level. (c) depicts the ejection of an Auger electron from $L_{2,3}$ accompanying (b) to liberate any excess energy from the system.

3.6.13 Experimental Procedure

All AES spectra reported in this thesis were performed using an electron source (PreVac) coupled with the high-resolution electron energy analyser (VG Scienta), described in section 3.6.9. The electron source produces a high energy (4 keV) beam of electrons that is used to irradiate the surface. Any emitted Auger electrons are detected by the hemispherical energy analyser. The camera sends the Auger electron image to the instrument computer where it is converted to a spectrum of intensity *vs* kinetic energy. Figure 3.18 shows the arrangement of the electron gun and energy analyser around the central UHVC cavity. The commissioning of the AES technique is described in chapter 6.

3.7 Summary

This chapter has described the RISA experiment that was used to obtain the results presented in chapter 6 of this thesis. Rich qualitative, quantitative and kinetic information can be extracted from data recorded using this apparatus, which will offer an in-depth analysis of any radical-surface chemistry that may occur in the proposed radical beam experiment. In addition, this apparatus can be used to study anion-surface chemistry and desorption experiments can also be performed. The next chapter will describe the commissioning of each experimental component described.

3.8 Bibliography

1. M. Bacal, *Nuclear Fusion*, 2006, **46**, S250-S259.

2. N. M. M. Nibbering, *Mass Spectrometry Reviews*, 2006, **25**, 962-1017.

3. Y. Takahata and D. P. Chong, *Journal of the Brazilian Chemical Society*, 1999, **10**, 354-358.

4. K. A. Peterson and M. Gutowski, *Journal of Chemical Physics*, 2002, **116**, 3297-3299.

5. R. Berman, E. L. Foster and J. M. Ziman, *Proceedings of the Royal Society of London Series a-Mathematical and Physical Sciences*, 1955, **231**, 130-144.

6. M. P. Collings, M. A. Anderson, R. Chen, J. W. Dever, S. Viti, D. A. Williams and M. R. S. McCoustra, *Monthly Notices of the Royal Astronomical Society*, 2004, **354**, 1133-1140.

7. W. A. Brown and D. A. King, *Journal of Physical Chemistry B*, 2000, **104**, 2578-2595.

8. G. Kumi, S. Malyk, S. Hawkins, H. Reisler and C. Wittig, *Journal of Physical Chemistry A*, 2006, **110**, 2097-2105.

9. S. Malyk, G. Kumi, H. Reisler and C. Wittig, *Journal of Physical Chemistry A*, 2007, **111**, 13365-13370.

10. R. Martin-Domenech, G. M. M. Caro, J. Bueno and F. Goesmann, *Astronomy & Astrophysics*, 2014, **564**, 12.

11. P. B. Rasmussen, P. A. Taylor and I. Chorkendorff, *Surface Science*, 1992, **269**, 352-359.

12. D. J. Burke and W. A. Brown, *Physical Chemistry Chemical Physics*, 2010, **12**, 5947-5969.

13. J. L. Edridge, K. Freimann, D. J. Burke and W. A. Brown, *Philosophical Transactions of the Royal Society a-Mathematical Physical and Engineering Sciences*, 2013, **371**.

14. J. Uppenbrink and D. J. Wales, *Journal of Chemical Physics*, 1992, **96**, 8520-8534.

15. A. S. Bolina, A. J. Wolff and W. A. Brown, Journal of Physical Chemistry B, 2005, 109, 16836-16845.

16. E. L. Wilson and W. A. Brown, *Journal of Physical Chemistry C*, 2010, **114**, 6879-6893.

17. S. D. Green, A. S. Bolina, R. Chen, M. P. Collings, W. A. Brown and M. R. S. McCoustra, *Monthly Notices of the Royal Astronomical Society*, 2009, **398**, 357-367.

18. L. K. Ono and B. R. Cuenya, *Journal of Physical Chemistry C*, 2008, **112**, 18543-18550.

19. J. C. Dupin, D. Gonbeau, P. Vinatier and A. Levasseur, *Physical Chemistry Chemical Physics*, 2000, **2**, 1319-1324.

20. S. Hufner, G. K. Wertheim, M. M. Traum and N. V. Smith, *Solid State Communications*, 1972, **11**, 323-&.

21. H. J. Freund and M. W. Roberts, *Surface Science Reports*, 1996, **25**, 225-273.

22. P. Prieto, V. Nistor, K. Nouneh, M. Oyama, M. Abd-Lefdil and R. Diaz, *Applied Surface Science*, 2012, **258**, 8807-8813.

23. R. A. Baragiola, *Nuclear Instruments & Methods in Physics Research Section B-Beam Interactions with Materials and Atoms*, 2005, **232**, 98-107.

24 M. Larsson, P. Baltzer, S. Svensson, B. Wannberg, N. Martensson, A. N. Debrito, N. Correia, M. P. Keane, M. Carlssongothe and L. Karlsson, *Journal of Physics B-Atomic Molecular and Optical Physics*, 1990, **23**, 1175-1195.

4 The electron transfer and bond-forming reactions of Ar^{2+}

4.1 Introduction

The reactivity of atomic and molecular doubly charged cations, termed dications, has been subject to numerous investigations since their discovery in the 1960s. Interest in the reactivity of dications gained impetus when modelling studies indicated that, in planetary ionospheres, dications could possess comparable abundances to chemically significant monocations.[1, 2] The main subject of previous investigations has been electron transfer (ET) reactivity, which dominates dication/neutral collision systems and is now reasonably well understood.[3-8] More recently, studies have focused on the bond-forming reactions of dications with neutrals, which can lead to the production of unusual molecules.[9]

The chemistry of rare gas (Rg) dications with neutral species has been the subject of some investigations, the reactions of which can form a variety of molecules that contain rare gas atoms. Indeed, the contrast in bond-forming reactivity between dicationic rare gas species and their neutral forms is stark; it has been shown experimentally and theoretically that Rg^{2+}/neutral collisions can form products as exotic as $ArC^{2+}$and $ArNH^{+}$.[9, 10] As such, a few studies have focused on the bond-forming reactivity of rare gas dications with a variety of neutrals.[9-13]

In this chapter, the chemistry of argon dications, Ar^{2+}, with a variety of fluorine containing neutrals (CF_4, C_2F_6, NF_3 and SF_6) is described. Each of the Ar^{2+}-neutral systems presented produced rich coincidence spectra, with products forming from both ET and bond-forming reactivity. Electrostatic models coupled with CM scattering diagrams have been used to analyze and explain the reactivity observed, and the results are detailed below.

4.2 Experimental details

All experiments detailed in this chapter were performed using the PSCO apparatus, following the procedure outlined in chapter 1. The Ar^{2+} species was formed *via* electron ionization of argon gas, from a commercial source.

The neutral gases used, CF_4, C_2F_6, NF_3 and SF_6, were also from commercial sources and were used without further purification.

4.3 Results and discussion

4.4 $Ar^{2+} + CF_4$

The PSCO apparatus has been used to detect pairs of ions formed following collisions between Ar^{2+} and CF_4 at CM collision energy, $E_{cm,}$ 6.88 eV. The pairs of monocations produced following such collisions are listed in Table 4.1. There are 5 product ion pair channels that form *via* electron transfer (ET) and bond-forming reactions. We observe an ion pair peak that contains an ArF^+ cation as one of its component ions. That is, we see evidence in the spectra that the Ar^{2+} dication has been fluorinated following collisions with CF_4. This bond-forming reaction makes a small, but non-negligible, contribution to the overall ion yield. The relative intensities of the pairs peaks taken from the coincidence mass spectra are also given in Table 4.1.

Table 4.1 **T**he product ions formed following collisions between Ar2+ and CF4, at a collision energy of 6.88 eV. The centre-of-mass collision energy and branching ratios into each channel are presented.

Reaction Type	Products	*R* %
SET	$Ar^+ + CF^+ + 3F$	42.3
SET	$Ar^+ + CF_2^+ + F_2/2F$	51.0
SET	$Ar^+ + CF_3^+ + F$	2.1
SET	$Ar^+ + CF_4^+$	3.8
Bond-forming	$ArF^+ + CF_2^+$	0.8

4.4.1 Non-dissociative SET

The different mechanisms by which single electron transfer (SET) may occur following collisions between Ar^{2+} and CF_4 are explored below. A pairs peak is present in the spectra that is indicative of a non-dissociative SET reaction: Ar^+ and CF_4^+. In this type of reaction, the reactants approach each other, an electron transfers from the neutral species to the dication and the two product monocations separate without undergoing further dissociation, as shown in equation 4.1.

$$Ar^{2+} + CF_4 \rightarrow Ar^+ + CF_4^+ \qquad 4.1$$

Figure 4.1 shows a scattering diagram constructed from the detection of pairs of Ar^+ and CF_4^+ that formed following collisions between Ar^{2+} and CF_4 at E_{cm} = 6.88 eV. A full description of the construction and interpretation of these diagrams was presented in chapter 2. Figure 4.1 shows the scattering of the detected product ions, Ar^+ and CF_4^+, about the CM. For clarity, the different product monocations are plotted on separate halves of the diagram: CF_4^+ is depicted by the black dots on the top half of the plot and Ar^+ is represented by the red dots in the lower half of the diagram. The scatter plot can be used to reveal the correlation between the product and reactant velocity vectors. The filled arrows in the diagram represent the direction of the reactant velocity vectors. The red and black circles correspond to given CM velocities of Ar^+ and CF_4^+ respectively and are used to provide a scale. The open headed arrow in the figure show the radius of each of these circles, and also indicate the general direction of the scattering of the relevant product ions.

Upon inspection of Figure 4.1, it is clear that the products of non-dissociative single electron transfer are strongly forward scattered relative to their respective reactant velocity vectors. That is, the $w(Ar^+)$ vector is strongly orientated in the same direction as the CM velocity of the reactant Ar^{2+} dication, and likewise the $w(CF_4^+)$ vector is strongly orientated with the CM velocity of the neutral target gas. Such scattering suggests a mechanism where the two reactants approach each other and an electron transfers from the neutral to the dication at large interspecies separations, leaving the

product ion trajectories largely unperturbed from their respective reactant species. That is, the resultant product ion velocity vectors are strongly oriented in the same direction as their respective reactant velocity vectors. This type of reaction is typical of SET reactions.[12, 14-16]

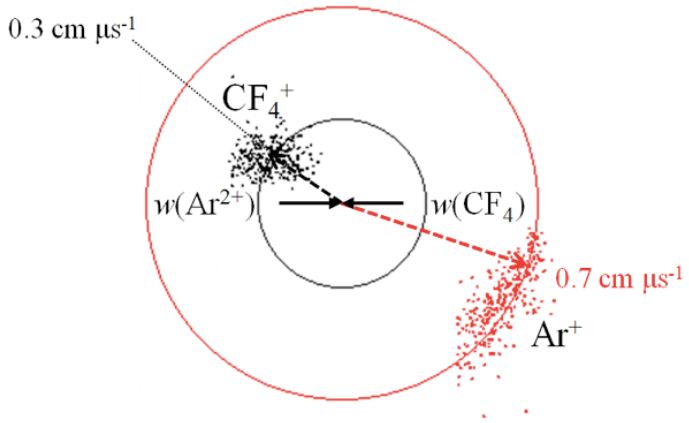

Figure 4.1 A scattering diagram in the CM frame to show product ion velocities (red and black circles) relative to the direction of reactants (filled arrowheads) following non-dissociative single electron transfer from CF_4 to Ar^{2+}. See text for details.

Thermochemical data, coupled with data extracted from the coincidence spectra recorded following collisions between Ar^{2+} and CF_4, can provide insight into the energetics of electron transfer reactions. As described in chapter 1, the exothermicity for a reaction channel can be determined by subtracting the E_{cm} from the total kinetic energy release (KER) measured for the reaction. A literature exothermicity for the reaction can be determined using thermochemical data that is readily available in the literature. These energetics can then be compared.

The experimentally derived exothermicity distribution for channel 4.1 is shown in Figure 4.2. Table 4.2 shows the literature exothermicities for the possible combinations of reactant and product electronic states that may have been involved in reaction 1.1. Figure 4.2 has two peaks, an intense peak at -6 eV and a weak shoulder at -10.2 eV. Comparing these values to the literature exothermicities given in table 4.2 will provide insight into the

electronic states of the product ions formed, and the electronic states of the reactants for this reaction channel.

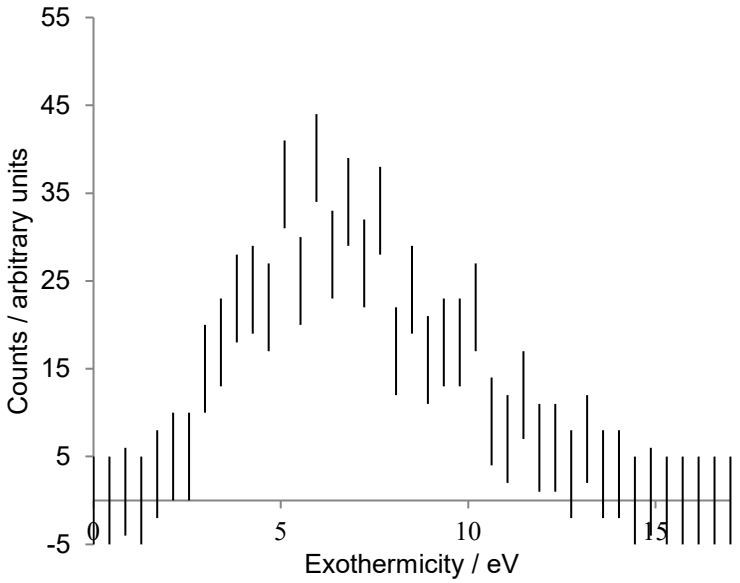

Figure 4.2 The exothermicity distribution for the products of channel 1.1, determined by subtracting the E_{cm} from the KER. Error is given by Poissonian statistics.

The target CF_4 molecules enter the chamber *via* an effusive jet, so we can be confident that only ground electronic state CF_4 molecules take part in the collisions. Ar^{2+} has an electronic configuration of [Mg]$3p^4$ and therefore has a ^3P ground state. The first two Ar^{2+} excited states are ^1D and ^1S, which lie 1.74 and 4.12 eV above the ground state respectively.[17] Our reactant Ar^{2+} dications may be formed in any of these three low lying states due to the excess energy associated with the electron ionization of argon with 150 eV electrons. Indeed, our dication beam may consist of a statistical combination of Ar^{2+} in its ground and first two excited states, which has previously been found to be 9:5:1.[12] Ar^+ is assumed to be formed in its ^2P state, as inspection of the available thermochemical data reveals the formation of Ar^+ in its ^2S state would be strongly endothermic for this reaction. Therefore, table 4.2 presents the literature exothermicities for $CF_4 + Ar^{2+}$ ($^3P/^1D/^1S$) → Ar^+ (^2P) + CF_4^+ in its ground and first four excited electronic states. Additionally, cross sections to SET for each combination of reactant and product ion electronic states are provided that have been determined by RW theory.

Table 4.2 Literature exothermicities for the possible combinations of reactant and product ion states that may have been involved in the SET reactions following Ar^{2+} collisions with CF_4 at E_{cm} = 6.88 eV. All cross sections were determined using RW theory as described in chapter 2.[11, 17, 20-23]

Electronic state of CF_4^+ product	Electronic state of Ar^{2+} reactant					
	^3P		^1D		^1S	
	ΔH/ eV	σ_{SET}	ΔH/ eV	σ_{SET}	ΔH/ eV	σ_{SET}
X $^2T_1$	-12.32	0.1	-13.88	0.15	-16.26	0.3
A $^2T_2$	-10.62	0.3	-12.13	0.2	-14.51	0.3
B ^2E	-9.42	0.5	-10.93	0.5	-13.31	0.4
C $^2T_2$	-6.02	3.9	-7.53	3.3	-9.91	0.5
D $^2A_1$	-2.61	10.7	-4.11	8.68	-6.49	1.5

TPEPICO experiments have found that the Franck-Condon regions of the ground (X) $^2T_1$, first (A) $^2T_2$ and second (B) ^2E electronic state PESs of the CF_4^+ ion are unstable to dissociation to CF_3^+ + F. The C $^2T_2$ electronic state of CF_4^+ is unstable to dissociation to CF_2^+, and the D $^2A_1$ state is dissociative, forming CF^+. Comparing our data to these experiments will aid in the identification of the product electronic states formed following reaction 1.1.

Comparing the experimentally determined exothermicity -5.95 eV with the literature values given in the table gives the following reaction mechanisms as possible reaction pathways that may describe channel 1.1.

$$Ar^{2+}(^3P) + CF_4 \rightarrow Ar^+(^2P) + CF_4^+(C\ ^2T_2) \quad 4.2$$

$$Ar^{2+}(^1D) + CF_4 \rightarrow Ar^+(^2P) + CF_4^+(C\ ^2T_2) \quad 4.3$$

$$Ar^{2+}(^1S) + CF_4 \rightarrow Ar^{+}(^2P) + CF_4^{+}(D\ ^2A_1) \quad 4.4$$

Mechanism 4.2 has the highest RW cross-section to SET of all the combinations of reactant and product electronic states in the table, suggesting that SET between the neutral and the dication would be most efficient for these states. Furthermore, Ar^{2+} (^3P) is the dominant species in our reactant dication beam, where the first three electronic states of Ar^{2+}, ^3P, ^1D and ^1S, are thought to be present in the statistical ratio 9:5:1. Indeed, this statistical ratio of dication states has been seen before for an Ar^{2+} beam generated by the PSCO apparatus.[11] Therefore, mechanism 4.2 is most likely to accurately describe reaction 1.1. However, the TPEPICO data states that the CF_4^+ (C $^2T_2$) state is unstable to dissociation to $CF_2^+ + 2F/F_2$. In fact, all $(CF_4^+)^*$ electronic states are dissociative and the TPEPICO experiments do not detect CF_4^+. Such TPEPICO experiments usually involve vertical electronic transitions to Franck-Condon regions of the CF_4^+ PEC. In contrast, in this work CF_4^+ has been detected in coincidence with Ar^+ following non-dissociative SET from CF_4 to Ar^{2+}, suggesting that this SET reaction is accessing a non-Franck-Condon region of the product's PEC that is stable to dissociation over the timescale of the experiment.

Various techniques have been employed to study the dissociation of CF_4^+, including: photoionization, ion-molecule reactions, ion imaging, velocity imaging photoionization coincidence, photoelectron fluorescence coincidence, PEPICO and TPEPICO.[18-22] Indeed, there are a number of studies in the literature pertaining to the dissociation of CF_4^+, of which only two have previously detected CF_4^+ as a stable ion. As such, it is well-established that the Franck-Condon regions of the ground and low-lying electronic states of the CF_4^+ PES are unstable to dissociation.

Quantum chemistry and dynamics calculations have found that CF_4^+ is stable in states close to its dissociation limit, however has an elongated, distorted structure. These calculations found that CF_4^+ can exist as a CF_3^+-F complex, where one C-F bond is elongated compared to the other three C-F bonds. Indeed, it has been found that CF_4^+ is stable in its ground electronic state with C_{3v} symmetry as opposed to T_d symmetry. They also found that

the FC region is narrow, and all vertical transitions to the upper CF_4^+ ground electronic state are to points above the CF_3^+ + F dissociation limit. CF_4^+ is stable in the condensed phase, with D_{2d} symmetry. These findings add confidence to the theory that Ar^{2+} / CF_4 collisions have accessed a non-Franck-Condon region of the CF_4^+ PEC. Such behaviour has been seen before following collisions between rare gases with CO^{2+}. It is of note that this is a very minor channel for this reaction system and SET is not very efficient between the electronic states in the RW.

4.4.2 Dissociative SET

Like non-dissociative SET, dissociative SET involves the transfer of an electron from a neutral species to a dication. However, a second step then occurs where one or more of the precursor product ions dissociate, giving another monocation and a neutral fragment(s). We see extensive dissociative SET in the coincidence data, with pairs peaks present that correspond to the detection of CF_3^+, CF_2^+ and CF^+ fragment ions in coincidence with Ar^+, as shown in reaction channels 4.5-4.7

$$Ar^{2+} + CF_4 \rightarrow Ar^+ + CF_4^+ \rightarrow Ar^+ + CF_3^+ (+ F) \quad 4.5$$

$$Ar^{2+} + CF_4 \rightarrow Ar^+ + CF_4^+ \rightarrow Ar^+ + CF_2^+ (+2F/F_2) \quad 4.6$$

$$Ar^{2+} + CF_4 \rightarrow Ar^+ + CF_4^+ \rightarrow Ar^+ + CF^+ (+3F/ F_2 + F) \quad 4.7$$

We cannot unambiguously determine the identity and number of neutral fragments formed for reactions 4.6 and 4.7. For example, reaction 4.6 may form F_2 or 2F alongside the detected product ions, as shown below.

$$Ar^{2+} + CF_4 \rightarrow Ar^+ + CF_4^+ \rightarrow Ar^+ + CF_2^+ + 2F \quad 4.6(a)$$

$$Ar^{2+} + CF_4 \rightarrow Ar^+ + CF_4^+ \rightarrow Ar^+ + CF_2^+ + F_2 \quad 4.6(b)$$

We can deduce which set of products are most likely to have formed following collisions between Ar^{2+} and CF_4 by comparing the literature reaction enthalpy for reaction 4.6(b) with the experimentally derived reaction exothermicity for this channel. Comparing these enthalpies is only used as a

guide as any internal excitation of the products is not determined. The scattering diagrams for reaction channels 4.5-4.7 are given in Figure 4.3. Reaction 4.6(a) is a four body reaction, therefore it cannot be compared to the exothermicity derived from the 3-body KER.

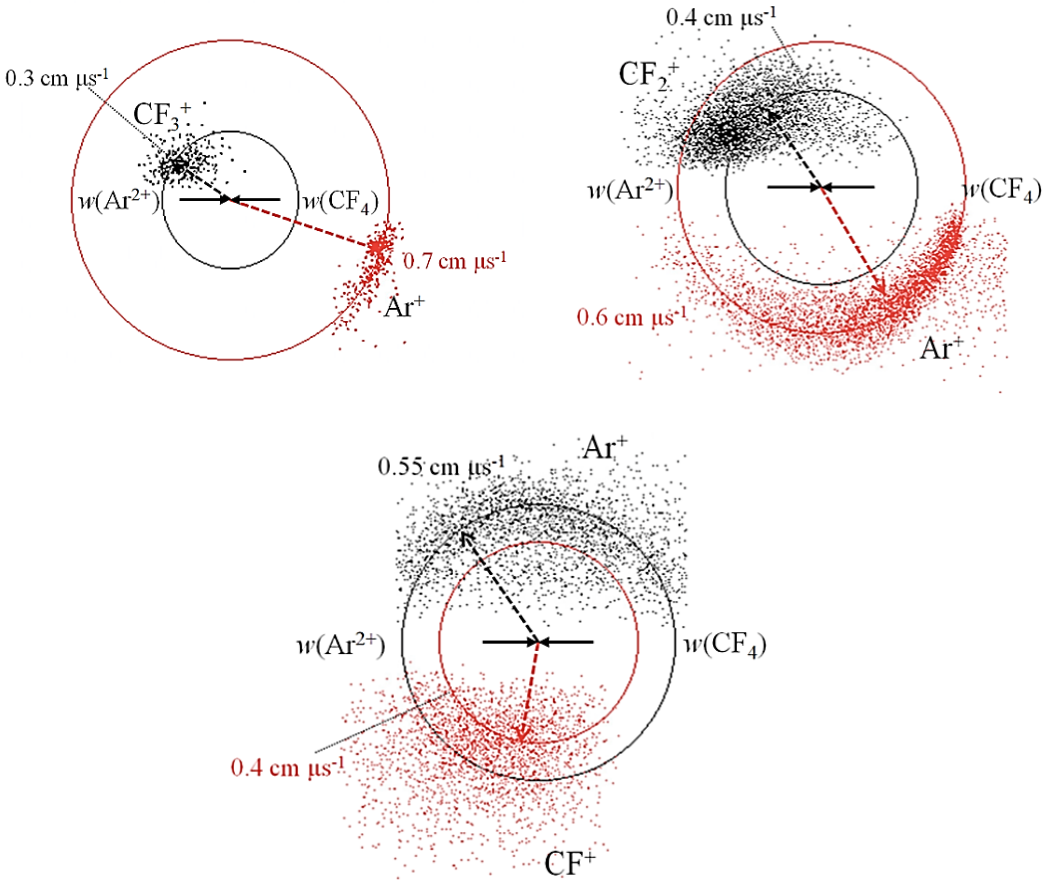

Figure 4.3 Scattering diagrams in the CM frame to show product ion velocities relative to the direction of reactants (filled arrowheads) following dissociative SET from CF_4 to Ar^{2+}. The red and black circles indicate the product ion velocity. The open headed arrows show the general scattering direction of the product ions and indicate the velocity scale. See text for details.

Upon inspection of the scattering diagram for reaction 4.5, the $w(Ar^+)$ vector is orientated with the dication CM velocity, and likewise the $w(CF_3^+)$ vector is orientated with the CM velocity of the neutral species. As mentioned above, such a relationship between product and reactant velocities is indicative of a SET reaction where the incoming reactant species only interact very briefly. Indeed, this scattering supports a reaction mechanism

where the dication and neutral approach, an electron is transferred at large interspecies separation and the resultant products separate, relatively unperturbed from their respective reactant trajectories.

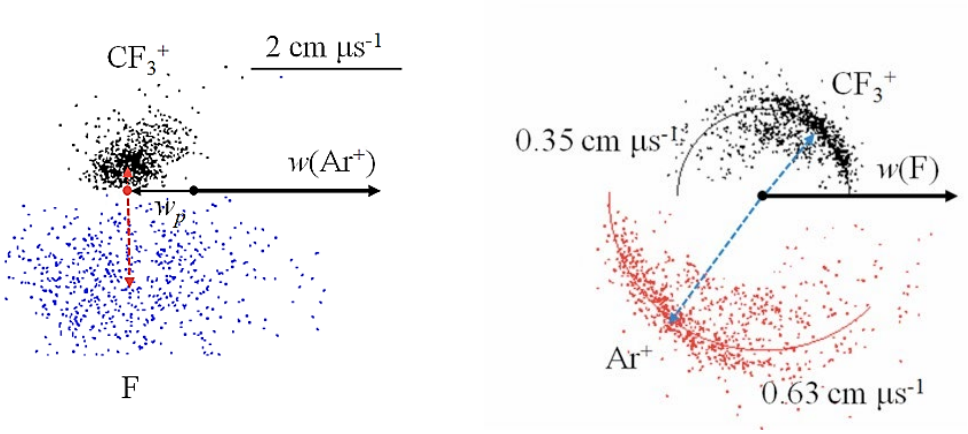

Figure 4.4 Internal frame scattering diagram for the reaction $Ar^{2+} + CF_4 \rightarrow Ar^+ + CF_3^+$ (+ F) recorded at E_{cm} = 6.88 eV. (a) displays the velocity vectors of CF_3^+ and F relative to Ar^+ velocity, where w_p is the precursor velocity. (b) shows the velocity vectors of CF_3 and Ar^+ relative to the neutral F fragment.

For three-body reactions, such as channel 4.5, we are able to determine the velocity of the neutral fragment that forms in addition to the detected product monocations. As such, to further investigate the kinematics of this reaction we have constructed internal frame scattering diagrams (chapter 1) for this channel. An internal frame scattering diagram is a polar histogram that shows the CM velocities of two products relative to the CM velocity of the third product in a three-body reaction. As with CM scattering plots, the diagram is split into two halves for clarity, corresponding to the two fragments. Figure 4.4 presents the internal frame diagrams for channel 4.5, showing the Ar^+, CF_3^+ and F velocity vectors relative to each other.

Figure 4.4 (b) provides further evidence that this reaction occurs *via* a direct mechanism, as the CF_3^+ and F product velocity vectors are strongly anti-correlated compared to Ar^+. Figure 4.4 (a) shows that the F and CF_3^+ product ions fragment about a point that is back scattered away from the

collision centre. This type of scattering implies that the product ions originate from a pre-cursor product ion that is scattered away from the Ar^+ ion. Clearly, by conservation of mass, this precursor must be $(CF_4)^{+*}$ which is formed following rapid electron transfer from CF_4 to Ar^{2+}. The velocity of the precursor species, w_p, can be determined by inspecting the scattering diagram, and also calculated by applying the principle of the conservation of momentum using the measured velocity of Ar^+. Both methods of determination yields a precursor velocity of approximately 0.3 cm μs^{-1}, supporting the mechanism. The scattering of the CF_3^+ and F around the precursor dissociation centre is isotropic, implying that the precursor CF_4^{+*} is dissociating out of the columbic field of the Ar^+ ion. Thus, the mechanism associated with reaction channel 4.5 can be unambiguously assigned, as shown below (1.8). Such a sequential reaction mechanism is typical of dissociative SET.[15]

$$Ar^{2+} + CF_4 \rightarrow Ar^+ + CF_4^{+*} \rightarrow Ar^+ + CF_3^+ + F \qquad 4.8$$

To explore the energetics of reaction 4.8, we can compare the energetically derived exothermicity for this channel with its literature enthalpy. The literature exothermicities determined for this channel are given in Table 4.3. As described in chapter 1, the experimental exothermicity for a channel can be determined by subtracting the E_{cm} from the measured KER associated with the separation of the two product monocations, and the neutral body, if present. For this channel, the experimentally derived exothermicity has been found to be -12.9 eV.

The experimentally derived exothermicity is very similar to the literature exothermicity determined for mechanism 4.9, with a difference of 0.2 eV. This close match suggests that this reaction channel is proceeding *via* mechanism 4.9 and that the product species are formed in their ground electronic states

The ground state reaction literature enthalpy for this reaction channel is -12.7 eV. RW theory states that the products of SET reactions form with an exothermicity of 2 to 6 eV. Therefore, we can estimate that the precursor

product ions, Ar^+ and CF_4^+, must form with a maximum total internal energy of 6-10 eV. This energy may reside in one of the nascent monocations or be distributed between them.

Table 4.3 The literature exothermicities for the possible reactant electronic states taking part in this channel. [26, 30]

ΔH_{lit} / eV	Reaction	Channel
-12.7	$Ar^{2+}(^3P) + CF_4 \rightarrow Ar^+ + CF_4^{+*} \rightarrow Ar^+(^2P) + CF_3^+ + F$	4.9
-14.5	$Ar^{2+}(^1D) + CF_4 \rightarrow Ar^+ + CF_4^{+*} \rightarrow Ar^+(^2P) + CF_3^+ + F$	4.10
-16.9	$Ar^{2+}(^1S) + CF_4 \rightarrow Ar^+ + CF_4^{+*} \rightarrow Ar^+(^2P) + CF_3^+ + F$	4.11

The formation of Ar^+ (^2S) is endothermic for this reaction system. Assuming negligible rotational excitation, we can estimate that the 6-10 eV of internal energy is distributed into the vibrational-electronic excitation of the CF_4^+ precursor product monocation, prior to fragmentation.

Considering the electronic excitation of CF_4^+, the C $^2T_2$ and D $^2A_1$ excited electronic states of $(CF_4^+)^*$ lie 6.3 eV and 9.71 eV above the ground state respectively, and would therefore fall in the RW for this channel. The RW calculations shown in table 4.2 strengthen this hypothesis, as they suggest that SET would be most efficient following collisions between Ar^{2+} (^3P) and ground state CF_4, when forming $(CF_4^+)^*$ in these electronic states. However, TPEPICO experiments state that these two electronic states of $(CF_4^+)^*$ fragment to form $CF_2^+ + 2F$ and $CF^+ + 3F$ respectively, which are not the detected products for this channel.

The CF_4^+ (B ^2E) electronic state lies ~3 eV lower in energy than the C $^2T_2$ state, and its ground vibrational state lies outside the RW. It is known from the TPEPICO experiments that this state fragments to form $CF_3^+ + F$. As mentioned previously, a limitation of the above analysis is that it assumes that there is negligible rovibrational excitation distributed amongst the

precursor product ions. However, the CF_4^+ (B ^2E) + Ar^+ (^3P) ions are quite likely to form with ~3 eV rovibrational energy in the molecular ion. The low cross-section to SET for this reaction may explain the low number of counts observed.

Figure 4.3 shows that the scattering of the products of reaction channel 4.6 is largely like the product ion scattering of channel 4.5. Indeed, the Ar^+ and CF_2^+ product ion velocity vectors are orientated to the nascent Ar^{2+} and CF_4 velocity vectors respectively. Therefore, we can deduce that channel 4.6 is also occurring *via* a direct mechanism followed by the dissociation of the nascent $(CF_4^+)^*$ product monocation.

Table 4.4 The literature exothermicities for the possible reactant electronic states taking part in this channel. Thermochemical data taken from references 20, 36,

ΔH_{lit} / eV	Reaction	Channel
-6.53	Ar^{2+} (^3P) + CF_4 → Ar^+ + CF_4^{+*}→ Ar^+ (^2P) + CF_2^+ + 2F	4.12
-8.36	Ar^{2+} (^1D)+ CF_4 → Ar^+ + CF_4^{+*}→ Ar^+ (^2P) + CF_2^+ +2F	4.13
-10.74	Ar^{2+}(^1S) + CF_4 → Ar^+ + CF_4^{+*}→ Ar^+ (^2P) + CF_2^+ +2F	4.14
-8.17	Ar^{2+} (^3P) + CF_4 → Ar^+ + CF_4^{+*}→ Ar^+ (^2P) + CF_2^+ + F_2	4.15
-10.00	Ar^{2+} (^1D)+ CF_4 → Ar^+ + CF_4^{+*}→ Ar^+ (^2P) + CF_2^+ +F_2	4.16
-12.38	Ar^{2+}(^1S) + CF_4 → Ar^+ + CF_4^{+*}→ Ar^+ (^2P) + CF_2^+ +F_2	4.17

The exothermicity derived from the experimentally measured three-body KER for this channel is -5.1 eV. This analysis assumes that the neutral formed is F_2. However, as mentioned above, we do not know whether a molecule of F_2 or two F atoms form alongside the detected molecular product ion upon the fragmentation of the $(CF_4^+)^*$ species. Clearly, the reaction would no longer be three-body if two F atoms formed. As such, if 2F atoms formed,

we would be unable to infer precisely the translational energy distributed into each neutral fragment upon the dissociation of the nascent $(CF_4^+)^*$. Comparing the experimentally derived three-body exothermicity with the literature exothemicities for the different possible reaction schemes for this channel, given in Table 4.4, may enable us to identify the products formed. That is, if we get good agreement then we can infer that F_2 formed.

Channel 4.15 involves the lowest literature exothermicity, -8.17 eV, for a reaction forming three-bodies following Ar^{2+}/CF_4 collisions. This value is ~3 eV more exothermic than the experimentally derived exothermicity for this channel and is therefore is not a likely description of this reaction. The three-body, experimentally derived exothermicity compares more favourably to the literature exothermicity for reaction 4.12, suggesting that this channel is in fact a four-body reaction. As such, we cannot perform an in-depth study of the energetics of this reaction channel as the coincidence data does not contain information pertaining to the distribution of energy into the multiple neutral fragments.

The significant branching ratio into this channel suggests that SET is efficient between the dication and the neutral. The RW calculations shown in Table 4.2 suggest that SET would be most efficient following collisions between Ar^{2+} (^3P) and ground state CF_4, when forming $(CF_4^+)^*$ in its C $^2T_2$ or D $^2A_1$ electronic states. The TPEPICO experiments state that these two electronic states of $(CF_4^+)^*$ fragment to form CF_2^+ + 2F and CF^+ + 3F respectively. Therefore, we can conclude that the product electronic states detailed below are being formed in channel 4.6.

$$Ar^{2+}\ (^3P) + CF_4 \rightarrow Ar^+\ (^2P) + CF_4^{+*}\ (^2T_2) \qquad 4.18$$

$$\text{Then}\quad CF_4^{+*}\ (^2T_2) \rightarrow Ar^+ + CF_2^+ + 2F$$

Perhaps surprisingly, inspection of Figure 4.3 reveals that the product ion scattering for reaction 4.7 is somewhat different to that observed for channels 4.5 and 4.6. The CF^+ and Ar^+ product ions are scattered more isotropically about the CM collision centre. It could be argued that the CF^+ ion is weakly forward scattered relative to the nascent velocity of CF_4

however, there are too few counts to confidently interpret this scattering motif.

Isotropic scattering of the product ions suggests that they were formed *via* an indirect mechanism, where the reactants associated into a collision complex. The isotropic nature of this scattering implies that the complex rotated at least once prior to dissociation. This rotation caused the product ions to lose any 'memory' of the nascent trajectories of their respective reactants.

We will now explore a reaction mechanism that may explain the second scenario suggested above, where the Ar^+ ion is scattered isotropically and the CF^+ ion is somewhat forward scattered relative to the CF_4 trajectory. The isotropic scattering of the Ar^+ product ion suggests that, as above, the ion formed following the dissociation of a $[Ar\text{-}CF_4]^{2+}$ collision complex that had undergone at least one complete rotation. If the CF^+ ion fragmented before the collision complex had undergone a complete rotation, it would display some orientation relative to the CF_4 trajectory. Arguably, this mechanism could explain the possible forward scattering of the CF^+ ion.

As stated above, there are too few counts detected for this channel to state definitively that the CF^+ is somewhat forward scattered. However, we are confident that this reaction channel proceeds *via* an indirect mechanism that involves the dissociation of a collision complex as shown below.

$$Ar^{2+}\ (^3P) + CF_4 \rightarrow [Ar\text{-}CF_4]^{2+} \qquad 4.19$$

$$\text{Then}\ \ [Ar\text{-}CF_4]^{2+} \rightarrow Ar^+ + CF^+ + 3F/F_2 + F$$

Dissociative SET following the complexation of the reactant species has been seen previously, for example in an SET reaction between $Ne^{2+}$and N_2 and elsewhere in this thesis.[23]

This reaction channel produces two or three neutral bodies in addition to the detected product monocations. As such, we cannot extract information pertaining to the electronic energy levels involved in this reaction. However, the high branching ratio into this reaction channel suggests that SET is

efficient between the reactant and product states involved. The RW cross-sections to SET given in Table 4.2 suggest that the combination of electronic states between which SET is most efficient are:

$$Ar^{2+}\ (^3P) + CF_4 \rightarrow Ar^{+}\ (^2P) + CF_4^{+*}\ (D\ ^2A_1) \qquad 4.20$$

The TPEPICO experiments have found that the D $^2A_1$ electronic state of CF_4^{+*} fragments to form CF^+ + 3F, which are the products of this reaction channel. Therefore, we can deduce that this channel is more accurately described by reaction 4.20.

$$Ar^{2+}\ (^3P) + CF_4 \rightarrow [Ar\text{-}CF_4]^{2+} \qquad 4.21$$

$$\text{Then}\ \ [Ar\text{-}CF_4]^{2+} \rightarrow Ar^{+}\ (^2P) + CF_4^{+*}\ (D\ ^2A_1)$$

$$CF_4^{+*}\ (D\ ^2A_1) \rightarrow CF^{+} + 3F/F_2 + F$$

4.4.3 Bond-forming reaction

The coincidence data contains one pairs peak that corresponds to the detection of a product ion with new chemical connectivity. Indeed, one bond-forming reaction has occurred following collisions between Ar^{2+} and CF_4 at E_{cm} = 6.88 eV, as shown below.

$$Ar^{2+} + CF_4 \rightarrow [Ar\text{-}CF_4]^{2+} \rightarrow ArF^{+} + CF_2^{+} + F \qquad 4.22$$

This reaction channel involves the transfer of a fluoride ion to the Ar^{2+} dication from the neutral, leading to the formation of a new Ar-F bond. Such bond-forming reactivity following dication-neutral collisions can be explained by an electrostatic model first proposed by Herman.[5] In this model, the series of curve crossings that are involved in the formation of a new bond following such collisions are explored, as shown in Figure 4.5.

The electrostatic model shown in Figure 4.5 describes the PES for reaction 4.20. The collision system first encounters a series of curve crossings (curve 1) in the entrance channel, which potentially lead to SET. If the collision system negotiates these crossings, Ar^{2+} and CF_4 can form a collision complex. The $[Ar\text{-}CF_4]^{2+}$ complex can then rearrange its bonding

and dissociate to form species with new connectivity. If the separating products undergo electron transfer in the exit channel (curve 3) a pair of monocations with new connectivity will be formed. Alternatively, the complex could back-dissociate into reactants. If the separating reactants undergo electron transfer, a pair of monocations will also form, however without new chemical connectivity.

Figure 4.6 shows the scattering pattern for channel 4.20 alongside two histograms that show the fragment ion scattering angles relative to the nascent dication velocity. As mentioned above, most bond-forming reactions that occur following dication-neutral collisions form *via* complexation.[23] There are some reported exceptions to this rule, such as the rapid transfer of hydride ions from neutral species to dications, which occur at large interspecies separations leading to a forward scattered products relative to their respective reactants.[24] The product ions for this channel are isotropically scattered around the CM collision centre, suggesting a reaction mechanism where a collision complex is formed, which dissociated into the detected product ions following at least one complete rotation.

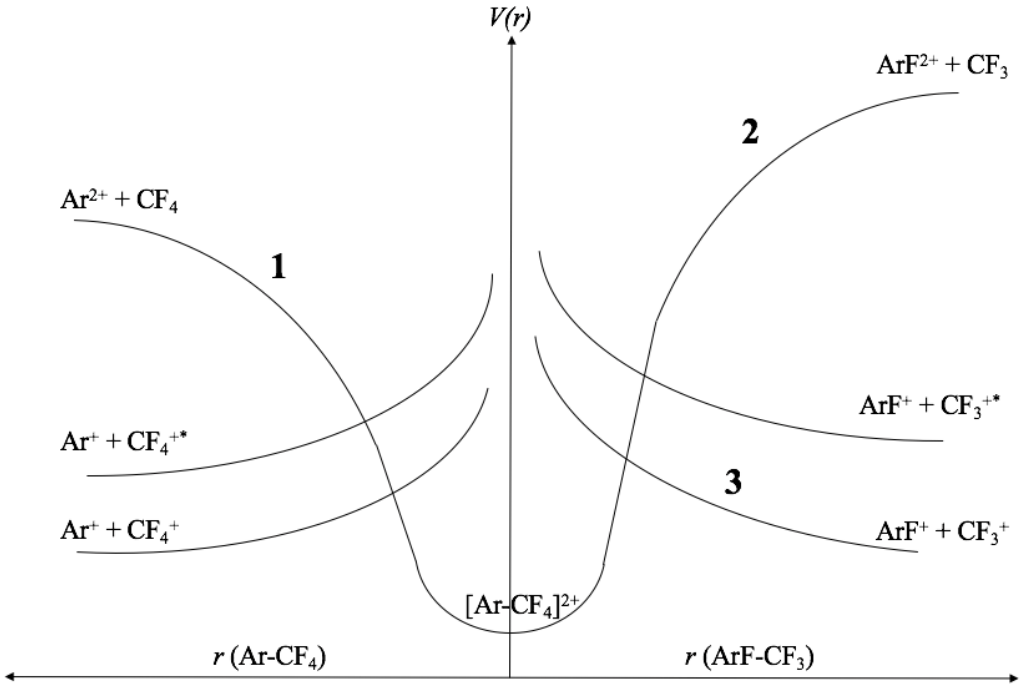

Figure 4.5 Schematic potential energy surfaces for a bond-forming reaction of Ar^{2+}, as proposed by Herman. See text for details.

Arguably, there is evidence of some correlation between the product ion scattering and the velocity vectors of their respective reactants. Figure 4.6 shows two histograms. The first shows the scattering of the ArF^+ product ion relative to $w(Ar^{2+})$ and the second shows the scattering of CF_2^+ relative to $w(Ar^{2+})$. The ArF^+ histogram is weakly peaked at 50°, and the CF_2^+ histogram is weakly peaked at 100°. For typical isotropic scattering, these histograms would both be peaked at 90° and would be broadly symmetrical in shape indicative of scattering around the collision centre. It can be argued that the ArF^+ is scattering somewhat in the direction of $w(Ar^{2+})$ and CF_2^+ is scattered somewhat in the direction of the CF_4 reactant trajectory. This type of scattering perhaps implies that the collision complex had a lifetime shorter on average than one complete rotation. As such, upon fragmentation, there is still a degree of correlation between the detected product ions and their respective reactant precursor velocity vectors prior to collision. We cannot definitively say this is the case, as there are too few counts to confidently interpret this motif in the scattering diagram, and the overall scattering is broadly isotropic.

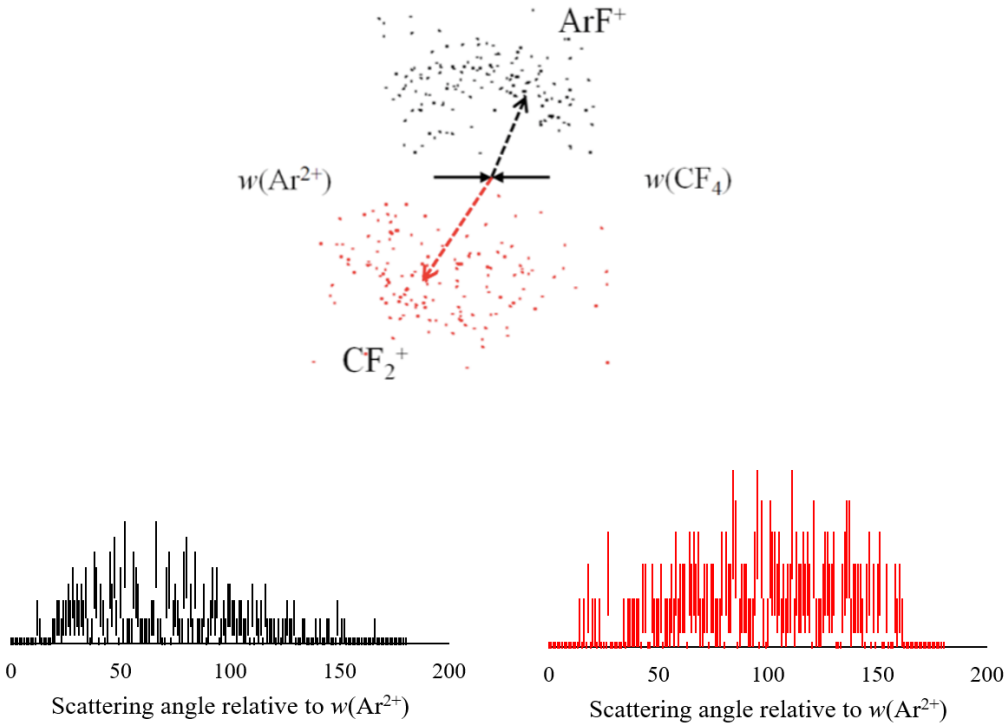

Figure 4.6 Scattering pattern and resultant scattering angle histograms for the ions ArF^+ and CF_2^+ that were detected in coincidence following Ar^{2+} collisions with CF_4. See text for details.

For this reaction channel, we are able to determine the velocity of the neutral body that forms in addition to the detected monocations. Internal frame scattering diagrams, showing the velocity vectors of the CF_2^+, ArF^+ and F fragments relative to each other, are presented in Figure 4.16. Inspection of Figure 4.16 (a) reveals that the velocities of the CF_2^+ and F species are both anti-correlated to the direction of the ArF^+ product ion. These fragments are scattered around the collision centre, suggesting that the collision complex dissociated in one step, as shown below (4.23).

$$Ar^{2+} + CF_4 \rightarrow [Ar\text{-}CF_4]^{2+} \rightarrow ArF^+ + CF_2^+ + F \qquad 4.23$$

Figure 4.16 (b) further indicates that the collision complex is short lived and dissociates in one step, as the ArF^+ is back scattered and the CF_2^+ is forward scattered relative to the *w*(F) vector, in a scattering pattern that is centred

around the collision centre. Thus, the dynamics of the bond-forming reaction 4.23 have been deduced based on the coincidence data.

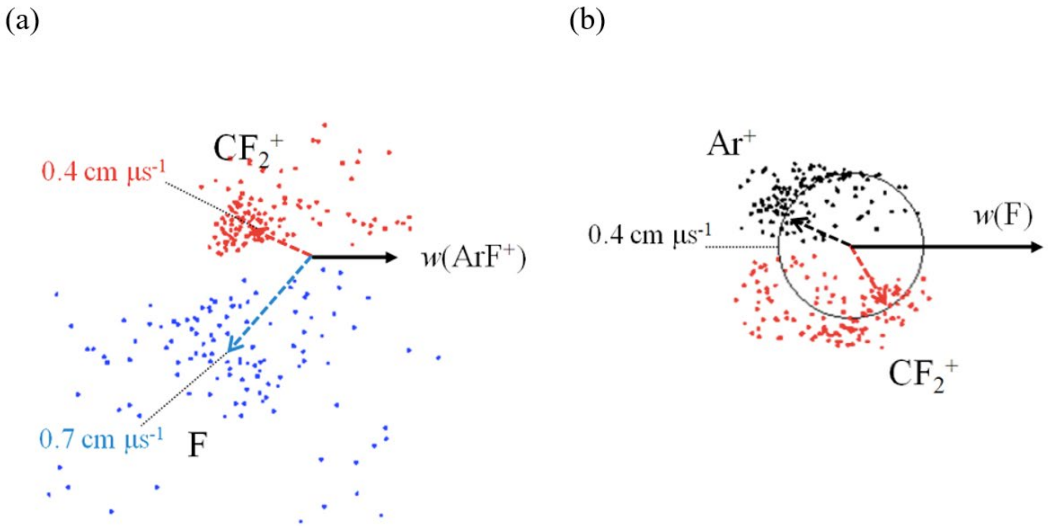

Figure 4.7 Internal frame scattering diagram showing the scattering of the velocity vectors for the various products of reaction 1.16, relative to each other. The open arrow head show the general direction of the scattering of the product ions. The closed arrow head shows the velocity of the reference product.

This section has described the reactions that occur following collisions between Ar^{2+} and CF_4 at E_{cm} = 6.68 eV. The dominant reactivity seen is dissociative SET, where an electron transferred from the neutral CF_4 to the Ar^{2+} forming two monocations. The ET step was followed by the dissociation of the molecular ion. A non-dissociative SET reaction occurs, forming CF_4^+, which suggests that the dication-neutral collisions accessed a non-Franck-Condon region of the PES. The products of a single bond-forming reaction have been detected, and this reactivity has been rationalized using a simple electrostatic model. The competition between SET and bond-forming reactions has been highlighted. The channel with the second highest branching ratio involves the formation of a collision complex, which back dissociated and underwent SET. Indeed, a $[Ar\text{-}CF_4]^{2+}$ collision complex is more likely to back-dissociate to reactants than separate along a different reaction-coordinate.

4.5 $Ar^{2+} + C_2F_6$

The product ions formed following collisions between Ar^{2+} and C_2F_6, at E_{cm} = 7.8 eV, are presented in Table 4.5

Table 4.5 The product ions formed following collisions between Ar^{2+} and CF_4, at a collision energy of 7.8 eV. The COM collision energy and branching ratios are presented.

Reaction Type	Products	*R* / %
SET	$Ar^+ + CF^+ + CF_3 + 2F/ F_2$	12.8
SET	$Ar^+ + CF_2^+ + CF_3 + F$	14.6
SET	$Ar^+ + CF_3^+ + CF_3$	23.3
SET	$Ar^+ + C_2F_4^+ + 2F/F_2$	2.1
DET	$CF_2^+ + CF^+ + 3F/(F_2 + F) + Ar$	15.5
DET	$CF_3^+ + C^+ + 3F/(F_2 + F) + Ar$	0.65
DET	$CF^+ + CF_3^+ + 2F/F_2 + Ar$	21.3
Bond-forming	$ArC^+ + CF_2^+ + 4F / 2F_2 / (2F + F_2)$	8.54
Bond-forming	$ArC^+ + CF_3^+ + 3F/ (F_2+F)$	0.70
Bond-forming	$ArF^+ + CF_3^+ + CF_3$	0.50

. In this collision system, we observe extensive SET, DET and evidence of three bond-forming reactions. Two types of bond-forming reactivity are seen: the formation of an Ar-C bond, and the formation of an Ar-F bond.

4.5.1 Dissociative SET

There is extensive SET following collisions between Ar^{2+} and C_2F_6 at E_{cm} = 7.8 eV. The SET reaction channels extracted from the coincidence data are outlined below.

$$Ar^{2+} + C_2F_6 \rightarrow Ar^+ + CF^+ (+ CF_3 + 2F/F_2) \quad 4.24$$

$$Ar^{2+} + C_2F_6 \rightarrow Ar^+ + CF_2^+ (+CF_3 + F) \quad 4.25$$

$$Ar^{2+} + C_2F_6 \rightarrow Ar^+ + CF_3^+ (+ CF_3) \quad 4.26$$

$$Ar^{2+} + C_2F_6 \rightarrow Ar^+ + C_2F_4^+ (+ 2F/F_2) \quad 4.27$$

As discussed previously, the PSCO apparatus detects the charged products formed following dication-neutral collisions. As such, we cannot unambiguously identify the neutral bodies formed for each reaction channel. We will explore the possible neutral fragments that could form for each reaction below. Firstly, we will explore the CM scattering for the SET reactions.

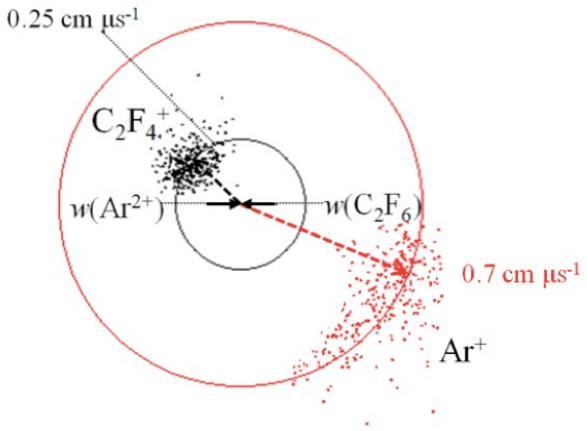

Figure 4.8 Scattering diagram for the product monocation $C_2F_4^+$ and Ar^+ formed via SET, following collisions between Ar^{2+} and C_2F_6 at E_{cm} = 7.8 eV.

Figure 4.8 shows the scattering of Ar^+ and $C_2F_4^+$ product ions formed following collisions between Ar^{2+} and C_2F_6 at E_{cm} = 7.8 eV, and is typical of all the SET collisions observed in this reaction system. The product ion velocities are strongly correlated to their respective reactant velocities, indicative of electron transfer at large interspecies separations.

We will now explore the energetics of the SET reactions. There is limited data pertaining to the fate of the excited electronic states of $(C_2F_6^+)^*$ ions in the literature. TPEPICO experiments have found that the ground and first excited electronic states of $C_2F_6^+$ are dissociative. The ground state of the $C_2F_6^+$ ion dissociates to form exclusively $C_2F_5^+$ ions.[25] The first excited state of $C_2F_6^+$ dissociates to form only CF_3^+ ions. Comparing our results to

this photoionization data will enable us to rationalize our observations. Unfortunately, at time of writing, there is no data pertaining to the dissociation of any other electronic states of the $(C_2F_6^+)^*$ ion.

Table 4.6 Literature exothermicities for the reaction between Ar^{2+} (X ^{3}P / A ^{1}D / B ^{1}S) + C_2F_6 $\rightarrow$Ar+ (X ^{2}P) + $C_2F_6^+$ in its ground and first excited electronic state. Cross-sections to SET calculated using RW theory are given in parentheses for exothermic reactions.[26, 36, 37]

		Ar^+	
Ar^{2+}	$C_2F_6^+$	^{2}P	^{2}S
X ^{3}P	X ^{1}A	-13.23 (2.21)	+0.25
	A	-10.23 (5.31)	+3.25
A^{1}D	X ^{1}A	-11.97 (2.46)	-1.49 (~0)
	A	-8.97 (7.94)	+1.51
B ^{1}S	X ^{1}A	-14.35 (3.75)	-3.87 (~0)
	A	-17.35 (1.2)	-0.87 (~0)

The experimentally derived three-body exothermicity for reaction 4.26 is -6.7 eV. The ground electronic state literature exothermicity for this channel, assuming the neutral body formed is CF_3, is -14.1 eV. This contrast between these exothermicities suggests that this reaction channel involves the production of multiple neutral bodies rather than CF_3. Unfortunately, we cannot expand further, as we cannot partition momenta into multiple neutral bodies.

This channel has the high branching ratio compared to all other reaction channels for this reaction system. Therefore, SET must be efficient between the dication and neutral. Table 4.6 shows the literature exothermicities for the possible $C_2F_6^+$ precursor product ion, forming in its ground and first excited electronic state. The RW cross-sections, given in

parentheses, indicate that SET would be most efficient between the Ar^{2+} and C_2F_6 when forming a $C_2F_6^{+*}$ in its first excited electronic state. The TPEPICO data states that the Franck-Condon region of this electronic states PEC dissociates to form CF_3^+. Therefore, we postulate that the following reaction describes channel 4.26.

$$Ar^{2+}\ (^3P/^1D/^1S) + C_2F_6 \rightarrow Ar^+\ (^2P) + C_2F_6^+\ (A) \qquad 4.28$$

$$\text{Then } C_2F_6^+\ (A) \rightarrow\ CF_3^+ + \text{neutrals}$$

The experimentally derived three-body exothermicity for reaction 4.27 is -7.8 eV. The ground electronic state literature exothermicity for this channel, assuming the neutral body formed is F_2, is -10.2 eV. The contrast between these exothermicities suggests that this reaction channel does not form F_2 alongside the detected monocations. Therefore, we can deduce that the products of reaction 4.27 are those shown below (4.29).

$$Ar^{2+} + C_2F_6 \rightarrow Ar^+ + C_2F_4^+ + 2F \qquad 4.29$$

Unfortunately, we cannot explore the kinematics of the dissociative SET channels further using the coincidence data. The treatment of multiple neutral bodies is a limitation to the data collected using the PSCO apparatus.

4.5.2 Double electron transfer reactions

We see DET in the coincidence spectra produced following collisions between Ar^{2+} and C_2F_6 at E_{cm} = 7.8 eV. In this type of reaction two electrons transfer from the neutral to the dication. The presence of $C_2F_6^{2+}$ in the singles mass spectrum cannot be unambiguously confirmed, as it appears at the same *m/z* as CF_3^+, one of the major products of dissociation following electron transfer and bond-forming reactivity in this collision system. However, the products of its dissociation appear in the coincidence pairs spectra. The DET reactions present in the pairs data collected following Ar^{2+}/C_2F_6 collisions are outlined below.

$$Ar^{2+} + C_2F_6 \rightarrow CF^+ + CF_2^+ + 3F + Ar \qquad 4.30$$

$$Ar^{2+} + C_2F_6 \rightarrow C^+ + CF_3^+ + 3F + Ar \qquad 4.31$$

$$Ar^{2+} + C_2F_6 \rightarrow CF^+ + CF_3^+ + 2F + Ar \qquad 4.32$$

Typically, the ion yield from SET is expected to be up to four times that of DET due to the cross-sections to SET being significantly higher.[26] Interestingly, for this reaction system, the separate branching ratios into DET and SET are comparable. In fact, reaction 4.30 has the second most abundant ion yield recorded in the pairs spectra. However, overall dissociative SET accounts for 51.9% of the reactivity following Ar^{2+}-C_2F_6 collisions, and dissociative DET accounts for only 38.4%.

Figure 4.9 shows the scattering diagram for channel 4.32. When investigating the kinematics of a DET reaction, two mechanisms must be considered. Firstly, DET may occur *via* the formation of a collision complex. The dissociation of a collision complex into the detected monocations would lead to isotropic scattering around the collision centre, which is not seen in Figure 4.9, therefore discounting this mechanism to explain the scattering for this channel.

The second mechanism to rationalize DET is the transfer of two electrons at large interspecies reactant separations, forming Ar and $[C_2F_6^{2+}]^*$. These two nascent products separate and the product dication can undergo a coulombic explosion, generating a pair of product monocations. Products formed *via* this direct mechanism have characteristic features in their CM scattering diagrams: the product ions are isotropically scattered around a point that is displaced away from the collision centre. The displacement corresponds to the velocity of the $[C_2F_6^{2+}]^*$ species prior to dissociation, and the isotropic scattering arises due to the rotation of the $[C_2F_6^{2+}]^*$ precursor. Evidence of this direct mechanism is seen in Figure 4.9, which is a typical scattering pattern for all the products of DET formed following collisions between Ar^{2+} and C_2F_6.

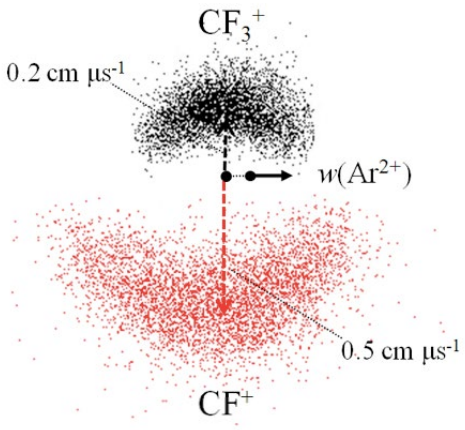

Figure 4.9 Scattering diagram of the products formed *via* DET, following collisions between Ar^{2+} and C_2F_6 at E_{cm} = 7.8 eV.

The direct DET mechanism described above can be broadly split into two further possible reaction pathways: a concerted or sequential electron transfer. The concerted pathway involves the rapid transfer of two electrons at a single crossing between the reactant and product potential energy curves whereas, for the sequential mechanism, the reactive system moves from the Ar^{2+} + C_2F_6 potential to the $C_2F_6^{2+}$ + Ar potential, *via* an intermediate $C_2F_6^+$ + Ar^+ potential.

Figure 4.10 shows a schematic of the PECs of the reactants and products involved in a DET reaction. Figure 4.10(a) shows the PECs for a sequential ET mechanism and Figure 4.10(b) shows the PECs for the concerted mechanism.

We can determine the energy separation between the reactant and product dication asymptotes, $\Delta E_{DET,}$ by finding the difference between the experimentally measured KER associated with the separation of the detected monocations and the ground state literature exothermicity for the reaction, ΔH_{lit}. For the concerted mechanism, both attractive potentials are in the dication + neutral form, and are therefore inherently very similar. In fact, under a simple electrostatic model, the only difference between the potentials depends upon the difference in polarizability of the neutral species. As such, the concerted pathway for electron transfer requires an energy separation between the two asymptotes to be very small (< 1 eV) for the

curve crossing (r_c) to fall within the RW. In contrast, the sequential DET model would allow access to product asymptotes over a larger exothermicity range, as shown in Figure 4.10. Thus, by determining ΔE_{DET} we can investigate the mechanism by which DET has occurred.

The experimental KER associated with the fragmentation of the $C_2F_6^{2+}$ dication formed *via* DET can be determined by summing the velocity vectors of the detected monocations. However, all DET channels observed for this system are dissociative, and some energy is distributed to the neutral fragments that formed alongside the monocations. Unfortunately, multiple fluorine atoms fragment from the dication in each DET reaction channel for this system. We cannot infer the translational energy of the many F atoms formed from the coincidence data. As such, we cannot determine the energy of the $C_2F_6^{2+}$ dication prior to dissociation and cannot compare the measured KER with literature enthalpies. However, the method described above has been used to rationalize DET reactions that occur in other dication-neutral systems.

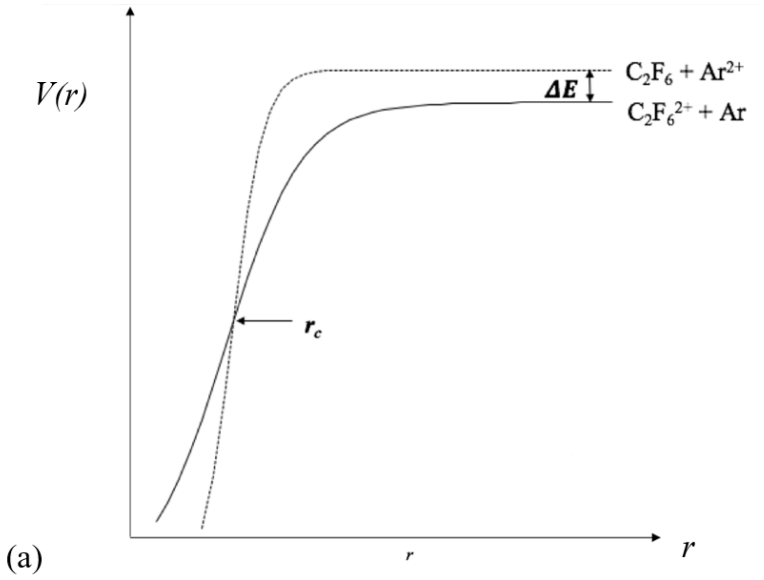

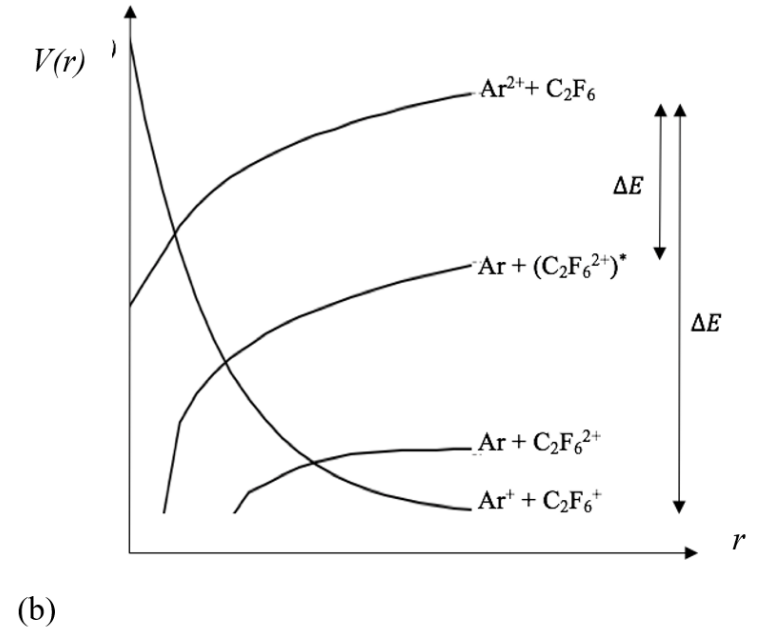

Figure 4.10 Schematic to show the potential energy curves involved in the concerted (a) and sequential (b) pathways for double electron transfer to occur following collisions between Ar^{2+} and C_2F_6.

4.5.3 Bond-forming reactions

Reactions 4.33-4.35 are channels that produce products in which new bonds have been made, the dynamics of which are explored below. Reaction 4.33 involves the formation of an Ar-F bond, whereas channels 4.34 and 4.35 both produce an ArC^+ monocation.

$$Ar^{2+} + C_2F_6 \rightarrow ArF^+ + CF_3^+ + CF_3 \quad 4.33$$

$$Ar^{2+} + C_2F_6 \rightarrow ArC^+ + CF_3^+ + 3F/(F_2+F) \quad 4.34$$

$$Ar^{2+} + C_2F_6 \rightarrow ArC^+ + CF_2^+ + 4F/2F_2/(2F + F_2) \quad 4.35$$

4.5.4 Fluoride transfer

Reaction channel 4.33 shows that ArF^+ is detected in coincidence with CF_3^+ following collisions between Ar^{2+} and C_2F_6. The CM scattering diagram associated with this reaction channel has been constructed to explore the kinematics of such an F^- transfer reaction, shown in Figure 4.11. The figure shows a hint of forward-scattering of the detected product monocations. That is, the $w(ArF^+)$ is somewhat orientated to the reactant dication velocity vector and the $w(CF_3^+)$ is somewhat orientated to the C_2F_6 velocity vector. Such scattering has been previously observed for bond-forming reactions involving hydride transfer and implies a reaction where the reactants interact at relatively large interspecies separations compared to reactions that occur *via* the formation of a collision complex.[27] Indeed, this type of scattering implies that the Ar^{2+} and C_2F_6 interacted very briefly and did not combine to form a collision complex, leaving the product velocity vectors largely unperturbed from those of the reactants. However, it is difficult to definitively state that this unusual mechanism is occurring with such low counts for this channel. Thus, we can tentatively state that the formation of the Ar-F bond following collisions between Ar^{2+} and C_2F_6 at E_{cm} = 7.8 eV proceeds *via* a direct mechanism in which a fluoride ion is stripped from the neutral C_2F_6 molecule at large interspecies separations.

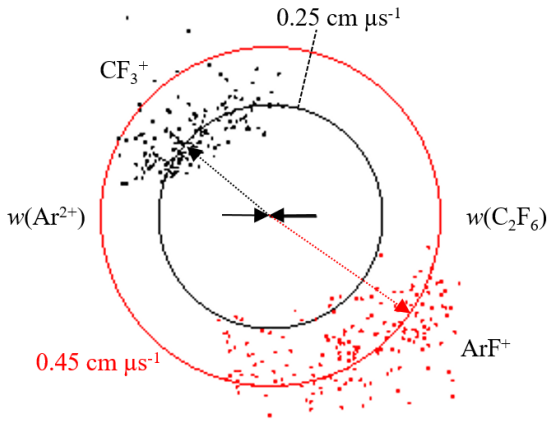

Figure 4.11 Scattering diagram for the product monocation $C_2F_4^+$ and Ar^+ formed *via* SET, following collisions between Ar^{2+} and C_2F_6 at E_{cm} = 7.8 eV.

4.5.5 Ar-C formation

Channels 4.34 and 4.35 involve the formation of ArC^+ in conjunction with CF_2^+ and CF_3^+ respectively. Scattering diagrams for both channels display similar scattering of the product ions formed. Figure 4.12 shows the CM scattering diagrams for channel 4.35. It clearly demonstrates that the product ions are scattered isotropically around the collision centre. Such scattering indicates that the reactant ions associated into a transitory collision complex, $[Ar\text{-}C_2F_6]^{2+}$, which then dissociated to give the detected monocations. The product ion velocity vectors are not orientated to their respective reactant velocity, which implies that the collision complex rotated at least once prior to dissociation.

The neutral fragment products of these bond-forming reaction channels may be formed as molecules or in their atomic forms. For example, reaction channel 4.35 may produce the neutral fragments 4F/ $2F_2$ / 2F + F_2 alongside the detected monocations. As such, detailed internal frame scattering diagrams cannot be constructed for either reaction channel. However, the CM scattering diagrams clearly indicate that the product monocations of reactions 4.34 and 4.35 formed *via* an indirect mechanism. That is, through the dissociation of an $[Ar\text{-}C_2F_6]^{2+}$ collision complex.

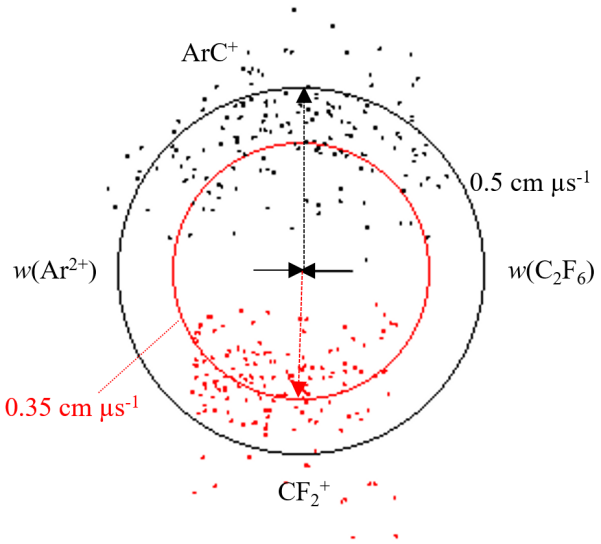

Figure 4.12 Scattering diagram for the product monocations ArC^+ and CF_2^+ formed *via* the formation of a $[Ar\text{-}C_2F_6]^{2+}$ collision complex, following collisions between Ar^{2+} and C_2F_6 at E_{cm} = 7.8 eV.

4.6 Ar^{2+} + NF_3

The product ions formed following collisions between Ar^{2+} and NF_3 at E_{cm} = 5.18 eV are listed in Table 4.7, alongside the branching ratio, *R,* for each channel.

Table 4.7 The product ions formed following collisions between Ar^{2+} and NF_3, at a CM collision energy of 5.18 eV. The branching ratios into each channel are presented.

Reaction Type	Products	R / %
SET	$Ar^+ + NF^+ + F_2/2F$	81.6
SET	$Ar^+ + N^+ + 3F/ (F_2+F)$	9.2
DET	$NF^+ + F^+ + F + Ar$	8.0
Bond-forming	$ArF^+ + N^+ + F_2/2F$	1.2

We observe that the product monocations Ar^+ and NF^+ are the most abundant ion pair detected, revealing that a strong, dissociative SET reaction dominates the reactivity of this system. In fact, the two reaction channels with the highest branching ratios are dissociative SET reactions. The products of a single bond-forming reaction are detected, which involves the formation of an Ar-F bond. The products of a single DET reaction are also observed.

4.6.1 Dissociative SET

There are two pairs peaks in the coincidence mass spectrum that correspond to the detection of product ions formed *via* dissociative SET. The ET reactions that led to the production of these products are outlined below.

$$Ar^{2+} + NF_3 \rightarrow Ar^+ + NF^+ + 2F / F_2 \qquad 4.36$$

$$Ar^{2+} + NF_3 \rightarrow Ar^+ + N^+ + 3F/ F_2 + F \qquad 4.37$$

We cannot unambiguously determine the identity and number of neutral fragments formed for reactions 1.36 and 1.37. For example, reaction 4.36 may form F_2 or 2F alongside the detected product ions, as shown below.

$$Ar^{2+} + NF_3 \rightarrow Ar^+ + NF^+ + F_2 \qquad 4.36\,(a)$$

$$Ar^{2+} + NF_3 \rightarrow Ar^+ + NF^+ + 2F \qquad 4.36\,(b)$$

We can deduce which set of products are most likely to have formed following collisions between Ar^{2+} and NF_3 by comparing the literature reaction enthalpy for reaction 4.36 (b) with the reaction exothermicity derived from the experimentally measured three-body KER for this channel, which assumes the neutral formed is F_2. Comparing these enthalpies is only used as a guide as any internal excitation of the products is not considered. If we get good agreement, we can infer that F_2 formed alongside the detected monocations.

The experimentally derived exothermicity for reaction channel 4.36 is -6.94 eV. The ground state literature enthalpy of formation for channel 4.36(a), where the two fluorine atoms fragment as a molecule of fluorine, is -9.25 eV. The ground state literature enthalpy for reaction 4.36(b), where the

two fluorine atoms fragment and do not form a molecule, is -10.9 eV. These values are both more exothermic than the experimentally derived exothermicity for this channel, and therefore we cannot definitively identify the number of neutral bodies formed.

Figure 4.13 shows a scattering diagram derived from the coincidence data. Both channels display very similar scattering patterns; Figure 1.13 shows the scattering diagram for channel 4.37. As typically observed for SET reactions following dication-neutral collisions the scattering diagram displays a hint of forward scattering of the products relative to their respective reactant velocity vectors. Indeed, there is a marked anisotropy of the product ions that is indicative of a direct reaction mechanism where the reactants interact very briefly. The similarity in the two scattering diagrams suggests that these two channels are both proceeding *via* a direct mechanism.

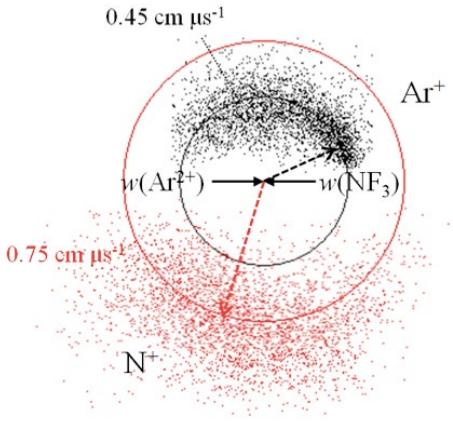

Figure 4.13 A scattering diagram that shows the product ions formed in reaction 4.37 following Ar^{2+} collisions with NF_3 at E_{cm} = 5.2 eV.

Reaction 4.36 has the highest branching ratio observed for this reaction system, therefore SET must be efficient between the neutral and the dication for this channel. TPEPICO experiments have found that NF_3^+ in its E ^2E electronic state fragments readily to form NF^+.[28] Reaction channel 4.37 shows the formation of N^+ and Ar^+ following SET between Ar^{2+} and NF_3^+. The TPEPICO data does not detect N^+ forming as a fragment ion following photoionization. Furthermore, electron ionization experiments, of energies up

to 200 eV, do not see N^+ forming as a fragment ion.[29] Therefore, the presence of this pairs peak suggests that these dication-neutral collisions are accessing a non-Franck-Condon region of the product PES. From the RW cross-sections in table 4.8 we can deduce that the pre-cursor NF_3^{+*} ion is probably formed in a highly excited electronic state.

Table 4.8 Literature exothermicities and calculated SET cross-sections (arbitrary units), in parentheses, for product ion states formed following Ar^{2+} collisions with NF_3 at E_{cm} = 5.2 eV. All cross sections were determined using RW theory as described in chapter 1. [20, 36, 38]

Electronic state of NF_3^+ product	Electronic state of Ar^{2+} reactant					
	^3P		^1D		^1S	
	ΔH_{lit}/ eV		ΔH_{lit}/ eV		ΔH_{lit}/ eV	
X $^2A_1$	-14.66	(~0)	-16.40	(~0)	-18.78	(~0)
A ^2E	-12.14	(~0)	-13.88	(~0)	-16.26	(~0)
B ^2E	-11.08	(~0)	-12.82	(~0)	-15.20	(~0)
C $^2T_2$	-10.47	(~0)	-12.21	(~0)	-14.59	(~0)
D $^2A_1$	-8.39	(~0)	-10.13	(~0)	-12.51	(~0)
E ^2E	-6.49	(2.50)	-8.23	(0.2)	-10.61	(~0)

Table 4.8 shows the RW cross-sections to SET for the formation of the possible NF_3^+ product ion electronic states. Interestingly, the cross-sections

are negligible for the formation of NF_3^{+*} in its ground or first four excited states. Indeed, the formation of NF_3^{+*} in its E ^2E electronic state is the only product ion state in the reaction window. Therefore, we can deduce that reaction 4.36 is more accurately described by the equation below:

$$Ar^{2+}(^3P) + NF_3 \rightarrow Ar^+ (^2P)\ Ar^+ + NF^+(\ E\ ^2E\ ) + \text{neutral(s)} \qquad 4.37$$

Reaction channel 4.37 shows the formation of N^+ and Ar^+ following SET between Ar^{2+} and NF_3. The TPEPICO data does not detect N^+ forming as a fragment ion following photoionization. Furthermore, electron ionization experiments, of energies up to 200 eV do not see N^+ forming as a fragment ion.[29] Therefore, the presence of this pairs peak suggests that these dication-neutral collisions are accessing a non-Franck-Condon region of the product PES. From the RW cross-sections in table 4.8 we can deduce that the precursor NF_3^{+*} ion is probably formed in a highly excited electronic state.

4.6.2 Bond-forming reactions

Inspection of the coincidence data, collected following collisions between Ar^{2+} and NF_3 at E_{cm} = 5.2 eV, reveals that a reaction is taking place that involves the formation of a new Ar-F bond, as shown in reaction 4.38.

$$Ar^{2+} + NF_3 \rightarrow ArF^+ + N^+ + 32/\ F_2 \qquad 4.38$$

Figure 4.14 shows the CM scattering diagram for this reaction channel. Upon inspection, the velocity vectors of the product monocations show little correlation to the nascent Ar^{2+} velocity, which is indicative of the formation of a collision complex prior to dissociation into the detected daughter ions. The displayed isotropic scattering suggests that the collision complex rotated at least once prior to dissociation, therefore losing any correlation to the direction of the reactant Ar^{2+}.

We cannot unambiguously correlate 2F or F_2 to the formation of the product ions of reaction 4.38. If 2F atoms formed, our data contains no information as to whether the fluorine atoms fragmented sequentially or simultaneously. However, if we assume that F_2 forms, we can construct

internal frame diagrams to investigate the different mechanisms by which the collision complex dissociated.

There are several mechanisms by which the $[ArNF_3]^{2+}$ collision complex could dissociate into ArF^+ and N^+, some of which are outlined below.

$$Ar^{2+} + NF_3 \rightarrow [ArNF_3]^{2+} \rightarrow \quad ArF^+ + N^+ + 2F/\ F_2 \qquad 4.38\ (a)$$

$$Ar^{2+} + NF_3 \rightarrow [ArNF_3]^{2+} \rightarrow \quad ArF^+ + NF_2^+ \qquad 4.38\ (b)$$

$$\text{Then } NF_2^+ \rightarrow N^+ + 2F/F_2$$

$$Ar^{2+} + NF_3 \rightarrow [ArNF_3]^{2+} \rightarrow \quad ArF_3^+ + N^+ \qquad 4.38\ (c)$$

$$\text{Then } ArF_3^+ \rightarrow ArF^+ + 2F/F_2$$

$$Ar^{2+} + NF_3 \rightarrow [ArNF_3]^{2+} \rightarrow \quad [ArNF]^{2+} + 2F/F_2 \qquad 4.38\ (d)$$

$$\text{Then } [ArNF]^{2+} \rightarrow ArF^+ + N^+$$

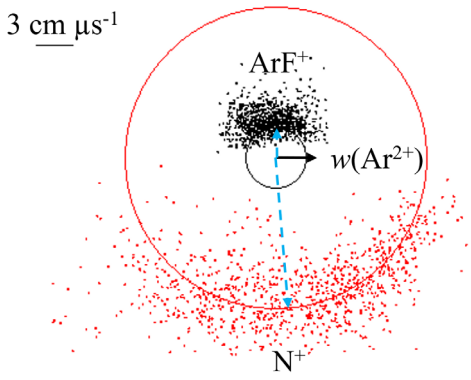

Figure 4.14 Scattering diagram for the products of a bond-forming reaction following Ar^{2+} and NF_3 collisions at E_{cm} = 5.2 eV. See text for details.

Internal frame diagrams have been constructed that present the product fragment velocity vectors relative to each other. To gain a qualitative understanding of the fragmentation of the $[ArNF_3]^{2+}$ collision complex, and to demonstrate the power of internal frame scattering diagrams, the two neutral F fragments are treated as a molecule of F_2. As such, we can determine their shared momenta and broadly distinguish between the mechanisms

presented above. The precise manner by which the F atoms fragment from the complex is not known and may be in either simultaneous or sequential.

Reaction 4.38 (a) shows the concerted dissociation of the $[ArNF_3]^{2+}$ collision complex. This reaction corresponds to a mechanism where, after at least one complete rotation, the complex undergoes a rapid coulombic explosion into the detected monocations and neutral fragments. It has been shown previously that such a concerted mechanism would lead to the product velocities having a strong fixed relationship relative to each other.[30] This mechanism can be ruled out for this case, as the scattering for this channel does not show such a fixed relationship.

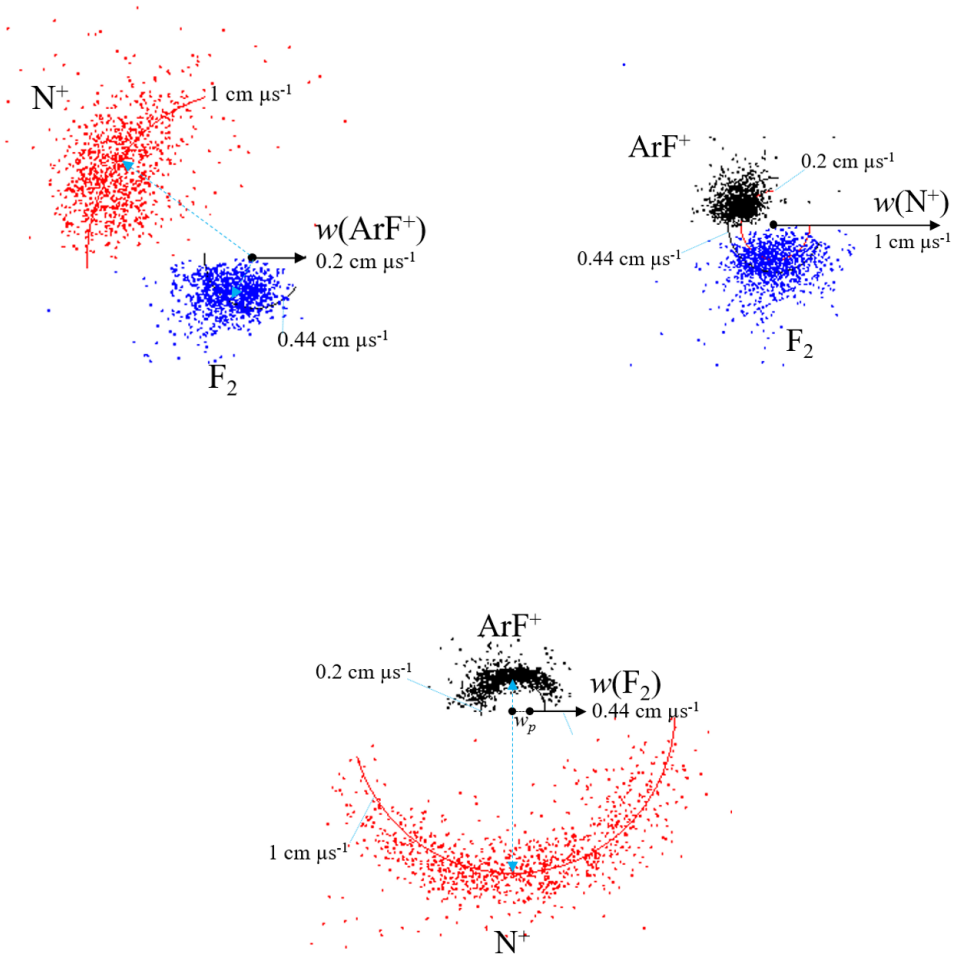

Figure 4.15 Internal frame scattering diagrams for the pairs peak ArF^+ and N^+, formed following collisions between Ar^{2+} and NF_3 at E_{cm} = 5.2 eV. See text for details.

Reaction 4.38 (b) shows a sequential dissociation of the $[ArNF_3]^{2+}$ collision complex into ArF^+ and NF_2^+, followed by the further dissociation of NF_2^+ into N^+ and F_2. If this mechanism was taking place, the internal frame scattering diagram would display the F_2 and N^+ fragments dissociating around a point that corresponds to the velocity of the precursor NF_2^+ species, displaced away from the collision centre. There is no evidence of such scattering in Figure 4.15 therefore we can rule out reaction 4.38 (b).

Reaction 4.38 (c) shows the collision complex initially dissociating into $[ArF_3]^+$ and N^+, followed by the dissociation of the $[ArF_3]^+$ species into ArF^+ and F_2. Similarly to reaction 4.38 (b), such a mechanism would display the ArF^+ and F_2 species dissociating around the $[ArF_3]^+$ precursor velocity, displaced from the collision centre. Again, no such scattering is shown in Figure 4.15, thus eliminating this reaction scheme.

Finally, reaction 4.38 (d) shows the loss of F_2 from the collision complex, followed by the dissociation of $[ArNF]^{2+}$. The scattering of such a mechanism in the internal frame scattering diagram would show the F_2 species scattering isotropically with respect to both the ArF^+ and N^+ velocity vectors. The N^+ and ArF^+ velocity vector would be anti-correlated with respect to each other, showing that the ions are formed in the same time frame, where each detected product monocation is formed in the Coulombic field of the other. Relative to the F_2 velocity vector, the ArF^+ and N^+ would scatter isotropically around a point that is displaced from the collision centre by the precursor velocity. Each internal frame scattering diagram in Figure 4.15 shows evidence for this mechanism, thus we can state that reaction 4.38 (d) best describes the dynamics of this reaction channel, based on the assumption that F_2 forms. The clear dynamics displayed in this analysis perhaps suggest that F_2 indeed forms alongside the detected product monocations for this channel.

4.7 $Ar^{2+} + SF_6$

The product ions formed following collisions between Ar^{2+} and SF_6 at E_{cm} = 7.1 eV are displayed in Table 4.9. Inspection of the coincidence

spectra revealed SET and bond-forming channels, which involve the formation of an Ar-F bond.

To minimise false coincidences, when collecting coincidence data we exclude a strip of TOFs centred around the *m/z* of the reactant dication from the pairs spectrum, in this case *m/z* 20. Unfortunately, this exclusion zone sometimes coincides with the TOF of a product ion. The spectrum recorded includes peaks that correspond to the formation of SF_3^+, SF_2^+ and SF^+ in coincidence with F^+. The formation of these ion pairs is clearly a result of DET. Unfortunately, the exclusion zone overlapped with these pairs peaks and they were excluded from any detailed analysis. As we are unable to quantify the number of ion pairs detected in these partially omitted peaks, these reactions have been excluded from Table 4.9, however, it is worth noting that DET occurs following Ar^{2+} collisions with SF_6 at E_{cm} = 7.1 eV. Furthermore, without a complete pairs data we are unable to construct CM scattering diagrams or extract information about the energetics of the DET systems. As such, we are unable to draw any conclusions about these DET reactions other than note their presence.

Table 4.9 The product ions formed following collisions between Ar^{2+} and SF_6, at a collision energy of 7.1 eV. The branching ratio, *R*, into each channel is given as a percentage.

Reaction type	Products	*R* / %
SET	$Ar^+ + S^+ + 6F$	2.7
SET	$Ar^+ + SF^+ + 5F$	3.8
SET	$Ar^+ + SF_2^+ + 4F$	21.5
SET	$Ar^+ + SF_3^+ + 3F$	67.0
Bond-forming	$ArF^+ + SF_3^+ + 2F/F_2$	2.2
Bond-forming	$ArF^+ + SF_2^+ + 3F/(F + F_2)$	2.8

4.7.1 Dissociative single electron transfer reactions

There are four pairs peaks in the coincidence mass spectra that indicate that dissociative SET has occurred following Ar^{2+} and SF_6 collisions, which are detailed below.

$$Ar^{2+} + SF_6 \rightarrow Ar^{+} + S^{+} + 6F \qquad 4.39$$

$$Ar^{2+} + SF_6 \rightarrow Ar^{+} + SF^{+} + 5F \qquad 4.40$$

$$Ar^{2+} + SF_6 \rightarrow Ar^{+} + SF_2^{+} + 4F \qquad 4.41$$

$$Ar^{2+} + SF_6 \rightarrow Ar^{+} + SF_3^{+} + 3F \qquad 4.42$$

As with the other systems studied, we cannot unambiguously identify the nature of the neutral bodies formed in each of these dissociative SET reactions. Unfortunately, it is very unlikely that any of the reactions above are two or three-body. Therefore, we cannot infer the momenta partitioned into the neutral fragment from the coincidence data.

Figure 4.16 shows the CM scattering diagram for the reaction that forms SF_3^{+} + Ar^{+} following collisions between Ar^{2+} and SF_6 at E_{cm} = 7.1 eV. There is clear evidence that both SF_3^{+} and Ar^{+} are scattered in the same direction as the direction of travel of their respective reactant species. Indeed, channel 4.42 exhibits a forward scattering motif that is indicative of rapid electron transfer at large interspecies separation, which is typical of electron transfer reactions between dications and neutrals.[11]

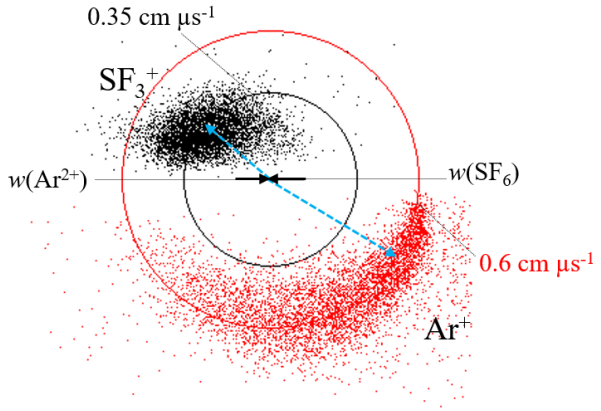

Figure 4.16 CM scattering diagram for the product monocations SF_3^+ and Ar^+ formed *via* SET, following collisions between Ar^{2+} and SF_6 at E_{cm} = 7.1 eV

The scattering diagrams constructed for reaction channels 4.39-4.41 reveal a markedly different product monocation scattering behaviour compared to the products of reaction4.42. Figure 4.17 shows the CM scattering for reaction 4.41. Channels 4.39 and 4.40 display identical scattering to 4.41, however the other channels are weaker.

Figure 4.17 shows that there is no anisotropy between the product and reactant velocities. That is, the detected product ions are scattered isotropically around the collision centre. As previously discussed, this type of scattering is indicative of the formation of a transitory species that forms by the temporary association of the reactants, which rotates at least once before dissociating into the observed ions. This rotation means that the products lose any correlation to their respective reactant velocity vectors. The formation of a collision complex goes against the generally accepted mechanism of a dissociative SET reaction between a dication and neutral following low energy collisions (0-10 eV), which is a stepwise process: an electron transfers from the neutral to the dication forming the products ions is some excited states. These excited states can then dissociate to form the detected product monocations. However, SET reactions following low energy dication-neutral collisions, that occur *via* the formation of a collision

complex, have been previously observed before, for example in the study of Ne^{2+} and N_2 collisions, and elsewhere in this work.[23]

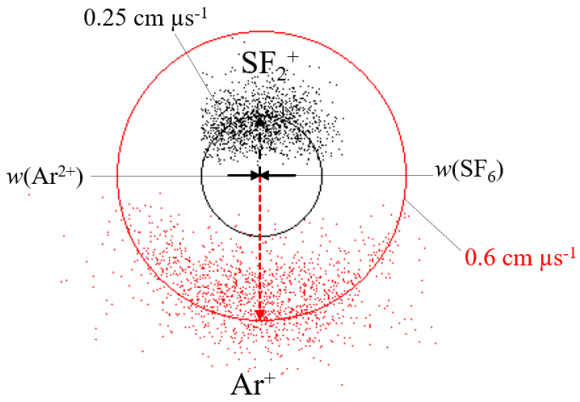

Figure 4.17 CM scattering diagram for the product monocation SF_2^+ and Ar^+ formed *via* SET, following collisions between Ar^{2+} and SF_6 at E_{cm} = 7.1 eV.

Having explored the dynamics of the SET reactivity for this reaction system, we can conclude that we see two distinct mechanisms by which SET occurs following collisions between Ar^{2+} and SF_6. One where the reactants approach each other and an electron transfer at large interspecies separations, and one where the reactant associate into a collision complex. This complex then back-dissociated to reactants, and dissociative SET occurred. The dissociative SET reactions for this system can are described below.

$$Ar^{2+} + SF_6 \rightarrow [Ar\text{-}SF_6]^{2+} \qquad 4.43$$

Then $[Ar\text{-}SF_6]^{2+} \rightarrow Ar^+ + S^+ + 6F$

$$Ar^{2+} + SF_6 \rightarrow [Ar\text{-}SF_6]^{2+} \qquad 4.44$$

Then $[Ar\text{-}SF_6]^{2+} \rightarrow Ar^+ + SF^+ + 5F$

$$Ar^{2+} + SF_6 \rightarrow [Ar\text{-}SF_6]^{2+} \qquad 4.45$$

Then $[Ar\text{-}SF_6]^{2+} \rightarrow Ar^+ + SF_2^+ + 4F$

$$Ar^{2+} + SF_6 \rightarrow Ar^+ + SF_3^+ + 3F \qquad 4.46$$

The branching ratios for each reaction mechanism are comparable, suggesting that it is quite likely that the Ar^{2+} and SF_6 will form a transitory complex upon collision.

Comparing the RW cross-sections given in Table 4.10 to the TPEPICO TPEPICO data, found in the literature, states that the Franck-Condon regions of the low-lying excited electronic states of $(SF_6^+)^*$ are dissociative. In fact, even the ground electronic state SF_6^+ (X $^2T_{1g}$) is unstable to dissociation forming SF_5^+. Likewise, the first two excited electronic states of SF_6^+ dissociate to form SF_5^+. SF_6^+ (C ^2E_g) and SF_6^+ (D $^2T_{2g}$) are unstable to dissociation to both SF_4^+ and SF_3^+. SF_6^+ (E $^2T_{1u}$) ions dissociate to form SF_2^+ and SF_6^+ (F $^2A_{1g}$) ions dissociate to form SF^+. Comparing our data to these TPEPICO results has enabled us to disentangle which electronic states are formed following low energy Ar^{2+} collisions with SF_6.

The data outlined above may provide insight into the product ion electronic states formed following the dissociative SET reactions outlined in this section. Reaction 4.42 involves the production of SF_3^+, and has the largest branching ratio of all the channels observed for this collision system. Therefore, we can infer that SET is efficient for this channel. According to the TPEPICO data, SF_6^{+*} (C ^2E_g) and SF_6^{+*} (D $^2T_{2g}$) dissociate to give SF_3^+. These states have significant RW cross-sections, and we can deduce that reaction 4.42 is described below.

$$Ar^{2+}\ (^3P/^1D/^1S) + SF_6 \rightarrow Ar^+\ (^2P) + SF_6^{+*}\ (C\ ^2E_g/\ D\ ^2T_{2g}) \qquad 4.47$$

$$\text{Then } SF_6^{+*}\ (C\ ^2E_g/\ D\ ^2T_{2g}) \rightarrow SF_3^+ + 3F/(F_2+F)$$

Reaction 4.41 involves the production of SF_2^+ and has the second highest branching ratio of the dissociative SET reactions observed following Ar^{2+} and SF_6 collisions. Therefore, we can infer that SET is also efficient for this reaction channel. The TPEPICO data states that SF_6^{+*} (E $^2T_{1u}$) dissociates to give SF_2^+. This electronic state has very large RW cross-

sections to SET, therefore we can deduce that reaction 4.41 is described below.

$$Ar^{2+}\ (^3P/^1D/^1S) + SF_6 \rightarrow [Ar\text{-}SF_6]^{2+} \qquad 4.48$$

$$\text{Then } [Ar\text{-}SF_6]^{2+} \rightarrow Ar^{+}\ (^2P) + SF_6^{+*}\ (\text{E}\ ^2T_{1u})$$

$$\text{Then } SF_6^{+*}\ (\text{E}\ ^2T_{1u}) \rightarrow SF_2^{+} + 4F/(F_2+2F)/2F_2$$

Reaction 4.40 involves the production of SF^+ and has the third highest branching ratio of the dissociative SET reactions for the system. Therefore, we can infer that SET is still somewhat efficient for this reaction channel. The TPEPICO data states that SF_6^{+*} (F $^2T_{1g}$) dissociates to give SF^+. This electronic state has a non-negligible RW cross-sections to SET, therefore we can deduce that reaction 4.40 is described below.

$$Ar^{2+}\ (^3P/^1D/^1S) + SF_6 \rightarrow [Ar\text{-}SF_6]^{2+} \qquad 4.49$$

$$\text{Then } [Ar\text{-}SF_6]^{2+} \rightarrow Ar^{+}\ (^2P) + SF_6^{+*}\ (\text{F}\ ^2T_{1g})$$

$$\text{Then } SF_6^{+*}\ (\text{F}\ ^2T_{1g}) \rightarrow SF^{+} + 5/(F_2+3F)/(2F_2 + F)$$

Reaction 4.39 involves the production of S^+ and has one of the lowest branching ratios observed for this reaction system. Therefore, we can deduce that SET is not very efficient for this reaction channel. The TPEPICO data does not see the formation of this fragment ion following the photoionization of SF_6 into its first five excited electronic states. Therefore, we can conclude that the S^+ has formed from some higher excited electronic state of SF_6^{+*}, which has a small cross-section to SET.

Table 4.10 Literature exothermicities and RW cross-sections for the different combinations of possible reactant and product electronic states following Ar^{2+}/ SF_6 collisions. Calculated SET cross sections, in arbitrary units, for product ion states formed following Ar^{2+} collisions with SF_6 at E_{cm} = 7.1 eV. All cross sections were determined using RW theory as described in chapter 1. * demarcates degenerate states. [20, 36,37]

	Electronic state of Ar^{2+} reactant					
Electronic state of SF_6^+ product	^3P		^1D		^1S	
	ΔH_{lit}/ eV		ΔH_{lit}/ eV		ΔH_{lit}/ eV	
X $^2T_{1g}$	-12.13	(3.96)	-13.87	(3.61)	-16.25	(3.57)
*A/B $^2T_{1u}$/$^2T_{2u}$	-10.93	(4.5)	-12.67	(3.81)	-15.05	(3.55)
C ^2E_g	-9.63	(5.6)	-11.37	(4.26)	-13.75	(3.63)
D $^2T_{2g}$	-8.43	(7.5)	-10.17	(5.04)	-12.55	(3.84)
E $^2T_{1u}$	-5.33	(11.3)	-7.07	(9.6)	-9.45	(7.8)
F $^2T_{1g}$	-0.8	(1.0)	-2.54	(7.1)	-4.92	(10.2)

4.7.2 Bond-forming reactivity

Inspection of the coincidence pairs spectra produced following collisions between Ar^{2+} and SF_6 at E_{cm} = 7.07 eV reveals that there are two reaction channels that led to the formation of an Ar-F bond, as shown below.

$$Ar^{2+} + SF_6 \rightarrow ArF^+ + SF_2^+ + 3F/(F_2 + F) \quad 4.50$$

$$Ar^{2+} + SF_6 \rightarrow ArF^+ + SF_3^+ + 2F/F_2 \quad 4.51$$

Channels 4.50 and 4.51 involve the detection of SF_2^+ and SF_3^+ in coincidence with ArF^+, respectively. The dynamics and possible mechanisms to formation for these bond-forming reactions are explored below.

4.51

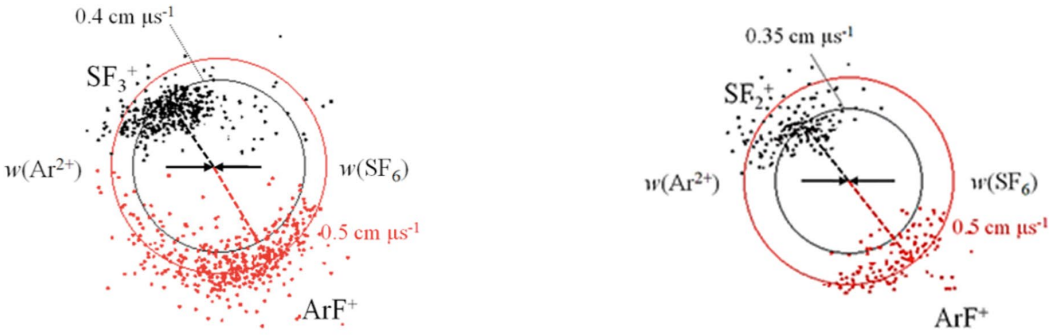

Figure 4.18 CM scattering diagrams for bond-forming reactions that occurred following collisions between Ar^{2+} and SF_6 a*t* E_{cm} = 7.1 eV. It can be argued that forward scattering of the product ions is observed. See text for details.

Figure 4.18 shows the scattering patterns derived from the coincidence data for reactions 4.50 and 4.51. Both scattering diagrams show a degree of orientation between the reactant and product velocity vectors. Indeed, the $w(ArF^+)$ vector is scattered somewhat in the direction of the nascent Ar^{2+} dication, and the $w(SF_x^+)$ vector, where x = 3 or 2, is coupled to the velocity of the neutral SF_6 molecule. Such scattering has been seen previously for hydride transfer reactions, and has been observed in this work following Ar^{2+}-C_2F_6 collisions. [30]

The tentative relationship between reactant and product velocity vectors implies a mechanism where the reactant species approach and interact very briefly, and at large interspecies separations, leaving the product ions unperturbed from the reactant trajectories. Indeed, this mechanism suggests that the reactant species may not associate into a collision complex, which is often observed for bond-forming reactions of this kind.[30] In these experiments, we have also observed SET reactions that have occurred following formation of a collision complex. Instead, this scattering implies a direct mechanism where a fluoride ion is stripped from the neutral SF_6 molecule to the Ar^{2+} dication rapidly and at large reactant separations. These findings perhaps highlights a direct competition between SET and

bond-forming reactivity. That is, if SET occurs efficiently following the complexation of a dication and neutral, then bond-forming reactions are impeded. However, as both channels have few counts, we cannot definitively state that the fluoride-stripping direct mechanism suggested above is how these reactions proceeded.

From studying the dissociative SET reaction channels, we know that a collision complex can form following collisions between Ar^{2+} and SF_6 at this collision energy. If these bond-forming channels proceeded *via* a direct mechanism, this would mean that all transitory complexes formed back-dissociated into reactants, followed by SET. Indeed, this study has highlighted the direct competition between SET and bond-forming reactivity. Furthermore, these bond-forming reactions would be in competition with SET at large interspecies separation.

4.8 Conclusions

The PSCO apparatus has been successfully used to investigate the reactions of Ar^{2+} with CF_4, C_2F_6, NF_3 and SF_6 at collision energies less than 10 eV in the CM frame. The SET reactivity between the dication and each neutral has been explored, revealing a variety of mechanisms by which these reactions can occur. Indeed, both direct and indirect SET mechanisms have been observed. Pathways to Ar-F and Ar-C bonds have been clearly identified. It has been revealed that fluoride transfer reactions may occur *via* a direct mechanism or complexation, whereas the formation of an Ar-C bond can only be formed following the association of the reactant species into a collision complex. The study of such systems is vital to further our understanding of the dynamics of the reactions that occur between dications and large neutral molecules at collision energies less than 10 eV.

4.9 Bibliography

1. O. Dutuit, N. Carrasco, R. Thissen, V. Vuitton, C. Alcaraz, P. Pernot, N. Balucani, P. Casavecchia, A. Canosa, S. Le Picard, J. C. Loison, Z. Herman, J. Zabka, D. Ascenzi, P. Tosi, P. Franceschi, S. D. Price and P. Lavvas, *Astrophysical Journal Supplement Series*, 2013, **204**.

2. G. Gronoff, J. Lilensten, C. Simon, O. Witasse, R. Thissen, O. Dutuit and C. Alcaraz, *Astronomy & Astrophysics*, 2007, **465**, 641-645.

3. C. L. Ricketts, D. Schroder, J. Roithova, H. Schwarz, R. Thissen, O. Dutuit, J. Zabka, Z. Herman and S. D. Price, *Physical Chemistry Chemical Physics*, 2008, **10**, 5135-5143.

4. J. Zabka, C. L. Ricketts, D. Schroder, J. Roithova, H. Schwarz, R. Thissen, O. Dutuit, S. D. Price and Z. Herman, *Journal of Physical Chemistry A*, 2010, **114**, 6463-6471.

5. Z. Herman, *International Reviews in Physical Chemistry*, 1996, **15**, 299-324.

6. A. Ehbrecht, N. Mustafa, C. Ottinger and Z. Herman, *Journal of Chemical Physics*, 1996, **105**, 9833-9846.

7. P. Champkin, N. Kaltsoyannis and S. D. Price, *International Journal of Mass Spectrometry*, 1998, **172**, 57-69.

8. M. Manning, S. D. Price and S. R. Leone, *Journal of Chemical Physics*, 1993, **99**, 8695-8704.

9. N. Lambert, D. Kearney, N. Kaltsoyannis and S. D. Price, *Journal of the American Chemical Society*, 2004, **126**, 3658-3663.

10. P. Tosi, R. Correale, W. Y. Lu and D. Bassi, *Journal of Chemical Physics*, 1999, **110**, 4276-4279.

11. J. F. Lockyear, M. A. Parkes and S. D. Price, *Journal of Physics B-Atomic Molecular and Optical Physics*, 2009, **42**, 9.

12. M. A. Parkes, J. F. Lockyear and S. D. Price, *International Journal of Mass Spectrometry*, 2009, **280**, 85-92.

13. D. Ascenzi, P. Franceschi, P. Tosi, D. Bassi, M. Kaczorowska and J. N. Harvey, *Journal of Chemical Physics*, 2003, **118**, 2159-2163.

14. W. P. Hu, S. M. Harper and S. D. Price, *Measurement Science & Technology*, 2002, **13**, 1512-1522.

15. W. P. Hu, S. M. Harper and S. D. Price, *Molecular Physics*, 2005, **103**, 1809-1819.

16. S. D. Price, *International Journal of Mass Spectrometry*, 2007, **260**, 1-19.

17. J. C. Creasey, H. M. Jones, D. M. Smith, R. P. Tuckett, P. A. Hatherly, K. Codling and I. Powis, *Chemical Physics*, 1993, **174**, 441-452.

18. C. Zener, *Proceedings of the Royal Society of London Series a-Containing Papers of a Mathematical and Physical Character*, 1932, **137**, 696-702.

19. C. Wittig, *Journal of Physical Chemistry B*, 2005, **109**, 8428-8430.

20. X. F. Tang, X. G. Zhou, M. M. Wu, Z. Gao, S. L. Liu, F. Y. Liu, X. B. Shan and L. S. Sheng, *Journal of Chemical Physics*, 2013, **138**, 9.

21. K. Stephan, H. Deutsch and T. D. Mark, *Journal of Chemical Physics*, 1985, **83**, 5712-5720.

22. H. U. Poll, C. Winkler, D. Margreiter, V. Grill and T. D. Mark, *International Journal of Mass Spectrometry and Ion Processes*, 1992, **112**, 1-17.

23. Y. J. Kime and P. A. Dowben, *Journal of Physical Chemistry*, 1989, **93**, 6881-6881.

24. Y. Ralchenko, A. E. Kramida and J. Reader, NIST Atomic Spectra Database, (accessed 1/12/2016, 2016).

25. S. D. Price, *Physical Chemistry Chemical Physics*, 2003, **5**, 1717-1729.

26. S. M. Harper, S. W. P. Hu and S. D. Price, *Journal of Chemical Physics*, 2004, **120**, 7245-7248.

27. J. Roithova, J. Zabka, J. Hrusak, R. Thissen and Z. Herman, *Journal of Physical Chemistry A*, 2003, **107**, 7347-7354.

28. J. S. Miller, S. H. Pullins, D. J. Levandier, Y. Chiu and R. A. Dressler, *Journal of Applied Physics*, 2002, **91**, 984-991.

29. G. K. Jarvis, K. J. Boyle, C. A. Mayhew and R. P. Tuckett, *Journal of Physical Chemistry A*, 1998, **102**, 3219-3229.

30. J. F. Lockyear, C. L. Ricketts, M. A. Parkes and S. D. Price, *Chemical Science*, 2011, **2**, 150-156.

31. R. Pepin, K. J. Laszlo, B. Peng, A. Marek, M. F. Bush and F. Turecek, *Journal of Physical Chemistry A*, 2014, **118**, 308-324.

32. M. Speranza, *International Journal of Mass Spectrometry*, 2004, **232**, 277-317.

33. D. P. Seccombe, G. K. Jarvis, B. O. Fisher and R. P. Tuckett, *Chemical Physics*, 1999, **250**, 335-346.

34. S. D. Price, *Journal of the Chemical Society-Faraday Transactions*, 1997, **93**, 2451-2460.

35. S. M. Harper, S. W. P. Hu and S. D. Price, *Journal of Chemical Physics*, 2004, **121**, 3507-3514.

36. P.J. Linstrom, W.G. Mallard (Eds.), NIST Chemistry WebBook, NIST Standard Reference Database Number 69, National Institute of Standards and Technology, Gaithersburg MD, June 2005 (http://webbook.nist.gov)

37. Chase, M.W., Jr., *NIST-JANAF Themochemical Tables, Fourth Edition*, J. Phys. Chem. Ref. Data, Monograph 9, 1998, 1-1951

5 The electron transfer and bond-forming reactions of SO^{2+}

5.1 Introduction

The existence of long-lived molecular dications has been known since the start of the last century, when they were discovered during the development of mass spectrometric techniques.[31] Extensive research into the reactivity of atomic dications followed in the 1970s, a reactivity which was found to be dominated by charge transfer reactions.[32, 33] Later, interest in the reactions of molecular dications with neutrals gained impetus and the rich chemistry of this class of interactions were discovered.[34, 35] Indeed, following molecular dication-neutral low energy (between 0-10 eV) collisions several types of reaction may occur including electron transfer (ET) and those that involve the formation of new chemical bonds.[34, 36, 37]

The ionization of SO_2 and the chemistry of the product species formed are important in many planetary atmospheres. The reactions of SO^{2+} with several neutrals are studied in this chapter. SO^{2+} is formed by the double ionization of SO_2. SO_2 is present in Earth's atmosphere at only 1 ppm, but it is present in much greater concentrations in the atmospheres of Venus and Mars.[38] On Io, Jupiter's inner-most moon, SO_2 makes up 90% of the atmosphere where it is ionized by UV radiation.[39] The SO_2^+ and other products of the ionization of SO_2, including SO^{2+}, are contained by Jupiter's magnetic field and the chemistry of these species play an important role in the atmosphere of this moon. The primary source of SO_2 in these different environments is volcanic activity. On Earth, the combustion of sulfur containing fuels also contributes to atmospheric SO_2 levels, however to a lesser extent. Recently, it has been suggested that injections of SO_2 into Earth's stratosphere would counter some of the effects of global warming.[40] Although research into such climate engineering projects is in its infancy, studies into the chemistry of the products of ionization of SO_2 are clearly required to deepen our understanding of these species. This chapter explores the chemistry that occurs following low energy collisions between SO^{2+} and molecular neutrals.

5.2 Experimental details

All experiments detailed in this chapter were performed using the PSCO apparatus, following the procedure outlined in chapter 2. The SO^{2+} species was formed *via* dissociative electron ionization of SO_2 gas, from a commercial source. The neutral gases involved, C_2F_6, NF_3 and SF_6, are also from commercial sources and were used without further purification.

5.3 Results and discussion

5.3.1 SO^{2+} + NF_3

Collisions between SO^{2+} and NF_3 were carried out at a CM collision energy, E_{cm}, of 7.75 eV. The resulting coincidence mass spectrum of ion pairs contained 5 peaks, which are identified in Table 5.1. Details of the construction and interpretation of such spectra are explained in detail in chapter 1. In brief, the products of a single dication-neutral collision are detected and recorded as an ion pair, which appears as a point in a pairs spectrum; a 2D histogram of product ion *m/z*. That is, for a reaction that produces two monocations, A^+ and B^+, the point in the resultant pairs spectrum would be at a coordinate that maps the *m/z* of A^+ on the *x*-axis and B^+ on the *y*-axis of the histogram.

Following collisions between NF_3 and SO^{2+}, three of these so-called 'pairs peaks' were found to correspond to the products of single electron transfer (SET), where an electron is passed from the neutral to the dication in a single crossing of the relevant potential energy curves. Two of these SET reactions were followed by the further dissociation of one of the nascent product ions. The remaining two peaks in the pairs spectrum were found to correspond to bond-forming reactions between the dication and neutral. That is, the ions pairs detected provide evidence of the formation of a new chemical bond: nominally, a fluoride ion has transferred from the neutral to the SO^{2+} species. One of these bond-forming reactions is later followed by the further dissociation of the primary product ions. Table 5.1 presents the ion pairs detected following collisions between SO^{2+} and NF_3 at E_{cm} = 7.75 eV and the branching ratio into each channel.

Table 5.1 The product ions formed following collisions between SO^{2+} and NF_3, at a CM collision energy of 7.75 eV. The reaction type and branching ratios into each channel are presented.

Reaction Type	Products	R %
SET	$SO^+ + NF_3^+$	1.5
SET	$SO^+ + NF_2^+ + F$	85.8
SET	$SO^+ + NF^+ + 2F/F_2$	6.7
Bond-forming	$SOF^+ + NF_2^+$	0.8
Bond-forming	$SOF^+ + NF^+ (+ F)$	5.2

5.3.2 Non-dissociative SET

An ion pair has been detected following SO^{2+}/NF_3 collisions at E_{cm} = 7.75 eV that corresponds to a non-dissociative SET reaction, as described below.

$$SO^{2+} + NF_3 \rightarrow SO^+ + NF_3^+ \qquad 5.1$$

In this reaction, the dication and neutral approach each other, an electron transfers from the NF_3 neutral to the SO^{2+} dication, and the resultant monocations separate and are detected in coincidence as SO^+ and NF_3^+. We can gain more information about this reaction through a more in-depth analysis of the pairs peak; details of this analysis are provided in chapter 1. Derived from the experimental data, the scattering diagram (Figure 5.1) shows the product ion velocity vectors relative to their respective reactant velocities. A point is plotted on the diagram for each product ion pair that is detected. For clarity, the two product monocations are displayed on separate halves of the scatter plot: the NF_3^+ product ion is depicted in black on the top half and the SO^+ in red on the lower half. The filled arrow heads indicate the reactant directions of travel prior to collision and the dashed arrows indicate the general direction of the velocities of the product ions.

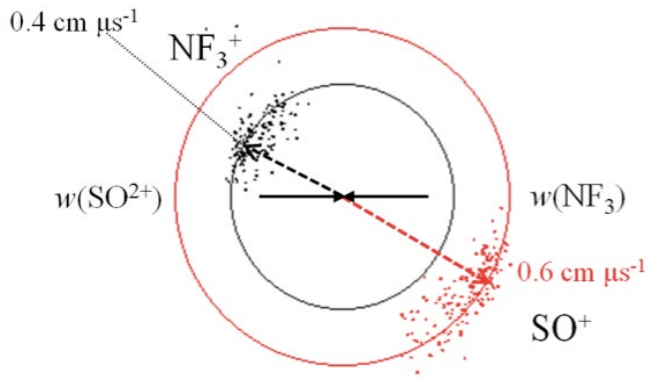

Figure 5.1 A centre-of-mass scattering diagram to show product ion velocities (open arrow heads) relative to the direction of reactants (filled arrowheads) following non-dissociative single electron transfer from CF_4 to Ar^{2+}. See text for details.

Figure 5.1 clearly shows that the product ion velocity vectors are orientated to their respective reactant trajectories. That is, $w(SO^+)$ is orientated to the incident SO^{2+} velocity and, likewise, $w(NF_3^+)$ is orientated to the NF_3 direction of travel. Such strong forward scattering describes a reaction where the reactant species approach and interact relatively weakly, leaving the product ions largely unperturbed from the trajectory of the corresponding reactant species. This picture corresponds to ET occurring rapidly, at relatively significant interspecies separations. This type of scattering, and indeed this type of reaction mechanism, is typical of SET reactions between a dication and a neutral.[5, 15]

The magnitudes of the product monocation velocities can be used to determine the kinetic energy release (KER) associated with reaction channel 5.1. As described in chapter 1, subtracting the E_{cm} from the experimentally measured KER for a reaction gives an exothermicity distribution for that channel. The exothermicity distribution for this channel is given in Figure 5.2, and peaks at -6.7 eV. There is a second peak in experimentally measured energy release, which occurs at ~ - 4 eV, although this peak is less intense.

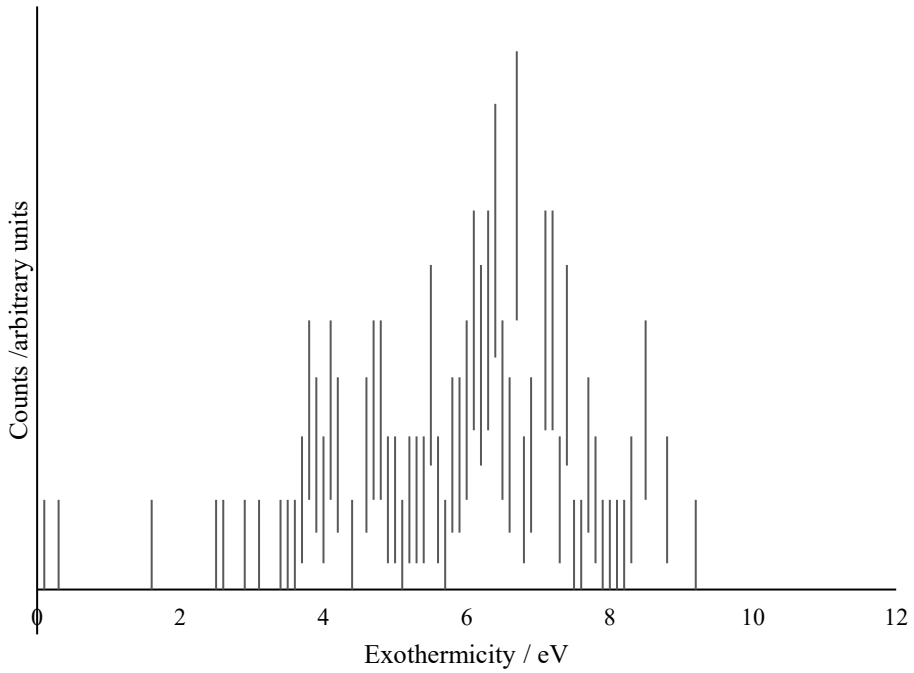

Figure 5.2 Exothermicity distribution of non-dissociative SET following SO^{2+}/ NF_3 collisions. The peak centre lies at 6.7 eV. Errors are given by Poissonian statistics.

SO^{2+} has two excited electronic states ($^3\Sigma^+$ and $^3\Delta$) that lie 3.45 and 6.74 eV above the ground state (X $^1\Sigma^+$) respectively.[41] Due to the excess energy associated with electron ionization with 150 eV electrons, the SO^{2+} dications in our beam may be present in any of these low lying excited electronic states. The reactant NF_3 neutral molecules are admitted to the PSCO apparatus *via* an effusive jet, and so we can safely assume that all NF_3 reactants are participating in collisions are in the ground electronic state (X $^2A_1$).

TPEPICO studies of NF_3 have provided insight into the excited electronic states of the NF_3^+ cation.[28] This study states that NF_3^+ (X $^2A_1$) is stable to dissociation, whereas the first five excited electronic states of the NF_3^+ cation are all dissociative. Specifically, the A (^2E) and B (^2E) states of NF_3^+ are said to dissociate to form NF_2^+ + F. The C (^2E) state is said to dissociate to form NF_2^+, following rapid internal conversion to the ground state potential. The two highest lying excited electronic states of NF_3^+ that we

will consider, D ($^2A_1$) and E (^2E), are thought to be unstable to dissociation to $NF^+ + 2F/F_2$. We can compare our results to these TPEPICO results to obtain a clearer picture of the kinematics of the SET reactions seen following SO^{2+}/ NF_3 collisions. Table 5.2 shows the different combinations of reactant and product electronic states that could be involved in this SET reaction.

Table 5.2 Literature exothermicities for the reaction between SO^{2+} ($X\ ^1\Sigma^+/A\ ^3\Sigma^+$) + NF_3 ($X\ ^2A_1$) $\rightarrow SO^+$ ($X\ ^2\Pi$ /$A\ ^4\Pi$ /$B\ ^4\Sigma$) + NF_3^+ in its ground and first five excited states. Thermochemical data taken from references 13 and 14. Cross-sections to SET calculated using RW theory is given in parentheses for exothermic reactions.

		Electronic state SO^+		
SO^{2+}	NF_3^+	$X\ ^2\Pi$	$A\ ^4\Pi$	$B\ ^4\Sigma$
$X\ ^1\Sigma^+$	$X\ ^2A_1$	-6.93 (0.1)	-3.73 (25.7)	-2.29 (1)
	$A\ ^2E$	-4.41 (9.7)	-1.21 (0)	+0.23
	$B\ ^2E$	-3.35 (20.7)	-0.15 (0)	+1.29
	$C\ ^2E$	-2.74 (0)	+0.46	+1.9
	$D\ ^2A_1$	-0.66 (0)	+2.54	+3.98
	$E\ ^2E$	+1.24 (0)	+4.44	+5.88
$A^3\Sigma^+$	$X\ ^2A_1$	-10.28 (0.1)	-7.03 (0.5)	-5.59 (3.5)
	$A\ ^2E$	-7.76 (0.3)	-4.51 (15.5)	-3.07 (14.4)
	$B\ ^2E$	-6.7 (0.89)	-3.45 (23.4)	-2.01 (0.1)
	$C\ ^2E$	-6.09 (1.8)	-2.84 (11.4)	-1.4 (0)
	$D\ ^2A_1$	-4.01 (23.4)	-0.76 (0)	+0.68
	$E\ ^2E$	-2.11 (0.1)	+1.14	+2.58

We have used thermochemical data available in the literature to determine the literature exothermicities, ΔH_{lit}, for all accessible SET reactions in the SO^{2+}/NF_3 collision system.[28, 41, 42] Table 5.2 presents these thermochemically derived values, where the possible combinations of reactant and product electronic states have been accounted for. To our knowledge, at time of writing there is no experimental data pertaining to the double ionization energy of SO. As such, a theoretically calculated value of 30.24 eV has been used for the thermochemical determinations of ΔH_{lit} presented in Table 5.2[41]

If the reactants and products associated with channel 5.1 were present in their ground electronic states, the literature exothermicity for this reaction would be -6.93 eV.[28, 41] This value is comparable to the maximum energy release recorded for reaction 5.1given in Figure 5.2, and lies within the range of values for which the reaction window theory predicts efficient SET will occur. Based on Landau-Zener theory, the RW model (chapter 1) predicts that efficient SET occurs when the reactant and product PECs intersect at interspecies separations of 2-7 Å. Under a simple electrostatic model, this separation corresponds to a reaction exothermicity of 2-7 eV.[43, 44] However, the cross-section calculated based on RW for this ground state reaction is relatively small (0.1). A caveat to the calculation of such a cross-section using the RW methodology is that no consideration is given to the intrinsic transition probability to any excited electronic state following dication-neutral collision. That is, the RW model calculates the cross-sections without accounting for Franck-Condon factors or intrinsic electron transition probabilities. Therefore, the calculated ΔH_{lit}, the measured reaction exothermicity and the TPEPICO data suggest that it is likely that NF_3^+ and SO^+ were formed in their ground electronic states. Thus, we can conclude that a non-dissociative SET reaction occurs following collisions between SO^{2+} ($X\ ^1\Sigma^+$) and NF_3 ($X\ ^2A_1$) at E_{cm} = 7.75 eV, leading to the production of SO^+ ($X\ ^2\Pi$) and NF_3^+ ($X\ ^2A_1$).

The second peak present in the exothermicity spectrum (Figure 5.2) shows an experimentally measured energy release of ~ - 4 eV. The literature exothermicity for a reaction where ground state reactants SO_2^{2+} + NF_3 form

NF_3^+ ($X\ ^2A_1$) + SO^+ ($A\ ^4\Pi$) is -3.73 eV. These comparable exothermicities lie within the range of energy releases over which RW theory predicts efficient SET between a neutral and dication can occur. Furthermore, the cross section to SET, determined by a model based on RW theory, is relatively high (25.7) compared to the other possible reactant and product electronic state combination given in Table 5.2. Therefore, we can conclude that the following two reactions result in non-dissociative SET following collisions between $SO^{2+}$and NF_3.

$$SO^{2+}\ (X\ ^1\Sigma^+) + NF_3\ (X\ ^2A_1) \rightarrow SO^+\ (X\ ^2\Pi) + NF_3^+\ (X\ ^2A_1) \qquad 5.2$$

$$SO^{2+}\ (X\ ^1\Sigma^+) + NF_3\ (X\ ^2A_1) \rightarrow SO^+\ (A\ ^4\Pi) + NF_3^+\ (X\ ^2A_1) \qquad 5.3$$

5.3.3 Dissociative SET

The coincidence spectra recorded following SO^{2+}/NF_3 collisions contain peaks that correspond to dissociative SET reactivity. Generally, reactions of this type proceed *via* two steps: the direct transfer of an electron from the neutral to the dication followed by the dissociation of one or more of the nascent product monocations.[37, 45] There are two dissociative SET pairs peaks in the coincidence spectra, which are described below.

$$SO^{2+} + NF_3 \rightarrow SO^+ + NF_2^+ + F \qquad 5.4$$

$$SO^{2+} + NF_3 \rightarrow SO^+ + NF^+ + 2F/F_2 \qquad 5.5$$

Channel 5.5 may be a three or four body reaction, depending upon the nature of the neutral bodies formed. If F_2 formed alongside the detected monocations, following the dissociation of $(NF_3^+)^*$, we can infer the velocity of the neutral body from the coincidence data. However, if two F atoms formed we cannot know unambiguously how much energy is distributed into each neutral body. Below, we compare the literature exothermicity for both reaction mechanisms to the exothermicity derived from the experimentally measured three-body KER. This comparison enables us to identify which reaction mechanism accurately describes this channel. First, we will explore the scattering and energetics of channel 5.4.

The CM scattering diagram for reaction 5.4, the most intense peak in the spectra collected following SO^{2+}/NF_3 collisions, is shown in Figure 5.3. The CM scattering diagram for channel 5.5 displays similar scattering, but the signal is less intense. The scattering in Figure 5.3 looks very like the scattering observed for the non-dissociative SET reaction 5.1 described above. Indeed, in general, like the non-dissociative SET reaction, the detected monocations exhibit strong forward scattering. This form of scattering indicates a direct electron transfer mechanism, where the SO^{2+} flies past the NF_3 neutral, stripping an electron. The precursor product ions then separate and the NF_3^+ species dissociates when significantly distant from the SO^+ species. Dissociation of the NF_3^+ can give rise to both NF_2^+ or NF^+, accounting for the similar scattering dynamics observed for reaction channels 5.4 and 5.5.

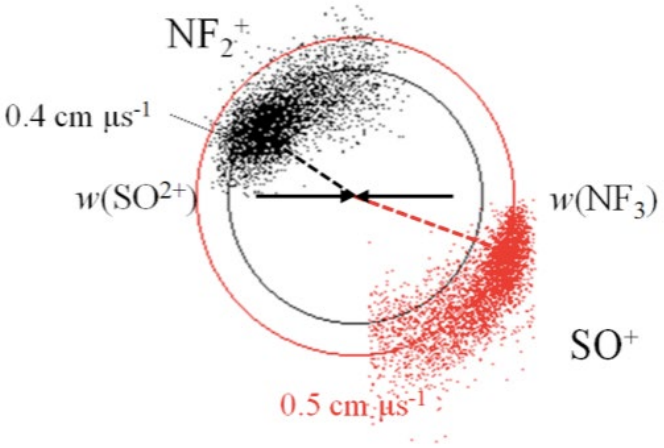

Figure 5.3 CM scattering diagram for the reaction $SO^{2+} + NF_3 \rightarrow SO^+ + NF_2^+$. The experiments were performed at E_{cm} = 7.75 eV. Strong forward scattering is displayed. See text for details.

An internal frame scattering diagram (chapter 2) is presented in Figure 5.4, where the scattering of two products, NF_2^+ and F, are presented relative to the velocity vector of the third product formed, SO^+. This diagram clearly shows that the NF_2^+ and F products are scattered away from the SO^+ ion. Furthermore, they are scattered isotropically around a point that is back scattered from the CM collision centre, which is indicated by the red square in Figure 5.4. This scattering implies a reaction mechanism where SO^+ and

$(NF_3^+)^*$ products form following SET, followed by the dissociation of the precursor $(NF_3^+)^*$, when well separated from the SO^+ product ion.

The velocity of this precursor ion, shown as a dashed line on Figure 5.4, can be determined from the coincidence data. The velocity of the SO^+ species is 0.56 cm μs^{-1}, and therefore, using the principle of the conservation of momentum, the velocity of the precursor $(NF_3^+)^*$ ion must be 0.4 cm μs^{-1}.

The experimental energy release associated with reaction channel 5.4 has been found to be -4.83 eV. The ground state literature enthalpy for this reaction is -4.06 eV.[REF] This close match suggests that the reactants and products involved in this dissociative SET reaction are in their ground electronic states, and that the products form with < 1 eV of rovibrational excitation distributed between them.

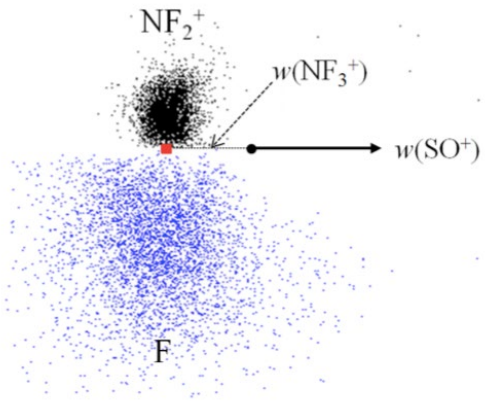

Figure 5.4 Internal frame scattering diagram for channel 1.2 that shows the NF_2^+ and F product velocities relative to $w(SO^+)$. The black circle indicates the CM collision centre and the red square indicates the point around which the NF_2^+ and F fragments dissociated.

The ground state reaction literature enthalpy for this reaction channel is -4.06 eV. RW theory states that the products of SET reactions form with an exothermicity of 2 to 6 eV. Therefore, we can estimate that the precursor product ions, SO^+ and NF_3^+, must form with a maximum total internal energy of 0-2 eV. This energy may reside in one of the nascent monocations or be distributed between them.

The SO^+ (A $^4\Pi$) electronic state is more than 3 eV above the ground electronic state of SO^+. Therefore, as the maximum internal energy of the precursor product ions has been found to be 0-2 eV, SO^+ must form in its ground electronic state. The NF_3^+ (A ^2E) excited state lies ~2 eV above the NF_3^+ ground electronic state.

The TPEPICO data states that the A (^2E) and B (^2E) states of NF_3^+ dissociate to form NF_2^+ + F. The C (^2E) state is said to dissociate to form NF_2^+, following rapid internal conversion to the ground state potential. If the $(NF_3^+)^*$ precursor ion has ~2 eV of internal energy, the NF_3^+ (A ^2E) state would be in the RW for this reaction.

Reaction channel 5.4 has the highest branching ratio for this reaction system. Therefore, we can predict that SET must be efficient between the interacting species. The following reaction scheme has a significant RW cross-section, as shown in Table 5.2, and involves the formation of $(NF_3^+)^*$ in its A ^2E state. Therefore, we can confidently assign the reactant and product electronic states involved in this dissociative SET reaction, as shown below.

$$SO^{2+}\ (X\ ^1\Sigma^+) + NF_3\ (X\ ^2A_1) \rightarrow NF_3^+\ (A\ ^2E) + SO^+\ (X\ ^2\Pi) \qquad 5.6$$

$$\text{Then } NF_3^+\ (A\ ^2E) + SO^+\ (X\ ^2\Pi) \rightarrow\ + NF^+ + 2F/F_2$$

NF^+ and SO^+ are detected in coincidence following collisions between SO^{2+} and NF_3. As mentioned above, we cannot unambiguously know whether the detected product ions form alongside 2F atoms or a molecule of F_2, as shown in reactions 5.7 and 5.8.

$$SO^{2+} + NF_3 \rightarrow NF^+ + SO^+ + 2F \qquad 5.7$$

$$SO^{2+} + NF_3 \rightarrow NF^+ + SO^+ + F_2 \qquad 5.8$$

Reaction 5.7 has a ground state literature exothermicity of -0.42 eV, and reaction 5.8 has a ground state literature exothermicity of -2.1 eV. The exothermicity derived from the three-body kinetic energy release measured for this channel is -1.92 eV. Such a close match between exothermicities suggests that reaction 5.8 describes this channel, and that F_2 forms alongside the detected monocations in their ground electronic states.

The branching ratio into this channel is small compared to channel 5.6. Therefore, the cross-section to SET may be smaller for this reaction channel. The TPEPICO data states that the D $^2A_1$ and E ^2E electronic states of $(NF_3^+)^*$ dissociate to form NF^+. Table 5.2 shows the RW cross-sections to SET for the possible combinations of electronic states that may be involved in this SET reaction. If the SO^{2+} dication was in its ground electronic state, X $^1\Sigma^+$, this reaction would be endothermic for all possible combinations of reactant and product electronic states apart from those shown in 5.9.

$$SO^{2+}\ (X\ ^1\Sigma^+) + NF_3\ (X\ ^2A_1) \rightarrow NF_3^+\ (D\ ^2A_1) + SO^+\ (X\ ^2\Pi) \qquad 5.9$$

$$\text{Then } NF_3\ (D\ ^2A_1)^+ \rightarrow\ NF^+ + 2F/F_2$$

However, the RW cross-section to SET for reaction 5.9 is negligible. Thus, SET would be inefficient between the reactant and product electronic states shown above, and it is unlikely that 5.9 accurately describes this reaction channel.

Taking the RW cross-sections into account for forming $(NF_3^+)^*$ in either its D $^2A_1$ or E ^2E excited electronic states shown in Table 5.2, the reaction shown in 5.10 has a high cross-section to SET.

$$SO^{2+}\ (A\ ^3\Sigma^+) + NF_3\ (X\ ^2A_1) \rightarrow NF_3^+\ (D\ ^2A_1) + SO^+\ (X\ ^2\Pi) \qquad 5.10$$

$$\text{Then } NF_3\ (D\ ^2A_1)^+ \rightarrow\ NF^+ + 2F$$

Therefore, reaction 5.10 may describe the electronic states involved in this reaction channel assuming that F_2 forms alongside the detected monocations. However, we have no other evidence that $SO^{2+}(A\ ^3\Sigma^+)$ is present in the dication beam.

5.3.4 Bond-forming reactivity

We see two bond-forming reaction channels in the coincidence spectra recorded following SO^{2+}/NF_3 collisions at E_{cm} = 7.75 eV, both of which involve the fluorination of the dication. That is, both pairs peaks in the

spectrum feature an SOF^+ product ion detected in coincidence with another product ion, as described below.

$$SO^{2+} + NF_3 \rightarrow SOF^+ + NF_2^+ \quad 5.11$$

$$SO^{2+} + NF_3 \rightarrow SOF^+ + NF^+ + F \quad 5.12$$

Such bond-forming reactivity can be rationalised using a simple electrostatic model first introduced by Herman, which is described in detail in chapter 1.[5]

Figure 5.5 shows a schematic of the potential energy surfaces involved in a bond forming reaction following SO^{2+} and NF_3 collisions. In the entrance channel (curve 1, Figure 5.5), the dication-neutral potential is dominated by the polarization attraction between the two species. The collision system encounters a series of repulsive curve crossings that would lead to SET. If the collision system does not undergo SET, the reactants may associate to form a collision complex, in this case $[SO\text{-}NF_3]^{2+}$. Indeed, the formation of a complex is in direct competition with SET. If formed, the collision complex may back dissociate into reactants or the products of SET. However, the complex can also rearrange to form new chemical bonds before separating along a different reaction coordinate (curve 2, Figure 5.5). In the exit channel (curve 2), the collision system will encounter further repulsive curve crossings that would lead to SET. SET in the exit channel would lead to the detection of two monocations, one of which would contain new atomic connectivity compared to the reactants. This type of reaction mechanism is the usual pathway by which bond-forming reactions occur following dication-neutral collisions.[16]

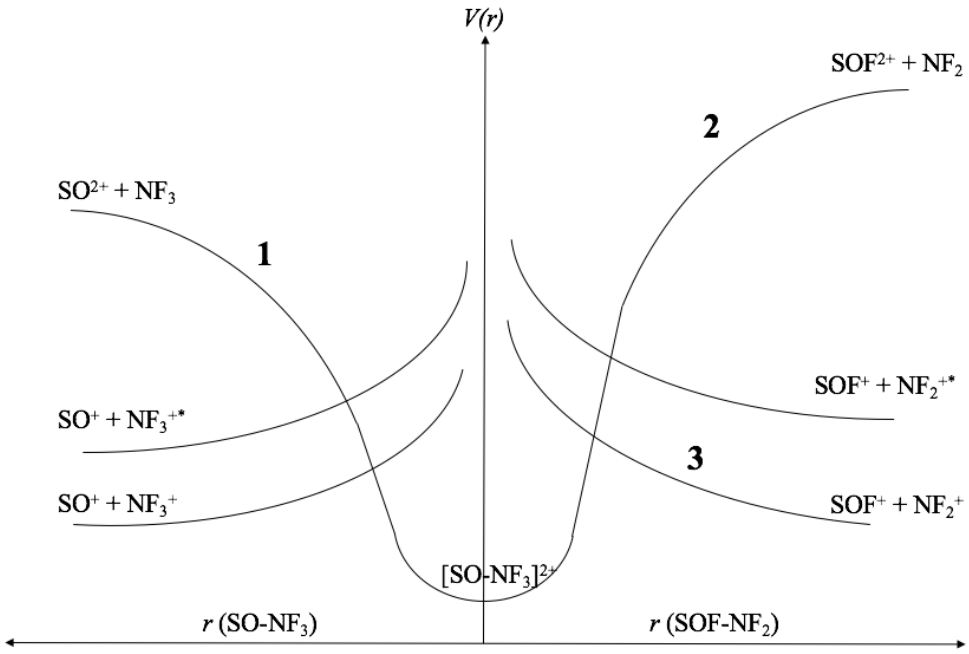

Figure 5.5 Schematic PESs involved in a bond forming reaction of SO^{2+}, based on an electrostatic model proposed by Herman.[5] See text for details.

Investigating the CM scattering of the products of bond-forming reactivity can illuminate the reaction mechanism by which they formed. Figure 5.6 shows the CM scattering diagrams for reactions 5.11 and 5.12. The CM scattering diagram for reaction 5.11 is given in Figure 5.6 (a), and the CM scattering of reaction 5.12 is given in Figure 5.6 (b). The scattering of the product monocations in both diagrams show no correlation to the velocity vectors of the reactant species. This scattering implies a reaction system where the reactants approach and temporarily associate into a collision complex. The lifetime of the complex is long compared to the time taken for the complex to complete a full rotation, therefore when it dissociates into the detected monocations they have lost any velocity correlation with their respective reactant species. This isotropic scattering is typical of bond-forming reactions following dication-neutral collisions at low energies and is consistent with the electrostatic model proposed by Herman.[5, 16, 46] Arguably, the scattering of the product ions in Figure 5.6 (a) show a degree of correlation to their respective reactant species, however the counts for this

channel are too low to definitively conclude that there is any anisotropy in the scattering diagram.

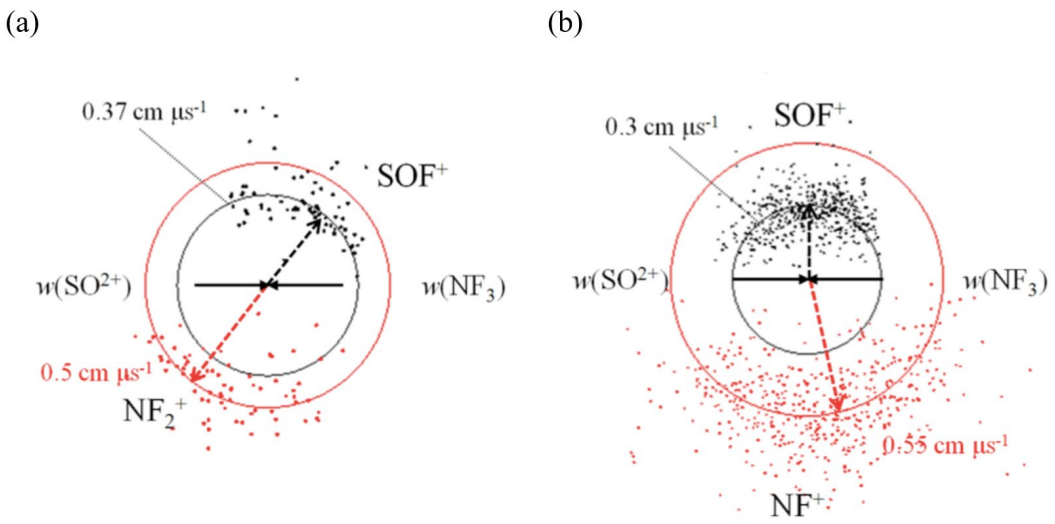

Figure 5.6 CM scattering diagrams for the two reaction channels that show evidence of bond-forming reactivity following SO^{2+}/NF_3 collisions. (a) shows the scattering of the product ions SOF^+ and NF^+, and (b) shows the scattering of the product ions NF_2^+ and SOF^+. See text for details.

The kinematics of reaction 5.11 can be explored further by examining an internal frame scattering diagram that shows the velocity vectors of the NF^+ and F products relative to the SOF^+ product ion velocity, as shown in Figure 5.7. The NF^+ product ion is backscattered away from the SOF^+ ion due to the repulsion between the two cations. The neutral F fragments isotropically around the collision centre. This scattering suggests that the complex dissociated into the detected monocations in one step: a coulombic explosion giving the detected products and the neutral F fragment. If the dissociation of the complex was sequential we would observe markedly different scattering in the internal frame. Indeed, if the reaction produced $SOF^+ + NF_2^+$ followed by a dissociative step, we would see the NF^+ and F fragments dissociating around a point backscattered away from the CM collision centre, as shown in Figure 5.4.

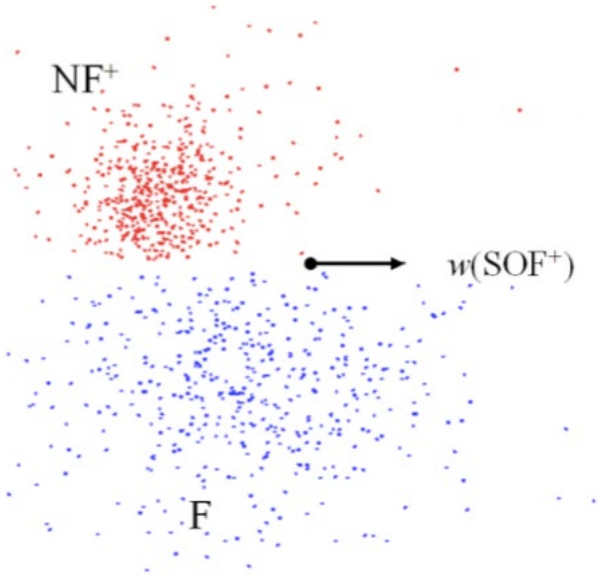

Figure 5.7 Internal scattering diagram that shows the velocity vectors of the products NF+ and F, relative to the SOF+ product ion velocity. The CM collision centre is marked by a circle. See text for details.

We have unambiguously identified, and rationalized, two different reaction mechanisms by which these bond-forming reactions occurred based on data extracted from the coincidence spectra recorded following SO^{2+}/NF_3 collisions at E_{cm} = 7.75 eV. One involves the formation of a collision complex, and the other involves the rapid stripping of a fluoride ion at large interspecies separations. The two reactions are detailed in equations 5.13 and 5.14.

$$SO^{2+} + NF_3 \rightarrow SOF^+ + NF_2^+ \qquad 5.13$$

$$SO^{2+} + NF_3 \rightarrow [SO\text{-}NF_3]^{2+} \rightarrow SOF^+ + NF^+ + F \qquad 5.14$$

5.3.5 SO^{2+}+ C_2F_6

Collisions between $SO^{2+}$and C_2F_6 were carried out at E_{cm} = 7.46 eV. The resultant coincidence mass spectrum showed evidence of five different reactions channels. The two most intense pairs peaks in the spectrum correspond to dissociative SET reactions. In both SET reactions, one of the nascent monocations formed dissociates following the ET step. Present, but

with a lower intensity compared to the SET reactions, are three pairs peaks that correspond to the detection of an SOF^+ ion in coincidence with various product ions; the spectrum shows evidence of the fluorination of the SO^{2+} dication. Table 5.3 details the different product ion pairs detected in the coincidence mass spectrum and the branching ratio, *R*, for each.

Table 5.3 The product ions formed following collisions between SO^{2+} and C_2F_6, at a collision energy of 7.46 eV. The reaction type and branching ratios into each channel are presented.

Reaction Type	Detected products	R %
SET	$SO^+ + C_2F_5^+$	50.0
SET	$SO^+ + CF_3^+$	45.5
Bond-forming	$SOF^+ + CF_3^+$	3.3
Bond-forming	$SOF^+ + C_2F_4^+$	0.7
Bond-forming	$SOF^+ + C_2F_5^+$	0.5

5.3.6 Electron transfer reactivity

We see two SET pairs peaks in the coincidence mass spectrum recorded following collisions between SO^{2+} and C_2F_6; two possible reactions schemes that outline the reactivity observed are given below.

$$SO^{2+} + C_2F_6 \rightarrow SO^+ + C_2F_5^+ + F \qquad 5.15$$

$$SO^{2+} + C_2F_6 \rightarrow SO^+ + CF_3^+ + \text{neutrals} \qquad 5.16$$

There as several possible neutral fragments that may form alongside the detected product monocations detailed in reaction 5.16, which will be discussed later in this chapter.

Generally, as mentioned above, SET reactions usually occur *via* a direct mechanism. That is, a mechanism where the reactants approach each

other, an electron rapidly transfers from the neutral to the dication, and the resulting monocations separate. After the ET step, the product ions may dissociate further into a monocation and neutral fragments. To gain insight into the precise kinematics of these SET reactions, the CM scattering diagrams for each channel are explored below.

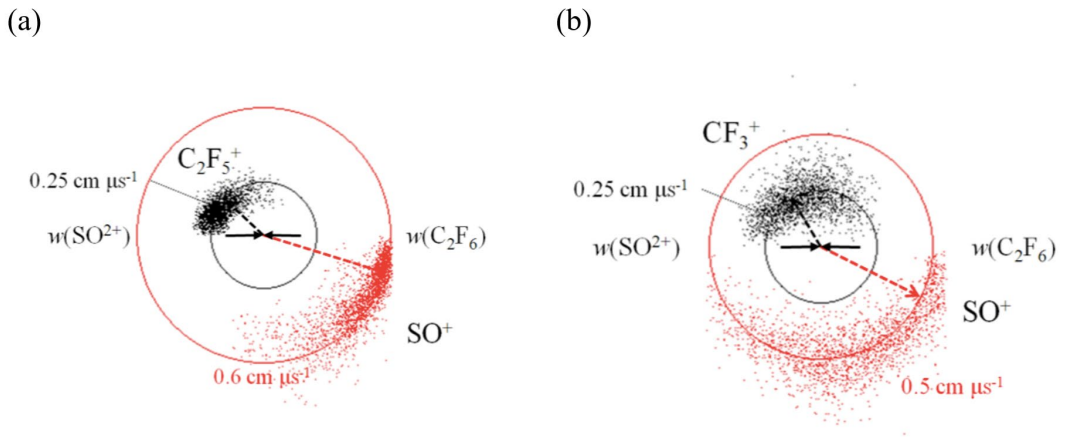

Figure 5.8 CM scattering diagrams for the two dissociative SET reaction channels. (a) shows the scattering of the product ions SO^+ and $C_2F_5^+$, and (b) shows the scattering of the product ions CF_3^+ and SO^+. See text for details.

The CM scattering diagram for reaction 5.15 (Figure 5.8, a) shows strong forward scattering of the product ions relative to the initial trajectory of their respective reactant species. Indeed, the velocity vectors of the products are clearly orientated to the velocities of the reactants.

To further investigate the dynamics of reaction 5.15 we have constructed an internal frame scattering diagram, which maps the scattering of the $C_2F_5^+$ ions and F neutral fragments relative to the SO^+ product velocity in the CM frame. It is clear from Figure 5.9 that the $C_2F_5^+$ ion back scatters relative to the SO^+ product ion velocity, as expected due to the repulsion between two monocations. Using the principle of the conservation of momentum, the velocity of the neutral F fragment has been determined (blue, Figure 5.9). The neutral body appears to scatter isotropically around the collision centre, which suggests that the $(C_2F_6^+)^*$ precursor product ion dissociates rapidly, and on the same time scale as the ET step.

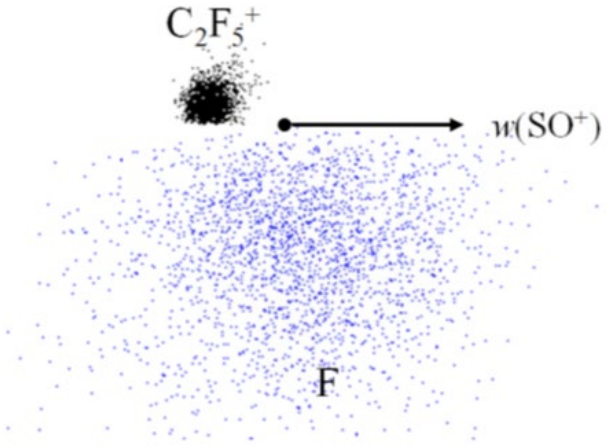

Figure 5.9 Internal frame scattering diagram that shows the scattering of the $C_2F_5^+$ and F products relative to the velocity vector of the SO^+ product. The circle marks the collision centre of the reaction. See text for details.

Figure 5.8 (b) shows the CM scattering of the products of reaction 5.16. Like the scattering displayed in Figure 5.8 (a), the products are somewhat correlated to their respective reactant species trajectories. However, the velocity vectors of the product ions are less strongly aligned to reactant velocity and show a degree of isotropy. The scattering displayed in Figure 5.8 (b) suggests that the reactants may have associated to form a transitory $[SO\text{-}C_2F_6]^{2+}$ complex. This complex then dissociated to give the detected products.

In the mechanism proposed above, the lifetime to dissociation of a $[SO\text{-}C_2F_6]^{2+}$ complex would affect the product ion scattering motifs in a CM scattering diagram. If a complex has a lifetime to dissociation that is less than the time taken to complete a full rotation, the CM scattering diagram would show a degree of correlation between the product ion trajectories and their respective reactant velocity vectors. Conversely, if the lifetime of the species was greater than the time taken for a full rotation of the complex, the product ions would be scattered isotropically around the reaction centre, as seen for reaction 5.14. The scattering of the product ions in in Figure 5.8 (b) could be described as isotropic, with a degree of correlation between the product and reactant velocity vectors. Therefore, we suggest that a degree of

short lived association gave rise to the scattering observed in the figure. Unfortunately, this reaction produces many neutral fragments, which we cannot unambiguously identify and partition momenta into each. Therefore, we are unable to construct internal frame scattering diagrams to explore the dynamics of this channel further.

Table 5.4 Literature exothermicities for the reaction between SO^{2+} (X $^1\Sigma^+$/A $^3\Sigma^+$) + C_2F_6 $\rightarrow SO^+$ (X $^2\Pi$ /A $^4\Pi$ /B $^4\Sigma$) + $C_2F_6^+$ in its ground and first excited electronic state. Cross-sections to SET calculated using RW theory are given in parentheses for exothermic reactions.

		Electronic state SO^+		
SO^{2+}	$C_2F_6^+$	X $^2\Pi$	A $^4\Pi$	B $^4\Sigma$
X $^1\Sigma^+$	X ^{1}A	-6.5 (13.35)	-3.3 (0.9)	-2.41 (~0)
	A	-3.5 (12.4)	-0.3 (~0)	+0.59
A $^3\Sigma^+$	X ^{1}A	-9.95 (0.72)	-6.75 (10.2)	-5.86 (1.4)
	A	-6.95 (9.5)	-3.75 (1.32)	-2.86 (~0)

As discussed previously, SO^{2+} has two excited electronic states ($^3\Sigma^+$ and $^3\Delta$) that lie 3.45 and 6.74 eV above the ground state (X $^1\Sigma^+$) respectively.[41] Due to the excess energy associated with electron ionization with 150 eV electrons, the SO^{2+} dications in our beam may be present in any of these low lying excited electronic states. The reactant C_2F_6 neutral molecules are admitted to the PSCO apparatus *via* an effusive jet, and so we can assume that all C_2F_6 reactants are participating in collisions are in the ground electronic state.

The literature exothermicities for the different combinations of reactant and product states that could lead to the products detected in channels 5.15 and 5.16 have been determined. The ground and first two excited electronic states have been considered for SO^+ and the ground and first excited electronic state has been considered for SO^{2+}.[41, 47] Due to the limited

available data in the literature pertaining to the energetics of the excited states of $C_2F_6^+$, only the ground and first excited state of $C_2F_6^+$ have been considered.[25, 48, 49]

TPEPICO experiments have found that the ground and first excited electronic states of $C_2F_6^+$ are dissociative. The ground state of the $C_2F_6^+$ ion dissociates to form exclusively $C_2F_5^+$ ions.[25] The first excited state of $C_2F_6^+$ dissociates to form only CF_3^+ions. Comparing our results to this photoionization data will enable us to rationalize our observations.

The exothermicity derived from the 3-body KER associated with channel 5.15 peaks is -5.6 eV. The ground state literature exothermicity for this channel is -3.7 eV, which suggests that the products are formed with ~2 eV distributed between them.

This channel has a high branching ratio: 50% of the reactive events following C_2F_6/SO^{2+} collisions formed the products detected in this channel. Therefore, SET must be efficient between the product and reactant electronic states involved in this reaction. Table 5.4 shows the RW cross-sections to SET determined using LZ theory. The TPEPICO data states that Franck-Condon-region of the ground electronic state of $(C_2F_6^+)^*$dissociates to give $C_2F_5^+$. Considering the RW cross-sections and the TPEPICO data, the reaction that describes this channel fully is detailed below.

$$SO^{2+}\ (X\ ^1\Sigma^+) + C_2F_6 \rightarrow SO^+\ (X\ ^2\Pi) + C_2F_6^+\ (X\ ^1A) \qquad 5.17$$

$$C_2F_6^+\ (X\ ^1A) \rightarrow C_2F_5^+ + F$$

There are several possible neutral fragments that may form alongside the detected monocations in reaction 5.16, which are detailed below alongside the literature exothermicities for each.

-5.3 eV $SO^{2+} + C_2F_6 \rightarrow SO^+ + CF_3^+ + CF_3$ 5.18

-1.5 eV $SO^{2+} + C_2F_6 \rightarrow SO^+ + CF_3^+ + CF_2 + F$ 5.19

+3.8 eV $SO^{2+} + C_2F_6 \rightarrow SO^+ + CF_3^+ + CF + 2F$ 5.20

+2.2 eV $SO^{2+} + C_2F_6 \rightarrow SO^+ + CF_3^+ + CF + F_2$ 5.21

+9.5 eV $SO^{2+} + C_2F_6 \rightarrow SO^+ + CF_3^+ + C + 3F$ 5.22

-1.2 eV $SO^{2+} + C_2F_6 \rightarrow SO^+ + CF_3^+ + C + F_2 + F$ 5.23

The reactions that are endothermic can be discounted as possible fragmentation patterns for reaction 5.16, which leaves reactions 5.18, 5.19 and 5.23. The exothermicity derived from the 3-body KER associated with this channel is -3.43 eV, which excludes reactions 5.19 and 5.23. Therefore, reaction 5.18 describes this reaction channel, where the products form with ~2 eV of internal energy distributed between them.

The ground state literature exothermicity for this channel is -5.3 eV. LZ theory states that the products of SET form with an exothermicity of 2-6 eV. Therefore, we can estimate that the precursor product ions, SO^+ and $C_2F_6^+$, must form with a maximum internal energy of 0-3.3 eV. This energy may reside in one of the nascent monocations, or be distributed between them.

The TPEPICO data states that the Franck-Condon region of the first excited electronic state of $(C_2F_6^+)^*$, which lies ~ 3 eV above the ground state, dissociates to give CF_3^+. Therefore, it is likely that this channel proceeds *via* a reaction where the $C_2F_6^+$ (*A*) excited electronic state potential is populated in its Franck-Condon region, and dissociates to give CF_3^+, as shown in reaction 5.24.

$$SO^{2+} + C_2F_6 \rightarrow SO^+ + C_2F_6^+ (A) \quad 5.24$$

$$\text{Then } C_2F_6^+ (A) \rightarrow CF_3^+ + CF_3$$

This channel has the second highest branching ratio following collisions between SO^{2+} and C_2F_6, therefore, we expect that SET is efficient between the reactant species involved in this reaction. Upon inspection of Table 5.4, it is clear that the following reaction has the largest RW cross-section to SET involving the $C_2F_6^+$ (*A*) electronic state, and is therefore likely to describe the reaction by which CF_3^+ and SO^+ pairs in the coincidence spectra were formed.

The electron transfer and bond-forming reactions of SO^{2+}

$$SO^{2+}\ (X\ ^1\Sigma^+) + C_2F_6 \rightarrow SO^+\ (X\ ^2\Pi) + C_2F_6^+\ (A) \qquad 5.25$$

Then $C_2F_6^+\ (A) \rightarrow CF_3^+ + CF_3$

5.3.7 Bond-forming reactivity

We see three reactions that form product ions with new chemical bonds in the coincidence spectra recorded following SO^{2+}/C_2F_6 collisions at E_{cm} = 7.46 eV, which are described below.

$$SO^{2+} + C_2F_6 \rightarrow SOF^+ + C_2F_5^+ \qquad 5.26$$

$$SO^{2+} + C_2F_6 \rightarrow SOF^+ + C_2F_4^+ \qquad 5.27$$

$$SO^{2+} + C_2F_6 \rightarrow SOF^+ + CF_3^+ \qquad 5.28$$

As above, we can use Herman's simple electrostatic model, outlined in section 5.3.4, to rationalize these bond-forming reactions.

The CM scattering diagrams, derived from the coincidence data, for each of the pairs peaks outlined above are given in Figure 5.10. Upon inspection, there are some clear similarities and differences between the product ion scattering distributions around the CM collision centre for reactions 5.26-5.28. Figure 5.10 (a) shows the scattering of the $C_2F_4^+$ and SOF^+ product ions following SO^{2+}/C_2F_6 collisions at E_{cm} = 7.46 eV. The product ions are scattered isotropically around the collision centre, showing no correlation to reactant velocity. As discussed previously, this scattering implies that the reactant species associated into a transitory species that had a lifetime to dissociation that was markedly greater than the time taken for a complete rotation of the complex.

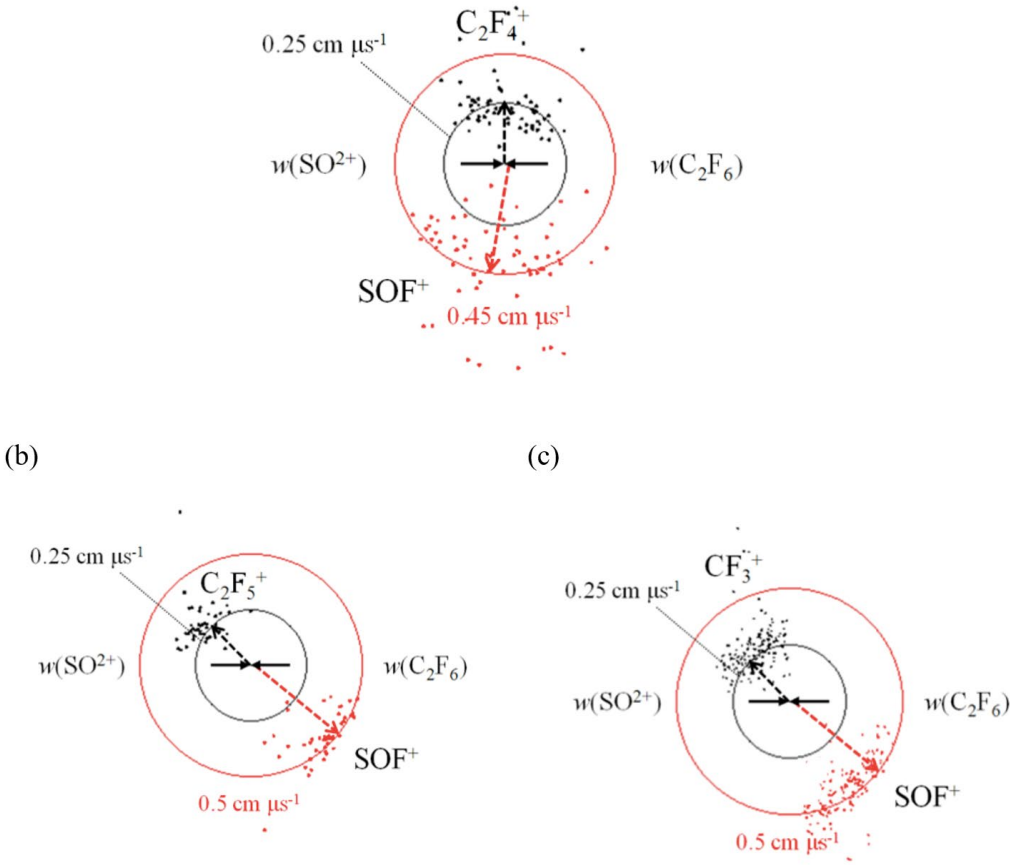

Figure 5.10 CM scattering diagrams for the three reactions that exhibit bond forming reactivity. (a) shows the scattering of the product ions SOF^+ and $C_2F_4^+$, (b) shows the scattering of the product ions $C_2F_5^+$, and SOF^+ and (c) shows the scattering of the product ions SOF^+ and CF_3^+. See text for details.

In contrast, diagrams (b) and (c), which correspond to the formation of ions pairs $C_2F_5^+ + SOF^+$ and $CF_3^+ + SOF^+$ respectively, show product ions that are broadly forward scattered relative to reactant trajectory. That is, the product ion velocity vectors show a clear correlation to their respective reactant trajectories. Such scattering indicates that the product ions were formed *via* a direct mechanism where the reactant species interacted only relatively briefly. Indeed, this scattering suggests that reactions 5.26 and 5.27 occur *via* a mechanism similar to ET: a fluoride ion is rapidly stripped from the neutral at large interspecies separations, as seen previously elsewhere and explored further below.[30]

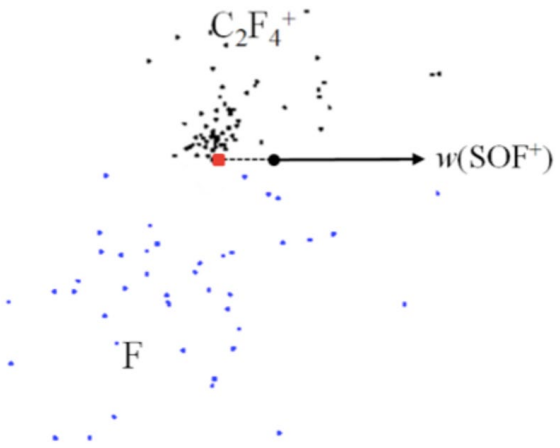

Figure 5.11 Internal frame scattering diagram that shows the scattering of product ions $C_2F_4^+$ and F relative to the SOF^+ velocity vector. The fragment ions displayed scatter around a point that is backscattered from the collision centre, demarcated by the red square. See text for details.

An internal frame scattering diagram has been constructed to investigate the dynamics of reaction 5.27. Figure 5.11 shows the scattering of $C_2F_4^+$ and F relative to the SOF^+ product ion velocity in the CM frame. The fragment ions appear to scatter around a point that is back scattered from the collision centre, which is shown by the red square in the figure. This scattering indicates that the $[SO\text{-}C_2F_6]^{2+}$ collision complex initially dissociated to form SOF^+ and $(C_2F_5^+)^*$, and the $(C_2F_5^+)^*$ precursor monocation went onto dissociate into the detected $C_2F_4^+$ and neutral F fragment. Using the principle of conservation of momentum, the velocity of the $C_2F_5^+$ precursor has been determined to be 0.26 eV.

The CM scattering diagrams extracted from the coincidence data have provided insight into the reaction dynamics that describe the bond-forming reactivity between the C_2F_6 and SO^{2+}. We have observed that $C_2F_5^+$ and SOF^+ ions can be formed *via* a direct mechanism, in which the SO^{2+} rapidly strips a fluoride ion from the neutral C_2F_6 molecule, or by a mechanism

where an $[SO\text{-}C_2F_6]^{2+}$ complex forms and dissociates to give a species with new chemical connectivity, SOF^+. The $C_2F_5^+$ ion formed *via* complexation dissociates to give $C_2F_4^+$ and F. The strong anisotropy of the product ions in Figure 5.10 (b) indicates that all $C_2F_5^+$ molecules detected in coincidence with SOF^+ were generated *via* the direct mechanism described above. It follows that any $C_2F_5^+$ ions formed *via* complexation must dissociate to form $C_2F_4^+$. Using the CM scattering diagrams, we can assign each bond-forming channel 5.26-5.28 to the reactions 5.29, 5.30 and 5.31 respectively.

$$SO^{2+} + C_2F_6 \rightarrow SOF^+ + C_2F_5^+ \qquad 5.29$$

$$SO^{2+} + C_2F_6 \rightarrow [SO\text{-}C_2F_6]^{2+} \rightarrow SOF^+ + C_2F_5^+ \qquad 5.30$$

$$\text{Then} \quad C_2F_5^+ \rightarrow C_2F_4^+ + F$$

$$SO^{2+} + C_2F_6 \rightarrow SOF^+ + CF_3^+ \qquad 5.31$$

5.3.8 SO^{2+} and SF_6

Collisions between SO^{2+} and SF_6 were carried out at E_{cm} = 6.02 eV. The resultant coincidence mass spectrum contains pairs peaks that correspond to six different chemical reactions: 3 SET and 3 bond-forming reactions. Each of the bond-forming reactions involved the fluorination of the SO^{2+} dication. The different pairs of product monocations detected in coincidence, and the corresponding branching ratios into each reaction channel, are given below.

SO^{2+}/SF_6 collisions result mainly in SET, accounting for 95.4 % of the ions detected. Indeed, as expected most dication-neutral collisions resulted in the transfer of an electron from the neutral to the dipositively charged species. The products of SO^{2+} fluorination make a small but non-negligible contribution to the overall ion yield.

Table 5.5 The product ions formed following collisions between SO^{2+} and SF_6, at a collision energy of 6.02 eV. The reaction type and branching ratios into each channel are presented.

Reaction Type	Detected products	*R* %
SET	$SO^+ + SF_5^+$	90.3
SET	$SO^+ + SF_4^+$	3.1
SET	$SO^+ + SF_3^+$	2.0
Bond-forming	$SOF^+ + SF_5^+$	2.2
Bond-forming	$SOF^+ + SF_4^+$	0.7
Bond-forming	$SOF^+ + SF_3^+$	1.7

5.3.9 Single electron transfer

The three pairs of product monocations produced following SET reactions between SO^{2+} and SF_6 are detailed below.

$$SO^{2+} + SF_6 \rightarrow SO^+ + SF_5^+ + F \qquad 5.32$$

$$SO^{2+} + SF_6 \rightarrow SO^+ + SF_4^+ + 2F/F_2 \qquad 5.33$$

$$SO^{2+} + SF_6 \rightarrow SO^+ + SF_3^+ + 3F/(F + F_2) \qquad 5.34$$

There are two possible combinations of neutrals that may form alongside the product ions detected in channels 5.33 and 5.34. Later in this section, we will determine which neutrals are likely to be formed in reaction 5.33 by comparing the literature enthalpies of formation of each possible reaction with the exothermicity derived from the measured 3-body KER associated with this channel. Unfortunately, this method cannot be adopted for channel 5.34 as more than three product species form. Therefore, we cannot use the experimentally measured 3-body KER to determine the likely identities of the neutral products formed.

As mentioned previously, the characteristic mechanism for SET reactivity between a dication and a neutral is one where the reactants interact very briefly, and at large interspecies separations.[15] In this mechanism the reactant species approach each other, an electron transfers when they are relatively far apart, and the product monocations separate largely unperturbed from their reactant trajectories. For reactions 5.32-5.34, the SET step is followed by the dissociation of the $(SF_6^+)^*$ nascent product monocation. CM scattering diagrams have been constructed to investigate the exact dynamics of the three reactions outlined above.

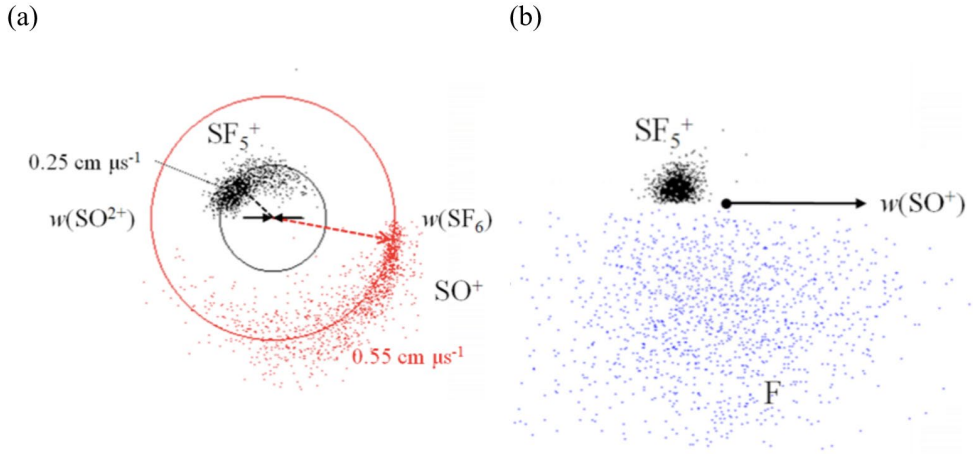

Figure 5.12 (a) - CM scattering diagram that shows the scattering of SO^+ and SF5+. (b) - Internal frame scattering diagram, where the scattering of SF_5^+ and F are plotted relative to the SO^+ ion velocity. See text for details.

The CM scattering diagram for reaction 5.32 is shown in Figure 5.12 (a) and displays strong forward scattering of the product ions. That is, $w(SO^+)$ is orientated to the velocity of the SO^{2+} dication, and likewise $w(SF_5^+)$ is correlated to the initial velocity vector of SF_6. Such scattering is typical of SET reactions and indicates a reaction that follows the scheme outlined above: the ET occurs rapidly and in a single step at interspecies separations between 2-7 Å.[50] To further investigate the dynamics of reaction 5.32 we have constructed an internal frame scattering diagram, displayed in Figure 5.12 (b). The diagram shows the scattering of SF_5^+ and F relative to the velocity vector of SO^+, which is depicted by the filled arrow in the figure. The

collision centre is shown by the filled circle. It is clear upon inspection that the SF_5^+ ion is backward scattered relative to the SO^+, which is expected owing to the coulombic repulsion between the two product monocations. The F neutral appears to be scattered isotropically around the collision centre, which indicates that the F fragment dissociated from the SF_6^+ nascent product ion in the same time frame as the ET step.

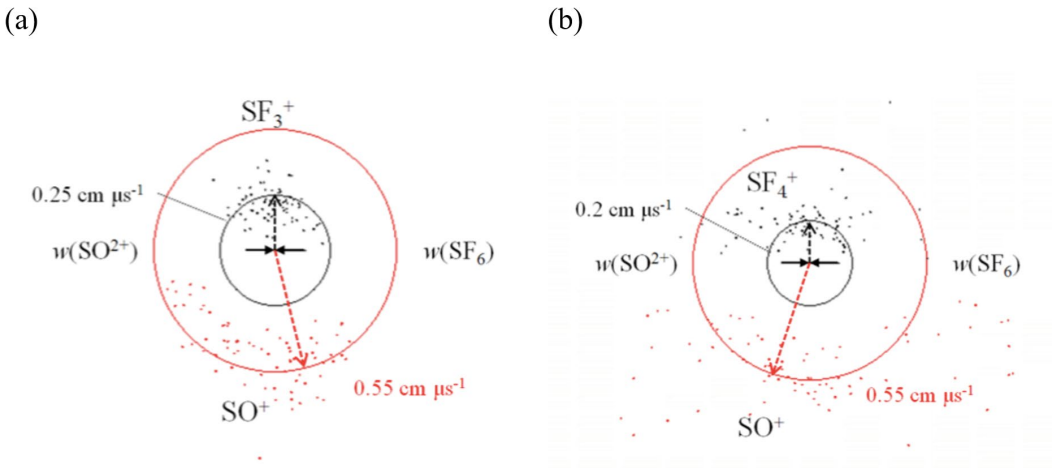

Figure 5.13 CM scattering diagrams that show the scattering of the products of SET around the SO^{2+}/ SF_6 reaction collision centre. The product ion pairs shown are SO^+ with SF_4^+ (a) and SF_3^+ (b). See text for details.

The CM scattering diagrams for reactions 5.34 and 5.33 are shown in Figure 5.13 (a) and (b) respectively, and clearly display a different scattering pattern compared to channel 5.32. In addition to being less intense, the scattering of the product ions shown in both Figure 5.13 (a) and (b) is relatively isotropic. That is, the scattering of each product ion shows no correlation to the velocity vector of their respective reactant species. Such displayed isotropy, as previously discussed, implies that the reactant species for these SET reactions associated together to form a transitory collision complex, which rotated at least once before dissociating into the detected monocations.

The reaction mechanism outlined above can be rationalized by considering Herman's electrostatic model, outlined in Figure 5.5. When a

dication approaches a neutral, the potential is dominated by the polarization attraction between the two species. Several PECs cross this 'entrance channel' that would result in direct SET. If the system avoids crossing onto one of these ET curves, the reactants can associate to form a collision complex, in this case $[SO\text{-}SF_6]^{2+}$. To explain the products of reactions 5.33 and 5.34, this proposed complex would back-dissociate along the same reaction coordinate and the system would then cross onto a PEC that leads to SET. If the collision complex completed one or more rotations, the product monocations formed following SET would have no 'memory' of their reactant trajectories. That is, the scattering in the CM diagram would be isotropic around the collision centre, as seen for reactions 5.33 and 5.34. Thus, the scattering observed in Figure 5.13 suggests that the product of these two reaction channels dissociated from an $[SO\text{-}SF_6]^{2+}$ collision complex. This type of reaction mechanism is not often seen following dication-neutral collisions, however it is predicted by the Herman model.

To gain further insight into the relevant SET reaction mechanisms, the energetics of channels 5.32-5.34 have been explored. As mentioned above, we can determine the exothermicity of a reaction channel by subtracting the E_{cm} from the measured 2- or 3-body KER associated with the separation of the detected monocations. Comparing this experimentally derived energy release to the ground state literature exothermicity for a reaction indicates whether the reactant and product species involved in the ET reaction were present in excited electronic states.

Reaction 5.32 is a three-body reaction, therefore comparing the exothermicity derived from the 3-body KER to the literature enthalpy can give an indication of the electronic states involved in this reaction. However, we cannot unambiguously know the identity of the neutrals formed in reactions 5.33 and 5.34 from the coincidence data.

The two possible combinations of products that may form in reaction 5.33 are outlined below.

$$SO^{2+} + SF_6 \rightarrow SO^{+} + SF_4^{+} + F_2 \qquad 5.35$$

$$SO^{2+} + SF_6 \rightarrow SO^{+} + SF_4^{+} + 2F \qquad 5.36$$

Reaction 5.35 forms 3 product species and has an enthalpy of formation of -1.9 eV. The exothermicity derived from the measured 3-body KER for this channel is -4.33 eV. The measured exothermicity is greater than the ground state literature enthalpy, therefore this reaction did not occur *via* this mechanism. Thus, by conservation of mass, we can deduce that 2F atoms form alongside the detected monocations for this channel. As such, we cannot explore the energetics of this channel any further.

Table 5.6 Literature exothermicities for the reaction between SO^{2+} ($X\ ^1\Sigma^+/A\ ^3\Sigma^+$) + $SF_6 \rightarrow SO^+$ ($X^2\Pi$ /A $^4\Pi$ /B $^4\Sigma$) + SF_6^+ in its ground and first 4 excited states. Thermochemical data taken from references Cross section to SET calculated using RW theory is given in parentheses for exothermic reactions.

		Electronic state SO^+		
SO^{2+}	SF_6^+	$X^2\Pi$	A $^4\Pi$	B $^4\Sigma$
X $^1\Sigma^+$	X $^2T_{1g}$	-4.67 (21.9)	-7.87 (0)	-9.31 (0)
	A $^2T_{1u}$	-4.49 (21.6)	-7.69 (0)	-9.13 (0)
	B $^2T_{2u}$	-3.29 (13.6)	-6.49 (0)	-7.93 (0)
	C ^2E_g	-1.99 (0.1)	-5.19 (0)	-6.63 (0)
	D $^2T_{2g}$	-0.79 (0)	-3.99 (10.1)	-5.43 (0)
A $^3\Sigma^+$	X $^2T_{1g}$	-8.17 (14.12)	-11.78 (0)	-13.22 (0)
	A $^2T_{1u}$	-7.99 (14.7)	-11.6 (0)	-13.04 (0)
	B $^2T_{2u}$	-6.79 (19.1)	-10.4 (0)	-11.8 (0)
	C ^2E_g	-5.49 (25.49)	-9.1 (0)	-10.54 (0)
	D $^2T_{2g}$	-4.29 (22.7)	-7.9 (0)	-9.34 (0)

.

Two possible combinations of products may form for channel 5.34, which are outlined below.

$$SO^{2+} + SF_6 \rightarrow SO^{+} + SF_3^{+} + F_2 + F \qquad 5.37$$

$$SO^{2+} + SF_6 \rightarrow SO^{+} + SF_3^{+} + 3F \qquad 5.38$$

Unfortunately, neither reaction outlined above is two- or three-body, therefore we cannot compare the experimentally derived exothermicity for this channel to their literature enthalpies of formation. Thus, we cannot explore the energetics of this channel further.

The energetics of reaction 5.32, which is a 3-body reaction, are explored below. TPEPICO data, found in the literature, states that all low-lying excited electronic states of $(SF_6^{+})^{*}$ are dissociative. In fact, even the ground electronic state SF_6^{+} ($X\ ^2T_{1g}$) is unstable to dissociation to form SF_5^{+}. Likewise, the first two excited electronic states of SF_6^{+} dissociate to form SF_5^{+}. SF_6^{+} ($C\ ^2E_g$) and SF_6^{+} ($D\ ^2T_{2g}$) are unstable to dissociation to both SF_4^{+} and SF_3^{+}. SF_6^{+} ($E\ ^2T_{1u}$) ions dissociate to form SF_2^{+} and SF_6^{+} ($F\ ^2A_{1g}$) ions dissociate to form SF^{+}. Comparing our data to these TPEPICO results has enabled us to disentangle which electronic states are formed following low energy SO^{2+} collisions with SF_6.

Reaction 5.32 has an experimentally derived exothermicity of -5.1 eV. The ground state literature enthalpy for this reaction is -4.8 eV. RW theory states that the products of SET reactions form with an exothermicity of 2-6 eV. Therefore, we can estimate that the precursor product ions, SO^{+} and SF_6^{+}, must form with a maximum internal energy of 0-3eV. This energy may reside in one of the nascent monocations, or be distributed between them.

Table 5.6 shows literature enthalpies for possible combinations of electronic states that may be involved in this reaction. The SF_6 reactant molecules are admitted to the PSCO apparatus through an effusive jet, therefore the neutrals are assumed to be present in their ground electronic state prior to reaction. The SO^{2+} dication may be present in the beam in either of its first two low lying electronic states, ($X\ ^1\Sigma^{+}$, $A\ ^3\Sigma^{+}$).

The ground and first excited electronic states of SF_6^+ are between 0-3 eV above the electronic ground state. The TPEPICO data states that the Franck-Condon region of these electronic states dissociate to give SF_5^+. This reaction has the highest branching ratio for this reaction channel. Therefore, we expect that SET is efficient between the reactants. Table 5.6 shows the different combinations of electronic states that may be involved in this reaction, alongside the RW cross-section to SET for each. The reactions with the highest cross-sections to SET involve the formation of SF_6^+ ($X\ ^2T_{1g}$) and SF_6^+ ($A\ ^2T_{1u}$). Therefore, we can deduce that the following reactions probably describe the electronic states involved in this reaction.

$$SO^{2+}\ (X\ ^1\Sigma^+) + SF_6 \rightarrow SO^+\ (X^2\Pi) + SF_6^+\ (X\ ^2T_{1g}) \qquad 5.39$$

$$SO^{2+}\ (X\ ^1\Sigma^+) + SF_6 \rightarrow SO^+\ (X^2\Pi) + SF_6^+\ (A\ ^2T_{1u}) \qquad 5.40$$

5.3.10 Bond-forming reactivity

Three pairs peaks in the coincidence mass spectrum recorded following SO^{2+}/SF_6 collisions at E_{cm} = 6.02 eV showed evidence of bond-forming reactivity, which are detailed below.

$$SO^{2+} + SF_6 \rightarrow SOF^+ + SF_5^+ \qquad 5.41$$

$$SO^{2+} + SF_6 \rightarrow SOF^+ + SF_4^+ + F \qquad 5.42$$

$$SO^{2+} + SF_6 \rightarrow SOF^+ + SF_3^+ + 2F \qquad 5.43$$

Figure 5.14 (a) shows the CM scattering diagram constructed for reaction 5.41. There is clear anisotropy in the displayed scattering of the product ions: the velocity vectors of the products are correlated to the nascent trajectory of their respective reactant species prior to collision. Such forward scattering, as described previously, is indicative of a direct mechanism in which the reactant species interact only very briefly. Indeed, such a scattering pattern implies a reaction mechanism where the reactants approach, a fluoride ion is stripped from the neutral at large interspecies separations and the products separate, leaving the resultant monocations relatively unperturbed from the trajectory of the reactant species. As

previously discussed, such a direct mechanism is relatively atypical for bond-forming reactions between dications and neutrals, which usually yield new chemical connections *via* the formation of a collision complex.[9, 51] However, such reactivity has been seen previously in hydride transfer reactions between dications and small, organic molecules.[12]

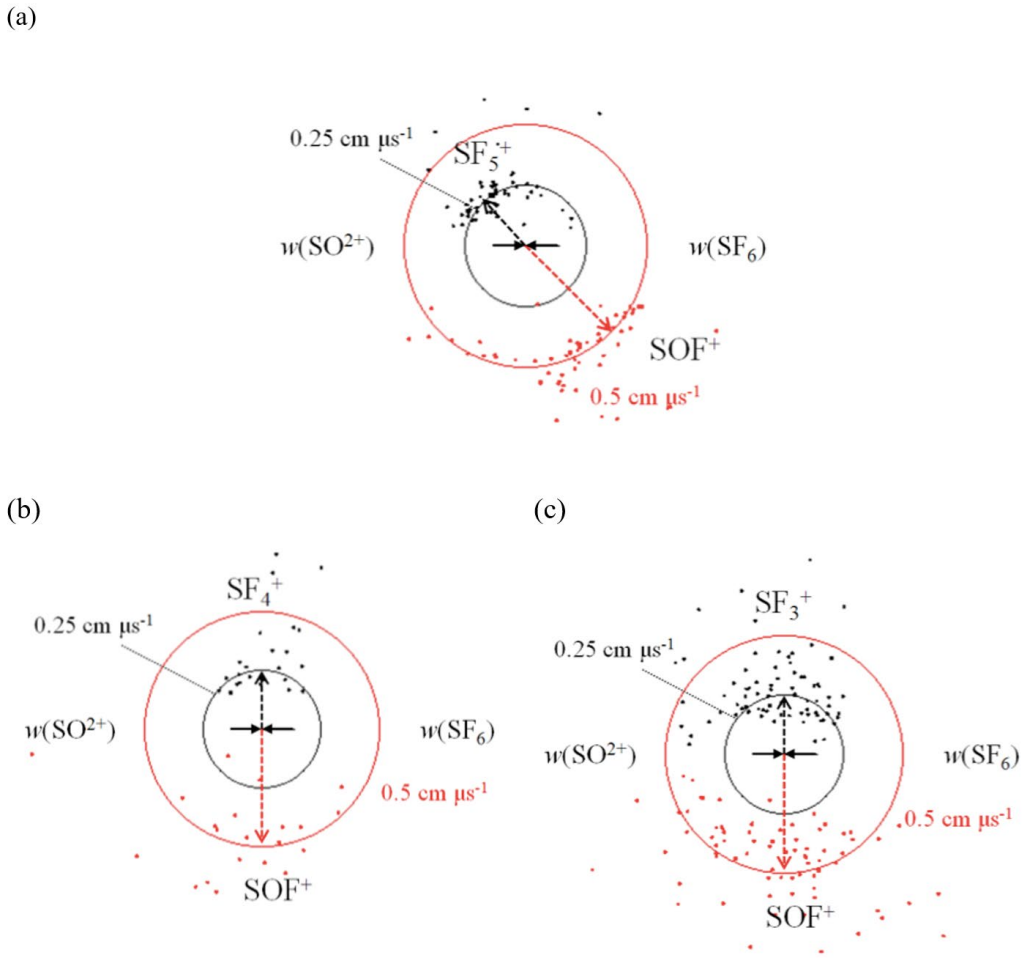

Figure 5.14 CM scattering diagrams for the three reactions that exhibit bond forming reactivity. (a) shows the scattering of the product ions SOF^+ and SF_5^+, (b) shows the scattering of the product ions SF_4^+, and SOF^+ and (c) shows the scattering of the product ions SOF^+ and SF_3^+. See text for details.

Figure 5.14 (b) and (c) shows the CM scattering diagrams for reactions 5.42 and 5.43 respectively. Both diagrams display isotropic scattering of the product ions around the collision centre. That is, the product ions show no correlation to their respective reactant velocity vectors. As previously discussed, this type of scattering is indicative of the association of

the reactant species into a transitory collision complex, $[SO\text{-}SF_6]^{2+}$. The complex then dissociates along a different reaction coordinate, leading to the formation of new chemical connection: a bond forming reaction has occurred. In the exit channel of the PES the collision system is likely to undergo SET producing two monocations. Prior to dissociation, the complex may have undergone at least one full rotation. If so, the product monocations scatter isotropically around the collision centre and any orientation between reactant and product ion trajectory would be lost, as seen in Figure 5.14 (b) and (c).

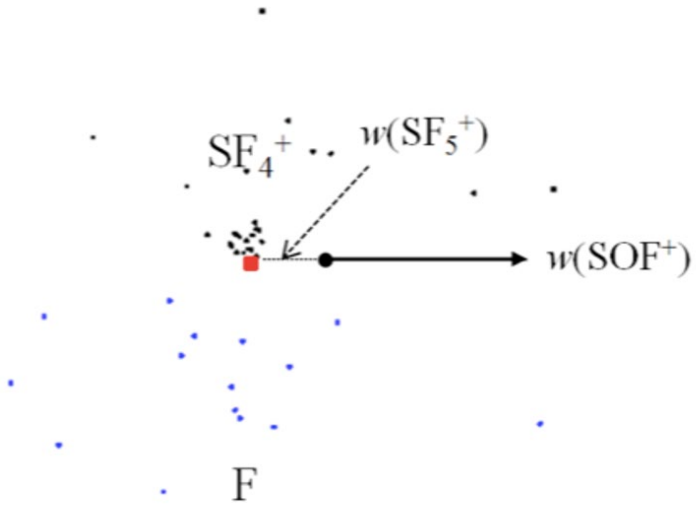

Figure 5.15 Internal frame scattering diagram that shows the scattering of products SF_4^+ and F relative to SOF^+ velocity. The products are clearly isotropically scattered around a point (red square) that is back scattered away from the collision centre (black circle). See text for details.

The dynamics of reaction 5.42 can be further investigated using an internal frame scattering diagram. Figure 5.15 shows the products SF_4^+ and F scattering relative to the velocity of the SOF^+ product ion. The scattering implies the SF_4^+ and F fragments separating around a point that is backscattered away from the collision centre, shown by a red dot in the figure. This scattering suggests that the complex did not dissociate in one step to form $SOF^+ + SF_4^+ + F$, but rather it dissociated *via* a two-step,

sequential process. Owing to the conservation of mass, the intermediate separation must be one in which SF_5^+ is formed, followed by a further dissociation into $SF_4^+$and F. Using the principle of the conservation of momentum, the velocity of the nascent precursor SF_5^+ ion has been determined to be 0.25 cm μs^{-1}. Given the low number of counts for this channel, we can only tentatively state that this reaction occurs *via* the reaction scheme given below.

$$SO^{2+} + SF_6 \rightarrow [SO\text{-}SF_6]^{2+} \rightarrow SOF^+ + SF_5^+ \qquad 5.44$$

$$\text{Then } SF_5^+ \rightarrow SF_4^+ + F$$

Although we cannot unambiguously partition momenta into the neutral fragments formed following reaction 5.42, an internal frame scattering diagram constructed assuming the production of F_2 displays similar scattering to that shown in Figure 5.15. Thus, we can tentatively state that this reaction occurs *via* a similar sequential reaction mechanism.

5.4 Conclusion

We have studied the collisions of the molecular dication SO^{2+} with neutral species for the first time, using the PSCO apparatus. Reactions with NF_3, SF_6 and C_2F_6 all result in bond-forming reactions in addition to electron transfer. The observations made following these collisions can be rationalized using a simple electrostatic model of dication-neutral collisions. Electron transfer reactivity dominated each collision system, and the reactivity seen has been fully explained using a combination of CM scattering diagrams and reaction-window calculations. Some reactive channels led to SET between neutral and dication *via* an indirect mechanism, in which the reactants associated to form a complex. Additionally, some bond-forming reactive channels proceeded *via* an unusual direct mechanism in which the fluoride ion was stripped from the neutral at relatively large interspecies separations. The work in this chapter highlights that there is still a great deal to be learned about dications and the dynamics of how these reactive species interact with neutrals.

Comparing the reactions of Ar^{2+} and SO^{2+} with NF_3 and C_2F_6, there are some stark differences. There is clearly more fragmentation when Ar^{2+} collides with these neutrals compared to reactions at similar collision energies with SO^{2+}. This observation may be explained by the difference in double ionization energy potential between SO and Ar, 30 and 43.5 eV respectively. Ar has a higher double ionization energy potential, and therefore a neutral-Ar^{2+} system may be able to access more fragmentation pathways compared to the same neutral colliding with SO^{2+} with the same collision energy. To definitively make this conclusion, more experiments would be required at different comparing Ar^{2+} and SO^{2+} reactions with neutrals at different collision energies.

5.5 Bibliography

1. O. Dutuit, N. Carrasco, R. Thissen, V. Vuitton, C. Alcaraz, P. Pernot, N. Balucani, P. Casavecchia, A. Canosa, S. Le Picard, J. C. Loison, Z. Herman, J. Zabka, D. Ascenzi, P. Tosi, P. Franceschi, S. D. Price and P. Lavvas, *Astrophysical Journal Supplement Series*, 2013, **204**.

2. G. Gronoff, J. Lilensten, C. Simon, O. Witasse, R. Thissen, O. Dutuit and C. Alcaraz, *Astronomy & Astrophysics*, 2007, **465**, 641-645.

3. C. L. Ricketts, D. Schroder, J. Roithova, H. Schwarz, R. Thissen, O. Dutuit, J. Zabka, Z. Herman and S. D. Price, *Physical Chemistry Chemical Physics*, 2008, **10**, 5135-5143.

4. J. Zabka, C. L. Ricketts, D. Schroder, J. Roithova, H. Schwarz, R. Thissen, O. Dutuit, S. D. Price and Z. Herman, *Journal of Physical Chemistry A*, 2010, **114**, 6463-6471.

5. Z. Herman, *International Reviews in Physical Chemistry*, 1996, **15**, 299-324.

6. A. Ehbrecht, N. Mustafa, C. Ottinger and Z. Herman, *Journal of Chemical Physics*, 1996, **105**, 9833-9846.

7. P. Champkin, N. Kaltsoyannis and S. D. Price, *International Journal of Mass Spectrometry*, 1998, **172**, 57-69.

8. M. Manning, S. D. Price and S. R. Leone, *Journal of Chemical Physics*, 1993, **99**, 8695-8704.

9. N. Lambert, D. Kearney, N. Kaltsoyannis and S. D. Price, *Journal of the American Chemical Society*, 2004, **126**, 3658-3663.

10. P. Tosi, R. Correale, W. Y. Lu and D. Bassi, *Journal of Chemical Physics*, 1999, **110**, 4276-4279.

11. J. F. Lockyear, M. A. Parkes and S. D. Price, *Journal of Physics B-Atomic Molecular and Optical Physics*, 2009, **42**, 9.

12. M. A. Parkes, J. F. Lockyear and S. D. Price, *International Journal of Mass Spectrometry*, 2009, **280**, 85-92.

13. D. Ascenzi, P. Franceschi, P. Tosi, D. Bassi, M. Kaczorowska and J. N. Harvey, *Journal of Chemical Physics*, 2003, **118**, 2159-2163.

14. W. P. Hu, S. M. Harper and S. D. Price, *Measurement Science & Technology*, 2002, **13**, 1512-1522.

15. W. P. Hu, S. M. Harper and S. D. Price, *Molecular Physics*, 2005, **103**, 1809-1819.

16. S. D. Price, *International Journal of Mass Spectrometry*, 2007, **260**, 1-19.

17. Y. Ralchenko, A. E. Kramida and J. Reader, NIST Atomic Spectra Database, (accessed 1/12/2016, 2016).

18. J. C. Creasey, H. M. Jones, D. M. Smith, R. P. Tuckett, P. A. Hatherly, K. Codling and I. Powis, *Chemical Physics*, 1993, **174**, 441-452.

19. H. Deutsch, K. Leiter and T. D. Mark, *International Journal of Mass Spectrometry and Ion Processes*, 1985, **67**, 191-197.

20. Y. J. Kime and P. A. Dowben, *Journal of Physical Chemistry*, 1989, **93**, 6881-6881.

21. K. Stephan, H. Deutsch and T. D. Mark, *Journal of Chemical Physics*, 1985, **83**, 5712-5720.

22. X. F. Tang, X. G. Zhou, M. M. Wu, Z. Gao, S. L. Liu, F. Y. Liu, X. B. Shan and L. S. Sheng, *Journal of Chemical Physics*, 2013, **138**, 9.

23. S. M. Harper, S. W. P. Hu and S. D. Price, *Journal of Chemical Physics*, 2004, **120**, 7245-7248.

24. J. Roithova, J. Zabka, J. Hrusak, R. Thissen and Z. Herman, *Journal of Physical Chemistry A*, 2003, **107**, 7347-7354.

25. G. K. Jarvis, K. J. Boyle, C. A. Mayhew and R. P. Tuckett, *Journal of Physical Chemistry A*, 1998, **102**, 3219-3229.

26. J. S. Miller, S. H. Pullins, D. J. Levandier, Y. Chiu and R. A. Dressler, *Journal of Applied Physics*, 2002, **91**, 984-991.

27. M. Speranza, *International Journal of Mass Spectrometry*, 2004, **232**, 277-317.

28. D. P. Seccombe, G. K. Jarvis, B. O. Fisher and R. P. Tuckett, *Chemical Physics*, 1999, **250**, 335-346.

29. J. R. Hamilton, J. Tennyson, S. Huang and M. J. Kushner, *Plasma Sources Science & Technology*, 2017, **26**, 16.

30. S. M. Harper, S. W. P. Hu and S. D. Price, *Journal of Chemical Physics*, 2004, **121**, 3507-3514.

31. O. Eisenhut and R. Conrad, *Zeitschrift Fur Elektrochemie Und Angewandte Physikalische Chemie*, 1930, **36**, 654-662.

32. R. K. Janev and H. Winter, *Physics Reports-Review Section of Physics Letters*, 1985, **117**, 265-387.

33. Z. Herman, J. Zabka, Z. Dolejsek and M. Farnik, *International Journal of Mass Spectrometry*, 1999, **192**, 191-203.

34. S. D. Price, M. Manning and S. R. Leone, *Journal of the American Chemical Society*, 1994, **116**, 8673-8680.

35. S. A. Rogers, S. D. Price and S. R. Leone, *Journal of Chemical Physics*, 1993, **98**, 280-289.

36. B. K. Chatterjee and R. Johnsen, *Journal of Chemical Physics*, 1989, **91**, 1378-1379.

37. S. D. Price, *Journal of the Chemical Society-Faraday Transactions*, 1997, **93**, 2451-2460.

38. J. H. Hoffman, R. R. Hodges, T. M. Donahue and M. B. McElroy, *Journal of Geophysical Research-Space Physics*, 1980, **85**, 7882-7890.

39. J. Pearl, R. Hanel, V. Kunde, W. Maguire, K. Fox, S. Gupta, C. Ponnamperuma and F. Raulin, *Nature*, 1979, **280**, 755-758.

40. B. Launder and J. M. T. Thompson, *Philosophical Transactions of the Royal Society a-Mathematical Physical and Engineering Sciences*, 2008, **366**, 3841-3842.

41. A. Ben Houria, Z. Ben Lakhdar, M. Hochlaf, F. Kemp and I. R. McNab, *Journal of Chemical Physics*, 2005, **122**, 10.

42. D. Mathur, *Physics Reports-Review Section of Physics Letters*, 1993, **225**.

43. C. Wittig, *Journal of Physical Chemistry B*, 2005, **109**, 8428-8430.

44. C. Zener, *Proceedings of the Royal Society of London Series a-Containing Papers of a Mathematical and Physical Character*, 1932, **137**, 696-702.

45. S. D. Price, J. D. Fletcher, F. E. Gossan and M. A. Parkes, *International Reviews in Physical Chemistry*, 2017, **36**, 145-183.

46. J. F. Lockyear, C. L. Ricketts, M. A. Parkes and S. D. Price, *Chemical Science*, 2011, **2**, 150-156.

47. P. C. Cosby, *Journal of Chemical Physics*, 1984, **81**, 1102-1107.

48. I. G. Simm, C. J. Danby and J. H. D. Eland, *Journal of the Chemical Society-Chemical Communications*, 1973, 832-833.

49. M. G. Inghram, G. R. Hanson and R. Stockbauer, *International Journal of Mass Spectrometry and Ion Processes*, 1980, **33**, 253-261.

50. N. Tafadar, N. Kaltsoyannis and S. D. Price, *International Journal of Mass Spectrometry*, 1999, **192**, 205-214.

51. M. A. Parkes, J. F. Lockyear and S. D. Price, *International Journal of Mass Spectrometry*, 2014, **365**, 68-74.

6 The RISA commissioning experiments and initial results

6.1 Introduction

This chapter, which is split into two sections, demonstrates that the RISA apparatus can produce pure beams of radicals and is equipped to interrogate any surface species that may form following radical-surface interaction. The first section will describe the development of the radical beam generation chamber, the design of which has undergone many changes over the building stage of this project; the varying, relative successes of each evolution of this chamber are described. Additionally, proof-of-principle results are presented that show the suitability of the RISA apparatus to produce pure beams of radicals. In the second section, initial results from the surface science chamber will be presented. A combined TPD and RAIRS study of CO_2 on amorphous silver at 30 K is used to show that accurate kinetic information can be extracted from the spectra gathered using the RISA set up. Indeed, the results presented in this chapter demonstrate that the RISA apparatus can perform the radical-surface experiments described in chapter 3, and that relevant kinetic data can be extracted.

6.2 Radical beam generation

The experimental process of radical beam generation is described in detail in chapter 3, but, in brief, a neutral radical be is produced through negative ion photo-detachment (NIP). Anions are produced by secondary electron attachment to a chosen target gas. A 532 nm, green light, diode laser irradiates the optimised, mass selected anion beam and NIP occurs if photons with energy greater than the relevant electron affinity interact with the negative ions. This section presents quantitative data regarding the first anion and radical beams produced using the RISA apparatus.

6.2.1 Negative ion results

During the development of the apparatus, several ion sources were designed, built and optimised to produce the highest possible flux of anions.

The experimental details of each ion source are given in chapter 3. For experiments involving interactions between gas–phase species and surfaces, typical reactant fluxes are in the 10^{12}–10^{16} cm^{-2} s^{-1} range.[1–3] Therefore, to perform the radical–surface experiments proposed in chapter 3, a radical flux within this range is required. A previous laser radiation based experiment employed NIP to produce a neutral radical beam and reported electron detachment efficiencies of over 50%.[4] Assuming a comparatively modest detachment efficiency of 10%, we require an anion beam flux in the 10^{13}–10^{17} cm^{-2} s^{-1} range. This section will detail the anion fluxes produced by five ion sources that have been designed and built over the development of this apparatus. Throughout this chapter anion beam flux will be expressed in Amps, which is approximately converted to flux by the relationship outlined in equation 6.1.

$$1\ \mathrm{A} = 1\mathrm{C}s^{-1} \qquad 6.1$$

$$-e = -1.602 \times 10^{-19}\mathrm{C}$$

$$-1\mathrm{C} = \frac{1}{-1.602\times10^{-19}}\ \text{anions}$$

$$-1\ \mathrm{A} = -1\mathrm{C}s^{-1} = 6.242 \times 10^{18}\ \text{anions}\ s^{-1}$$

In addition to optimising the five ion sources described in chapter 3, three target gases were tested to produce negative ion beams: SF_6 (SF_5^-), O_2 (O^-) and N_2O (O^-), with the fragment anionic species given in parentheses. The overall production and transmission of each anion beam through the apparatus is discussed below. Firstly, the identification and selection of the products formed following DEA to each target gas is described.

6.2.2 Mass selection of the anion beam

The products formed following secondary electron attachment to a neutral gas consists of anions and unattached electrons. The anions of interest must be separated from such a mixture to obtain a ‘pure’ anion beam. On the RISA apparatus, a velocity filter is employed to identify the products present in the beam and then mass select the anion of interest. The velocity filter used on this apparatus has been described in detail elsewhere (chapter 1) but, to explain briefly, the filter employs a pair of perpendicular

electric and magnetic fields to filter the beam based on ion velocity. The magnetic and electrostatic forces acting on an ion must balance for it to traverse the filter un–deflected. Maintaining a constant magnetic field and gradually increasing the electric field alters the mass of the ion that maintains a linear path through the filter. As such, the velocity filter can be used to produce a crude mass spectrum. Indeed, monitoring the anion current at the exit of the velocity filter whilst increasing the electric field enables us to determine the species present in the anion beam and the relative abundance of each. The relationship between magnetic field *B*, electric field *E* and an ion of mass *m* with kinetic energy E_k is given in equation 6.2.

$$E = B\left[\frac{2E_k}{m}\right]^{\frac{1}{2}} \qquad 6.2$$

Electric field is force (*F*) per unit charge (*q*) and voltage is work (*w*) per unit charge. Thus, for a fixed distance *d*, the electric field scales linearly with voltage as shown in equation 6.3.

$$Ed = \frac{Fd}{q} = \frac{w}{q} = \Delta V \qquad 6.3$$

It follows that increasing the voltage applied to the electrodes of the velocity filter, which are at a fixed distance, increases the resultant electric field linearly. The flux of anions passing through the velocity filter can be measured on a Faraday plate, positioned behind the exit aperture of the filter. A Faraday plate, as described in chapter 3, is a copper plate. We can measure the current generated by impinging charges on the face of the plate using a picoammeter. As the voltage applied to the velocity filter electrodes is increased, the measured current at the exit of the filter will become more negative if anions are travelling a linear path through the filter and impinging upon the Faraday plate. Therefore, a measured increase in negative current is analogous to a peak in a mass spectrum. Noting the voltages at which the ‘peaks’ in measured occur enables the identification of the species present using the relationship outlined in equation 6.2, and the relative intensities of the peaks provide an estimate of the branching ratio of the parent mono–anion to the various products. The construction of such a mass spectrum

enables the facile identification and isolation of the anion of interest to form a pure beam.

6.2.3 Sulfur hexafluoride, SF_6

SF_6 is an electronegative gas that is often used in the electrical industry as an electron scavenger and electrical insulator.[5, 6] Indeed, a low energy (< 10 eV) electron will readily attach to a molecule of SF_6 at room temperature.[7–10] The total electron attachment cross section to SF_6 is reported to be in the 10^{-22} – 10^{-16} m^2 range, which is exceptionally high compared to most other gases.[9] For this reason, SF_6 was chosen as an appropriate target gas to test the anion production of each ion source. Upon attachment, $(SF_6^-)^*$ forms in an excited state. The three most likely relaxation pathways following excitation are outlined in equations 6.4–6.6.[7, 8]

$$SF_6 + e^- \rightarrow (SF_6^-)^* \rightarrow SF_6^- \qquad 6.4$$

$$SF_6 + e^- \rightarrow (SF_6^-)^* \rightarrow SF_5^- + F \qquad 6.5$$

$$SF_6 + e^- \rightarrow (SF_6^-)^* \rightarrow F^- + SF_5 \qquad 6.6$$

The total electron attachment cross section is dominated by the production of SF_6^-, the parent mono–anion, at attaching electron energies below 0.2 eV, SF_5^- at electron energies between 0.2–1.5 eV and F^- at electron energies greater than 2 eV.[9] We do not know the energy of our ionising secondary electrons, thus the identity of the anions in our beam cannot be determined based upon the published cross sections at specific secondary electron energies. As such, we employed the velocity filter, in the manner described above, to identify the most abundant fragment ion in the anion beam.

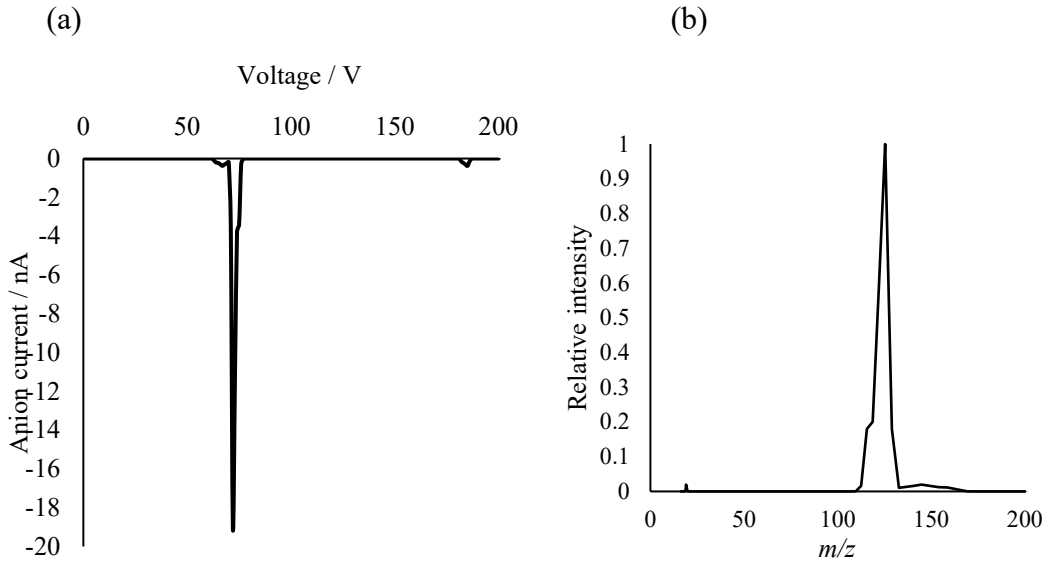

Figure 6.1 The peaks in negative ion current measured on a Faraday plate at the exit of the velocity filter. (a) shows the 'peaks' in negative ion current, indicative of the presence of a mass selected anion, following the mass selection of the products of DEA to SF_6 (b) presents the resultant mass spectrum. See text for details.

Figure 6.1 (a) shows three negative ion peaks that were detected on the Faraday plate at the exit of the filter when the electric field was varied at a constant magnetic field. The anion beam was generated using the simple filament ion source, described elsewhere. Figure 6.1 (b) shows the 'mass spectrum' that was derived using the relationship shown in equation 6.3, assuming the beam was monoenergetic. The three peaks in the spectrum are centred approximately on *m/z* 19, 125 and 144, which correspond to the fragments F^-, SF_5^- and the parent mono–anion SF_6^- respectively, which concurs well with the most likely relaxation pathways outlined in the literature.[8] The branching ratio to each fragment is shown in Table 6.1. The major fragmentation pathway is (b), forming SF_5^-. This result indicates that most of the ionising secondary electrons in the source region of the apparatus have energies in the 0.2–1.5 eV range, where the total electron

attachment cross section is reported to be dominated by the formation of SF_5^-.[9] Similar branching ratios were observed following the mass selection of the products of dissociative electron attachment to SF_6 in all of the five ion sources tested, however the overall intensity of the peaks varied.

Table 6.1 The anions that are observed following electron attachment to SF6, together with the relative branching into each channel as a percentage of the total anion flux detected.

	Relaxation pathway	Branching ratio / %
(a)	$SF_6 + e^- \rightarrow (SF_6^-)^* \rightarrow SF_6^-$	1.4
(b)	$SF_6 + e^- \rightarrow (SF_6^-)^* \rightarrow SF_5^- + F$	96
(c)	$SF_6 + e^- \rightarrow (SF_6^-)^* \rightarrow F^- + SF_5$	2.6

6.2.4 Oxygen, O_2

Molecular oxygen is, by mass, the third most abundant species in the universe and is fundamental to life on Earth. DEA to molecular oxygen has therefore been studied extensively in the literature; it is thought that such reactions may occur in the upper atmosphere and in industrially relevant gas discharges and plasmas.[11] The RISA apparatus was used to produce beams of O^- following electron attachment to O_2 in the simple filament source region. The total cross section for negative ion formation following electron attachment to O_2 is in the 10^{-17} – 10^{-20} m^2 range for low energy, secondary electrons (4–10 eV).[12, 13] Unlike SF_6, this cross section is not remarkably high compared to the other electronegative gases. However, molecular oxygen has a positive electron affinity and was readily available, so seemed like a suitable choice as a target gas. An advantage of using O_2 over SF_6 is that it raises considerably fewer environmental concerns.

Upon electron attachment, $(O_2^-)^*$ forms in an excited state, which can decay *via* the relaxation pathways outlined in equations 6.7 and 6.8.

$$O_2 + e^- \rightarrow (O_2^-)^* \rightarrow O_2 \qquad 6.7$$

$$O_2 + e^- \rightarrow (O_2^-)^* \rightarrow O^- + O \qquad 6.8$$

The O_2^- species is believed to be formed on a repulsive resonance state which rapidly dissociates to form O^-.[14] An anion beam formed following electron attachment to O_2 will therefore consist overwhelmingly of the O^- species. We employed the velocity filter to identify the anionic species present in the beam produced following DEA to O_2 using the simple filament source region.

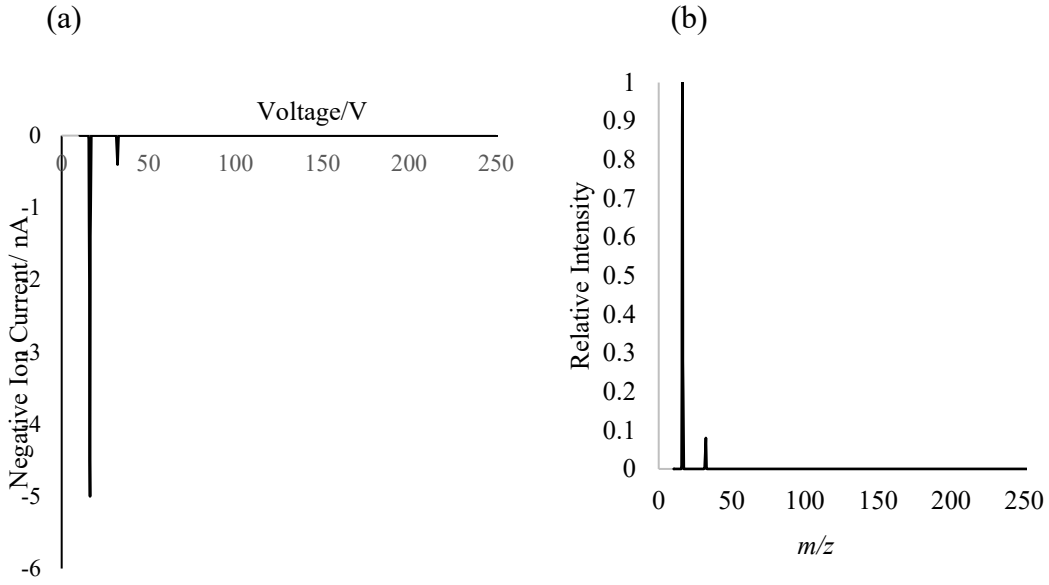

Figure 6.2 The peaks in negative ion current measured on a Faraday plate at the exit of the velocity filter following the mass selection of the products of electron attachment to O_2. (a) shows the 'peaks' in negative ion current with increasing voltage applied to the velocity filter. (b) presents the resultant mass spectrum. See text for details.

Upon increasing the electric field, we detected two negative ion peaks at *m/z* 16 and 32, as shown in Figure 6.2. The dominant product was found to be O^- (*m/z* 16) , in concurrence with the cross sections to fragmentation of $(O_2^-)^*$ reported in the literature.[13] However, we also detected a small amount of O_2^- (*m/z* 32), which reportedly forms on a purely repulsive state that rapidly dissociates into O^- and O, or auto–ionises to O_2.[15] There are several

electronic states that the transient $(O_2^-)^*$ species may form in following electron attachment to the neutral molecule. The lifetime to dissociation of each anionic state will depend upon the internal energy and the electron affinity of the molecule, and the Franck–Condon factors associated with the attachment. It is reported that some species with positive electron affinities, such as O_2, formed anions in excited electronic states following electron attachment with lifetimes of up to 10^{-6} seconds.[16, 17] Indeed, we may be measuring a negative ion signal at *m/z* 32 associated with a metastable $(O_2^-)^*$ anion that has yet to dissociate to form O^- and O. The branching ratios presented in Table 6.2 are mirrored in the mass spectra collected following the mass selection of ion beams formed following the DEA to O_2 in all other ion source regions tested.

Table 6.2 The possible fragmentation pathways following electron attachment to O_2. The branching ratio to each channel is given as a percentage of the total anion flux detected.

	Relaxation pathway	Branching ratio / %
(a)	$O_2 + e^- \rightarrow (O_2^-)^* \rightarrow O^- + O$	96.5
(b)	$O_2 + e^- \rightarrow (O_2^-)^*$	3.5

6.2.5 Nitrous oxide, N_2O

In recent years, nitrous oxide, N_2O, has been recognised as a potential contributor to the destruction of ozone in the stratosphere. As such, several studies have been carried out that investigate the destruction and decomposition of N_2O in the gas phase.[18] One of the possible destruction pathways is through the dissociation of the products of electron attachment to N_2O.[19] Indeed, a plethora of information pertaining to the products formed following DEA to N_2O are available in the literature.

Despite the abundance of published data, there is some debate as to the exact mechanism by which O^- is formed following the DEA to N_2O. However, there is widespread agreement that O^- is the sole fragment ion formed at room temperature by low energy (< 10 eV) electrons, as shown in equation 6.9.[20–23]

$$N_2O + e^- \rightarrow (N_2O^-)^* \rightarrow O^- + N_2 \qquad 6.9$$

A retrospective study of the literature pertaining to this decomposition highlights some controversy surrounding the exact value of the electron affinity of N_2O. Initial experimental studies performed in the 1970s produced various EA values ranging from –0.15 $\pm$ 27 eV.[24–26] Studies in the 1990s, aided by the advance of theoretical techniques, produced further discordant EA values ranging from –0.021 $\pm$ 0.8 eV.[27, 28] In 2001, Kryachko *et al* performed an extensive mapping of the N_2O^- ground state potential energy surface which resulted in the calculation of a negative EA of –0.03 eV, which is now widely accepted.[29] The disparity between the experimental and theoretical EAs has been attributed to an incorrect determination of the dissociation energy of N_2O, a value which was then used to determine the EA thermochemically. Despite such debate, the cross section to the formation of O^- following the DEA of low energy electrons (0–10 eV) to N_2O is known to be in the 10^{-19} to 10^{-17} m^2 range.[16] We employed the velocity filter to determine the species present in our beam following electron attachment to N_2O in the simple filament source region.

It is clear from Figure 6.3 that only one peak is observed in the ‘mass spectrum’ collected at the exit of the velocity filter, which corresponds to *m/z* 16. That is, the sole fragment ion observed is O^-. This result agrees with the published data pertaining to the fragmentation of N_2O^- following electron attachment. Similarly, mass selection of the products of DEA to N_2O in the other ion sources tested yielded a mass spectrum with a single peak that corresponds to O^-.

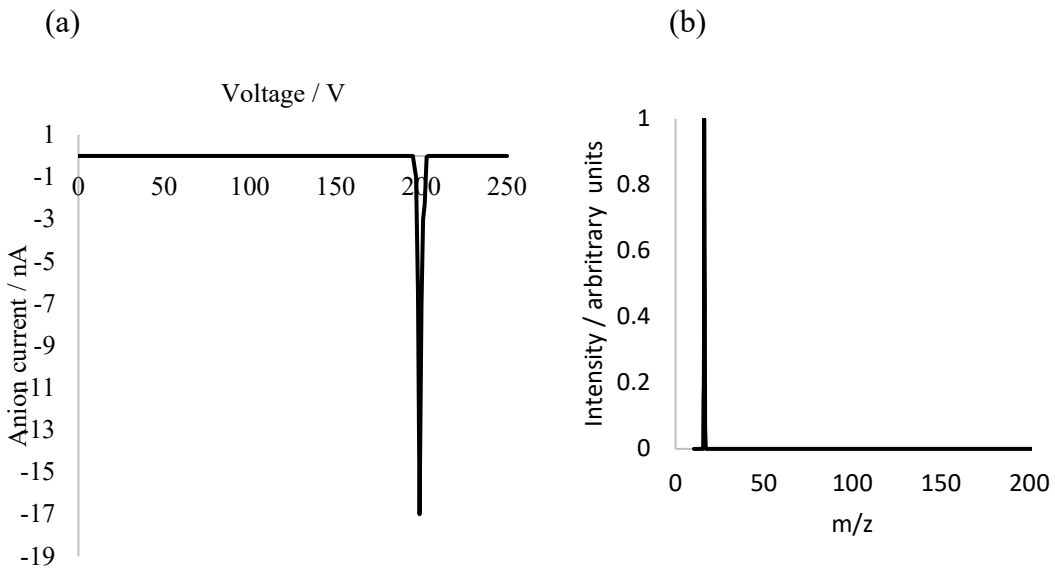

Figure 6.3 The peaks in negative ion current measured on a Faraday plate at the exit of the velocity filter following the mass selection of the products of electron attachment to N_2O. (a) shows the sole peak in negative ion current with increasing voltage applied to the velocity filter. (b) presents the resultant mass spectrum. See text for details.

The velocity filter results presented in this section for the products of electron attachment to SF_6, O_2 and N_2O broadly tally with the well–established, widely accepted fragmentation patterns following DEA to these gases published in the literature. In addition to enabling the identification of the ions present in the various beams formed during the commissioning experiments, these findings provide confidence that the velocity filter is well calibrated; in future experiments, we will be able to tune the electric field to a specific voltage to detect ions at a chosen *m/z*.

6.2.6 Beam optimisation and anion transmission

To quantify the anion beam production of each ion source, the negative ion flux was measured at various points along the chamber. The first point of measurement was behind the skimmer (Figure 3.2, chapter 3) to measure the efficiency of anion extraction from the source region. The second point of measurement was at the entrance to the velocity filter (Figure 3.7Figure 3.8,

chapter 3). The anion beam was also measured at the exit of the velocity filter to ensure the highest possible flux of the mass selected beam was transmitted through the filter. The anion flux could then be measured on a Faraday plate placed in the centre of the quadrupole lenses (Figure 3.8, chapter 3) and finally at the entrance to the UHV chamber (Figure 3.9, chapter 3). Measuring the flux at successive positions in the chamber enabled the optimisation of the voltages applied to the shaping lenses in each section and gave an indication of the percentage transmission of the ion beam. Figure 6.4 presents a comparison of the negative ion flux results of each ion source, at each point of measurement, for each target gas.

Prior to analysing the results presented above, it is worth noting that several factors must be considered when measuring negative current as anion flux. Firstly, the current measured is the net charge of the species impinging upon the Faraday plate: any cations present will make the measured current more positive, which would appear as a lower flux of anions. Secondly, electrons may be present in the beam, which would be measured as an increase in negative current, irrespective of whether an electron or an anion impinged upon the plate. This issue is particularly pertinent to measurements made near the source region due to the proximity to the electron gun. A precaution that was taken when measuring the anion flux near the source region was the placement of a magnet above the extracting lenses. The resultant magnetic field was of significant strength to deflect most of the electrons from the anion beam, whilst leaving the heavier anions unperturbed.

Upon examining Figure 6.4, there are clear trends in anion transmission shared by each ion source, irrespective of the target gas used. For all ion sources, there is a significant loss of negative current from the first point of measurement (position 1) to the last (position 5). Indeed, transmission from positions 1–5 can be zero.

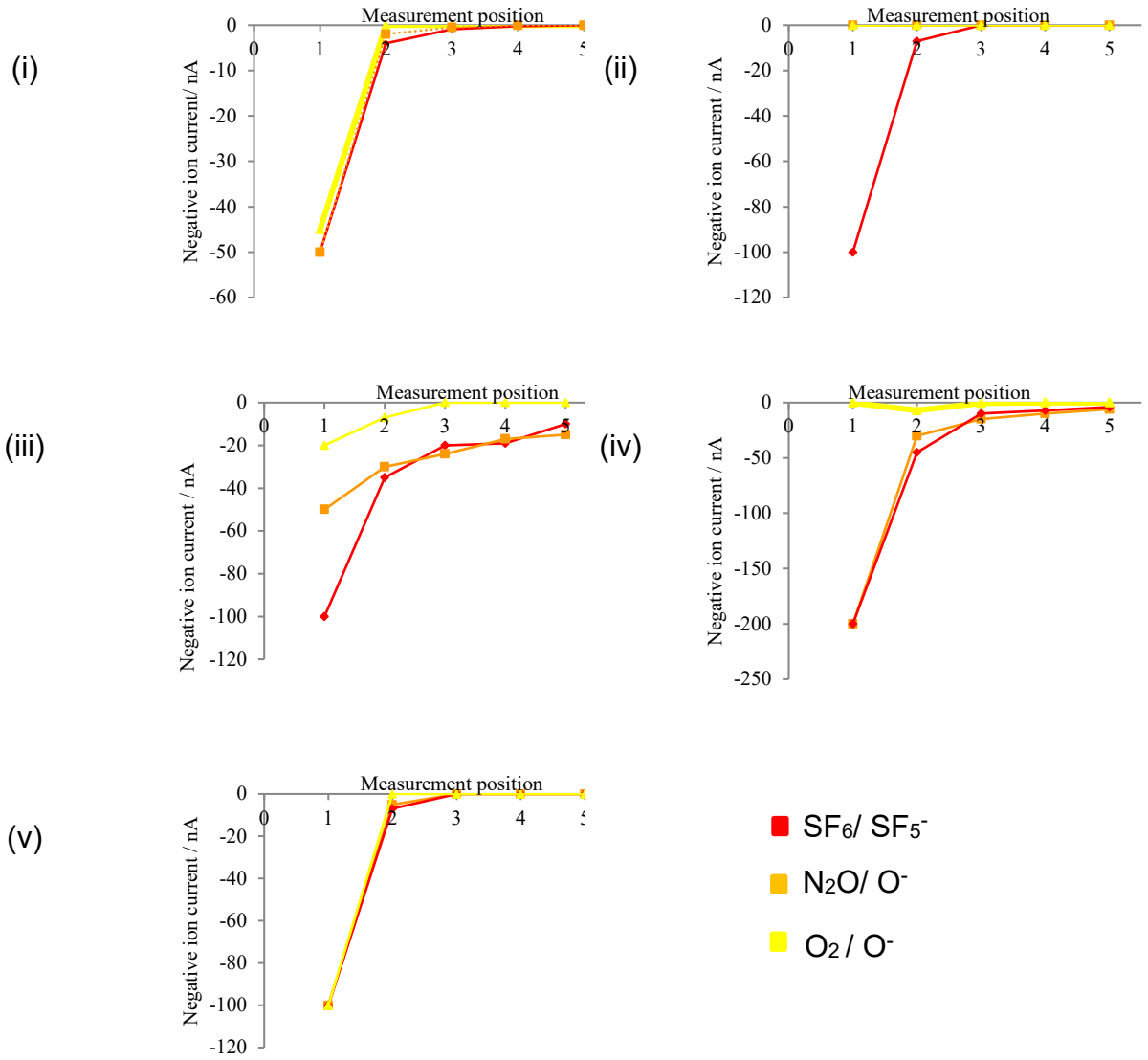

Figure 6.4 The various ion beam current measurements taken at positions 1–5 for each ion source, where: 1 = behind the skimmer, 2 = velocity filter entrance, 3 = velocity filter exit, 4 = quadrupole lenses, 5 = entrance to UHV chamber. The Roman Numerals i–v represent the different ion sources, where i = yttria coated iridium cathode gun (YCIC), ii = homemade yttriated tungsten filament gun, iii = simple mounted filament, iv = adapted YCIC and v = discharge source.

As previously discussed, the flux measurement taken at position 1 is likely to be an over–estimation of anion current, due to the presence of electrons in the beam. A transverse magnetic field was therefore established between positions 1 and 2 to deflect any electrons out of the beam, so the measurement at position 2 is likely to be a more realistic measurement of the ion current leaving the source region.

The negative current transmission between positions 2–3 further decreases. This decrease in detected negative current is expected due to the mass selection process: only ions of a specific *m/z* ratio will reach position 3, whilst any other fragment ions or any remaining electrons will be deflected out of the beam.

Positions 4 and 5 are placed before and after the 90 turn in the chamber respectively. Comparing the ion current transmission from the exit of the velocity filter to these two positions, indicates the percentage of the mass–selected beam that is successfully turned through 90^{o} by the quadrupole lenses. A large percentage loss here would indicate one of three things: that the quadrupole lenses are not optimised correctly, that the lenses of the quadrupole are not perfectly aligned, or that the mass–selected beam ion beam is not monoenergetic. A detailed analysis of the anion transmission for beams produced by each ion source tested is presented below.

Figure 6.4 (i) shows the transmission of the ion beams produced following electron attachment to each target gas by the YCIC electron gun, described in section 3.4.2. It is clear from Figure 6.4 that there is a pronounced decrease in negative ion current measured between positions 1–2. In fact, for each target gas there is a 90% decrease in ion current detected between these two points. Such losses, where a magnetic field is applied to deflect unwanted electrons from the beam, suggests that much of the current measured at point 1 was due to electrons. A negligible ion current was detected for each gas following the mass selection of the beam. Indeed, we were unable to mass select the low flux of ions that were produced by this ion source.

When each target gas was admitted into the chamber perpendicularly to the flow of electrons, the emission current of the YCIC gun dropped significantly due to the change in emissivity of the filament associated with the increasing gas pressure. It was found that emission from the yttria–coated iridium cathode was totally suppressed at pressures greater than 1×10^{-5} Torr. As the probability of secondary electron attachment increases in correlation to gas pressure, the highest possible gas pressure was used that did not suppress electron emission below –0.1 mA. This gas pressure was found to be 4×10^{-6} Torr. Although this gun produced a high flux of electrons, the anion current measured at the exit of the velocity filter was negligible and much of the measured negative current was from electrons. I believe that the lower operating gas pressure limited the ability of this source region arrangement to produce higher fluxes of anions.

Figure 6.4 (ii) shows the ion beam transmission through the chamber following electron attachment to each target gas, by the yttriated tungsten filament gun, which is described in section 3.4.3. The similarity between the results presented in (i) and (ii) is clear: the current measured at position 1 significantly decreases when measured at position 2, followed by a total loss of current recorded at position 3. Again, this suggests that much of the measured current at position 1 is comprised of electrons. However, the tungsten filament did not respond to increasing gas pressure in the same way as the cathode in the YCIC gun. Upon optimising the gas pressure maximum negative current was measured behind the skimmer at 1×10^{-5} Torr. Thus, low electron emission at higher gas pressures was not the problem. The low ion flux measured at position 3 was attributed to poor overlap between the electron beam and the target gas in the source region.

Both the YCIC and the ytttriated tungsten filament gun, which have been described elsewhere (chapter 3), were mounted on an ISO–KF flange on the chamber. The distance between the electron exit aperture in both the guns was approximately 150 mm away from the centre of the source region, where the density of target molecules is highest. It was thought that the fields established within the source to extract any negative ions formed affected the fields within the electron guns and deflected the resultant electron beam.

Thus, anion flux was negligible at position 3 due to minimal interaction between the electrons and neutrals in the source region. To minimise the effect of such stray fields on the electron beam, two field–shielding plates were added to the source region, which are described in detail in chapter 3.

Figure 6.4 (iii) shows the transmission through the chamber of the ion beams formed following the DEA of the target gases by the simple filament electron source. Upon comparison, it is clear this source arrangement produced a higher flux of anions compared to all other sources, at all measurement positions following mass selection. Indeed, this arrangement yielded a non–negligible ion current at the entrance to the UHV chamber following electron attachment to SF_6 (SF_5^-) and N_2O (O^-). The success of this source arrangement may be due to the decreased distance (5 mm) between the electron source and the area of the chamber where the target gas is most dense. Additionally, the shrouds that were added to the chamber to minimise stray fields within the ion source are thought to have further prevented deflection of the electron and resultant anion beam.

Figure 6.4 (iv) shows the transmission of the negative ion beams produced by the adapted YCIC following electron attachment to the three target gases outlined above. The original YCIC mounting flange was replaced with a zero–length flange. This adaptation decreased the distance between the electron gun exit aperture and the centre of the source region by 100 mm. The negative current measured at position 1 is four times that measured at this point for the original YCIC arrangement (i). Indeed, an increase of approximately 75% in negatively charged species are present in the beam due to the decreased changes made to the YCIC source. This finding indicates that, in the case of the original YCIC arrangement, the fields in the source region were deflecting the electron beam away from the centre of the source region. Of course, the –200 nA detected at position 1 is a combination of both electrons and ions. However, there is a more negative current detected at all positions for the adapted YCIC. In fact, mass selected beams of SF_5^- (–10 nA) and O^- (–15 nA), formed following electron attachment to SF_6 and N_2O respectively, have been detected at the entrance to the UHV chamber.

Despite the improvements made to this source region, the anion flux produced by the simple filament arrangement was approximately 2.5 times higher following electron attachment to both N_2O and SF_6. The decrease in emissivity of the cathode in the YCIC gun at pressures > $4x10^{-6}$ Torr was limiting anion production. The tungsten filament used as an electron gun in the simple filament arrangement can withstand pressures up to $1x10^{-5}$ Torr. Over the 10^{-6}–10^{-5} Torr pressure range, the cross section to electron attachment increases with increasing gas pressure. Thus, we can conclusively confirm that the YCIC cannot be used for the proposed radical surface experiments owing to the effect of high gas pressures on the cathode.

The use of an electrical discharge to produce anions is a well–established technique.[30] Indeed, discharge based negative ion sources have been used in studies as varied as investigating the dynamics of anion reactions to determining the electronic and IR spectra of C_{60}^- with a view to assign the diffuse interstellar bands.[31, 32] Figure 6.4 (v) shows the anion transmission results recorded following electron attachment to SF_6, N_2O and O_2 in an electrical discharge source, described elsewhere (chapter 3). At time of writing, the discharge source is undergoing optimisation and Figure 6.4 (v) presents preliminary results. –0.1 mA of negative current has been detected at position 1 for all target gases. This flux is comparable to the ion flux measured at position 1 for the simple filament arrangement, the most successful source region at producing anion beams. With further optimisation, we are confident that the discharge source arrangement will be able to produce beams of anions with sufficient fluxes to perform the proposed radical–surface experiments.

A maximum negative flux of – 7 nA and –17 nA was detected in the UHV chamber for beams of SF_5^- and O^- respectively, which were produced following electron attachment to the appropriate neutral in the simple filament source region. A higher flux of O^- is generated following DEA to N_2O compared to O_2 because N_2O has a higher cross section to electron attachment. However, SF_6 has a higher cross section to electron attachment over all electron energies compared to N_2O, yet a lower flux of the relevant

anion has been measured at the entrance to the UHV chamber. SF_6 was the first gas that was used to test each ion source. Therefore, compared to when N_2O was used as a target gas, less time had been spent optimising the shaping and quadrupole lenses throughout the chamber to maximise negative ion transmission. I believe for this reason, transmission of the SF_5^- beam is lower compared to the O^- beam generated by DEA to N_2O.

This section has outlined the relative success of each ion source (described in (chapter 3) at producing beams of anions following electron attachment to the target gases SF_6, N_2O and O_2. The RISA apparatus was used to successfully produce anion beams of SF_5^- and O^-, which were detected at the entrance to the surface science chamber. The simple filament source region proved to be the most effective arrangement at producing negative ions. Indeed, fluxes of –10 and –15 nA were detected following electron attachment to SF_6 and N_2O in this source region.

The next section details the production of a radical beam *via* electron photo–detachment.

6.2.7 Photodetachment

The RISA apparatus is designed to produce pure beams of free radicals to investigate radical–surface interactions. As described above, the radical source uses the photo–detachment of an intense beam of mass–selected anions to give a pure beam of the corresponding neutral species. This section will detail the photo–detachment of the O^- beam formed following electron attachment to N_2O in the simple filament ion source.

SF_6 was chosen as a target gas to produce beams of anions owing to its exceptionally high cross section to electron attachment. Indeed, the initial relatively intense fluxes of negative ions enabled the facile initial optimisation of the components of the radical source, such as the velocity filter and the shaping lenses. However, the RISA experiment is equipped with a diode laser that emits radiation at 532 nm, which is sufficient to detach electrons from beams of negative ions with electron affinities below 2.5 eV. For anions with electron affinities greater than 2.5 eV, such as SF_5^-, the green laser light would have to be frequency doubled. Light of 532 nm will usually be

sufficient to photo–detach most relevant negative ions to produce radicals of interest.

As the simple filament source produced the highest flux of O^- following secondary electron attachment to N_2O, beams of O^- generated in this way were used to optimise the photo–detachment process. O^- has an electron affinity of 1.6 eV, therefore a photon from the diode laser will have sufficient energy to photo–detach an electron from the charged species, leaving a neutral O radical (^3P).

To quantify electron detachment from the O^- beam the negative ion current was measured on a Faraday plate at the entrance to the UHV chamber. A picoammeter attached to a Faraday plate measures the net charge of the plate. Indeed, both anions and electrons impinging upon the plate contribute to the current measurement. As such, a magnet was placed above the Faraday plate to deflect any detached electrons from the beam. The anion flux was measured before and after laser irradiation. A decrease in negative ion current was observed, which is indicative of electron detachment and therefore the formation of neutral radicals.

The Beer–Lambert law states that the intensity of our laser beam will decrease exponentially with increasing path length over which it overlaps with an anion beam, assuming that the flux of anions in the overlap region and the cross section to electron detachment of the anions remains constant. Therefore, the greater the overlap between the laser and ion beam, the more radicals will be produced. Whilst considering this relationship, we irradiated the ion beam at several different laser beam chamber entry angles, relative to the ion beam, noting the resultant change in negative ion current measured on a Faraday plate located at the entrance to the UHV chamber. We avoided shining the laser light directly parallel to the ion beam as, although this set–up would potentially maximise ion–photon overlap, irradiation of the faraday plate may have led to excessive heating of the chamber lenses and feedthroughs. During radical-surface experiments, the laser would also irradiate the surface. A mirror was positioned at the entry aperture of the exit chamber lenses on a purpose–built mount with 3 degrees

of freedom, which could be manoeuvred to guide the laser beam out of the chamber *via* a viewport.

Initially, the negative ion current was measured following irradiation of the ion beam by a single pass of the laser through the chamber. The negative ion current became more positive by approximately 1 nA. This is a proof–of–principle result which shows that neutral radicals can be generated using this experimental arrangement. That is, we successfully generated a neutral beam of O radicals through the irradiation of an O^- beam.

We overlapped the laser beam and the ion beam several times by positioning a mirror at the exit port to guide the laser light back into the chamber, where the photons reflected off the highly polished inner chamber surfaces. Although we cannot quantify the increase in overlap path length, the negative ion current became more positive by approximately 7 nA following the multipass. This result corresponds to photo–detachment of 47 % of the anions measured prior to irradiation. Recall, as outlined in section 6.2.1, comparable experimental arrangements have reported electron detachment efficiencies of up to 50%.[4] Furthermore, recall we require radical fluxes of 10^{12}-10^{16} $cm^{-2}s^{-1}$. The 7 nA measured indicates a flux of ~7 x 10^9 radicals per second, which shows that we are close to being within the required range to perform radical-surface experiments. This proof–of–principle result shows that the RISA apparatus can produce radical beams that consist overwhelmingly of one species, with a detachment efficiency close to those published in the literature.

6.2.8 Radical beam conclusion and future development

This section has described the commissioning experiments performed on the radical source chamber of the RISA apparatus. The best experimental arrangement to produce beams of anions was the simple filament arrangement, described in detail in chapter 3. The RISA apparatus was used to produce two different ion beams: SF_5^- and O^-. Pure beams of neutral oxygen radicals were produced following the irradiation of an O^- anion beam with a laser beam at 532 nm. Although the yield of radicals produced is insufficient to perform the proposed radical–surface experiments, the proof–

of–principle results presented nonetheless show that pure beams of free radicals can be produced.

Future work is planned to increase the flux of neutral radicals that the RISA apparatus can produce. To increase radical flux, the anion beam flux should be increased. A key lesson from the work presented in this chapter is that the high gas pressures required to generate high fluxes of negative ions are incompatible with the delicate tungsten filaments, and cathodes, of the electron guns used to date. As such, the discharge source will be optimised to produce negative ions. Alternatively, a separate chamber to house the electron gun could be produced, and maintained at a low pressure. The electron beam could then be extracted into a reaction chamber, filled with the target gas.

6.3 Commissioning the surface science chamber

The surface science commissioning experiments outlined in this section are all performed using carbon dioxide as a precursor gas. The motivations behind this choice are manifold, and are briefly outlined below. Carbon dioxide is an important molecule in the ISM, where it is found predominantly in the solid phase accreted onto interstellar dust grains.[33] Observations from the infrared space observatory (ISO) and Spitzer telescope have shown that frozen CO_2 is ubiquitous in ice mantles in dense molecular clouds. Consequently, there is a wealth of data pertaining to the cold temperature (< 50 K) adsorption and desorption of this simple molecule available in the literature.[34, 35] Indeed, several TPD experiments studying CO_2 adsorbed onto a variety of surfaces, ranging from water ice to gold, have been performed.[33, 36–39] The availability of such information has enabled the comparison of our initial results to well-known literature values, which has provided the motivation for using CO_2 for the preliminary TPD experiments that will be discussed in this section.

Table 6.3 The IR active bands that feature in the gas phase spectrum of CO_2, taken from reference Mate (2009).

Band Type	Wavenumber / cm^{-1}	Assignment
Fundamental	2349	$^{12}CO_2$ ν_3
Fundamental	2280	$^{13}CO_2$ ν_3
Fundamental	660	ν_2 bend
Combination	3705	$\nu_1 + \nu_3$
Combination	3600	$2\nu_2 + \nu_3$

Another factor that led to the use of CO_2 in the commissioning of the surface science chamber is that there are a well–defined, characteristic set of vibrational frequencies available for reference in the literature. Indeed, several IR studies of CO_2 have been performed on a range of surfaces and in the gas-phase.[40–52] Such well documented data has enabled the assignment of the RAIRS bands that appear in the first spectra recorded using the RISA apparatus and has provided confidence in the technique for use in future studies. Table 6.3 details the 5 infra–red active bands that appear in the gas phase spectrum of CO_2.

6.3.1 Surface cleanliness, XPS and AES

The commissioning surface science experiments described in this chapter were performed under UHV conditions (10^{-9} - 10^{-10} Torr). Despite such a low pressure, the presence of background gases is non–negligible and, if ignored, could saturate the surface rapidly during low temperature experiments. The surface was therefore cleaned prior to each experiment to ensure that any adsorbed background species were removed.

Before each experiment, the silver surface, described in chapter 3, was sputtered by high energy Ar^+ ions, which were generated by an ion gun, at room temperature for 15 minutes. The surface drain current, which is the current generated on the surface by the impinging ions, was maintained at 150 μA. Immediately after sputtering, the surface was annealed to 500 K and was held at this temperature for 3 minutes. The sample was then allowed to

cool to the desired surface temperature, which for these commissioning experiments was 30 K. XPS and AES spectra were recorded following each sputter/anneal cycle to measure surface cleanliness. To further confirm sample cleanliness, a TPD spectrum was recorded of the clean surface.

Figure A 1, Figure A 2 and Figure A 3, in the appendix, contrast three XPS spectra recorded from an amorphous silver surface following 9, 6 and 1 cycles of sputtering and annealing respectively. Each peak can be confidently assigned upon comparison to an XPS database. The characteristic XPS peaks for Ag $3d_{5/2}$ and Ag $3d_{3/2}$ electrons are at binding energies of 368.2 eV and 375 eV respectively. Typically, an XPS spectrum of silver will also contain Auger electron peaks at 726.5 eV and 720.5 eV. The presence of C (284.4 eV), O (532.0 eV) or N (403.9 eV) peaks in these spectra is indicative of the presence of background adsorbates.

Comparing Figure A 1, Figure A 2 and Figure A 3, each of the silver XPS and Auger peaks can be seen growing in relative intensity with increasing sputter/anneal cycles. Indeed, the more the surface was cleaned, the greater number of surface atoms were silver. Furthermore, with increasing cycles of cleaning the impurity peaks decreased to be indistinguishable from the baseline of the final spectrum, showing spectroscopically that the surface was clean. The only species present on the target following 9 cycles of sputtering and annealing, following the recipe outlined above, are silver atoms.

XPS and AES are powerful, quantitative elemental analysis tools. The figures in the appendix show that the RISA apparatus can successfully produce spectra of ejected electron binding energies following x–ray irradiation. As such, beyond verifying surface cleanliness, these two techniques will be used to aid in the identification of any products that may form following the proposed radical–surface experiments.

6.3.2 TPD study of multilayer CO_2 on amorphous silver

This section will describe the initial TPD experiments that were performed using the RISA apparatus. This section aims to demonstrate that relevant

and accurate kinetic data can be extracted from TPD spectra collected using this apparatus, by a variety of data processing techniques.

6.3.2.1 TPD experiment

All experiments were performed as outlined in chapter 3. To give a brief reprise, the commissioning TPD experiments were performed to investigate the adsorption of carbon dioxide on amorphous silver by background filling the chamber in a controlled manner *via* a high–precision leak valve. Prior to sample cleaning, CO_2 was flushed through the inlet line several times and was passed into the chamber whilst monitoring the QMS to ensure no background contaminants entered the chamber with the target gas. All exposures are presented in Langmuir (L), where 1 L is equivalent to background filling the chamber to a pressure of 7.5×10^{-7} Torr for 1 second.

The Langmuir unit can be derived from kinetic theory. The number of atoms or particles per unit area, or coverage θ, on a surface can be given by the integral of the number flux, *N*, with respect to time.

$$\theta = \int N \, dt \text{ dt} \qquad 6.10$$

The number flux of a gas can be derived from the kinetic theory of gases, where σ is the mean speed of the molecules, *p* is the pressure, *k* is the Boltzmann constant, is the temperature, and *m* is the mass of the gaseous species.

$$N = \frac{p}{kT} \times \frac{\sigma}{4} \qquad 6.11$$

$$\text{Where } \sigma = \sqrt{\frac{8kT}{\pi m}}$$

Therefore, equation 6.10 becomes

$$N = p\sqrt{\frac{1}{2\pi mkT}} \qquad 6.12$$

Assuming all gaseous species that collide with the surface stick to it, i.e. the sticking coefficient is equal to 1, one Langmuir corresponds to a coverage of approximately one monolayer.

It is essential that TPD spectra are recorded with a linear heating rate. All TPD spectra presented in this section were recorded at a heating rate of 9 K min^{-1}. The heating rate is controlled by a temperature controller of commercial design (nanodac). Figure 6.5 shows the heating rate of the sample whilst performing a TPD experiment following the adsorption of CO_2 onto amorphous silver at 30 K.

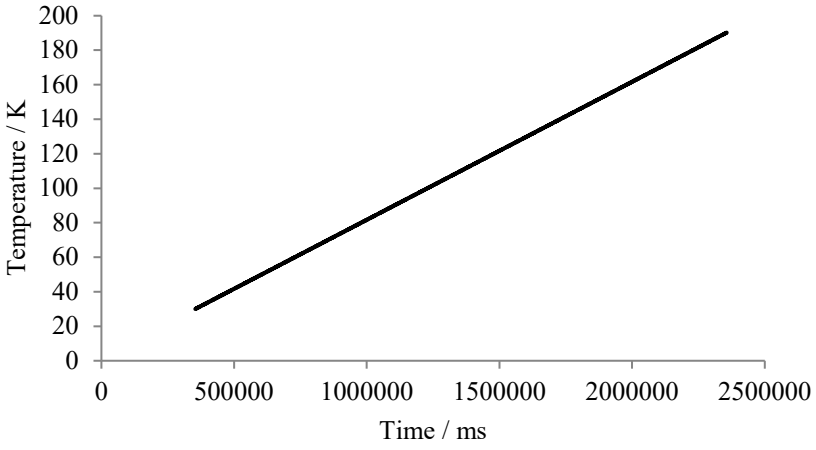

Figure 6.5 A plot to show the linear relationship between time and temperature, recorded whilst heating the amorphous silver surface from 30 – 200 K. The heating rate can be obtained from the gradient of the straight line, and is 9 K min–1. This heating profile, and therefore heating rate, is typical for all the TPD experiments that have contributed to the results presented in this chapter.

6.3.2.2 TPD results and discussion

TPD spectra were recorded for the adsorption of CO_2 on amorphous silver at 30K. A series of these spectra for increasing exposures of CO_2 are presented in Figure 6.6. It is clear from inspecting the TPD spectra that only one multilayer peak is observed following adsorption of CO_2 onto amorphous silver. The TPD peak temperature increases with increasing exposure. The peaks presented following 200 L – 50 L share a perfect common leading

edge, implying a zero–order desorption process, which will be discussed below. The peak cannot be saturated, implying that it corresponds to a multilayer adsorption. Further evidence for the assignment of this peak as multilayer is discussed below.

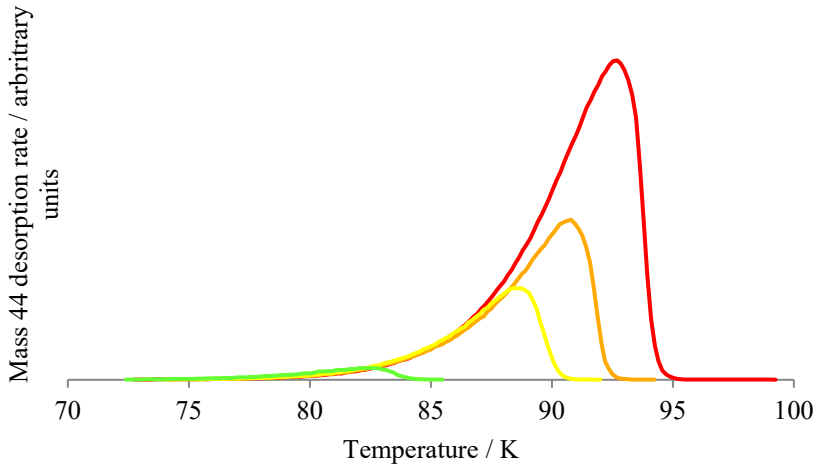

Figure 6.6 TPD spectra recorded following exposures of 200 L (red), 100 L (orange), 50 L (yellow) and 5 L (green) of CO2 adsorbed on amorphous silver at 30 K.

The peak formed following 5 L exposure does not share the perfect common leading edge mentioned above, implying a non–zero order desorption. In fact, for exposures below 5 L, monolayer character begins to appear in the peak shape. Indeed, a secondary peak begins to appear as a shoulder in the 5L spectrum at a slightly higher temperature compared to the multilayer peak. This high temperature shoulder corresponds to CO_2 adsorbates with a higher desorption energy compared to the multilayer adsorbates due to interactions with the silver surface. For these commissioning experiments, multilayer characteristics were investigated thus a full, quantitative analysis will exclusively be performed on the multilayer peaks formed following CO_2 exposures between 200 – 50 L.

6.3.2.3 Uptake curve

The signal intensity recorded by the mass spectrometer, I(T), is proportional to the rate of desorption of the adsorbate from the surface.

Thus, the area under each peak is proportional to the coverage of the adsorbate on the surface. For these commissioning experiments, the absolute coverage has not been measured, therefore the area below each TPD peak corresponds to a relative coverage of the CO_2 adsorbates on the silver surface. An uptake curve has been plotted for the adsorption of CO_2 on amorphous silver at 30 K as a function of increasing exposure, using the data directly extracted from Figure 6.6, which is presented in Figure 6.7. The integrated areas were calculated by subtracting the background intensity from the spectrum and using Simpson's rule over the peak temperature range. Simpson's rule is a method of numerical integration where we use parabolic approximations of the function *f* to determine an approximate integral value.

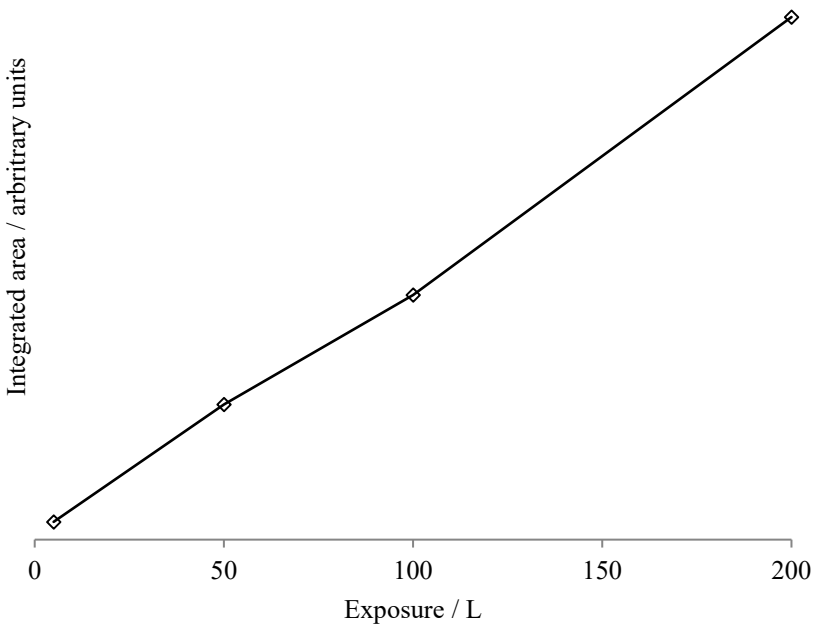

Figure 6.7 The total integrated area under the peaks presented in Figure 6.6, as a function of exposure. The area under each plot is proportional to the amount of desorbed species and thus the initial surface coverage. A constant uptake of species with increasing coverage is indicated by the linear plot, which is indicative of the growth of multilayers.

It is clear from inspecting Figure 6.7 that there is a linear trend between coverage and exposure, indicating a constant sticking probability of CO_2 molecules to the amorphous silver surface. This result is characteristic of the growth of physisorbed multilayers of CO_2.

6.3.2.4 Desorption order

To use the Polanyi–Wigner equation to acquire kinetic information about an adsorbate–surface system, the desorption order for the desorbing species must be determined. This procedure is detailed in chapter 3, but in brief, the desorption order can be determined by plotting $\ln[I(T)]_x$ against $\ln[\theta_{rel}(T)]_x$, where $[I(T)]_x$ is the intensity of the peak in the mass spectrum of the adsorbed species at a chosen fixed temperature T_x and $[\theta_{rel}(T)]_x$ is the corresponding relative coverage at that temperature. We assume that the pre–exponential factor in the Polanyi-Wigner equation and desorption energy are both independent of coverage and temperature. Figure 6.8 shows a desorption order plot at temperatures, T_x, of 75, 80 and 85 K. The gradients, and hence the desorption orders, obtained from the trend lines plotted in Figure 6.8 are presented in Table 6.4.

Table 6.4 the desorption orders derived from the gradients of the plots in Figure 6.8 for a variety of T_x values, for CO_2 adsorbed onto an amorphous silver surface. The errors shown are derived from the standard deviation of the average gradient of the maximum and minimum lines of fit.

Temperature (T_x) / K	Desorption Order
75	-0.005 ± 0.01
80	-0.3 ± 0.3
85	-0.003 ± 0.06

It is possible to determine the desorption energy for CO_2 multilayers adsorbed on amorphous silver using the Polanyi Wigner equation. Therefore, we can acquire information about the binding strength between molecules within the adsorbate overlayer. The desorption energy has been investigated by three methods: the complete analysis technique, a second technique that requires the desorption order to be known and the leading–edge technique.

Each method is based upon the Polanyi– Wigner equation, shown in equation 6.13.

$$R_{des} = \frac{-d\theta}{dt} = A\theta^{n}\mathrm{e}^{\frac{-E_{des}}{RT}} \qquad 6.13$$

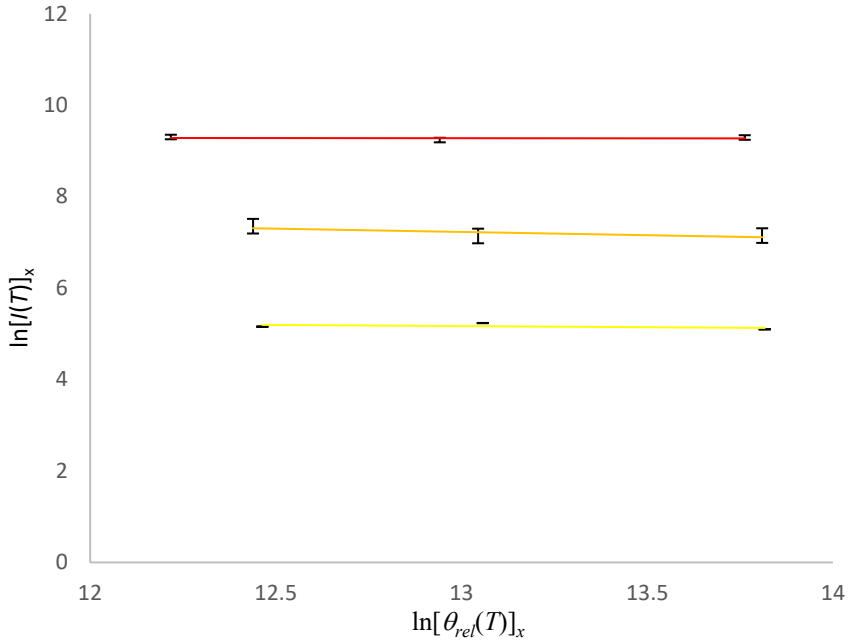

Figure 6.8 The uptake of adsorbates with increasing exposure to CO_2. To construct this plot, the TPD traces recorded following exposures of CO_2 between 50 – 200 L were read at three fixed temperatures: T_x = 75 (yellow), 80 (orange) and 85 (red) K. At each T_x the intensity and relative coverage of the surface have been recorded and a plot of $\ln[I(T)]_x$ against $\ln[\theta_{rel}(T)]_x$ has been constructed. The error bars show the standard deviation from the mean of three measurements taken at each temperature.

The complete analysis method uses a collection of TPD spectra recorded at different exposures of target gas to garner kinetic information about the desorption system through application of the Polanyi–Wigner equation. Rearranging and taking logarithms of equation 6.13 gives

$$\ln I(T) \propto n \ln[A] + n \ln[\theta_{rel}] - \frac{E_{des}}{RT} \qquad 6.14$$

This technique involves the conversion of the TPD spectra, given in Figure 6.6, to a plot of coverage against temperature. A fixed relative coverage is then chosen and the corresponding temperature at which this coverage occurs is recorded for every plot in the collection. As such, the relative coverage becomes constant across all exposures and equation 6.14 becomes

$$\ln I(T) \propto n \ln[A] - \frac{E_{des}}{RT} \qquad 6.15$$

The temperatures recorded at this fixed relative coverage, for all exposures, are then related back to the corresponding intensity on their original TPD curve. Assuming the pre–exponential factor, *A*, and the desorption energy do not vary with coverage or temperature, an Arrhenius plot of ln *I(T)* vs $\frac{1}{T}$ then gives a straight line with a gradient of $\frac{E_{des}}{R}$. The conversion of the collection of TPD curves, shown in Figure 6.9, into a plot of relative coverage against temperature is presented below.

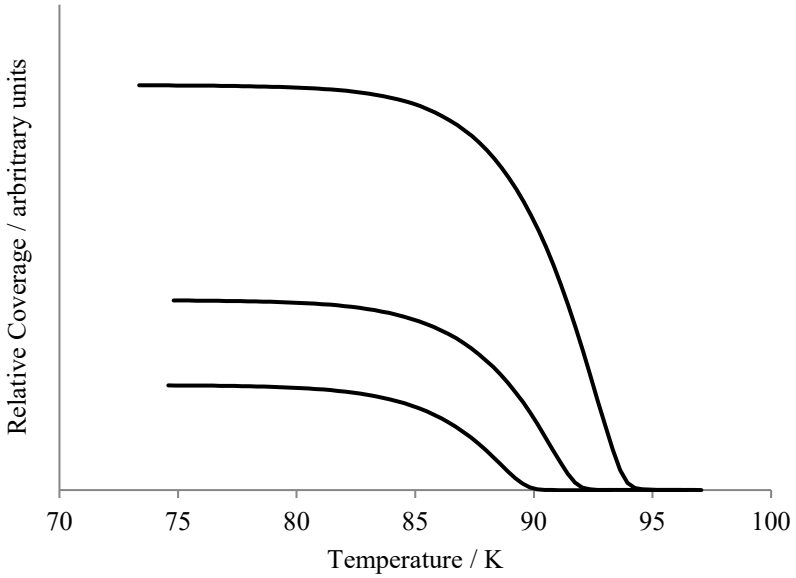

Figure 6.9 The relative coverage as a function of surface temperature for CO_2 adsorbed on amorphous silver at 30 K. These plots have been constructed from the TPD traces in figure 1.8. Reading from bottom

to top, the curves correspond to 50, 100 and 200 L.

Figure 6.10 shows the Arrhenius plot constructed for a chosen fixed relative coverage of 2 x 10^5 counts. The desorption energy obtained from the gradient of this plot is 18.97 kJ mol^{-1}. The complete analysis was performed for several relative coverage values. The resultant desorption energies are listed in Table 6.5. An average desorption energy of 17.97 $\pm$ 1.3 kJ mol^{-1} has been determined from Table 6.5 for multilayers of CO_2 on amorphous silver at 30 K. This value implies that the CO_2 molecules are weakly physisorbed in the overlayer.

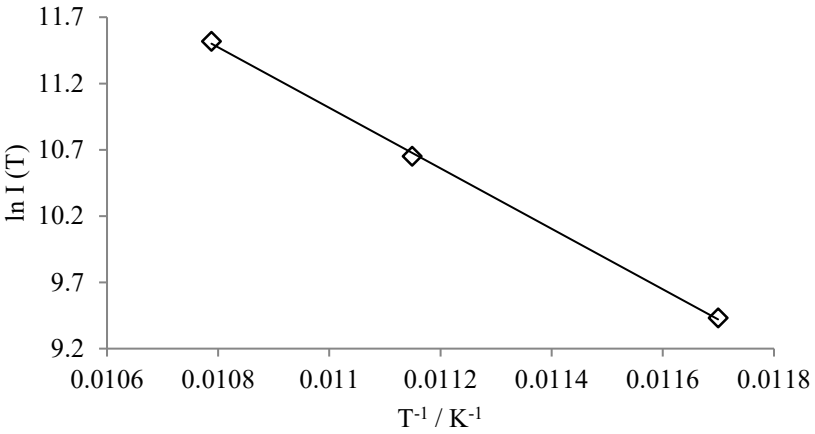

Figure 6.10 Arrhenius plot of the temperatures extracted at a fixed relative coverage of 2x10^5 counts for CO_2 adsorbed on amorphous silver at 30 K. The gradient of this plot give a desorption energy for this adsorbate–surface system.

Table 6.5 The desorption energies for multilayer CO_2 adsorbed onto amorphous silver at 30 K, derived by the complete analysis technique.

Fixed relative coverage / x 10^5 counts	Desorption Energy / kJ mol^{-1}
2	18.97$\pm$0.5
2.3	17.43$\pm$0.7
2.5	19.18$\pm$0.9

The second technique that has been used to extract the desorption energy of CO_2 molecules adsorbed onto amorphous silver at 30 K from the TPD traces shown in Figure 6.8 is also derived from the Polanyi–Wigner equation (6.13). Further rearrangement gives

$$\ln I(T) - n \ln \theta_{rel} \propto n \ln[A] - \frac{E_{des}}{RT} \qquad 6.16$$

Therefore, plotting $\ln I(T) - n \ln \theta_{rel}$ against $\frac{1}{T}$ gives a straight line with a gradient of $\frac{-E_{des}}{R}$. Such a plot was constructed for multilayer CO_2, for the range of desorption orders, *n*, displayed in Table 6.4**.** The desorption energy was calculated from several sets of TPD traces at each coverage, and are shown in Table 6.6. The error is the standard deviation from the mean desorption energy at that coverage.

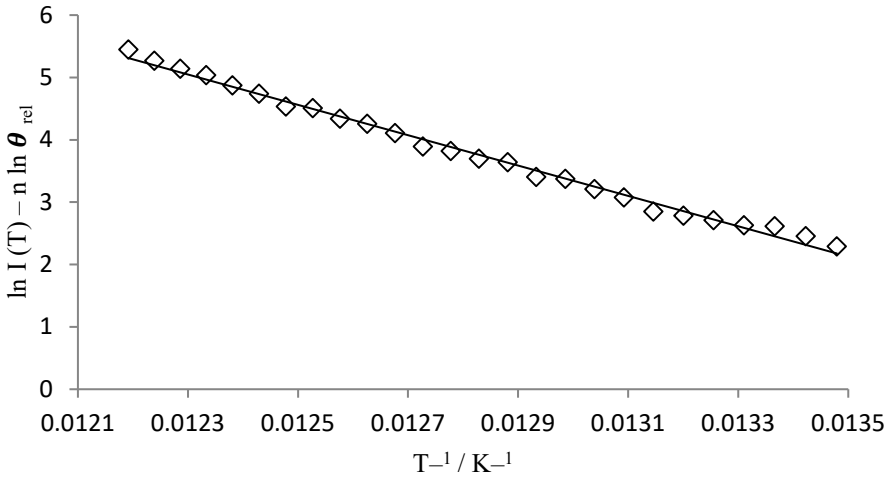

Figure 6.11 A plot of $\ln I(T) - n \ln \theta_{rel}$ against $\frac{1}{T}$ using data from a TPD trace recorded following an exposure of CO_2 of 50 L on amorphous silver at 30 K.

Table 6.6 shows how the desorption energy for the multilayer varies with CO_2 exposure on amorphous silver at 30 K. Clearly, the desorption energy does not vary with exposure and 20.6 $\pm$2.8 kJ $mol^{-1}$is an average desorption energy across all exposures.

Table 6.6 The desorption energies calculated for the TPD traces following various exposures of CO_2 on amorphous silver at 30 K. Each desorption energy is the average value taken from several TPD curves at each exposure. The error indicates the standard deviation.

Exposure of CO_2 / L	Desorption Energy / kJ mol^{-1}
50	20.21$\pm$2.3
100	21.40$\pm$1.3
200	20.12$\pm$0.9

The final technique that was employed to determine the desorption energy of CO_2 multilayers on amorphous silver is the leading–edge technique, which is once again based upon rigorous application of the Polanyi Wigner equation. This technique is applied to a section at the beginning of a single TPD curve's leading edge, as the coverage in this region is assumed to be relatively constant compared with the rest of the peak. That is, the coverage in this region is assumed to equal the total coverage of the surface. Thus, equation 6.14 becomes

$$R_{des} = \frac{-d\theta}{dt} = n\ln[A] - \frac{E_{des}}{RT} \qquad 6.17$$

A plot of $\frac{-d\theta}{dt}$ against $\frac{1}{T}$ gives a straight line with a gradient of $-\frac{E_{des}}{R}$. Figure 6.12 shows such a plot, taken at the leading edge of a TPD trace of 200 L of CO_2 on amorphous silver at 30 K. The section of the leading edge taken was when < 5% of the total coverage had desorbed.

The Arrhenius plot in Figure 6.12 gives a desorption energy of 19.28 kJ mol^{-1}. Several plots of this kind were constructed from TPD traces of 50, 100 and 200 L of CO_2 to find the average desorption energy for each exposure on amorphous silver at 30 K, which are presented in

Table 6.7. The average desorption energy, determined by leading edge analysis, for multilayer CO_2 desorbing from amorphous silver has been found to be 19.17 ± 1.31 kJ mol^{-1}.

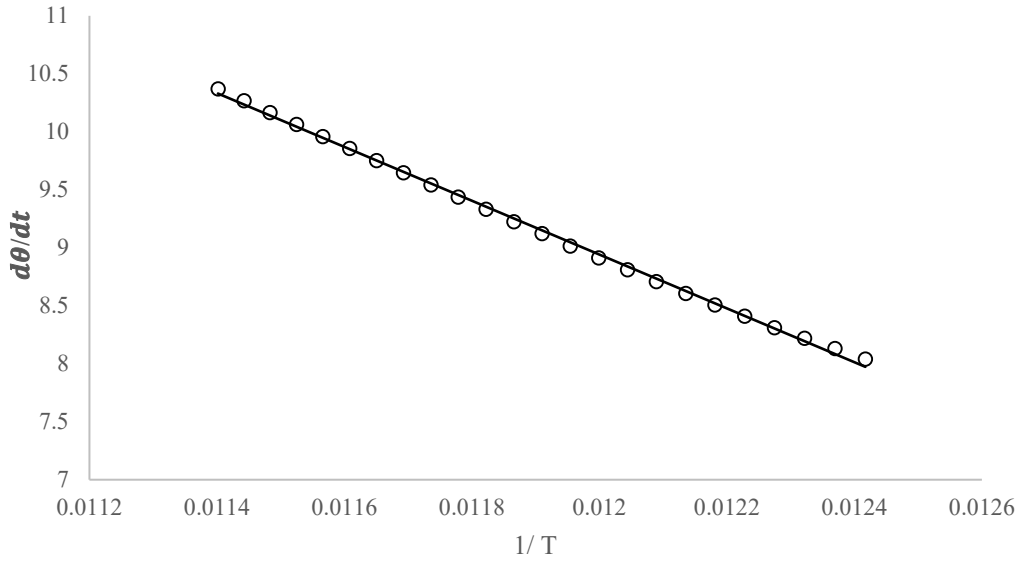

Figure 6.12 An Arrhenius plot used to determine the desorption energy of multilayer CO_2 from amorphous silver at 30 K, constructed following a leading-edge analysis of a TPD trace recorded following an exposure of 50 L of CO_2.

Table 6.7 The desorption energies calculated for the TPD traces following various exposures of CO_2 on amorphous silver at 30 K. Each desorption energy is the average value taken from several TPD curves at each exposure. The error indicates the standard deviation from the mean.

Exposure of CO_2 / L	Desorption Energy / kJ mol^{-1}
50	19.30 ± 0.4
100	17.99 ± 1.1
200	20.23 ± 0.1

The Polanyi–Wigner equation has been manipulated in three different ways to determine the desorption energy of CO_2 from amorphous silver at 30 K. Each method generated a value in the 17.97 – 20.57 kJ mol^{-1} range. Therefore, the average desorption energy for all methods of determination is 19.23 $\pm$ 3.35 kJ mol^{-1}. The three methods of kinetic analysis outlined above yielded a desorption energy lower than the enthalpy of sublimation, ΔU_{sub}, of CO_2, which is 25.2 kJ mol^{-1}. The average desorption energy we determined is also lower than desorption energies of multilayer CO_2 from similar surfaces in the literature, which are all within $\pm$ 2 kJ mol^{-1} of the enthalpy of sublimation. This discrepancy may be due to the amorphous nature of the silver surface used. This undefined surface has many different, unknown surface sites, each with a unique binding energy. The amorphous nature of this surface may explain these discrepancies.

The surface science chamber of the RISA apparatus can successfully generate accurate kinetic information about adsorbate–surface systems. Any of the three analysis methods outlined in this section are suitable to interrogate any species formed on the surface *via* TPD following radical–surface interactions.

6.3.2.5 Pre–exponential Factor

The pre–exponential factor of the Polanyi–Wigner equation cannot be determined directly from the Arrhenius equations constructed following any of the three analyses outlined above, because the absolute coverage of the surface is not known. The method by which the RISA apparatus could be used to obtain pre–exponential factors following the TPD study of an adsorbate–surface system requires the atomic structure of the surface to be known. That is, the surface must be well–defined. The CO_2 experiments described in this section were carried out on an amorphous surface. As such, the atomic structure of this surface is not known and a value for the pre–exponential factor cannot be determined from these data sets. However, for completion, the method by which pre–exponential factors could be obtained following such experiments on a defined surface will now be described.

Coverage is defined as

$$\theta = \frac{N_{ads}}{N_s} \qquad 6.18$$

where N_{ads} is the number of adsorbate atoms/molecules per unit area, and N_s is the number of surface atoms per unit area. N_s can be further defined as

$$N_s = \frac{atoms\ per\ surface\ unit\ cell}{area\ per\ unit\ cell} \qquad 6.19$$

To demonstrate the procedure by which the pre–exponential factor will be determined in future adsorption experiments, consider Ag 111. The surface atomic structure and unit cell are shown in Figure 6.13. The sides of the surface unit cell, which is depicted by the red parallelogram, are the length of the diameter of a silver atom, $1.65 \times 10^{-10}\ \mathrm{m}$. To find the area of the unit cell, the shape is split into two triangles as shown below. The area of the unit cell is therefore given in equation 6.20

$$area\ of\ unit\ cell = 2 \times \frac{1}{2} \times a \times \frac{\sqrt{3}}{2} a \qquad 6.20$$

where *a* is the atomic diameter of a silver atom. Therefore, the area per unit cell of Ag 111 is $9.431 \times 10^{-20}\ \mathrm{m}^2$. It is clear from Figure 6.13 that each unit cell contains four quarters of an atom, which is of course equal to one atom. Therefore, the surface density of Ag 111 can be calculated using equation 6.18 and is found to be $1.06 \times 10^{19}\ \mathrm{atoms\ m}^{-2}$. The number of atoms that make up a 20 x 20 mm Ag 111 surface can be determined by multiplying the area of the target by the surface density, which gives $4.24 \times 10^{17}\ \mathrm{atoms}$.

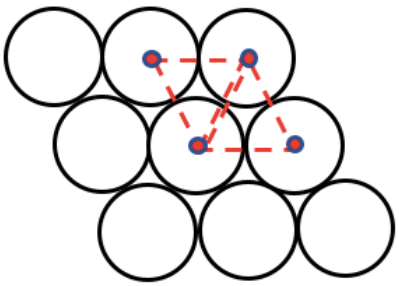

Figure 6.13 A schematic to show the atomic arrangement of an Ag 111 surface. The red parallelogram represents the unit cell.

To determine the number of adsorbate molecules present on the surface, and thus determine the absolute coverage at each exposure, some assumptions must be made. Firstly, the exposure at which monolayer saturation occurs must be identified from a collection of TPD traces. When examining TPD traces of different exposures, the first multilayer peak has a lower peak temperature compared to the monolayer peak. Additionally, the second multilayer peak will share a perfect leading edge with the first multilayer peak. If the adsorbed species were CO_2, to estimate the number of molecules present in this first saturated layer the adsorbates are treated as spheres, with a radius of the C–O bond length, 1.16×10^{-10} m. The distance between each CO_2 sphere can be taken as the Van der Waals radius of oxygen, which is 1.4×10^{-10} m. The area occupied by each sphere of CO_2 can then be determined, as shown in equation 6.21.

$$area\ occupied\ per\ molecule = \pi r^2 \qquad 6.21$$

$$= \pi[1.4 \times 10^{-10} + 1.16 \times 10^{-10}]^2$$

$$= 8.24 \times 10^{-19}\ \mathrm{m}^2 a$$

Hence, adsorbates per unit area of the target can be determined as

$$adsorbates\ per\ unit\ area = \frac{1}{8.24 \times 10^{-19}\ \mathrm{m}^2} \qquad 6.22$$

$$= 1.21 \times 10^{18}\ \mathrm{molecules\ m}^{-2}$$

The absolute coverage at monolayer saturation of CO_2 on Ag 111 can then be determined using equation 6.23, as shown below. Recall, the surface density for Ag 111 was determined previously using equation 6.19

$$\theta = \frac{N_{ads}}{N_s} = \frac{1.21 \times 10^{18}}{1.06 \times 10^{19}} = 0.1\ \mathrm{ML} \qquad 6.23$$

As the coverage is related proportionally to the exposure, the area under the monolayer TPD trace is linked directly to the number of molecules on the surface. Therefore, we can determine a scaling factor for all TPD trace intensities to convert them from relative coverages to absolute

coverages. Then the pre–exponential factor can be determined by using a rearranged form of the Polanyi–Wigner equation

$$A = \frac{I(T)}{\theta^n \times e^{\frac{-E_{des}}{RT}}} \qquad 6.24$$

where *I(T)* is the scaled TPD intensity, θ^n is the absolute coverage determined from the scaled intensity, *n* is the desorption order and E_{des} is the desorption energy.

6.3.2.6 TPD conclusion

A TPD study has been carried out to investigate the adsorption of CO_2 onto amorphous silver at 30 K. The peaks observed share a leading edge and correspond to multilayers of physisorbed CO_2 on the target. A desorption order of -0.06 ± 0.08 has been determined for multilayer CO_2. An average desorption energy of 19.23 ± 3.4 kJ mol^{-1} was determined *via* three different data–processing methods, which corresponds to physisorbed species and broadly agrees with other multilayer studies of CO_2 adsorbates on a variety of surfaces. A procedure to determine the pre–exponential factor of the Polanyi–Wigner equation has been outlined for a well–defined surface. Therefore, one can conclude that the RISA apparatus is suitable to interrogate any species that may form following the proposed radical–surface experiments *via* TPD and can extract relevant kinetic information pertaining to the adsorbate–surface system. Indeed, this section has demonstrated the successful extraction of kinetic parameters that could be included in surface reaction computational models.

6.3.3 RAIRS study of CO_2 adsorbed onto amorphous silver

Figure 6.14 shows sections of RAIRS spectra recorded following the adsorption of exposures of 5 – 50 L of CO_2 on amorphous silver at 30 K. The sections chosen are over the frequency range 2310 – 2410 cm^{-1}, where the most intense CO_2 vibrational band is observed and is unobscured by any bands that may form due to the vibrations of background gases. An initial exposure of 10 L produced a peak at 2362 cm^{-1}. Subsequent spectra recorded with increasing CO_2 exposure feature this band growing in

intensity, and shifting to higher wavenumbers. As the exposure is increased to 30 L and above, another spectral feature appears at 2350 cm^{-1}.

Figure 6.14 shows exposures of 100 and 200 L of CO_2 on amorphous silver at 30 K. It is clear from these spectra that a further increase in exposure increases the intensity of the peaks featured in the 50 L RAIRS trace, but does not affect the wavenumber at which they appear and they do not saturate. Such behaviour with increasing exposure is indicative of physisorbed multilayers on the surface. Additionally, for exposures of CO_2 above 100 L, a third band appears at 2371 cm^{-1}.

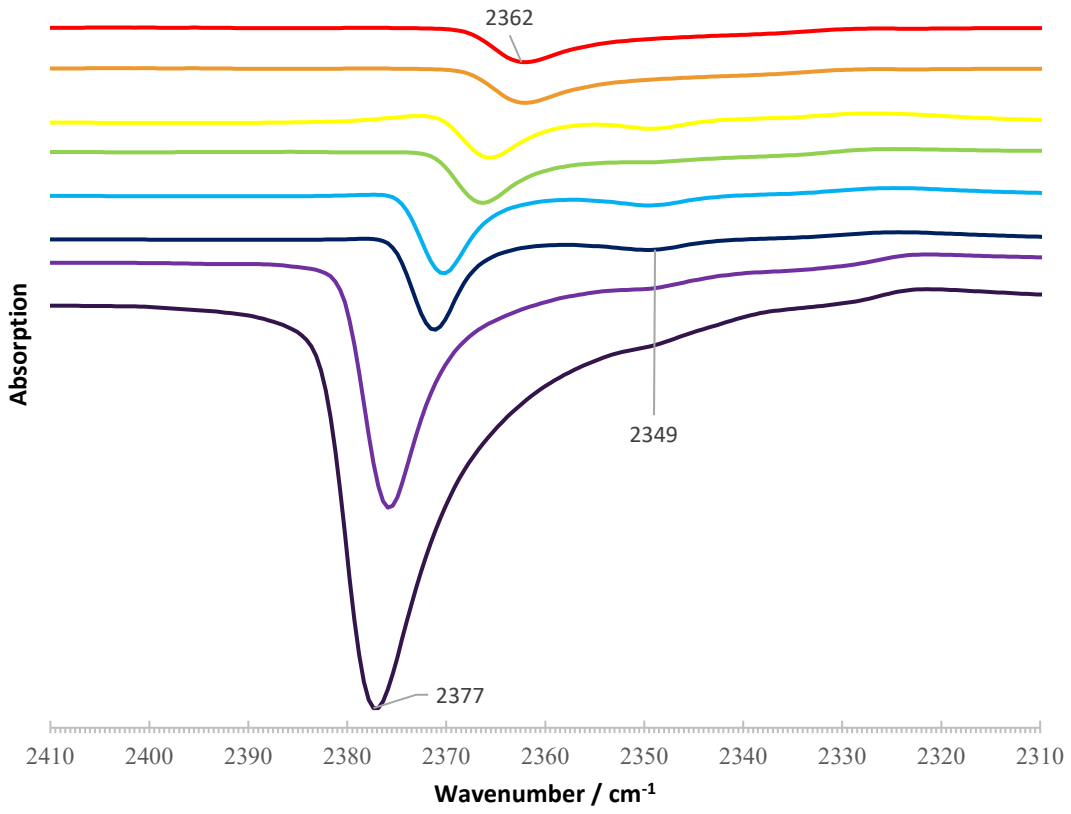

Figure 6.14 RAIR spectra recorded following a range of exposures of CO_2 adsorbed onto amorphous silver at 30 K.

The bands featured in figure 6.14 and 6.15 are comparable to those that feature in RAIRS studies of CO_2 adsorbed onto other surfaces.[33, 41, 42] Indeed, the bands present in this set of RAIRS spectra can be assigned confidently upon comparison with the gas–phase IR spectrum of CO_2 and other CO_2 adsorption–substrate RAIRS studies. A band at 2349 cm^{-1} is present in the gas phase spectrum of CO_2, which matches the band observed at the same frequency in this work, and is assigned to the v_3 stretching mode of the molecule. Such a match indicates that the interaction between the surface and the CO_2 adsorbates is minimal, suggesting a physisorbed multilayer of CO_2. Further evidence for this assignment is that the band first appears in the 20 L spectrum and continues to grow in intensity with increasing CO_2 exposure. Indeed, the band at 2349 cm^{-1} can be confidently assigned to the v_3 stretching mode of CO_2 molecules that are present on the amorphous silver surface in physisorbed multilayers, which agrees with several IR studies in the literature.

The remaining bands featured in the RAIRS spectra above are more difficult to assign. The band that initially appears at 2362 cm^{-1} in Figure 6.14 and shifts in frequency with increasing exposures of CO_2 to 2379 cm^{-1} in Figure 6.15 is reported to correspond to a stretching mode of $^{13}CO_2$ in gas–phase IR studies. However, the CO_2 sample used contained <1% $^{13}CO_2$. A band at 2379 cm^{-1} does not feature in IR studies of amorphous CO_2 ice where the incident beam is positioned normal to the surface. However, in IR studies of crystalline and amorphous CO_2 where the incident beam interacts with the molecules at grazing angles do feature a band at this frequency. In a previous CO_2 thin film study, Baratta and Palumbo stated that the longitudinal (LO) and transverse (TO) optical phonon modes of the film split in energy when IR light interacted with the surface at grazing angles.[47] This eponymous effect was first observed by Berreman, who stated that at certain angles of incidence the electric field generated by IR light enhances LO frequency absorption by molecules in an overlayer, whilst TO resonances result in close to 100 % reflection. The Berreman effect is enhanced when the substrate is backed by a metallic substance, as in this case. Thus,

assignment of the band featured between 2362 – 2379 cm^{-1} requires consideration of the phonon modes of the adsorbate overlayer.

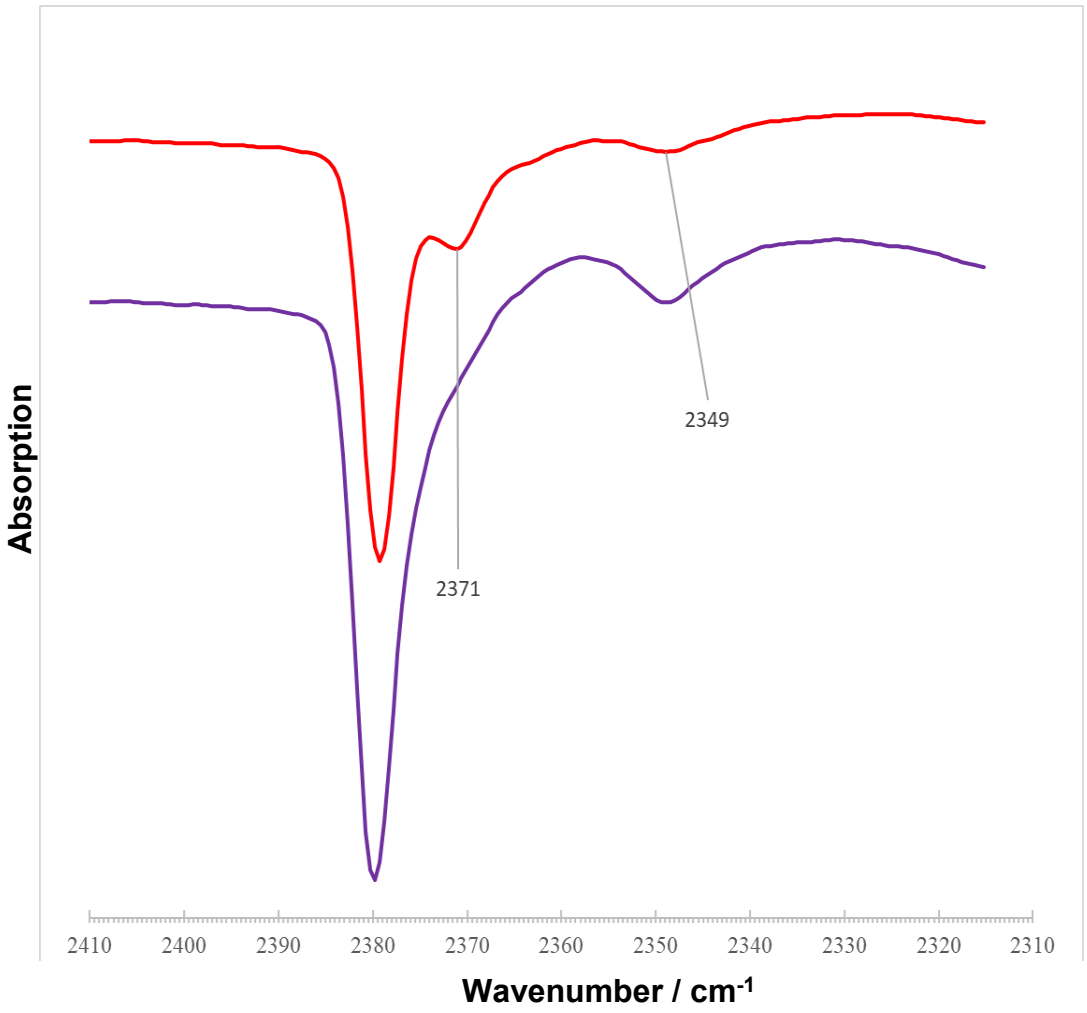

Figure 6.15 RAIR spectra recorded following exposures of 100 (red) and 200 L (purple) of CO_2 on amorphous silver at 30 K.

There are many IR studies of CO_2 ices available in the literature. Of these studies, those performed where the incident radiation is at grazing angles to the substrate have featured and assigned a band at 2780 cm^{-1} to the LO phonon mode, and a band at 2341 cm^{-1} to the TO mode. Therefore, we can confidently assign the band at 2379 cm^{-1}, featured in the RAIRS spectra presented in this work, to the LO phonon mode of the CO_2 adsorbate overlayer. However, a band at 2341 cm^{-1} does not feature in our spectra.

The Berreman effect predicts that there will be close to 100 % reflection at wavelengths of light that are resonant with the TO phonon modes, thus the absence of a band at 2341 cm^{-1} in our spectra may be explained by the enhanced reflectivity the silver surface backing the CO_2 ice provides compared to the substrates used in the literature studies.[53]

A common feature in RAIRS studies of heterogeneous substrates is broadening of the bands that correspond to the LO and TO phonon modes.[54] Indeed, in a recent RAIRS study of CO_2 adsorbed onto HOPG, a broad band featured in the spectrum at a wavenumber that lies between the two bands ascribed to the LO and TO phonon modes, at 2382 cm^{-1} and 2341 cm^{-1} respectively.[33] This broadening is thought to be due to the heterogeneous nature of the CO_2 substrate leading to a modification of the polarisation of the phonons within the CO_2 film. Therefore, the broad band that features at 2371 cm^{-1} in the RAIRS spectra presented here can be attributed to the heterogeneous, amorphous nature of the CO_2 ice.

The band observed at 2362 cm^{-1} following a 5 L exposure of CO_2 shifts to higher wavenumbers with increasing exposure. For exposures of 100 L and above, the frequency at which this band appears stops shifting. That is, for exposures of 100 L or more the LO phonon mode band appears consistently at 2379 cm^{-1}. This behaviour can be explained by considering the co–ordination of the surface atoms with increasing coverage of the surface. As the first layer of surface adsorbates is growing, the co–ordination of each CO_2 adsorbate on the surface increases, and the energy of vibration of those adatoms decreases. Once the monolayer is saturated, multilayers begin to form. With increasing exposure, the multilayer grows thicker and the net co–ordination of the adatoms becomes relatively constant compared to when the first monolayer was adsorbing. Therefore, as multilayers of CO_2 build up following exposures of 5–100 L, the band shifts from 2362 cm^{-1} to 2379 cm^{-1}. Furthermore, as the multilayer grows the polarisation of the ice will be modified, which in turn will modify the extent to which the adatoms interact with the electric field generated by the *p*–polarized light. Of course, this is a tentative explanation as the orientation of the CO_2 molecules with respect to the surface is unknown and affects the interaction with the IR

radiation and subsequent band frequency. Additionally, the nature of the ice growth on the silver is unknown owing to the amorphous substrate used in these experiments.

Table 6.8 Assignment of the peaks that appear in the RAIRS spectra recorded of an amorphous silver surface, following 10–200 L exposures of CO2 at 30 K. See text for details.

Wavenumber / cm^{-1}	Assignment
2350	υ_3 stretching mode
2362–2377	LO phonon mode
2371	LO/TO phonon broadening

6.3.3.1 RAIRS conclusion

A RAIRS study to investigate CO_2 adsorbed on amorphous silver at 30 K has been performed. Three bands were present in the subsequent RAIRS spectra at 2349 cm^{-1}, shifting over the wavenumber range 2362 – 2379 cm^{-1} and at 2371 cm^{-1}. The bands have been successfully assigned to the v_3 stretching mode of multilayer CO_2 adsorbates, the LO phonon mode of the adsorbate overlayer and a mixture of the LO and TO phonon modes respectively. Therefore, one can conclude that the RISA apparatus is suitable to interrogate any polar species that may form following the proposed radical–surface experiments *via* RAIRS. Furthermore, RAIRS spectra provide information about how an overlayer grows which, in combination with TPD, can be used to extract quantitative information about a reaction system.

6.4 Conclusion

This chapter has described the commissioning experiments performed using the RISA apparatus. A neutral O radical beam has been successfully produced *via* the irradiation of an O^- anion beam produced following DEA to N_2O. The first results from TPD and RAIRS experiments conducted using the surface science chamber are presented, and kinetic information has been successfully extracted from the resultant spectra. Indeed, a combined TPD

and RAIRS study of CO_2 on amorphous silver at 30 K has provided values for the desorption order, desorption energy, and the energies of the vibrational modes of the system. The comparison of this experimental data with work previously published has provided confidence in the surface science arrangement. XPS and AES have been successfully employed to perform an elemental analysis of the surface to ensure cleanliness prior to each experiment. In combination, the proof–of–principle work presented in this chapter shows that the RISA apparatus is suitable to perform the radical–surface experiments proposed in chapter 3.

6.5 Bibliography

1. S. C. Creighan, J. S. A. Perry and S. D. Price, *Journal of Chemical Physics*, 2006, **124**, 10.

2. M. D. Ward, I. A. Hogg and S. D. Price, *Monthly Notices of the Royal Astronomical Society*, 2012, **425**, 1264–1269.

3. M. Minissale and F. Dulieu, *Journal of Chemical Physics*, 2014, **141**, 8.

4. K. Hayashi, H. Konno, T. Oseki, H. Kojima and T. Kanayama, *Nuclear Instruments & Methods in Physics Research Section B–Beam Interactions with Materials and Atoms*, 2003, **206**, 403–408.

5. Fehsenfe.Fc, *Journal of Chemical Physics*, 1970, **53**, 2000–&.

6. A. Chutjian and S. H. Alajajian, *Physical Review A*, 1985, **31**, 2885–2892.

7. E. C. M. Chen and E. S. Chen, *Physical Review A*, 2007, **76**.

8. L. G. Christophorou and J. K. Olthoff, *Journal of Physical and Chemical Reference Data*, 2000, **29**, 267–330.

9. L. G. Christophorou and J. K. Olthoff, *International Journal of Mass Spectrometry*, 2001, **205**, 27–41.

10. T. M. Miller, A. E. S. Miller, J. F. Paulson and X. F. Liu, *Journal of Chemical Physics*, 1994, **100**, 8841–8848.

11. V. Laporta, R. Celiberto and J. Tennyson, *Physical Review A*, 2015, **91**, 5.

12. D. Rapp and D. D. Briglia, *Journal of Chemical Physics*, 1965, **43**, 1480–&.

13. Y. Itikawa, *Journal of Physical and Chemical Reference Data*, 2009, **38**, 1–20.

14. R. J. Vanbrunt, *Physical Review A*, 1970, **2**, 1899–&.

15. H. Sambe and D. E. Ramaker, *Surface Science*, 1992, **269**, 444–451.

16. L. G. Christophorou, *Contributions to Plasma Physics*, 1987, **27**, 237–281.

17. J. P. Astruc, R. Barbe, A. Lagreze and J. P. Schermann, *Chemical Physics*, 1983, **75**, 405–416.

18. N. Russo, D. Fino, G. Saracco and V. Specchia, *Catalysis Today*, 2007, **119**, 228–232.

19. D. A. Parkes, *Journal of the Chemical Society–Faraday Transactions I*, 1972, **68**, 2103–&.

20. N. E. Bradbury and H. E. Tatel, *Journal of Chemical Physics*, 1934, **2**, 5.

21. A. V. Phelps and R. E. Voshall, *Journal of Chemical Physics*, 1968, **49**, 3246–&.

22. H. U. Suter and T. Greber, *Journal of Physical Chemistry B*, 2004, **108**, 14511–14517.

23. E. L. Chaney and L. G. Christophorou, *Journal of Chemical Physics*, 1969, **51**, 883–+.

24. W. E. Wentworth, E. Chen and R. Freeman, *Journal of Chemical Physics*, 1971, **55**, 2075–+.

25. S. J. Nalley, R. N. Compton, H. C. Schweinler and V. E. Anderson, *Journal of Chemical Physics*, 1973, **59**, 4125–4139.

26. D. G. Hopper, A. C. Wahl, R. L. C. Wu and T. O. Tiernan, *Journal of Chemical Physics*, 1976, **65**, 5474–5494.

27. G. S. Tschumper and H. F. Schaefer, *Journal of Chemical Physics*, 1997, **107**, 2529–2541.

28. M. C. McCarthy, J. W. R. Allington and K. O. Sullivan, *Molecular Physics*, 1999, **96**, 1735–1737.

29. E. S. Kryachko, C. Vinckier and M. T. Nguyen, *Journal of Chemical Physics*, 2001, **114**, 7911–7917.

30. E. Garand, T. I. Yacovitch and D. M. Neumark, *Journal of Chemical Physics*, 2009, **130**.

31. R. B. Metz, A. Weaver, S. E. Bradforth, T. N. Kitsopoulos and D. M. Neumark, *Journal of Physical Chemistry*, 1990, **94**, 1377–1388.

32. J. Fulara, M. Jakobi and J. P. Maier, *Chemical Physics Letters*, 1993, **211**, 227–234.

33. J. L. Edridge, K. Freimann, D. J. Burke and W. A. Brown, *Philosophical Transactions of the Royal Society a–Mathematical Physical and Engineering Sciences*, 2013, **371**.

34. L. J. Allamandola, M. P. Bernstein, S. A. Sandford and R. L. Walker, *Space Science Reviews*, 1999, **90**, 219–232.

35. S. Ioppolo, Y. van Boheemen, H. M. Cuppen, E. F. van Dishoeck and H. Linnartz, *Monthly Notices of the Royal Astronomical Society*, 2011, **413**, 2281–2287.

36. O. Galvez, I. K. Ortega, B. Mate, M. A. Moreno, B. Martin–Llorente, V. J. Herrero, R. Escribano and P. J. Gutierrez, *Astronomy & Astrophysics*, 2007, **472**, 691–698.

37. S. Malyk, G. Kumi, H. Reisler and C. Wittig, *Journal of Physical Chemistry A*, 2007, **111**, 13365–13370.

38. M. P. Collings, M. A. Anderson, R. Chen, J. W. Dever, S. Viti, D. A. Williams and M. R. S. McCoustra, *Monthly Notices of the Royal Astronomical Society*, 2004, **354**, 1133–1140.

39. H. Ulbricht, R. Zacharia, N. Cindir and T. Hertel, *Carbon*, 2006, **44**, 2931–2942.

40. F. A. van Broekhuizen, I. M. N. Groot, H. J. Fraser, E. F. van Dishoeck and S. Schlemmer, *Astronomy & Astrophysics*, 2006, **451**, 723–731.

41. S. A. Sandford and L. J. Allamandola, *Astrophysical Journal*, 1990, **355**, 357–372.

42. P. Ehrenfreund, A. C. A. Boogert, P. A. Gerakines, D. J. Jansen, W. A. Schutte, A. Tielens and E. F. vanDishoeck, *Astronomy & Astrophysics*, 1996, **315**, L341–L344.

43. E. Dartois, K. Demyk, L. d'Hendecourt and P. Ehrenfreund, *Astronomy & Astrophysics*, 1999, **351**, 1066–1074.

44. R. Hodyss, J. D. Goguen, P. V. Johnson, C. Campbell and I. Kanik, *Icarus*, 2008, **197**, 152–156.

45. K. I. Oberg, H. J. Fraser, A. C. A. Boogert, S. E. Bisschop, G. W. Fuchs, E. F. van Dishoeck and H. Linnartz, *Astronomy & Astrophysics*, 2007, **462**, 1187–1198.

46. M. A. Ovchinnikov and C. A. Wight, *Abstracts of Papers of the American Chemical Society*, 1993, **205**, 166–PHYS.

47. G. A. Baratta and M. E. Palumbo, *Journal of the Optical Society of America a–Optics Image Science and Vision*, 1998, **15**, 3076–3085.

48. G. Kumi, S. Malyk, S. Hawkins, H. Reisler and C. Wittig, *Journal of Physical Chemistry A*, 2006, **110**, 2097–2105.

49. B. E. Wood and J. A. Roux, *Journal of the Optical Society of America*, 1982, **72**, 720–728.

50. K. Pokrovski, K. T. Jung and A. T. Bell, *Langmuir*, 2001, **17**, 4297–4303.

51. V. Mennella, G. A. Baratta, M. E. Palumbo and E. A. Bergin, *Astrophysical Journal*, 2006, **643**, 923–931.

52. O. Galvez, B. Mate, V. J. Herrero and R. Escribano, *Icarus*, 2008, **197**, 599–605.

53. B. Harbecke, B. Heinz and P. Grosse, *Applied Physics a–Materials Science & Processing*, 1985, **38**, 263–267.

54. M. A. Ovchinnikov and C. A. Wight, *Journal of Chemical Physics*, 1993, **99**, 3374–3379.

7 Conclusions and future work

This thesis has reported the development of a pure radical source for radical-surface science, and the investigations of the reactivity of two dications, Ar^{2+} and SO^{2+}, with a variety of neutral molecules. This final chapter outlines the major conclusions that can be drawn from this work, and describes possible avenues of future investigations.

7.1 RISA

The results of the commissioning experiments of the RISA apparatus, presented in Chapter 6, demonstrate that the apparatus is suitable to generate pure fluxes of radicals. The surface science experiments, which are also presented in chapter 6, show that the RISA apparatus is appropriately equipped to investigate surface science through a number of scientific methods: TPD, RAIRS, XPS and AES. Indeed, meaningful results have been extracted from the proof-of-principle experiments presented. O^- and SF_5^- anion beams have been generated, and an O radical flux was formed following photo-detachment of the O^- beam.

There are two immediate next steps that could be taken to develop the RISA apparatus. Firstly, we could work to increase the radical flux through increasing the initial anion flux. The discharge anion source that has recently been built and added to the equipment has the potential to increase the anion flux. Another factor that affects the radical flux is the overlap between the photo-detaching laser beam and the anion beam. Increasing this overlap may increase the electron detachment efficiency, and therefore increase the radical flux. A possible next step could be to design a more sophisticated multipass cell, which would increase the path length of the laser-anion beam interaction, and therefore increase the radical flux. In the longer term, future work should include radical-surface experiments relevant in the ISM, and in industrial plasmas.

7.2 PSCO-MS

In chapter 4, the reactions of Ar^{2+} with CF_4, C_2F_6, NF_3 and SF_6 at collision energies less than 10 eV in the CM frame are presented. The SET

reactivity between the dication and each neutral has been explored, revealing a variety of mechanisms by which these reactions can occur. Both direct and indirect SET mechanisms have been observed. Pathways to Ar-F and Ar-C bonds have been clearly identified. It has been revealed that fluoride transfer reactions may occur *via* a direct mechanism or complexation, whereas the formation of an Ar-C bond can only be formed following the association of the reactant species into a collision complex.

In chapter 5, the collisions of the molecular dication SO^{2+} with neutral species have been presented. Reactions with NF_3, SF_6 and C_2F_6 all result in bond-forming reactions in addition to electron transfer. The observations made following these collisions were rationalized using a simple electrostatic model of dication-neutral collisions. Electron transfer reactivity dominated each collision system, and the reactivity seen was fully explained using a combination of CM scattering diagrams and reaction-window calculations. Some reactive channels led to SET between neutral and dication *via* an indirect mechanism, in which the reactants associated to form a complex. Additionally, some bond-forming reactive channels proceeded *via* an unusual direct mechanism in which the fluoride ion was stripped from the neutral at relatively large interspecies separations.

The work presented in these chapters indicates that there is still a lot to be learned about the reactivity between dications and neutrals. To further the investigations presented in chapters 4 and 5, the collisions could be investigated at a variety of collision energies. This would highlight any relationship between collision energy and the types of reactivity observed. The work presented could be reinforced through the calculation of the stationary points and product asymptotes on the dication-neutral PESs, for each collision system. This computational investigation would indicate whether the models used to rationalize the reactivity observed satisfactorily describe the collisions.

8 Appendix

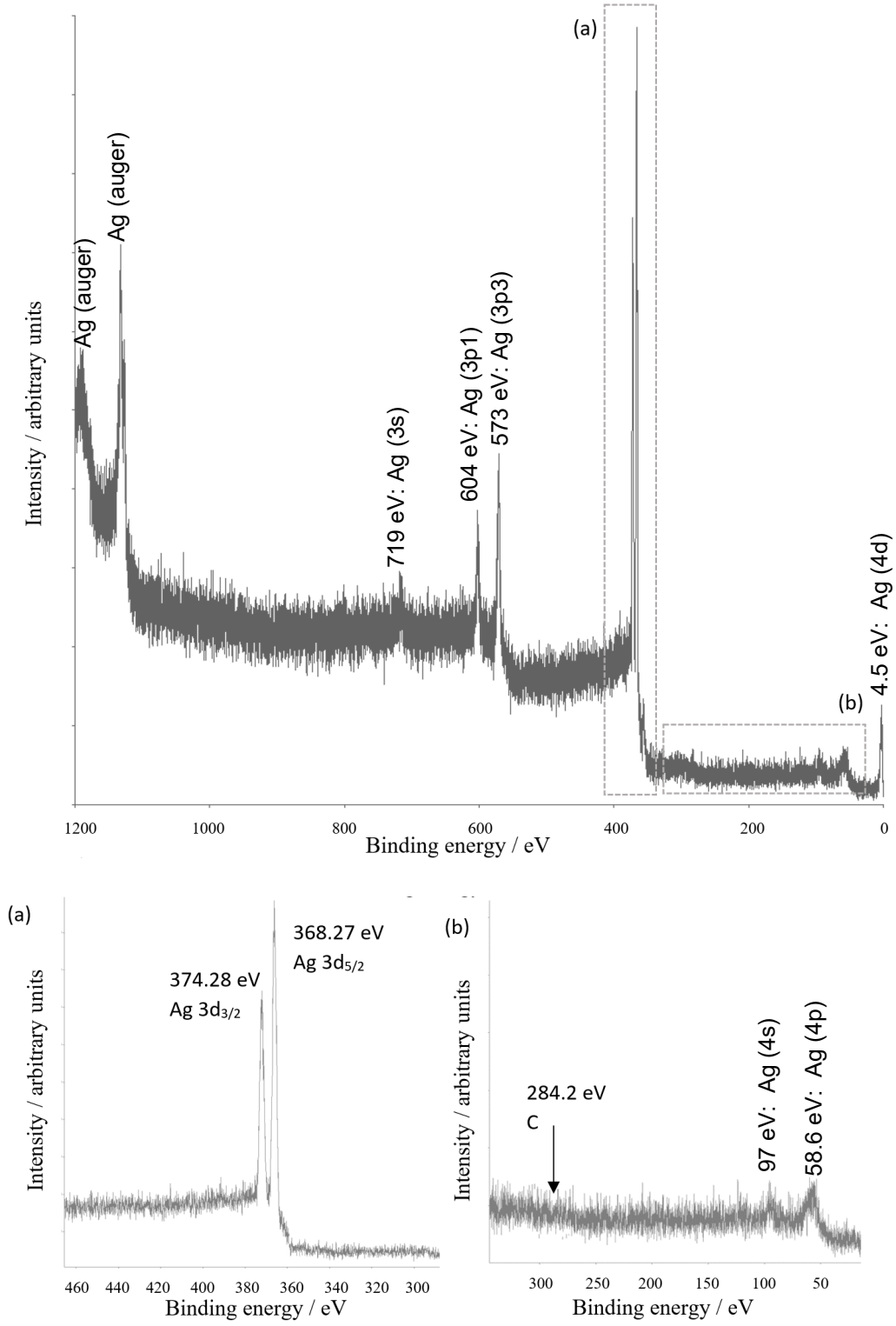

Figure A 1 An XPS spectrum taken following 9 cycles of sputtering and annealing, as described elsewhere. (a) shows a magnified section of the spectrum that highlights the chemically specific silver XPS peaks. (b) shows a magnified section of the spectrum where a C XPS peak would feature.

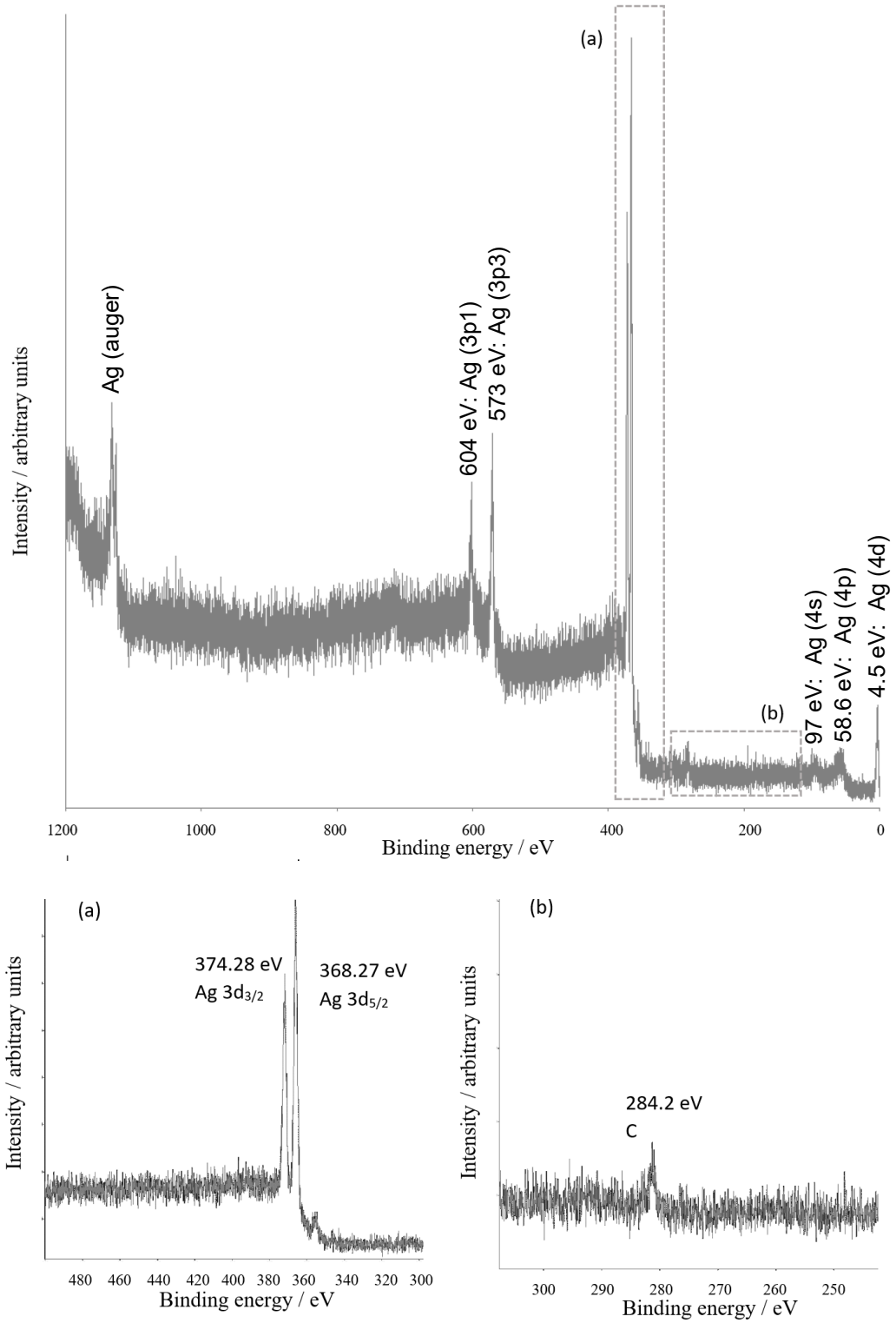

Figure A 2 An XPS spectrum taken following 6 cycles of sputtering and annealing, as described elsewhere. (a) shows a magnified section of the spectrum that highlights the chemically specific silver XPS peaks. (b) shows a magnified section of the spectrum where a C XPS peak would feature.

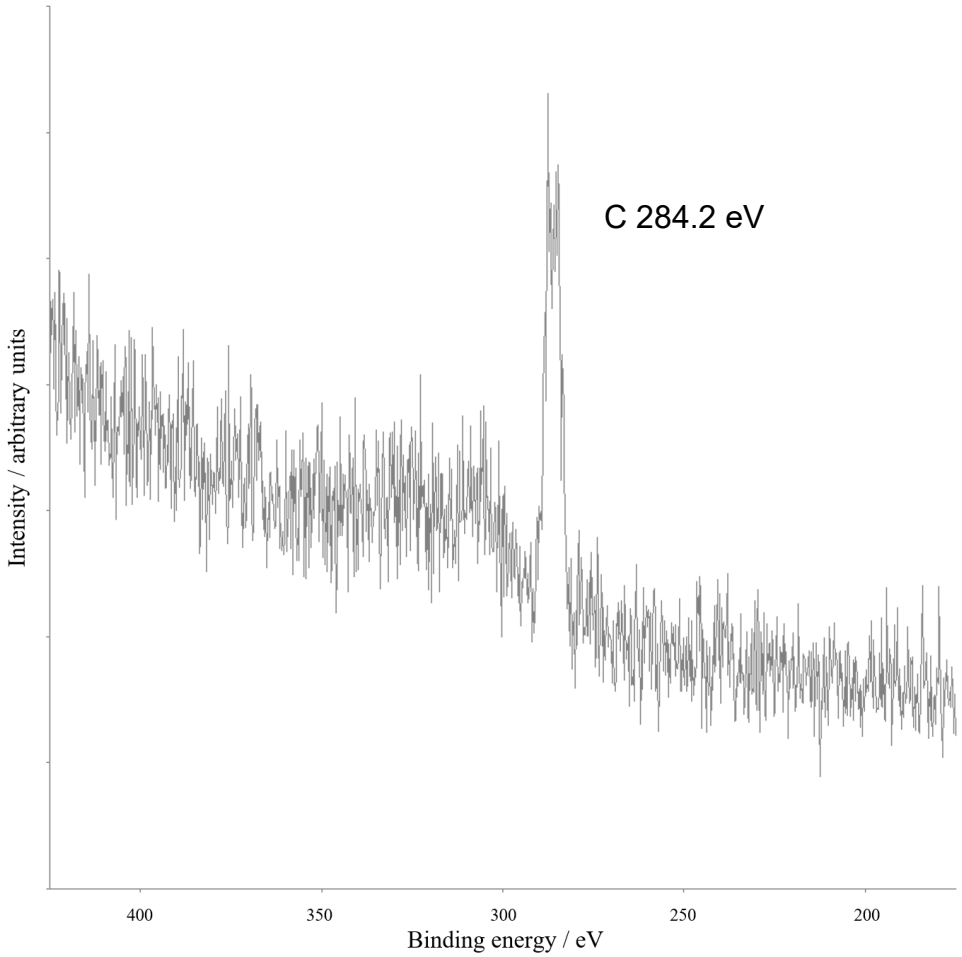

Figure A 3 An excerpt of an XPS spectrum taken following 1 cycle of sputtering and annealing. The silver XPS peaks are clearly less well-defined, and weaker compared to the spectra shown in figures A1 and A2. The carbon peak is clearly the dominant peak in the spectrum.